

Functionalized mesoporous titania film coatings for bone implants with antibacterial and enhanced osseointegrative properties

Dissertation presented to the
Polymer Science and Technology Department of the
University of the Basque Country (UPV/EHU), San Sebastian
for the degree of
Doctor in Applied Chemistry and Polymeric Materials

Presented by
Ane Escobar Fernández

Thesis Supervisors: Dr. Sergio E. Moya & Dr. Marek Grzelczak
University Tutor: Dr. Isabel Goñi

eman ta zabal zazu



Universidad Euskal Herriko
del País Vasco Unibertsitatea

San Sebastián, 2018

This thesis has been carried out at:



CIC BiomaGUNE
Soft Matter
Nanotechnology Group
Donostia – San Sebastián,
Spain



Comisión Nacional de
Energía Atómica
Grupo Química de
nanomateriales
Buenos Aires, Argentina



University of Greifswald
ZIK-HIKE
Nanostructure Group
Greifswald, Germany

Acknowledgements

While my thesis comes to an end many people come to my mind. All of them have contributed somehow to development of my thesis and they deserve my gratitude because they have been next to me in one of the most significant periods of my life.

I would like to acknowledge first to my supervisors; Sergio and Marek, thank you so much. I really appreciate you both; you are quite different from each other but you have been the perfect team, the best supervisors I could imagine. Thanks for having always encourage me to do what I like and for giving me freedom throughout my research. My sincere thanks.

A very big thanks goes to my group members, present and former. María, Elena, Ele, Nikos, Joseba, Rich, Danijela, Guocheng, Marta, Edu, Ángel, Pat, Desiré and Cristian thank you all. Some of you took part in the begging of my thesis, others at the end. It was wonderful to work with you. You made enjoyable coming to work! Gracias a todos! Gracias por los momentos en el lab, fuera del lab, las cenas, despedidas, que nunca me gustaron, y esta vez me toca a mí... Todos habéis influido en mi tesis positivamente, pero Marta, tú estás ahora mismo sufriendo mi fin, te voy a echar mucho de menos!

I cannot forget of all the people visiting our lab. To people coming from Argentina, Brazil, Armenia and France many thanks for your collaboration and moments shared in the lab. Nico, tu ayuda ha sido imprescindible. No hace falta que diga lo mucho que te aprecio, me has demostrado ser una persona maravillosa, mil gracias. Joaquín, se te echa mucho de menos, qué pena que no sigas aquí con lo que nos gustaban las charlas junto con Marta, mi momento preferido en el trabajo! Gracias Eli, por tu cariño, generosidad y consejos, nos veremos pronto de nuevo.

I also want to say thank to people from the people from the Nanostructure Group at ZIK-HIKE in Greifswald. It was a very fruitful stay where I met lots of people. Special thanks to Michaela, thanks for your support and help. Thanks also to people from the Grupo de Química de Nanomateriales at CNEA in Buenos Aires, I would never forget the months I spent there. Especialmente gracias a Paula y Andrea, por siempre estar dispuestas a ayudarme y a resolver todas mis dudas, sin vosotras este

trabajo no hubiera ocurrido. Verdaderamente habéis sido muy importantes durante todo el desarrollo de mi tesis, gracias de corazón.

I gratefully acknowledge the University of the Basque Country, especially to my tutor Dr. Isabel Goñi. Thanks to the funding sources that made my PhD possible. I was funded by the Spanish Ministry of Economy and during my stays abroad by the Marie Curie Seventh Framework Program; Viroma and HYMADE projects.

Más especialmente quiero agradecerérselo todo a mi familia, mis aitas y mi sis. Agradezco que siempre hayáis estado a mi lado, sin dudar nunca de mis capacidades para llevar esto adelante. Simplemente, os quiero.

A mis amigas, gracias, a Ania y Patri por siempre estar ahí, aunque mis problemas sean absurdos siempre estáis dispuestas a escuchar y semanas sin hablar no hacen que nada cambie entre nosotras. El mejor trio piña que pueda haber. A Andrea, por su sincera amistad, muchas gracias pollito!

A la kuadri por las risas y por los buenos momentos que siempre me han animado y ayudado a desconectar, diría que esto se puede parecer a la carrera... cuatro años más viéndonos a cuentagotas!

Las raras, vaya nombre para un grupo de WhatsApp... Gracias por los viajes, las cenitas y las farras, no se me olvida ninguna. Especialmente a Irene, Lorena, Nere y Esti, muchas gracias por todo lo compartido, sobretodo el sufrimiento en la carrera. No es broma, hasta en exámenes nos lo pasábamos bien. Sin vosotras todo hubiera sido muy diferente.

Al principio Joana solo parecía que fuera a alegrar mi estancia en Greifswald, pero no fue así. Eres una amiga 10, te quiero. Te lo escribo en castellano para que practiques!

A los bombones Nadi y Adri, lo bien que lo pasé en Buenos Aires os lo debo, fuisteis mis mejores amigas allí. Quilombo de países! No me olvido de vosotras, tenemos un buen viaje pendiente. Gracias por seguir manteniendo el contacto a pesar de que ya hayan pasado 3 años sin vernos. Hay que ponerle solución!

Simplemente gracias a todos.

A mi familia,

Contents

Summary	1
Resumen	5
I. INTRODUCTION.....	11
Synthetic implants	12
Titanium implants.....	14
Revision surgery and implant infection	16
Layer-by-Layer technique for supramolecular structure deposition	20
Mesoporous titania	24
Chemical functionalization of mesoporous titania.....	27
Pores as reservoirs for drug delivery	28
Bone remodeling process.....	29
Bioactive ions.....	33
II. AIM AND OBJECTIVES OF THE THESIS	39
III. MATERIALS AND METHODS.....	41
Materials	41
Methods.....	41
Spin coating and dip coating	42
X-Ray photoelectron spectroscopy (XPS)	42
Atomic force microscopy (AFM).....	44
Nanoindentation.....	45
Small-angle X-ray scattering (SAXS)	45
Confocal laser scanning microscopy (CLSM).....	46
Scanning electron microscopy (SEM) and Transmission electron microscopy (TEM).....	46
Inductively coupled plasma mass spectrometry (ICP-MS)	48
Quartz crystal microbalance with dissipation monitoring	49
Ellipsometry and environmental ellipsometric porosimetry (EEP)	49
Contact angle goniometer	52

Dynamic light scattering (DLS)	53
Gentamicin detection	54
Diffuse Reflectance Infrared Fourier Transform Spectroscopy (DRIFT).....	54
X-Ray Reflectometry (XRR)	56
Cell culture and assays	57
MC3T3-E1 pre-osteoblastic cell line	57
MC3T3-E1 cell culture.....	57
Actin cytoskeleton and focal adhesion staining.....	57
MC3T3-E1 cell proliferation	58
MC3T3-E1 cell differentiation.....	59
Alkaline phosphatase activity	59
<i>Staphylococcus aureus</i>	60
<i>S. aureus</i> culture	61
<i>S. aureus</i> growth on surfaces.....	61

IV. CHAPTER 1..... 63

MTFs with embedded Gentamicin and surface modified with rhBMP-2

1.2. Experimental section.....	65
1.2.1. MTF synthesis and characterization	65
1.2.2. rhBMP-2 and Gentamicin functionalization and characterization	66
1.2.3. Gentamicin release study	66
1.2.4. MC3T3-E1 cell bioactivity experiments	66
1.2.5. Antibacterial study.....	67
1.3. Results and discussion.....	67
1.3.1. MTF synthesis and functionalization with rhBMP-2 and gentamicin.....	67
1.3.2. Gentamicin release from MTFs	73
1.3.3. Biocompatibility and bioactivity evaluation.....	75
1.4. Conclusions and perspectives.....	83

V. CHAPTER 2..... 87

Antibacterial PEMs based on PLL and PAA-gentamicin complexes

2.1. Motivation.....	87
2.2. Experimental section.....	89
2.2.1. Poly (acrylic acid) and gentamicin complex preparation and characterization	89
2.2.2. Poly (acrylic acid) and gentamicin complexes and poly-L-lysine multilayer preparation and characterization.....	90
2.2.3. QCM-D Measurements.....	90
2.2.4. Gentamicin release study	91
2.2.5. Antibacterial study.....	91
2.3. Results and discussion.....	91
2.3.1. PAA-gentamicin complex synthesis and characterization	92
2.3.2. Layer-by-Layer assembly of PLL/PAA-gentamicin complexes.....	96
2.3.3. Gentamicin release from PEMs	100
2.3.4. Evaluation of the antibacterial properties of the PEMs	101
2.4. Conclusions and perspectives.....	103

VI. CHAPTER 3..... 105

SrTiO₃ mesoporous coating for enhanced osseointegration

3.1. Motivation.....	105
3.2. Experimental section.....	107
3.2.1. SrTiMF synthesis and characterization	107
3.2.2. Strontium detection and release study.....	108
3.2.3. MC3T3-E1 cell bioactivity experiments	108
3.3. Results and discussion.....	109
3.3.1. SrTiMF synthesis and functionalization	109
3.3.2. Strontium release	113
3.3.3. Biocompatibility and bioactivity evaluation.....	115
3.4. Conclusions and perspectives.....	119

VII. CHAPTER 4.....	121
COOH-functionalized Si and Ti mesoporous films to complex metallic ions	
4.1. Motivation.....	121
4.2. Experimental section.....	123
4.2.1. COOH-functionalized mesoporous silica film synthesis	124
4.2.2. COOH-functionalized mesoporous titania film synthesis	126
4.2.3. Films characterization.....	127
4.2.4. Pb ²⁺ complexation study	128
4.2.5. Sr ²⁺ complexation and release studies.....	128
4.2.6. MC3T3-E1 cell biactivity experiments.....	129
4.3. Results and discussion.....	129
4.3.1. COOH-functionalized Si mesoporous films	129
4.3.2. Pb ²⁺ complexation study	139
4.3.3. COOH-functionalized Ti based mesoporous films.....	141
4.3.4. Sr ²⁺ complexation study	145
4.3.5. Sr ²⁺ release study	152
4.3.6. Biocompatibility and bioactivity evaluation.....	153
4.4. Conclusions and perspectives.....	158
VIII. GENERAL CONCLUSIONS	161
IX. REFERENCES.....	165
List of Publications.....	183

List of Figures

I. INTRODUCTION

- Figure I-1.** Properties that a biomaterial should display to be a good candidate for its use in an implantable device14
- Figure I-2.** Schematic diagram of an artificial hip joint (left) and knee implant (right)15
- Figure I-3.** Mechanism of action of aminoglycosides to inhibit bacterial protein synthesis. The aminoglycosides bind irreversibly to the rRNA (ribosomal RNA) in the 30S subunit of bacterial ribosomes. They interfere with the translation reducing the rejection rate for tRNA (transcriptional RNA) that are not matches for the codon, leading to a misreading of the aminoacids, interfering with the protein synthesis 20
- Figure I-4.** Chemical formula of the Gentamicin molecule20
- Figure I-5.** Layer-by-layer assembly method. Alternatively, positively and negatively charged molecules are adsorbed one after the other on a substrate. This process can be repeated n times to a final film thickness21
- Figure I-6.** Scheme of the thickness increase in PEMs following a linear or exponential growth as function of the number of polyelectrolyte bilayers assembled23
- Figure I-7.** a) Poly-L-lysine and b) Poly (acrylic acid) monomer chemical structure24
- Figure I-8.** Schematic representation of a titanium implant recovered with a mesoporous film used for knee and hip implants.....25
- Figure I-9.** Evaporation Induced Self-Assembly (EISA) process scheme.....27
- Figure I-10.** Bone remodeling cycle. Bone surface is resorted by osteoclasts and pre-osteoblast differentiate to osteoblasts for new bone formation and osteocyte differentiation30
- Figure I-11.** BMP pathway to induce bone formation.....33

III. MATERIALS AND METHODS

- Figure III-1.** Schematic representation of XPS. A core electron is excited with X-ray source, a photoelectron is ejected from the atom for a value of the binding energy, the kinetic energy and the work function of the spectrometer43
- Figure III-2.** Geometry of an Ellipsometric measurement.....50
- Figure III-3.** Vector representations of Young's equation on a sessile drop for measuring Young's contact angle52

IV. CHAPTER 1

MTFs with embedded Gentamicin and surface modified with rhBMP-2

Figure IV-1. Mesoporous titania film (MTF) structural characterization by electron microscopy, 2D-SAXS and EEP. a) TEM image, insert; 2D-SAXS pattern, b) SEM image of the surface, c) SEM image of a transversal cut and d) EEP of water vapour adsorption and desorption68

Figure IV-2. Nanoindentation studies performed on mesoporous titania films. a) Shows the partial-load/unload vs displacement curve used for the tests and b) the results of the analysis of each unload section for Elastic modulus (Er)69

Figure IV-3. XPS high resolution spectra of Titanium (Ti) and Sulphur (S) and S/Ti atomic percentage calculation on top of each graph for each film. a) Ti and b) S of MTF, c) Ti and d) S of MTF with gentamicin, e) Ti and f) S of MTF with 100 ng mL⁻¹ rhBMP-2 and g) Ti and h) S of MTF with 100 ng mL⁻¹ rhBMP-2 and gentamicin substrates.....71

Figure IV-4. Contact angle measurements. a) Bare MTF b) MTF with gentamicin, c) MTF with 100 ng mL⁻¹ rhBMP-2 and d) MTF with 100 ng mL⁻¹ rhBMP-2 and gentamicin72

Figure IV-5. AFM images (height, phase and height section) of MTF, MTF with 100 ng mL⁻¹ rhBMP-2 and MTF with 100 ng mL⁻¹ rhBMP-2 and loaded gentamicin. a) height, b) phase and c) section of MTF substrates, d) height, e) phase, f) section of MTF with 100 ng mL⁻¹ rhBMP-2 substrate, showing an increase in the height, and g) height, similar to MTF with 100 ng mL⁻¹ rhBMP-2 sample, h) height and i) section image of MTF with 100 ng mL⁻¹ rhBMP-2 and loaded with gentamicin.....73

Figure IV-6. Release profile of gentamicin from MTF. Region I shows the burst release (the insert is a zoom of region I) and region II the sustainable release. The release is followed up to 35 days by emission measurements at 455 nm.....75

Figure IV-7. CLSM images of vinculin (first row), actin (second row), the merge of the actin, the vinculin and the nucleus (third row) and the zoom of the merge image (fourth row) at 2h (first column), 24h (second column) and 48h (third column) of growth of MC3T3-E1 cell line on MTFs substrates at 63x.....77

Figure IV-8. CLSM images of vinculin (first row), actin (second row), the merge of the actin, the vinculin and the nucleus (third row) and the zoom of the merge image (fourth row) at 2h (first column), 24h (second column) and 48h (third column) of growth of MC3T3-E1 cell line on MTF with 100 ng mL⁻¹ rhBMP-2 substrates at 63x.78

Figure IV-9. CLSM images of vinculin (first row), actin (second row), the merge of the actin, the vinculin and the nucleus (third row) and the zoom of the merge image (fourth row) at 2h (first column), 24h (second column) and 48h (third column) of

growth of MC3T3-E1 cell line on MTF with 100 ng mL⁻¹ rhBMP-2 and gentamicin substrates at 63x.....79

Figure IV-10. Proliferation of MC3T3-E1 pre-osteoblasts cultured on Glass, Ti dense and MTF substrates for 1, 2 and 3 days.80

Figure IV-11. Proliferation of MC3T3-E1 pre-osteoblasts cultured on MTF, MTF with 10 ng mL⁻¹ rhBMP-2, with 100 ng mL⁻¹ rhBMP-2 and with 100 ng mL⁻¹ rhBMP-2 and gentamicin substrates for 2 h, 1, 2 and 4 days. * means that the difference is statistically significant (p < 0.05)81

Figure IV-12. Alkaline phosphatase activity after 2, 5 10 and 20 days of MC3T3-E1 pre-osteoblastic cell culture in osteogenic medium on MTF, MTF with 100 ng mL⁻¹ rhBMP-2 and MTF with gentamicin and 100 ng mL⁻¹ rhBMP-2 substrates. * means the difference is statistically significant (p < 0.05).....82

Figure IV-13. CFU counting after *S. aureus* growth on agar plates for 24h and cell observer images of *S. aureus* growth on MTF and MTF functionalized with rhBMP-2 and gentamicin. a) Three samples with cultured *S. aureus* for 24 h on LB agar plates. *S. aureus* cultured in 1/10,000 dilution for MTF and 1/1 dilution for MTF with 100 ng mL⁻¹ rhBMP-2 and gentamicin and MTF with gentamicin. b) Zoom of Sample 1 of agar plates with cultured *S. aureus* on MTF, c) Zoom of Sample 1 of agar plates with cultured *S. aureus* on MTF with rhBMP-2 and gentamicin and cell observer images of 24 h of growth of *S. aureus* on d) MTF and d) MTF with rhBMP-2 and gentamicin substrates.....83

V. CHAPTER 2

Antibacterial PEMs based on PLL and PAA-gentamicin complexes

Figure V-1. A) Scheme of the formation of gentamicin and PAA complexes in 500 mM NaCl at pH 4.5. B) LbL assembly of PLL and PAA-gentamicin complexes. The LbL assembly was performed in 500 mM NaCl at pH 4.5 in 4 steps: 1) 15 min incubation of 100 μ L drop of 1 mg mL⁻¹ PLL, 2) removal of the PLL that has not been adsorbed by dipping the substrate in 500 mM NaCl pH 4.5, 3) 15 min incubation of 100 μ L drop of PAA-gentamicin complexes and 4) removal of the complexes that have not been adsorbed by dipping the substrate in 500 mM NaCl pH 4.5. This cycle is repeated 4 times. C) Scheme of PEMs showing 4 bilayers of PLL/PAA-gentamicin complexes grown on top of titania films.....89

Figure V-2. Changes in the hydrodynamic diameter of PAA-gentamicin complexes over time for different NaCl and gentamicin concentrations at pH 4.5. DLS measurements of complexes measured immediately after being prepared, and at 2 and 4 h after preparation. Complexes were prepared with 0.1, 0.25, 0.3 and 0.45 mg mL⁻¹ gentamicin in a) H₂O, b) 10 mM, c) 500 mM and d) 2 M NaCl93

Figure V-3. a) Intensity plot of size distribution at different times after complex formation for PAA-gentamicin complexes prepared in 500 mM NaCl at pH 4.5 with 0.3 mg mL ⁻¹ gentamicin. b) TEM image of complexes 2 h after preparation	95
Figure V-4. QCM-D monitoring of layer-by-layer assembly of PLL and PAA-gentamicin complexes prepared with 0.3 mg mL ⁻¹ gentamicin and film degradation. a) LbL assembly of 4 bilayers of PLL and PAA-gentamicin (0.3 mg mL ⁻¹) complexes in 500 mM NaCl and pH 4.5, b) plot of frequency changes after each bilayer is deposited, and c) film degradation in 500 mM NaCl at pH 13.	97
Figure V-5. SEM cross-sectional image of the PEM deposited on top of the MTF. The glass and the MTF can be distinguished, as well as the PEM grown on top.....	98
Figure V-6. AFM images of the assembly of 4 PLL/PAA-gentamicin (0.3 mg mL ⁻¹) complex bilayers. a) Height, b) phase, c) height of section in a and d) 3D graph of the height of 15 μm x 15 μm image and e) height, f) phase, g) height of section in a and h) 3D graph of the height of 5 μm x 5 μm image.....	99
Figure V-7. Release profile of gentamicin from PEMs formed of 4 bilayers of PLL/PAA-gentamicin complex on top of titania thin films. Region I shows the burst release (the insert is a zoom of region I) and region II the sustainable release. The release is followed up to 35 days using emission measurements at 455 nm.....	101
Figure V-8. S. aureus growth on PAA-gentamicin PEM coatings and on glass substrates immersed in gentamicin. Cell observer images following 24 h of incubation of S. aureus on a) PEM coating on top of titania films and b) glass immersed in gentamicin. c) CFU of the adhered bacteria on the PEM and glass with gentamicin	102

VI. CHAPTER 3

SrTiO₃ mesoporous coating for enhanced osseointegration

Figure VI-1. SrTiMF structural characterization by electron microscopy, SAXS and EEP. a) TEM image, insert 2D-SAXS pattern taken at 90°, b) SEM image of the surface and c) water adsorption-desorption isotherm, obtained by EEP	110
Figure VI-2. Nanoindentation study a) Shows the partial-load/unload vs displacement curve used for the tests and the results of the analysis of each unload section for Elastic modulus (Er) of b) the SrTiMF.	111
Figure VI-3. XPS a) Survey spectra and high resolution b) Ti and c) Sr spectra from SrTiMF.....	112
Figure VI-4. a) and b) STEM images of SrTiMF and c) EDX analysis of the points in image a (white crosses) and area in image b (white rectangle).....	113
Figure VI-5. Percentage of strontium loss from SrTiMF over time measured with ICP-MS.....	114

Figure VI-6. TEM representative micrograph of SrTiMTF after being immersed 24 h in 10 mM PBS.....	114
Figure VI-7. CLSM images of vinculin (first row), actin (second row), the merge of the actin, the vinculin and the nucleus (third row) and the zoom of the merge image (fourth row) at 2h (first column), 24h (second column) and 48h (third column) of growth of MC3T3-E1 cell line on SrTiMF substrates at 63x.....	116
Figure VI-8. Proliferation of MC3T3-E1 pre-osteoblasts cultured on MTF and SiTiMF substrates for 2 h, 1, 2 and 3 days. * means the difference is statistically significant ($p < 0.05$).....	117
Figure VI-9. Alkaline phosphatase activity after 5, 10, 15 and 20 days of MC3T3-E1 pre-osteoblastic cell culture in osteogenic medium on MTF and SrTiMF. * means the difference is statistically significant ($p < 0.05$).	118

VII. CHAPTER 4

COOH-functionalized Si and Ti mesoporous films to complex metallic ions

Figure VII-1. Scheme of the synthetic pathway to obtain alkoxy-silanes with MAA and MSA.....	129
Figure VII-2. TEM micrographs and 2D-SAXS patterns of: a) SiF MSA 5 % 1 h, b) SiF MSA 12.5 % 24 h, c) SiF MSA 20 % 1 h, d) SiB MSA 5% 1 h, e) SiB MSA 12.5 % 1 h and f) SiB MSA 20 % 1 h.....	131
Figure VII-3. TEM micrographs and 2D-SAXS patterns of: a) SiF MAA 5 % 1 h, b) SiF MAA 12.5 % 24 h, c) SiF MAA 20 % 24 h, d) SiB MAA 5 % 1 h, e) SiB MAA 12.5 % 1 h and f) SiB MAA 20 % 1 h	132
Figure VII-4. EEP results for a) SiF-MSA 20 % 1 h, b) SiB-MSA 20 % 1 h, c) SiF-MSA 20 % 24 h and d) SiB-MSA 20 % 24 h thin films.....	134
Figure VII-5. XPS spectra wide scan for SiB-MSA 20% 1 h system.....	136
Figure VII-6. High resolution spectra of a) S of SiB MSA 5 %, b) Si of SiB MSA 5 %, c) S of SiB MSA 12.5 %, d) Si of SiB MSA 12.5 %, e) S of SiB MSA 5 % and f) Si of SiB MSA 5 % of films prepared with 1h aged sols.....	137
Figure VII-7. High resolution spectra of a) S of SiB MSA 5 %, b) Si of SiB MSA 5 %, c) S of SiB MSA 12.5 %, d) Si of SiB MSA 12.5 %, e) S of SiB MSA 5 % and f) Si of SiB MSA 5 % of films prepared with 24 h aged sols.....	138
Figure VII-8. DRIFTS spectra of scratched films after extraction: a) SiF, b) SiF-MSA 20 % 1 h; c) SiF- MSA 20 % 1 h after contact with HCl and d) SiF-MSA 20 % 1 h after contact with Pb ²⁺ . Left: wide spectra. Right: enlargement of the COOH region	141
Figure VII-9. Scheme of the synthetic pathway to attach MSA to the vinyl groups present in the Ti-Si hybrid mesoporous films	142

Figure VII-10. STEM images of MTF with a) 10 % and b) 20 % of Si -Vinyl and c) EDX analysis of the images.....	143
Figure VII-11. XPS high resolution spectra of a) Ti and b) S of MTF with 10 % of Si-Vinyl reacted with C1 MSA, c) Ti and d) S of MTF with 10 % of Si-Vinyl reacted with C2 MSA, e) Ti and f) S of MTF with 20 % of Si-Vinyl reacted with C1 MSA and g) Ti and h) S of MTF with 20 % of Si-Vinyl reacted with C2 MSA.....	144
Figure VII-12. XPS high resolution spectra of a) Ti and b) Sr of MTF with 100 mM SrCl ₂ and c) Ti and b) Sr of MTF with 500 mM SrCl ₂	146
Figure VII-13. XPS high resolution spectra of a) Ti and b) Sr of MTF with 10 % of Si-Vinyl with 100 mM SrCl ₂ and c) Ti and d) Sr of MTF with 10 % of Si-Vinyl with 500 mM SrCl ₂	147
Figure VII-14. XPS high resolution spectra of a) Ti and b) Sr of MTF with 10 % of Si-vinyl reacted with C1 MSA with 100 mM SrCl ₂ and c) Ti and d) Sr of MTF with 10 % of Si-vinyl reacted with C1 MSA with 500 mM SrCl ₂	148
Figure VII-15. DRIFTS spectra of scratched films: a) MTF with 10 % Si-Vinyl, b) MTF with 10 % Si-Vinyl and C1 MSA and c) MTF with 10 % Si-Vinyl and C1 MSA after contact with Sr ²⁺	149
Figure VII-16. Characterization of MTF with 10 % Si-Vinyl, reacted with C1 MSA and then with 100 mM SrCl ₂ . Characterization through TEM (a, c and e), 2D-SAXS patterns (insert in a and c) and XRR (b, d and f).....	151
Figure VII-17. Released strontium percentage over time from a) MTFs and b) MTFs with 10 % of Si-Vinyl reacted with C1 MSA, previously immersed in 100 mM SrCl ₂ for 3 hours measured by ICP-MS	153
Figure VII-18. CLSM images of vinculin (first row), actin (second row), the merge of the actin, the vinculin and the nucleus (third row) and the zoom of the merge image (fourth row) at 2 h (first column), 24 h (second column) and 48 h (third column) of growth of MC3T3-E1 cell line on MTF with 100 mM SrCl ₂ substrates at 63x.....	155
Figure VII-19. CLSM images of vinculin (first row), actin (second row), the merge of the actin, the vinculin and the nucleus (third row) and the zoom of the merge image (fourth row) at 2 h (first column), 24 h (second column) and 48 h (third column) of growth of MC3T3-E1 cell line on MTF with 10 % of Si-Vinyl reacted with C1 MSA with 100 mM SrCl ₂ substrates at 63x.....	156
Figure VII-20. Proliferation of MC3T3-E1 pre-osteoblasts cultured on MTF, MTF with 100 mM SrCl ₂ and MTFs with 10 % of Si-Vinyl reacted with C1 MSA with 100 mM SrCl ₂ substrates for 1, 2, 3 and 7 days. * means the difference is statistically significant.....	157
Figure VII-21. Alkaline phosphatase activity after 5, 10, 15 and 20 days of MC3T3-E1 pre-osteoblastic cell culture in osteogenic medium on MTF with 100 mM SrCl ₂	

and MTFs with 10 % of Si-Vinyl reacted with C1 MSA with 100 mM SrCl₂ substrates.
* and ** means the differences are statistically significant 157

List of Tables

I. INTRODUCTION

Table I-1. Implant materials classification by the biologic response they exhibit after implantation.....13

Table I-2. Summary of the effects of various ions on bone regeneration.....35

V. CHAPTER 2

Antibacterial PEMs based on PLL and PAA-gentamicin complexes

Table V-1. Time evolution of the hydrodynamic diameter of PAA-gentamicin complexes prepared with 0.3 mg mL⁻¹ gentamicin and different NaCl concentrations at pH 4.5. DLS measurements of complexes were conducted immediately after preparation, and 2 h and 4 h after complex preparation. Complexes were prepared with 0.3 mg mL⁻¹ of gentamicin in water and 10 mM, 500 mM and 2 M NaCl. The standard deviation calculated from three replicates is shown.....95

VII. CHAPTER 4

COOH-functionalized Si and Ti mesoporous films to complex metallic ions

Table VII-1. Reagents used for the synthesis of mesoporous silica and mesoporous titania films functionalized with carboxylic groups..... 124

Table VII-2. Description of explored systems regarding type of carboxylate function, surfactant, percentage of silane in the material and sample aging 126

Table VII-3. d₋₁₁₀ interplanar distances (in nm) obtained from 2D-SAXS patterns for the SiF-MSA system..... 130

Table VII-4. Data obtained from EEP measurements of thickness (nm), porosity (%) and pore diameter (nm)..... 134

Table VII-5. Atomic Percentages for S and Si and S/Si Relation calculated from XPS spectra of the different systems containing the MSA moiety 139

Table VII-6. S/Ti atomic relative percentages of mesoporous titania films with 10 % and 20 % of Si-Vinyl reacted with C1 and C2 of MSA obtained from XPS measurements..... 143

Table VII-7. Sr/Ti atomic relative percentages of MTF with 100 and 500 mM SrCl₂, MTF with 10 % of Si-Vinyl with 100 and 500 mM SrCl₂ and MTF with 10 % of Si-Vinyl reacted with C1 MSA with 100 and 500 mM SrCl₂ obtained from XPS measurements..... 146

Table VII-8. Total amount of Sr present in the substrates and the percentage of released Sr over time from MTFs and MTFs with 10 % of Si-Vinyl reacted with C1 MSA previously immersed in 100 mM SrCl₂ for 3 hours measured by ICP-MS..... 152

Summary

There is an urgent need for the development of effective antibacterial coatings to cope with more and more resistant bacterial strains in medical environments, and particularly to prevent nosocomial infections following bone implant surgery. There are two main approaches to tackle this important issue: (I) directly prevent bacterial infection by the use of antibacterial coatings or (II) indirectly avoid bacteria proliferation by enhancing pre-osteoblast attachment, proliferation and differentiation in order to get a faster osseointegration of the implant and form the protective capsule, which would avoid infection, as fast as possible.

This thesis presents different approaches for mesoporous titania film (MTF) functionalization with growth factors and antibiotics. Antibiotics are incorporated to the coating alone or by means of complex assembly in polyelectrolyte multilayers (PEMs). Also, bioactive ions can boost the proliferation and differentiation processes of pre-osteoblasts. They can be directly incorporated to the titania matrix or be complexed on the pore walls that have been previously functionalized with carboxylic groups.

In **Chapter 1**, MTFs are used for gentamicin loading and delivery, and surface functionalization with recombinant human Bone Morphogenetic Protein 2 (rhBMP-2). MTFs are synthesized by spin coating on top of rounded glass coverslips through the evaporation induced self-assembly (EISA) method. The resulting film has a thickness of 80 nm with pores of 5.7 nm in diameter connected by necks of 4.2 nm. They show a porosity of a 30.7 %, obtained by Environmental Ellipsometric Porosimetry (EEP). The elastic modulus of the MTFs is of 25.5 ± 5 GPa, which makes the coating optimal for bone implants.

Gentamicin is incorporated in the MTF pores by immersion of the porous materials in gentamicin solution while rhBMP-2 is adsorbed electrostatically on top of the MTF. Contact angle and X-ray Photoelectron Spectroscopy (XPS) measurements are performed to prove gentamicin loading and rhBMP-2 functionalization. An initial burst release of gentamicin takes place in physiological media, and the 36 % of the total released gentamicin is liberated, followed by a prolonged release that lasts weeks. Such a release profile is highly appealing for bone implants where a high concentration of antibiotics is necessary during implant surgery while a lower

Summary

antibiotic concentration is needed until tissue is regenerated. The MTF loaded with gentamicin and functionalized with rhBMP-2 are effective against *S. aureus* colonization and the presence of rhBMP-2 enhances MC3T3-E1 pre-osteoblastic cell attachment, proliferation and differentiation, which are slowed down when gentamicin is present.

In **Chapter 2**, polyelectrolyte multilayers (PEMs) based on poly-L-lysine (PLL) and complexes of poly (acrylic acid) (PAA) and gentamicin have been fabricated applying the layer-by-layer (LbL) technique. The PEM is assembled on top of MTFs. Complexes are prepared by mixing PAA and gentamicin solutions in 500 mM NaCl at pH 4.5. The most stable complexes are obtained in these experimental conditions. The assembly of PLL and the complexes follows an exponential growth allowing a high loading of gentamicin in a 4 bilayer PEM. The PEM is stable till pH 13 meaning that it does not degrade at physiological pH, besides; there is a continuous release of gentamicin at pH 7.4. PEMs show an initial burst release of gentamicin in the first 6 hours, which liberates 48 % of the total gentamicin, followed by a sustainable release lasting over weeks, where around 80 % of the total gentamicin inside the PEM is released. PEMs are effective in preventing the proliferation of *S. aureus*. Bacteria grown on top of the PEM is 3 orders of magnitude lower than on glass coverslips immersed in gentamicin, used as control.

In **Chapter 3**, strontium titanate mesoporous films (SrTiMFs) with 30 % pore volume and a 20 % Strontium (Sr) molar content have been prepared by the EISA method. The resulting films have a pore diameter of 5.5 nm connected by bottlenecks of 3.2 nm and have a thickness of 85 nm. SrTiMFs display a large internal surface area available for exchange of Sr. Sr release is followed through Inductively Coupled Plasma Mass Spectrometry (ICP-MS) measurements. A 44 % of the Sr inside the titania matrix is released in the cell media within the first 8 h.

SrTiMFs improve attachment of MC3T3-E1 pre-osteoblastic cells, which show larger filopodia and more elongated features than cells attached to plain MTFs. Cell proliferation and differentiation rates are also largely improved. Overall, Sr incorporation in mesoporous titania coatings can lead to an enhanced osseointegration at early stages of tissue formation, at day 2 the cell proliferation is

64 % higher if compared to cells grown on top of MTFs and the alkaline phosphatase (AP) activity is higher from the 5th day of osteogenic cell culture.

In **Chapter 4**, inorganic–organic hybrid mesoporous silica and titania thin films with covalently bonded carboxylic acid groups are synthesized. Silica films are produced in one-step synthesis using carboxylic derivatized alkoxy silanes obtained by photochemical radical thiol-ene addition (PRTEA). The organosilanes are synthesized by clicking mercaptosuccinic (MSA) or mercaptoacetic (MAA) thioacids with vinyltrimethoxysilane (VTMS), using benzophenone as the photoradical initiator. Films are synthesized by EISA from a sol containing a mixture of tetraethoxysilane and different quantities of the organosilanes, without any further treatment after the PRTEA reaction. Titania films are synthesized in two steps; the sol is prepared mixing VTMS and the Ti precursor, and after film synthesis, the photochemical reaction with the MSA incorporates the carboxylic groups to the mesoporous film surface.

Structural characterization with electron microscopy, porosimetry measurements, and Small Angle X-ray Scattering with two-dimensional (2D-SAXS) detection confirm mesoporous phases of silica films whose degree of ordering depended on the amount of added organosilane. The incorporation of the functional vinyl and carboxyl groups is shown by XPS, and the presence of the COOH groups is confirmed by Diffuse Reflectance Infrared Fourier Transform Spectroscopy (DRIFTS). The availability of the COOH groups for further chemical modification is demonstrated by DRIFTS by following the changes in the typical carbonyl IR bands during proton exchange and metal complexation. Pb^{2+} is complexed to silica films, while Sr^{2+} is complexed to titania films. Sr release experiments show a prolonged release of Sr^{2+} lasting a week which enhances proliferation and differentiation processes in the MC3T3-E1 pre-osteoblastic cell line.

Resumen

Cada vez hay más cepas bacterianas resistentes a antibióticos y su presencia en entornos médicos supone un riesgo cuando los pacientes son sometidos a una intervención quirúrgica. Cuando una persona es sometida a una cirugía para la sustitución de un hueso por un implante hay riesgo de desarrollar una infección nosocomial y no conseguir una buena osteointegración del implante. En estos casos, es necesario realizar una segunda cirugía para evitar la proliferación de la infección en la zona donde se sitúa el implante, siendo necesaria su sustitución.

En la actualidad, para evitar infecciones se suministran antibióticos oralmente; su mayor desventaja es que la concentración que llega a la zona deseada, en este caso el implante, es baja, y en muchos casos no es lo suficientemente alta para evitar la proliferación bacteriana. En este marco surge la necesidad de desarrollar recubrimientos antibacterianos efectivos. Hay dos rutas principales para conseguir una buena osteointegración del implante; (I) evitar la proliferación bacteriana empleando superficies antibacterianas, esta sería la forma más directa, y (II) se puede evitar de una manera indirecta la infección mejorando la adhesión de pre-osteoblastos al implante, lo que hará que se forme la cápsula protectora más rápidamente evitando así la proliferación bacteriana y consiguiendo una rápida proliferación y diferenciación celular.

Esta tesis presenta diferentes métodos de funcionalización de películas de titanio mesoporoso mediante el uso de antibióticos y factores de crecimiento. Es posible incorporar antibióticos directamente, por inmersión, o también se pueden formar complejos con el antibiótico y ensamblar una película basada en multicapas de polielectrolitos (PEM, por sus siglas en inglés). Los iones bioactivos pueden estimular procesos celulares como la proliferación y diferenciación en pre-osteoblastos. Estos iones se pueden incorporar a la matriz de titanio o complejarse en las paredes del film mesoporoso que se ha funcionalizado previamente con grupos carboxilo.

En el **Capítulo 1**, se utilizan películas mesoporosas de titanio para encapsular y liberar controladamente gentamicina. La superficie mesoporosa se funcionaliza con la proteína morfogenética ósea recombinante humana 2 (rhBMP-2, por sus siglas en

Resumen

inglés). La gentamicina es un antibiótico de amplio espectro que se emplea en infecciones serias que han podido ser causadas tanto por bacterias gram negativas como positivas; como *P. aureginosa*, *E. Coli* o *Citrobacter*, *Streptococos* o *Estafilococos*. La gentamicina es un aminoglucósido y por tanto su mecanismo de acción consiste en unirse al ARN ribosomal de la subunidad 30S de los ribosomas bacterianos, interfiriendo así en la síntesis proteica. La rhBMP-2 es una proteína ósea, y se ha demostrado que promueve la formación ósea y se emplea para reconstruir defectos óseos patológicos.

Las películas se sintetizan mediante recubrimiento por centrifugación sobre cubreobjetos de vidrio a través del método de autoensamblaje inducido por evaporación (EISA, por sus siglas en inglés). La película obtenida tiene un espesor de 80 nm con poros de 5.7 nm de diámetro conectados por cuellos de 4.2 nm de diámetro. Muestran una porosidad del 30.7 %, obtenida por Porosimetría Elipsométrica Ambiental (EEP, por sus siglas en inglés). El módulo de elasticidad de las películas se midió por nanoindentación, resultando tener un valor de $25,5 \pm 5$ GPa, lo que hace que la superficie sea óptima para su uso en implantes óseos. A pesar de que las superficies de titania densa muestran un módulo de elasticidad en el rango de 100 a 120 GPa, mayor que el de películas mesoporosas de titania, el módulo elástico del hueso varía entre 4 y 30 GPa, donde se encuentra el valor de las películas mesoporosas.

La gentamicina se incorpora en los poros por inmersión, mientras que la rhBMP-2 se adsorbe electrostáticamente sobre la superficie de la película. Mediante medidas de ángulo de contacto y Espectroscopía Fotoelectrónica de Rayos-X (XPS, por sus siglas en inglés) se prueba la presencia de gentamicina y rhBMP-2. Se observa que la liberación de la gentamicina del interior de los poros de la película ocurre en dos fases; al inicio un 36 % de la gentamicina encapsulada se libera rápidamente, seguida por una segunda fase que ocurre más prolongadamente y que dura semanas. Este perfil de liberación resulta óptimo en implantes óseos donde es necesaria una alta concentración de antibiótico durante la cirugía y en las horas posteriores, viéndose necesaria su disminución cuando el tejido óseo se está formando. Las películas en base a titania funcionalizadas con gentamicina y rhBMP-2 han resultado ser eficaces contra la colonización por *S. aureus*. Cuando se sembraron 1,000

unidades formadoras de colonias (UFC), éstas no proliferaron, demostrando la eficacia de la gentamicina que se libera del interior poroso de la película. La presencia de rhBMP-2 mejora la adhesión celular, evaluada con la línea celular preosteoblástica MC3T3-E1, lo que contrarresta el efecto que la gentamicina tiene en la proliferación y diferenciación celular. Después de 10 días de cultivo en medio osteogénico la diferenciación celular es el doble si se compara con películas mesoporosas no funcionalizadas.

En el **Capítulo 2**, se fabrican multicapas en base a poli-L-lisina (PLL) y complejos de ácido poli(acrílico) (PAA) y gentamicina mediante la técnica de ensamblado capa por capa (LbL, por sus siglas en inglés). La técnica LbL consiste en la adsorción sucesiva de polielectrolitos con carga opuesta mediante interacciones electrostáticas. La multicapa se fabrica sobre películas mesoporosas de titania. Los complejos se preparan mezclando PAA y gentamicina en 500 mM NaCl a pH 4.5 con el objetivo de obtener complejos de tamaño estable. Se necesitan aproximadamente 2 h para fabricar la multicapa, y los complejos se estabilizan durante 2 h, después de mezclar el PAA con la gentamicina. Una vez han transcurrido estas 2 h se comienza a fabricar la multicapa. El tamaño de los complejos se mantiene estable durante la formación de la multicapa con un tamaño alrededor de 300 nm de diámetro. El ensamblado del PLL y los complejos sigue un crecimiento exponencial, observado cuando el ensamblado es monitoreado en la Microbalanza de Cristal de Cuarzo con monitoreo de la disipación (QCM-D, por sus siglas en inglés), permitiendo una alta carga de gentamicina en una PEM de únicamente 4 capas. Las imágenes de Microscopía Electrónica de Barrido (SEM, por sus siglas en inglés) y Microscopía de Fuerza Atómica (AFM, por sus siglas en inglés) demuestran que la superficie del ensamblado es irregular, lo que unido al crecimiento exponencial observado por QCM-D, da lugar a asociar este tipo de crecimiento a un crecimiento por “islas” descrito previamente en otros trabajos. Hasta pH 13 la PEM es estable, sin embargo, a pH fisiológico la gentamicina se libera. El 48 % de la gentamicina total es liberada en las 6 primeras horas, dando lugar después a una liberación paulatina del 80 % que dura más de un mes.

Para estudiar la actividad de la gentamicina liberada de la multicapa se siembran 1,000 UFC de *S. aureus* sobre las multicapas y sobre los sustratos control, que

Resumen

consisten en cubreobjetos de vidrio sumergidos en gentamicina. Se incuban las bacterias durante 24 h y posteriormente se despegan las que se han adherido y se siembran sobre placas de agar, para proceder al conteo visual de las UFC después de dejarlas crecer una noche (aproximadamente 18 h). Las multicapas sintetizadas son eficaces para prevenir la proliferación de la *S. aureus*, en comparación con el control, la cantidad de bacterias que crecen sobre la multicapa son 3 órdenes de magnitud inferior.

En el **Capítulo 3**, se preparan películas mesoporosas de titanato de estroncio (SrTiMFs) con un 30 % de volumen poroso y un contenido molar de estroncio (Sr) del 20 %. Las películas presentan un diámetro de poro de 5,5 nm conectados por cuellos de 3,2 nm y tienen un espesor de 85 nm. Los SrTiMFs muestran una gran área superficial interna disponible para el intercambio de Sr. Los espectros obtenidos en diferentes zonas de la película por Microscopía Electrónica de Barrido por Transmisión (STEM, por sus siglas en inglés) han demostrado que el Sr se encuentra distribuido homogéneamente en la estructura de titania y no se observan agregados o islas de Sr.

La liberación del estroncio se monitorea mediante mediciones de Espectrometría de Masas de Plasma Acoplado Inductivamente (ICP-MS, por sus siglas en inglés). Los resultados indican que en las 8 primeras horas el 44 % del Sr que contenía la película es liberado al medio celular. Después de las 8 horas, se observa que más Sr se libera, pero en cantidades inferiores, y debido a que no se ha liberado el 100 % se espera que haya una liberación más lenta y paulatina.

Los SrTiMFs mejoran la adhesión de pre-osteoblastos mostrando una mayor filopodia, se observa que las células están más alargadas, si se compara con células cultivadas sobre sustratos de titania que no contienen estroncio. Las tasas de proliferación y diferenciación celular también mejoran gracias a la presencia de estroncio. En general, la incorporación de Sr en los recubrimientos de titania mesoporosa puede dar lugar a una más pronta osteointegración en las etapas tempranas de formación de tejido óseo. En el segundo día, la proliferación celular es un 64% mayor, comparada con la proliferación celular sobre sustratos sin estroncio, y la actividad de la alcalina fosfatasa también es mayor después del quinto día de cultivo en medio osteogénico.

En el **Capítulo 4**, se sintetizan películas híbridas de sílice inorgánica-orgánica mesoporosa y de titania con grupos funcionales de ácido carboxílico covalentemente unido a las paredes de los poros. Las películas de sílice se fabrican en un solo paso utilizando alcoxisilanos derivados de ácidos carboxílicos obtenidos mediante la reacción clic de adición radicalaria tiol-eno iniciada fotoquímicamente (PRTEA, por sus siglas en inglés). Los organosilanos se preparan mediante una reacción clic entre tioácidos mercaptosuccínicos (MSA, por sus siglas en inglés) o mercaptoacéticos (MAA, por sus siglas en inglés) y el viniltrimetoxisilano (VTMS, por sus siglas en inglés). Las películas se sintetizan mediante EISA a partir de una solución que contiene una mezcla de tetraetoxisilano y diferentes cantidades de organosilanos. Las películas de titania se obtienen en dos pasos; el sol se prepara mezclando VTMS y el precursor de Ti, y después de la síntesis de la película, se somete la película a una reacción fotoquímica con MSA para incorporar los grupos carboxilo en la superficie porosa de la película.

Las películas se caracterizan mediante microscopía electrónica, mediciones de porosimetría y Dispersión de Rayos-X de Ángulo Pequeño con detección bidimensional (2D-SAXS, por sus siglas en inglés). El grado de ordenamiento de las películas de sílice depende de la cantidad de organosilano agregado en la síntesis. La incorporación de los grupos vinilo y carboxilo funcionales se muestra mediante XPS, y la presencia de los grupos COOH se confirma mediante Espectroscopia de Transformada de Fourier de Infrarrojo por Reflectancia Difusa (DRIFTS, por sus siglas en inglés). La disponibilidad de los grupos COOH para la modificación química se demuestra mediante DRIFTS siguiendo los cambios en las bandas IR típicas de carbonilo durante el intercambio de protones y la complejación de metals. Para películas de sílice se estudia la complejación de Pb^{2+} , y para películas de titania Sr^{2+} .

La liberación del estroncio se estudia por ICP-MS, mostrando una liberación prolongada de Sr que dura una semana, beneficiando así los procesos de diferenciación y proliferación de pre-osteoblastos. Se observa una mejora en la proliferación a 3 día de cultivo y la diferenciación celular se mejora después de 15 días de cultivo en medio osteogénico. Estos resultados se obtienen comparando con la proliferación y la diferenciación celular sobre películas de titania mesoporosa sumergidos en $SrCl_2$.

Resumen

Este capítulo muestra la posibilidad de sintetizar películas mesoporosas con grupos funcionales disponibles para la complejación de iones bioactivos, como pueden ser el magnesio o el calcio, que también ayudan en procesos celulares relacionados con la regeneración de hueso.

En general, se ha demostrado la versatilidad de las películas mesoporosas de titania para mejorar la osteointegración y evitar la proliferación bacteriana. Los materiales mesoporosos son muy versátiles siendo posible modificar la estructura mesoporosa y la orientación de los poros cambiando el surfactante empleado para la síntesis. También se puede modificar el espesor cambiando los parámetros de velocidad de centrifugación o inmersión y, por último, también es posible sintetizar películas híbridas mesoporosas, pudiendo obtenerse así películas con diversas funcionalidades. Modificando la síntesis de las películas mesoporosas, varía la concentración de moléculas que quedan atrapadas en el interior de la estructura porosa. Además, el área superficial interna disponible para el intercambio iónico también se puede ampliar.

I. INTRODUCTION

Biomaterials are widely used with the aim to enhance the longevity and the life quality of human beings. They are used in different parts of the human body as replacement implants for knees, dental structures or hips, as artificial valves for the heart or for stents in blood vessels, to cite a few examples.^[1-5]

Bone grafting is one of the most commonly used surgical methods to augment bone regeneration in orthopaedic procedures.^[6] Over two million bone grafting procedures are performed annually worldwide, which is the second most frequent transplantation in humans right after blood transfusion.^[7] Among all clinical available grafts, autologous bone is still being considered as the gold standard since all necessary properties required in bone regeneration in term of osteoconduction, osteoinduction and osteogenesis are combined.^[8] However, there is a limited supply and alternative to autologous grafting, synthetic bone substitutes have been largely developed during the past decades.^[9]

Professor Themistocles Glück (1853–1942) from Berlin implanted the first artificial knee in 1890 and manufactured and implanted the first artificial hip in 1891 as well. The ivory head was fixed to the bone with a nickel plate and screws.^[10] With the introduction of Vitallium® interposition implant (Co-Cr-Mo alloy), the American surgeon Marius Smith Petersen (1886–1953) achieved the first predictable and lasting results after an arthroplasty.^[11] In this period surgeons experimented with real bone-joint replacements from various materials. The implant from the brothers Robert (1901–1980) and Jean Judet (1905–1995) from Paris achieved the greatest popularity.^[12] Until this moment the prosthesis for hip replacement were made entirely of polymethylmethacrylate (PMMA) and frequently broke, this implant was afterwards reinforced with the introduction of a steel rod, but they still prone to fatigue fractures and loosening.^[13,14] The called Judet hip prosthesis was introduced in 1948 to a patient, and the particularity of this implant was that to reconstruct the femoral head, an acrylic femoral head was used. This implant holds the current world record in the implant in vivo durability (51 years).^[12] Artificial knees were developed in the same period but they were less successful if compared to hip implants. The reason for the inferior results was probably not in the implants itself but resulted from an inadequate surgical technique.

Introduction

The modern concept of low-friction hip arthroplasty was developed in the 1970s using polyethylene in the cup, stainless steel in the femoral head and stem, and polymethyl methacrylate (PMMA) as bone cement (John Charnley, 1911-1982).^[15] Charnley's total hip arthroplasty has a long and well-established record with long-term survival in more than 90 % of patients over 60 years of age.^[16] Contemporary principles of mechanical axis balance and the importance of joint stability evolved only in the mid-1980s. Further development of the implants was based on the introduction of new materials, different ways of fixation, advances in implant design, properties and coatings, and new, less invasive surgical techniques. Today there is a very extensive list of materials used for production of artificial joints.^[17]

Synthetic implants

Besides a vast number of available materials, ceramics, titanium and its alloys or polymers are the most used materials for orthopedic implants.^[18-20] A classification of the different type of materials used for implants can be done based on the biologic response that they elicit once implanted.^[21] The material can be biotolerant, those materials that form a thin fibrous tissue interface; bioinert, typically oxides that integrate well into bone and do not cause a reaction with the host; and bioactive materials.^[21,22] These last ones have been proven to promote tissue regeneration by interacting with the bone.^[22] The materials classified by their biologic response are summarized in **Table I-1**.

Biodynamic activity	Chemical composition		
	Metals	Ceramics	Polymers

Biotolerant	Gold Co-Cr alloys Stainless steel Niobium Tantalum	Polyethylene Polyamide Polymethylmethacrylate Polytetrafluoroethylene Polyurethane
Bioinert	Commercially pure titanium Titanium alloy (Ti-6AL-4U)	Al oxide Zirconium oxide
Bioactive		Hydroxyapatite Tricalcium phosphate Bio glass Carbon-silicon

Table I-1. Implant materials classification by the biologic response they exhibit after implantation.^[21]

The properties and therefore the design and composition of a material for an implant is application-driven. Mechanical properties, the resistance to corrosion and wear as well as osseointegration and biocompatibility are some of the properties the biomaterial should exhibit when selecting a candidate for bone replacement.^[20] Depending on the type of bone, the modulus of elasticity varies between 4 to 30 GPa.^[23] The implant should exhibit high tensile and compressive strength to prevent fractures and be functionally stable. An increase in the hardness of the implant leads to a decrease in wear, which prevents fracture of the implants.^[21] Regarding the surface properties of the implant, is quite important the wettability, the more hydrophilic is the surface, the better osteoblast adhesion have been proved.^[24] Many works have also shown the importance of the roughness of the surface in order to improve the cell and tissue response.^[25,26]

The material cannot be toxic and does not have to cause any inflammatory or allergic reactions in the body, thus the success depends on how the human body reacts after the implantation.^[20] The low wear and the corrosion resistance ensure the longevity of the material. Such resistance suppress the release of non-compatible metal ions into the body which cause allergic or toxic reactions.^[27] Since the implant loosening is often the cause of the weak surface compatibility with adjacent bone or other tissues, the surface characteristics of the implant are of fundamental importance

having a direct impact on osseointegration.^[28] **Figure I-1** shows a scheme of the properties that must be taken into account for the design of a biomaterial for an implant.

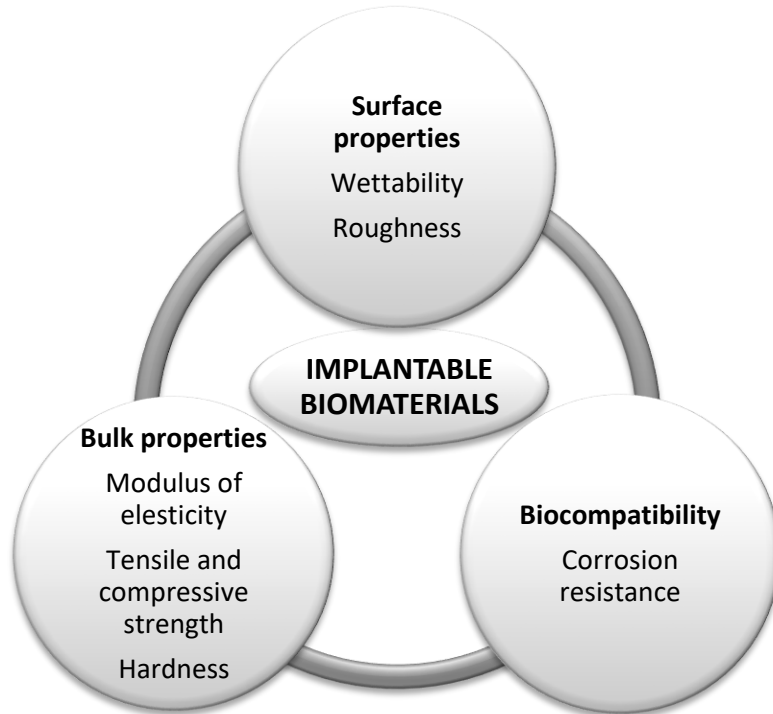


Figure I-1. Properties that a biomaterial should display to be a good candidate for its use in an implantable device.

Titanium implants

The increased use of titanium and its alloys as biomaterials is a result of their superior biocompatibility and excellent low corrosion properties.^[29,30] Since the role of an implant is the replacement of the bone, it needs to mimic the biological environment and mechanical properties of the bone. Although currently used commercial titanium implants satisfies the required mechanical properties with a Young's modulus within the range of 100 and 120 GPa,^[31] the chemical instability and deformations of protective oxide layer usually results in poor osseointegration. Surface deformations of the protective layer liberate metal ions forming Lewis Acids and lowering the pH in the implant environment.^[32] The acidic environment formed at the implant surface favors bacterial infection and causes immunogenic response which can lead to an aseptic loosening of the implant.^[33]

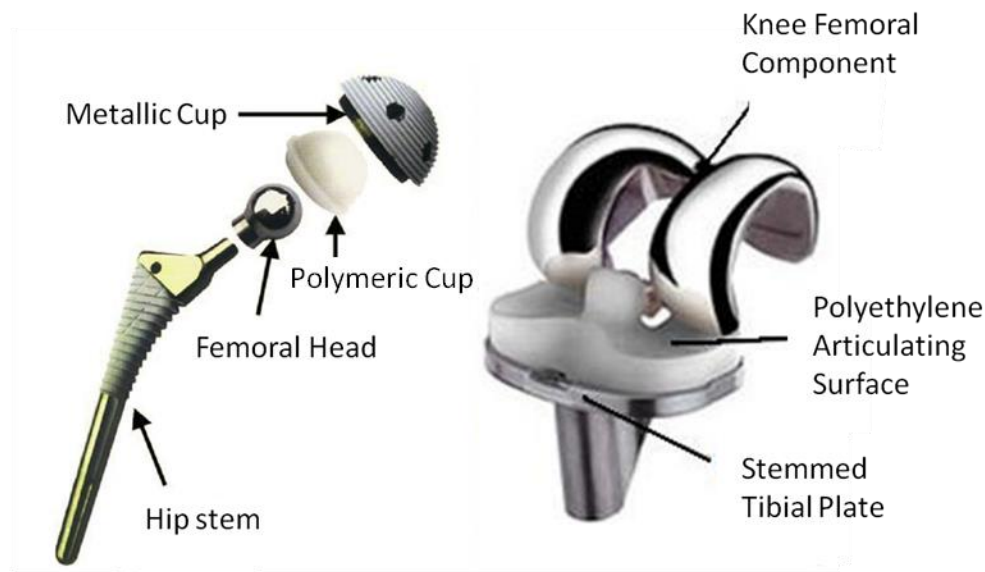


Figure I-2. Schematic diagram of an artificial hip joint (left) and knee implant (right).^[34]

Many elements such as Ag, Cu, Fe or Zn form alloys with titanium, enhancing the stability of the implant in physiological media.^[21] Among all titanium materials and titanium based alloys, the most used materials in biomedical field are the commercially pure titanium and the Ti-6Al-4V alloy. One of the most common applications of titanium alloys is as artificial hip joints that consist of an articulating bearing (femoral head and cup) and stem,^[35] where metallic cup and hip stem components are made of titanium. They are also often used in knee joint replacements, which consist of a femoral and tibial component made of titanium and a polyethylene articulating surface.^[35]

Most metals and alloys that resist well against corrosion are in the passive state. Metals in the passive state have a thin oxide layer on their surface, the passive film, which separates the metal from its environment.^[36] Typically, the thickness of passive films formed on these metals is about 3-10 nm ^[35] and they consist of metal oxides. The natural oxide is amorphous and it is known that protective and stable oxides on titanium surfaces are able to provide favourable osseointegration. The stability of the oxide depends strongly on the composition structure and thickness of the film.^[37] Because of the presence of an oxide film, the dissolution rate of a passive metal at a given potential is much lower than that of an active metal. It depends mostly on the properties of the passive film and its solubility in the environment.^[38]

Surface engineering can play a significant role in extending the performance of orthopaedic devices made of titanium several times beyond its natural capability. The main objectives of surface treatments mainly consist of the improvement of the tribological behaviour, corrosion resistance and osseointegration of the implant. There are coatings for enhanced wear and corrosion resistance by improving the surface hardness of the material that can be applied by different surface modifications techniques such as surface oxidation, physical deposition methods like ion implantation and plasma spray coatings, as well as thermo-chemical surface treatments such as nitriding, carburizing and boriding.^[39,40]

As previously mentioned, one of the main drawback of titanium implants is the high risk of bacterial infection, thus the aseptic loosening, which leads to the need of perform a second surgery to replace the infected implant.^[41]

Revision surgery and implant infection

Even with the development of prophylactic antibiotic therapies, environmental control and improvements in surgical techniques, the incidence of infection varies between 1 – 2 % in primary arthroplasties and 3.5 – 5 % in revision surgeries.^[42,43] The main risk factors associated with infection in knee arthroplasty are a previous surgery, advanced age, female gender, rheumatoid arthritis, obesity, diabetes and immunodeficiencies.^[44] The post-implantation surgical trauma weakens the local defense system, raising the risk of infection, if prolonged requires further surgical interventions to replace the implant.^[41] The revision surgery, however, is less successful than the initial surgery because of higher risk of trauma and longer bone healing period.^[45] Once the implant is exposed into physiological conditions a protein layer can be formed on the surface, making feasible bacterial colonization and in the worst case the biofilm formation,^[46,47] which acts as a protecting layer against the host defence and bactericidal agents. Therefore, it remains highly challenging and critical to avoid the infection just after the implantation surgery.^[47]

To treat the infection, if there is still no need to replace the implant, the infection focus has to be removed surgically and then the patient is treated for a long time with antibiotics.^[48] The classification of the infection, used to determine the required treatment, differentiates infections developed early (< 3 months), intermediate (3 – 24 months) and late (> 24 months), classification proposed by

Zimmerli *et al.*^[49] Early and intermediate infections are usually acquired during prosthetic implantation, whereas late infections results from haematogenous spread of the focus at a distance.^[49,50]

Two-thirds of the infections in orthopaedic implants are caused by *Staphylococcus* pathogens and they also are the responsible for two of the major bone infections: arthritis and osteomyelitis, which suppose the inflammatory destruction of joints and bones.^[51] More specifically *Staphylococcus aureus* and *Staphylococcus epidermidis* account together for two out of three infections in orthopaedics.^[51]

Nosocomial infections are the ones associated with healthcare acquired in an hospital.^[52] *Staphylococcus aureus* is an important nosocomial pathogen, able to cause a variety of human disease conditions. It can often be found as a commensal and a transient or persistent part of the resident flora of the skin and anterior nares in a large proportion (20 – 50 %) of the human population. However, when cutaneous/mucous barriers are breached, severe and at times life threatening infections can develop. Nosocomial infections by *S. aureus* are particularly frequent in immunocompromised and severely debilitated patients, and prevail in the presence of indwelling medical devices. Treatment of *S. aureus* infections is often complex, namely due to the emergence of methicillin-resistant *S. aureus* (MRSA) strains and resistance to other classes of antibiotics. Because of its pathogenic potential and complexity of its treatment, MRSA has received more attention than its methicillin-sensitive counterpart (MSSA). MRSA are resistant to β -lactam antibiotics (oxacillin, penicillin and amoxicillin), including third generation cephalosporins, streptomycin, tetracycline and sulfonamides; and upon exposure to vancomycin and other glycopeptide antibiotics, certain MRSA strains become less susceptible to these antibiotics. *S. aureus* possesses several cell-surface adhesive molecules that facilitate its binding to the bone matrix. Binding involves a family of adhesins that interact with extracellular matrix (ECM) components and these adhesins have been termed microbial surface components recognizing adhesive matrix molecules (MSCRAMMs). Specific MSCRAMMs are needed for the colonization of specific tissues and for the adhesion to biomaterials and to the ECM proteins deposited on the biomaterial surface. Particular MSCRAMMs include fibrinogen-binding proteins, elastin-binding adhesin and collagen-binding adhesin.

Introduction

A number of these adhesins have already been thoroughly investigated and identified as critical virulence factors implicated in various phases of infection, including early colonization, invasion, tissue localization and cell internalization.^[53-55] In recent years, the polysaccharide intercellular adhesin (PIA) has been found in many *S. aureus* strains, and is required for biofilm formation and bacterium-bacterium adhesion.^[56] This adhesin is responsible for the production of the extracellular polysaccharide matrix that develops the biofilm. It is known that once the biofilm is formed, the bacteria within the biofilm are protected from phagocytosis and antibiotics.^[55]

S. aureus produces virulence factors to facilitate disease progression, and rapidly develops antimicrobial resistance. The cell-surface virulence factors include the MSCRAMMs as receptors in the human host, other surface proteins, polysaccharide intercellular adhesin and capsular polysaccharides. The cell-surface MSCRAMMs typically are produced during exponential growth phase. The role of these various virulence factors is to provide nutrients required for survival in the host, and microbial cell protection from the host immune system during lesion formation. The secreted virulence factors, typically produced during the post-exponential and stationary phases, include a large group of exoenzymes, such as proteases, glycerol ester hydrolase and nucleases that make nutrients available to the microorganism.^[55]

A large body of works has been dedicated to the development of proper coatings for titanium implants, which make the surface antibacterial and avoid bacterial adherence. Due to the diversity of bacterial ecosystems the coatings should be tailored to tackle the different bacteria. On the other hand, tissue integration might also be taken into account. It has been demonstrated that the growing and proliferating cells on the surface of the implant can suppress bacterial proliferation. Although post-implementation supply of antibiotics to the patients can prevent infection, the low drug concentration at the target site remains as major disadvantage.^[41]

Gentamicin, cephalothin, amoxicillin, tobramycin or vancomycin are some of the most used antibiotics due to their broad antibacterial spectra.^[57-61] Nonantibiotic organic antimicrobial agents can also be used because of the risk of drug resistance

when antibiotics are used.^[41,62,63] Inorganic materials such as silver have also been proposed as an attractive dopant for titanium implants since it exhibits a broad antibacterial spectrum. However, silver compromises the activity of osteoblasts and epithelial cells.^[64,65] The treatment of the implants with UV irradiation or by changing the surface crystallinity leads usually to alteration of physicochemical properties, allowing thus the decreases in the bacterial activities.^[66] Bioactive polymers coatings, such as chitosan are also investigated because they can reduce bacterial adhesion.^[67] Interestingly, the use nitric oxide has also been proposed as it inhibits the growth of a wide variety of bacteria.^[68] Nitric oxide augments the antimicrobial ability of the immune system thus it loaded into xerogels for subsequent release.^[69] Still, the combination of nitric oxide with titanium implants remains unproven.

Paying special attention to the antibiotics, aminoglycosides as gentamicin or tobramycin, penicillins, glycopeptides like vancomycin, tetracyclines or rifamycins are the drugs that have been used to give antibacterial properties to implants.^[70] Aminoglycosides bind to the bacterial 30S ribosomal subunit. Ribosomes are the protein factories of cells. They are composed of two subunits in bacteria, a 30S and a larger 50S. By binding to the ribosome, aminoglycosides inhibit the translocation of tRNA (transcriptional) during translation and leaving the bacterium unable to synthesize proteins necessary for growth. Although the eukaryotic cells of humans also have ribosomes, these cellular protein factories differ in size and structure from the ribosomes of prokaryotes. That is why aminoglycosides do not interfere with protein synthesis in human cells. The mechanism of action of the aminoglycosides is shown in **Figure I-3**. Especially important is gentamicin, which is used for serious infections caused by either gram positive or negative bacterial strains, as *P. aeruginosa*, *E. coli* or *Citrobacter*, *Streptococcus* and *Staphylococcus* species.^[71] This broad-spectrum antibiotic contains five amino groups which gifts the molecule with a positive charge in acidic environment because the pKa of the amino groups range in between 5.5 and 9.^[72-74] **Figure I-4** shows the gentamicin molecule.

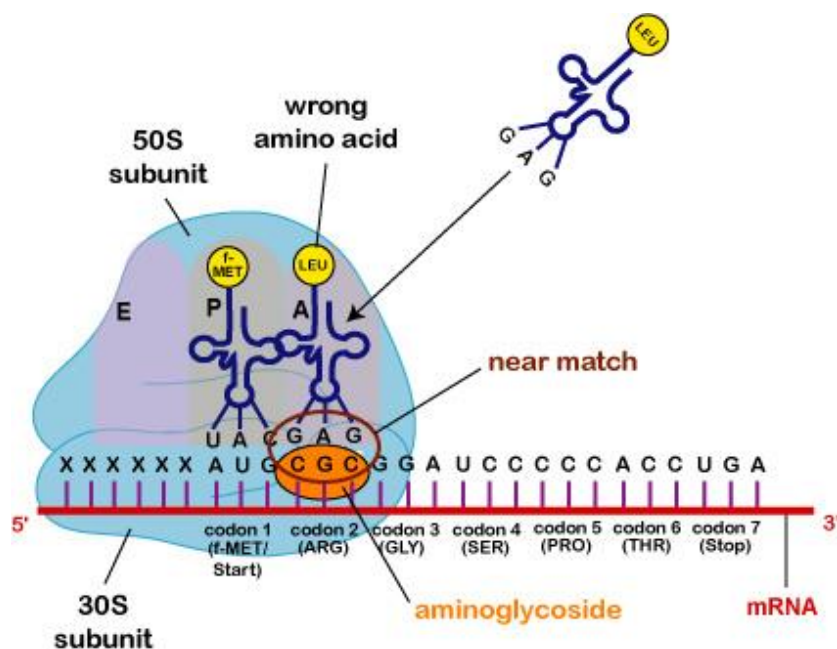


Figure I-3. Mechanism of action of aminoglycosides to inhibit bacterial protein synthesis. The aminoglycosides bind irreversibly to the rRNA (ribosomal RNA) in the 30S subunit of bacterial ribosomes. They interfere with the translation reducing the rejection rate for tRNA (transcriptional RNA) that are not matches for the codon, leading to a misreading of the aminoacids, interfering with the protein synthesis.^[75]

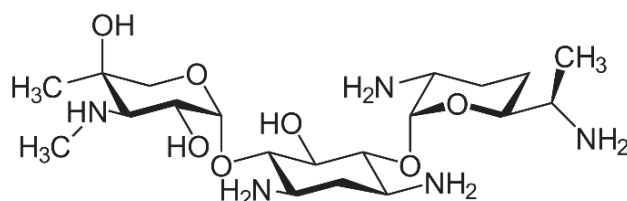


Figure I-4. Chemical formula of the Gentamicin molecule.^[76]

Layer-by-Layer technique for supramolecular structure deposition

The build-up of multilayer films of polyelectrolytes using the layer-by-layer technique (LbL) was demonstrated by Decher *et al.*^[77] The LbL technique is based on the alternative deposition of oppositely charged polyelectrolytes on top of charged surfaces, this process is shown in a scheme in **Figure I-5.**^[78–80] The assembly is driven by attractive electrostatic interactions and entropy considerations.^[81,82]

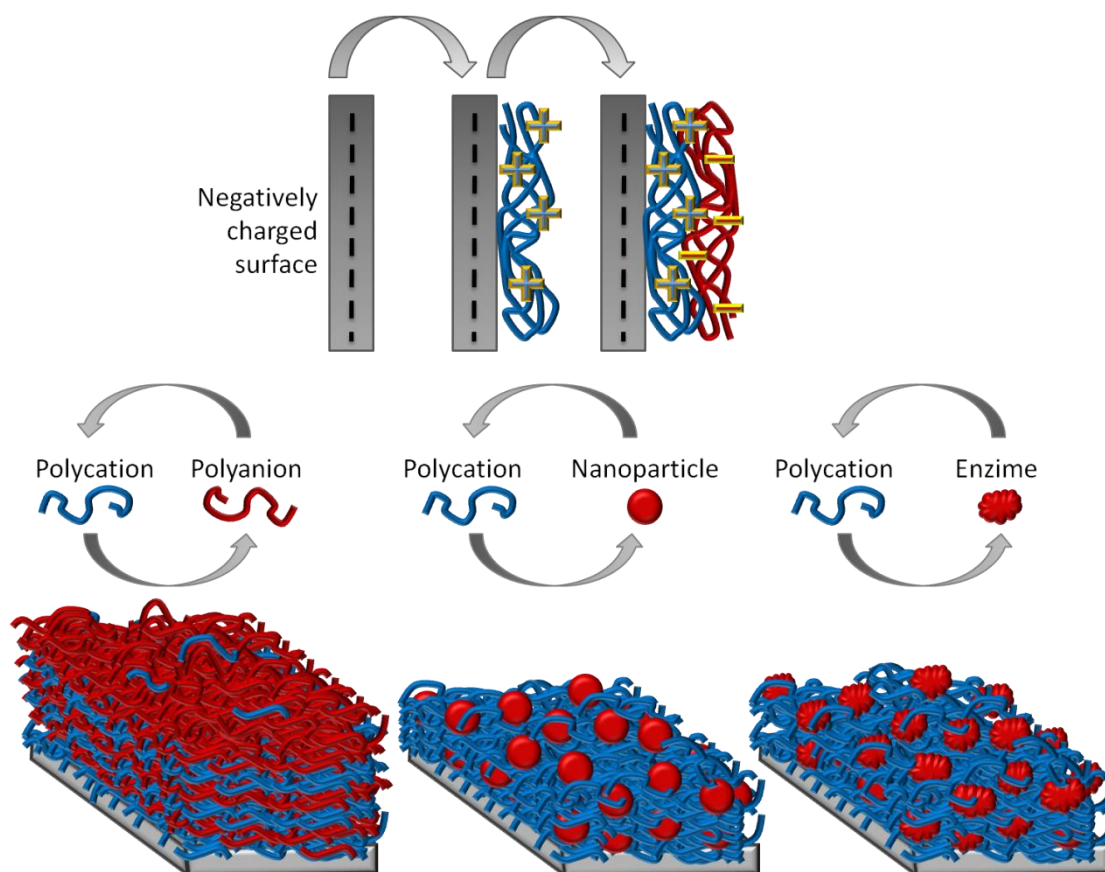


Figure I-5. Layer-by-layer assembly method. Alternatively, positively and negatively charged molecules are adsorbed one after the other on a substrate. This process can be repeated n times to a final film thickness.^[83]

This technique is a powerful strategy for non-covalent modification of charged surfaces. Is an easy and reliable method for surface engineering and has many potential applications in diverse areas such as optoelectronics, nanofiltration, tissue engineering or devices such as carriers for drug delivery.^[79,84–86]

Significant research has been done using the LbL technique to produce polyelectrolyte multilayers (PEMs) films combining a diversity of components. Biopolymers such as proteins and nucleic acids, lipids, and inorganic particles have been introduced in the fabrication of multilayer films.^[87,88] For biosensing purposes or multistep catalysis, research has been conducted in the incorporation of enzymes to the LbL films.^[78] Möhwald *et al.*^[89] extended the deposition of thin films of PEMs on top of colloidal particles, instead of using planar surfaces. As the LbL assembly was proven to work on colloidal particles, the use of sacrificial templates for the LbL assembly allowed the fabrication of empty capsules retaining the size and the shape of the original colloidal template. Capsules based on PEMs have been fabricated aiming a controlled release and targeting.^[89]

PEMs assembled by the LbL process can be also considered as a special case of polycation/polyanion complex formation. Due to the step-wise assembly of polycations and polyanions, the film has a layered structure. However, the layers are not fully stratified, as there is a certain degree of interdigitation among them due to the free space within a deposited polyelectrolyte layer, which gets filled when more layers are deposited.^[90]

PEMs result to be very stable. They cannot be easily removed unless one of the components loses charges by means of a change in pH, or when a specific ion or surfactant interacts with the polymers weakening the electrostatic interaction between the PEs.^[91,92] Only at very high ionic strength the films can be partially erased.^[93]

Due to a wide range of PEs available to assemble multilayer films, as well the ability to tailor their properties by varying the deposition conditions, PEMs are being incorporated into a variety of biological applications. Their use includes coatings to either promote or prevent cell adhesion, and more importantly in directing or maintaining cellular phenotypes.^[94] In addition to electrostatic interactions, multilayer films have been assembled from DNA strands using complimentary base pairing,^[95] by click chemistry utilizing covalent bonding, and through hydrogen bonding to create degradable multilayers for drug release applications.^[96,97]

PEMs have been assembled from synthetic as well as naturally occurring polymers.^[80,98,99] Synthetic PEMs have been assembled from cationic PEs such as poly (allylamine hydrochloride) (PAH), poly (diallyldimethylammonium chloride) (PDAC) and poly-L-lysine (PLL) and anionic PEs such as poly (acrylic acid) (PAA) and sulfonated polystyrene (SPS).^[94,100,101] PEMs have also been fabricated from naturally occurring PEs such as, polypeptides, polysaccharides, DNA, and proteins.^[102-106]

A self-assembled PEM can grow in a linear or exponential manner (**Figure I-6**).^[99,102] Linear growth typically occurs when the PEs are highly charged and do not diffuse freely throughout the PEM. Highly charged PEs exhibiting linear growth include cationic PAH and anionic SPS, to name some.^[99] On the other hand, exponential growth occurs in the presence of weak PEs as PLL, alginate (ALG), and poly-(lactide-co-glycolide) (PLGA).^[102,103,107,108] In a few cases, linear growth in the presence of

weak PEs has also been observed.^[109] To explain the exponential growth of PEMs three models can be found in the literature;^[110] the first one is called the 'Diffusion Model'. This model states that the exponential PEM growth is largely due to the diffusion of at least one PE through the film, resulting in an exponentially increasing thickness, as additional bilayers are added to the film.^[108,111-113] The 'Dendritic Model' is also used to describe the exponential growth of PEMs and is based on the well-known tendency of PE to form brushes when are in contact with oppositely charged structures.^[110,114,115] Lastly, the 'Island Model' is proposed which states that the first PE only coats part of the surface forming 'islands'. Then, further adsorption steps continue growing the initially formed islands increasing the available surface area showing an exponential growth of the formed PEM.^[110,116] Researchers have exploited the two different modes of growth within the same PEM to create distinct regions within a multilayer. ^[117]

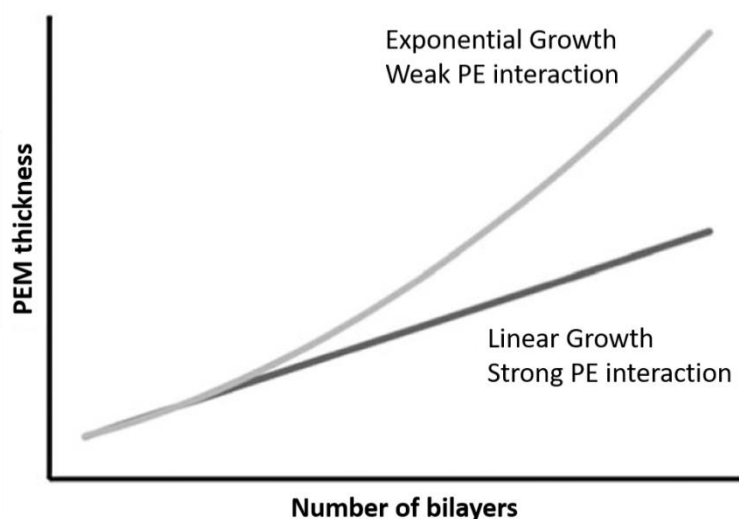


Figure I-6. Scheme of the thickness increase in PEMs following a linear or exponential growth as function of the number of polyelectrolyte bilayers assembled.

Polyamine acids facilitate the attachment of cells and proteins to solid surfaces in biological applications. In cell cultures normal attachment, growth, and development of many cell types are dependent on attachment factors and extracellular matrix components. α -Polylysine is a synthetic polymer, which can be composed of either L-lysine or D-lysine. "L" and "D" refer to the chirality at lysine's central carbon. This results in poly-L-lysine and poly-D-lysine respectively.^[118] PLL is commonly used to coat tissue culture ware as an attachment factor and has a pK_a

Introduction

of 10.5.^[119] It improves cell adherence which is based on the interaction between the positively charged polymer and negatively charged cells or proteins.^[120]

PAA is a synthetic high-molecular weight polymer of acrylic acid. In a water solution at neutral pH, PAA is a weak anionic polymer with a pK_a of 3.9,^[119] i.e. many of the side chains of PAA will lose their protons and acquire a negative charge. This makes PAA PE, with the ability to absorb and retain water and swell many times their original volume.^[121]

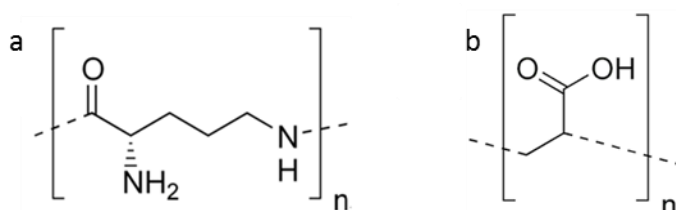


Figure I-7. a) Poly-L-lysine and b) Poly (acrylic acid) monomer chemical structure.

PEMs assembled through the LbL technique can retain a high drug concentration, which creates new opportunities for the release of therapeutic molecules in a localized manner.^[122] Drug reservoirs are constructed by exploiting the characteristic diffusivity associated only with exponentially growing PEMs, not normally observed under linear growth.^[117] Assembly conditions modulate the mechanical properties of PEMs. Drug reservoirs take advantage of exponentially grown PEMs in which bioactive molecules are incorporated. Due to the higher diffusivity associated with such regions, bioactive molecules can easily diffuse, thereby providing a means for localized delivery at high concentration.^[107]

In order to fabricate films entailing a small positively charged biomolecule, such as an antibiotic (Gentamicin for example), these could be assembled at the place of polycations in the PEM. Although gentamicin sulfate, positively charged, can be assembled in LbL multilayers by alternating deposition with negatively charged polyelectrolytes,^[123,124] its weak charge leads to low concentrations of drug loading and a low structural stability of the film that causes degradation.^[122]

Mesoporous titania

Several surface modification techniques have been proposed to achieve a good interaction between titanium implants and bone tissue.^[125] Since rougher surfaces promote bone and implant interlocking the coating of implant surface with

mesoporous film become an attractive method to improve bioactivity of the implant.^[126,127]

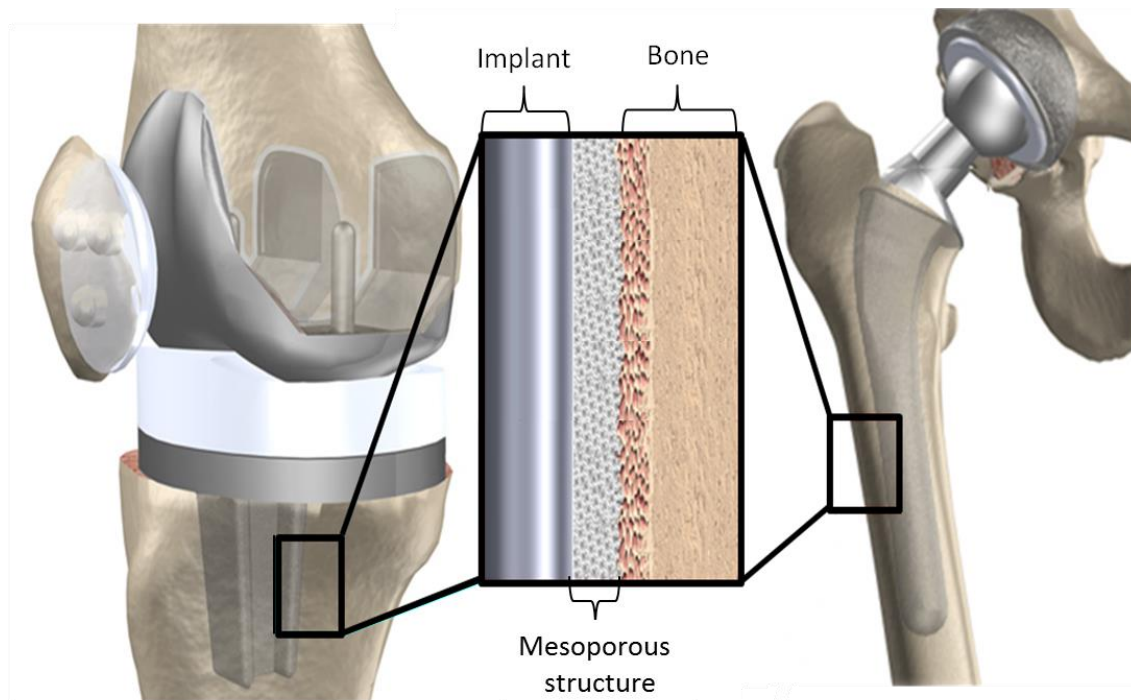


Figure I-8. Schematic representation of a titanium implant recovered with a mesoporous film used for knee and hip implants. ^[128,129]

The IUPAC classification defines three types of mesoporous materials depending on the pore size. Thus, microporous materials exhibit pores $< 2\text{nm}$, while the pore size between 2 and 50 nm corresponds to mesoporous materials. The macroporous materials have pores larger than 50 nm.^[130] Mesoporous materials can be found in the form of powder, nanoparticles or films, and the framework composition can be organic, inorganic or metallic.^[131]

Mesoporous titania is obtained through the sol-gel process assisted by a surfactant as structure-directing agent. The synthesis of material with homogenous pores requires highly controllable experimental conditions since the titania precursors (titanium alkoxides and titanium tetrachloride) undergo rapid hydrolysis and condensation leading to the rapid TiO_2 precipitation without forming mesopores.^[131] Several methods have been developed for the synthesis of films of which the Evaporation-Induced Self-Assembly (EISA) is considered the most convenient to prepare mesoporous TiO_2 films (MTFs),^[132] where TiCl_4 is the most used titanium source.^[131]

Introduction

The EISA process was first reported by Brinker and Ozin and was originally designed for the preparation of mesostructured silica thin films.^[133,134] The solute (precursor) is dispersed in a solvent (usually alcohol), first, colloidal particles are formed and the called sol is formed. The colloidal particles aggregate to form a 3D network, called gel. In the sol-gel process the two most important reaction that occur are the hydrolysis and the condensation, leading to the formation of M-OH-M or M-O-M bridges.^[135]

Amphiphilic surfactants have the ability to self-assemble into a variety of structures. The surfactants have the natural ability to organize into different shapes and at a certain concentration, called Critical Micelle Concentration (CMC) the surfactants assemble into spherical micelles. The inorganic phase then undergoes condensation around the surfactant phase, called Liquid Crystal Templating (LCT) mechanism. The elimination of the surfactant molecules leads to the formation of the mesoporous material.^[135]

For a mesoporous thin film formation, by the EISA process, a solution containing the surfactant, the metal alkoxide or salt, the alcohol, water and often acid are mixed. At the beginning the surfactant concentration is lower than CMC, and the solution can be casted on a substrate through spray, spin or dip coating and the evaporation of the alcohol starts and the surfactant and the metal oxide concentrations start to increase. Due to the surfactant concentration increase the self-assembly of the organic-inorganic hybrid leads to a Liquid Crystal (LC) phase. Micelles are formed when the CMC is reached and an organized LC phase is formed, where the inorganic network is not still fully condensed, this phase is called Tuneable Steady State (TSS). In the TSS water and solvent molecules are in equilibrium with the environment and the duration of this state depends on the relative humidity (RH). Finally, the template is removed to give the porosity to the film and get a full condensation of the inorganic network. The film undergoes a calcinations process in a temperature range of 300 - 550 °C to remove the surfactant.^[135] This process is shown schematically in **Figure I-9**.

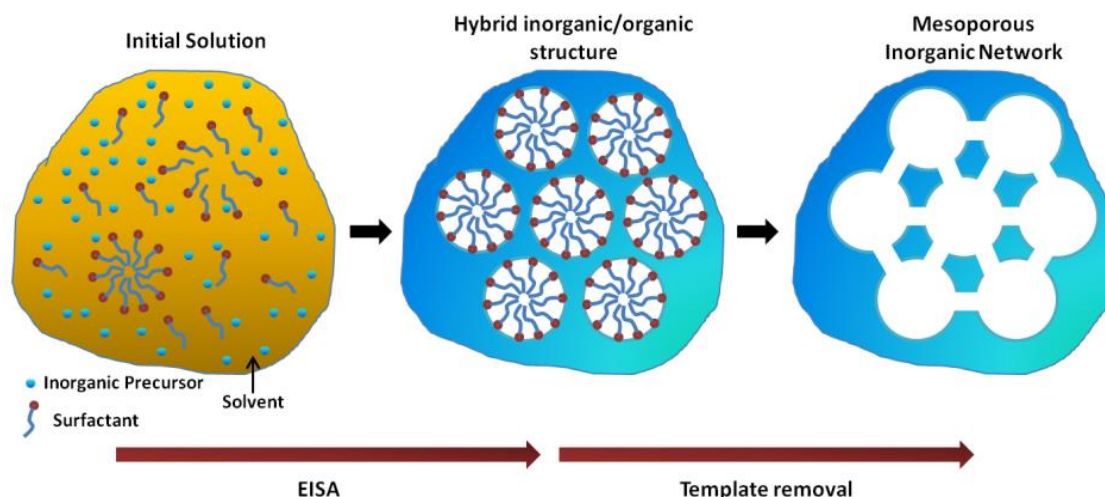


Figure I-9. Evaporation Induced Self-Assembly (EISA) process scheme.

Chemical functionalization of mesoporous titania

The progress in the fabrication of mesoporous materials was accompanied with the development of novel strategies to incorporate organic functional groups within the pores. There are two main synthesis routes; the post-grafting (post-functionalization), where the functional groups are incorporated to the porous matrix after the material is fabricated through vapour deposition or solution impregnation, and the co-condensation (one-step approach), where in one step the functionalization is achieved. In the post-grafting method, to achieve the functionalization, new bonds are formed between the Si-OH or M-OH groups that are in the surface react with the functionalizing agent. The co-condensation method requires the mixing of inorganic and functionality-containing precursors.^[136,137] While the former method is relatively easy to implement, the latter method is time-efficient and both the functionalization and condensation take place simultaneously. Usually organosilanes are used for the co-condensation approach, which can be mixed with titanium precursors to obtain mixed and functionalized mesoporous films. However, some of the functional groups will remain entrapped inside the network, remaining unavailable for further reactions.^[138]

Many different organic moieties have been incorporated to the pore surface, such as mercaptoalkyl, aminoalkyl, phenyl, glycidyl, vinyl, cyanoalkyl, and alkyl groups.^[139,140] Functionalization with carboxylic groups has been less explored than other functional groups. There is a need to perform two steps for the functionalization due to the lack of suitable commercial reagents. This is the reason

why there is a lack of reported methods that allow the incorporation of COOH functional groups. Nevertheless, several methodologies have been described to achieve the incorporation of the COOH group into silica powders (SBA-15, MCM type, SiO₂ nanoparticles) by co-condensation or post-grafting.^[140] These strategies include: modification of a NH₂-functionalized surface with succinic acid, co-condensation or post-grafting with an aqueous solution of carboxyethylsilanetriol, or grafting of an organosilane bearing an ester group that results in a free carboxylic moiety after a hydrolysis step.^[140] Another possible approach is the use of cyanide to carboxylic methods, wherein the COOH group is obtained after hydrolysis of the -CN group with sulphuric acid using hard experimental conditions: high temperature and long reaction times.^[141] Liu *et al.* have shown successful incorporation of carboxylic groups into mesoporous thin films through a co-condensation method, applying the cyanide to carboxylic conversion in a two-step method.^[142] Despite some works can be found about co-condensation strategies for chemical functionalization of silica based mesoporous films and particles, no reports can be found in literature about chemical functionalization of titania based mesoporous structures.

The functionalization with carboxyl groups brings a pH-dependent switch-ability to the pore surface, whose adsorption capability or catalytic activity can be varied by changing the solution acidity. This also brings the possibility to anchor biomolecules, such as proteins, antibodies, or folic acid to the COOH groups and can also be used as ligands for metal complexation in decontamination or detection processes.^[141,143,144] Carboxylic groups could also be used to entrap bioactive ions, allowing a sustainable release of entrapped ions.

Pores as reservoirs for drug delivery

A typical implant replacement intervention requires the prescription of antibiotics to minimize the risk of the failure of implant integration and infectious responses.^[145] To decrease the amount of drugs dosage, the local and controllable drug delivery becomes an alternative scenario to increase implant adaptation. By this mean, the delivery of the drugs occurs in an specific site of the human body where the local amount of drug and his release can be regulated.^[146]

The goal of any drug delivery vehicle is to provide therapeutic amounts of drug to the proper site in the body to achieve promptly and to maintain desired drug concentration.^[147] Delivery of drugs by means of the so called controlled release technology began in the 1970s and has continued to expand rapidly.^[148] Various drug delivery systems, such as liposomes, micelles, emulsions, polymeric micro/nanoparticles have shown great promise in controlled and targeted drug delivery. Among these systems porous materials are emerging as a new category of host/guest systems.^[149-152]

As expected, a large surface area and large pore volume enable mesoporous materials to act as drug reservoirs. The most important requirement for mesoporous coatings is that they must have the ability to load and release drugs. The substrate has to be able to hold the drug and deliver it gradually in the specific target site.^[153] The dose of the drug and the necessary release time vary on the application. Drug release from porous carriers may be complete within 10 min or be incomplete after several hours or days. Solvent polarity and surface properties play an important role in the adsorption and release of drugs from porous carriers.^[154,155] Adsorption is the accumulation of concentration of substances at a surface or interface; the phenomenon by which the molecules of gas, vapour and liquid spontaneously concentrate at a contacting surface without undergoing chemical reaction, thereby forming a surface or interfacial layer.

The advantage of using MTFs is their tuneable pore size and films thickness that translates to a well-controlled amount of drug to be loaded.^[156] Typical loading is performed through capillary action by immersing the templates in a concentrated drug solution. The release profiles have an initial burst release and a decreasing tail distribution, which is lower due to the pore interconnection and the presence of necks, making the molecules to get entrapped inside the film and making slower their release. Although the period just after the implantation is the most critical stage that brings the high risk of infection, the antibacterial properties of the implant should remain for longer time until the complete integration of the implant.^[46,157]

Bone remodeling process

To ensure the implant integration in the human body is important to understand how the bone is remodelled and behaves in order to perform in vitro experiments

and be sure about the biocompatibility and the osseointegration capability of the implantable material.

The skeleton is a very dynamic tissue and remains in a constant repairing of mechanical microdamage. The cell forming actions are the processes that ensure the secure integrity of the skeleton resorption during the exchange of old bone with new bone. These processes are regulated by local and systemic factors that maintain the subtle balance between the resorption and bone formation, avoiding the excessive bone loss or gains, which may cause risk of fracture or compression syndromes. Osteoclasts, osteoblasts and osteocytes take part in those processes.^[158] The process of remodelling commences by osteoclastic resorption that forms a lacuna with a depth between 40 and 60 μm leading to completed refilling of lacuna with new bone.^[159,160] Many transcription factors are involved in the osteoblast differentiation process, which are derived from mesenchymal cells differentiating from progenitors into proliferating pre-osteoblasts, osteoblasts and osteocytes or bone-lining cells. Runt-related transcription factor 2 (Runx2) is essential for cell differentiation and it regulates the expression of diverse genes.^[161] Alkaline phosphatase (AP) and type I collagen are expressed once osteoblast are differentiated and they are important for bone matrix synthesis and the mineralization process.^[162] Mature osteoblasts differentiate to osteoclasts, whose objective is to break down bone tissue, so a balance is found between new bone formation and resorption. Osteocytes are a type of osteoblasts that get entrapped in the bone matrix and form the so-called osteoid, a non-mineralized organic part of the bone.^[158] All this process is shown schematically in **Figure I-10**.

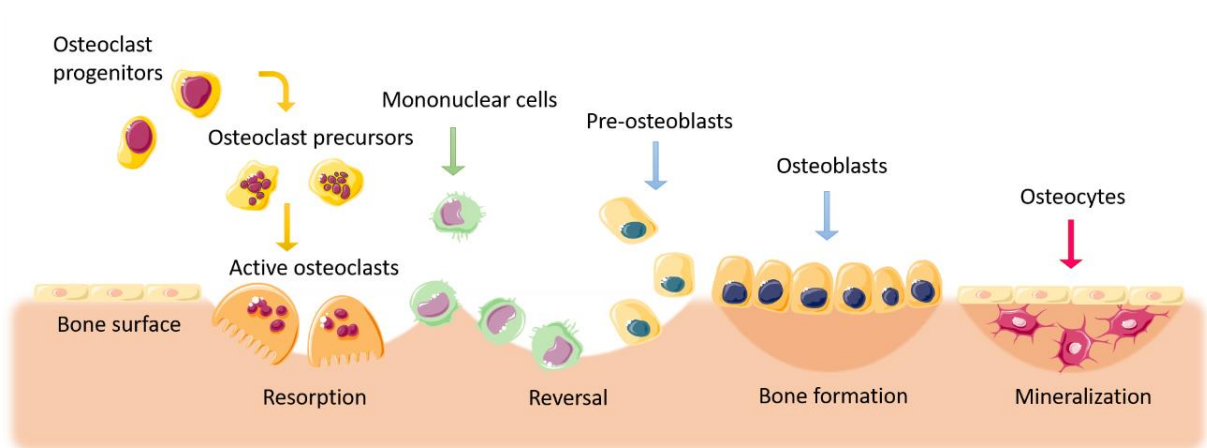


Figure I-10. Bone remodeling cycle. Bone surface is resorted by osteoclasts and pre-osteoblast differentiate to osteoblasts for new bone formation and osteocyte differentiation.

The underlying surface is of major importance because it defines the proper bone cells attachment to form focal adhesions. Through the focal adhesions, cells interact with the surrounding and mediate a bidirectional signaling. Integrins play a major role in the process through bounding to the actin cytoskeleton inside the cell and to the substrate outside the cells.^[163] Growth and differentiation of pre-osteoblasts are regulated by transcription factors activity and gene and protein expression, which are activated due to the mechanotransductive signaling the integrins mediate.^[164]

As previously mentioned, it is well known that cell proliferation allows fast implant integration in the tissue (osseointegration), avoiding bacterial growth. Implant surface modifications can enhance the interactions that occur with the biological fluids and cells and accelerate osseointegration. Many bioactive coatings have been reported. For example, calcium phosphate coatings have been shown to increase the biochemical interlock between bone and implant materials. Similarly, collagen coating promotes osseointegration.^[165-167] Also, the use of growth factors can enhance osteoblast growth, proliferation and differentiation, as has been demonstrated in the case of bone morphogenetic protein 2 (BMP-2).^{[168],[169]}

Bone morphogenetic proteins regulate growth, differentiation, chemotaxis, and apoptosis, and play pivotal roles in the morphogenesis of a variety of tissues and organs.^[170] They are members of the transforming growth factor- β (TGF- β) proteins, which includes a large families of growth and differentiation factors.^[171]

Whereas the BMPs are multifunctional proteins, implantation of the osteogenic BMPs such as BMP-2 and BMP-7 at an osseous site results in bone and cartilage formation. *In vivo*, these BMPs act primarily as differentiation factors, turning responsive mesenchymal cells into cartilage- and bone-forming cells. This is supported by many *in vitro* studies showing that the BMPs turn on specific markers of the osteoblast or chondroblast phenotype in a number of cells.^[172]

The activity of BMPs is tightly controlled at many levels. Outside the cell, soluble inhibitory proteins can bind certain BMPs and inhibit their binding to cell surface receptors. It has been found that BMPs can up-regulate the expression of some of these inhibitors, suggesting a negative feedback loop that limits the activity of BMPs. A number of negative regulators of BMP action exist within the nucleus. All of these

Introduction

regulatory mechanisms together cause the bone-induction process to be controlled tightly and self-limiting.^[173,174]

Recombinant human BMP-2 (rhBMP-2) induces the expression of osteocalcin, a bone specific protein^[172] and induces expression of the osteoblast lineage markers. BMP-3, the most abundant BMP in adult bone, is an antagonist of osteogenic BMPs.^[175] BMP-3 inhibits BMP-2 mediated induction of *Msx2*, a gene that provides instructions for producing a protein that is necessary for proper development of cells and tissues throughout the body, and blocks BMP2-mediated differentiation of osteoprogenitor cells into osteoblasts.

BMPs bind to two types of receptors termed as Type 1 and Type 2 receptors, required for signal transduction.^[176] The overall structures of Type 1 and Type 2 receptors, named as BMPR-I and BMPR-II respectively, are similar. They have a short extracellular domain with some conserved cysteine residues, a single transmembrane domain, and an intracellular domain containing a serine/threonine kinase motif. Even BMPs can interact directly with BMPR-I, signal transduction for BMPs require both receptors, because BMPs in the first moment BMPs interact with BMPR-II, because this is the specific receptor, which facilitates afterwards the interaction with BMPR-I, that is in charge of mediating the signals inside the cells to activate Smad proteins.^[173,177-179] Smad proteins are also part of the TGF- β superfamily, and are very important to regulate cell development and growth.^[180]

Once inside the cell membrane, the Smads are phosphorylated by Type 1 receptor kinase so they can be transported to the cell nucleus and the accumulation of these complexes in the nucleus leads to the regulation of transcriptional responses.^[181] All the process described above is schematically shown in **Figure I-11**.

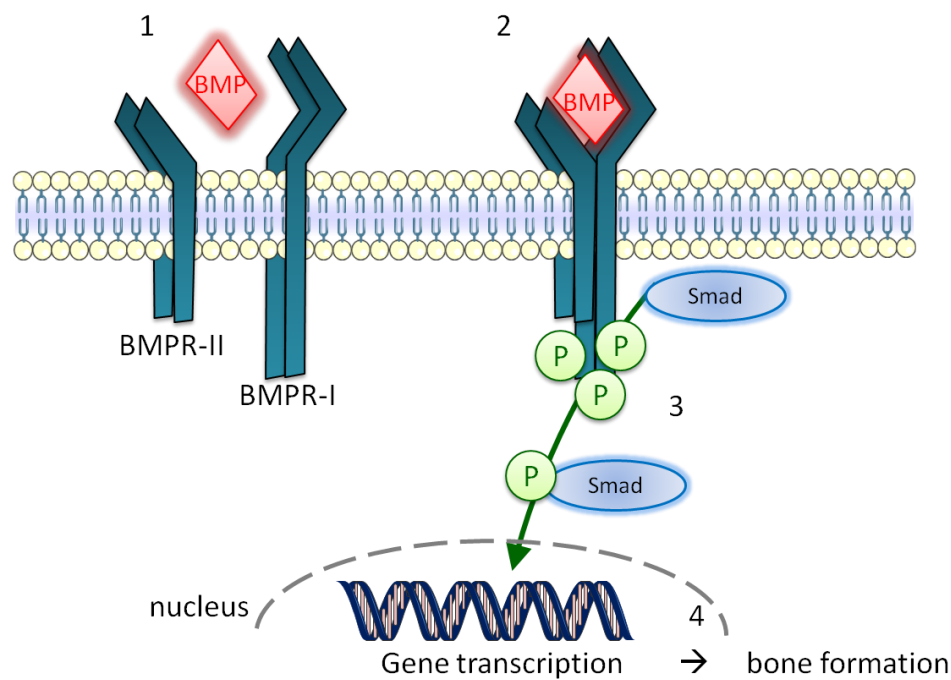


Figure I-11. BMP pathway to induce bone formation.

Bioactive ions

Bone surface chemistry has a large influence on proper and fast osseointegration. Human bone mineral consists of various ion-substituted apatites, thus, the use of bioactive elements is being developed to induce the ability of bone formation.^[182] Several ions have been shown to be capable of inducing osteoblast precursor differentiation through growth factor signalling pathways, or to stimulate other processes in support of bone tissue growth. These ions include boron (B^{3+}), calcium (Ca^{2+}), cobalt (Co^{2+}), copper(II) (Cu^{2+}), fluoride (F^-), lithium (Li^+), magnesium (Mg^{2+}), niobium (Nb^{5+}), phosphate (PO_4^{3-}), silicate (Si^{4-}), silver (Ag^+), strontium (Sr^{2+}), vanadium (V^{5+}), and zinc (Zn^{2+}). Compared with protein growth factors, the advantages of using such ions to induce bone tissue repair are manifold, including lower cost, greater simplicity, higher stability, and more efficacy at low concentrations.^[183] **Table I-2** summarized the main effects observed for the mentioned ions.

Ion	Effects and <i>in vivo</i> main results	References
Boron (B^{3+})	<ul style="list-style-type: none"> Promote osteogenic differentiation through enhanced ALP activity and increased expression of osteogenic gene markers, improved mineralization, proliferation and adhesion. 	[184–186]

	<ul style="list-style-type: none"> • Scaffolds comprising nanogels combined with boron-containing mesoporous bioactive glass showed improved bone tissue formation in critical-sized rat femur defects 	
Calcium (Ca²⁺)	<ul style="list-style-type: none"> • Increased adhesion, proliferation, and differentiation of osteoblasts. • Titanium implants modified with Ca²⁺ demonstrated elevated bone density and osseointegration after 12-weeks post implantation in a sheep tibia model. 	[187-189]
Cobalt (Co²⁺)	<ul style="list-style-type: none"> • Downregulates some osteogenic markers and reduces proliferation of osteoblasts; also stimulates osteoclast activity; is important in angiogenesis. • Cobalt-treated implants had improved vascularization in mouse models. 	[190,191]
Copper(II) (Cu²⁺)	<ul style="list-style-type: none"> • Borate bioactive glass scaffolds doped with 3 wt% CuO demonstrated improved angiogenesis and bone formation in rat calvarial defects after 8 weeks. 	[192-195]
Fluoride (F⁻)	<ul style="list-style-type: none"> • Fluoride promotes proliferation, increases mineralization, upregulates osteogenic marker genes, and modulates apoptotic processes. • Fluoride-substituted apatite containing 0.48 wt% F showed increased rate of bone formation 2 weeks post implantation in rats. 	[183,196-198]
Lithium (Li⁺)	<ul style="list-style-type: none"> • Increases proliferation, cementogenic differentiation and ALP activity. • Local application of Li₂CO₃ accelerated bone regeneration by promoting osteoblastogenesis and inhibiting osteoclastogenesis in male Wistar rats. 	[199,200]
Magnesium (Mg²⁺)	<ul style="list-style-type: none"> • Increases expression of collagen and matrix mineralization; increases spreading. Decreases osteoclast differentiation, increases cell adhesion to biomaterial surfaces. • Enhances osseointegration by increasing bone-to-implant contact. 	[201-204]
Niobium (Nb⁵⁺)	<ul style="list-style-type: none"> • Has been shown to stimulate osteoblast activity, promote mineralization, and control cytotoxicity in bone tissue cultures; combined with HA, it can increase calcification, ALP activity, and osteoblast function. • Ti-Nb alloy demonstrated osseocompatibility and osseointegration at 2, 4, and 12 weeks post implantation in female beagle dogs. 	[198,205]
Phosphate (PO₄³⁻)	<ul style="list-style-type: none"> • Induces apoptosis in osteoclasts and inhibits osteoclast differentiation and bone resorption activity. • P is involved in osteoblast differentiation and ECM mineralization. 	[206-209]

Silicon (Si⁴⁻)	<ul style="list-style-type: none"> • Can induce osteoblast differentiation and collagen I production and promotes osteogenesis and angiogenesis. [183,196] • In female Sprague–Dawley rats, dietary silicon. Influences bone growth through modulation of turnover of collagen and sialic acid-containing ECM proteins.
Silver (Ag⁺)	<ul style="list-style-type: none"> • Has antimicrobial actions when used in tissue culture. Furthermore, exposure of bone progenitor cells to silver based nanoparticles accelerated osteogenesis. [183,210,211]
Strontium (Sr²⁺)	<ul style="list-style-type: none"> • Increases expression of Runx-2, BMP-2, OCN, OPN, BSP, and Col1, ALP activity and matrix mineralization. Enhances attachment, proliferation, and differentiation in osteoblastic cells; reduces osteoclast activity. [204,212–216] • Promotes bone formation, remodeling and osseointegration by increasing the bone-to-implant contact.
Vanadium (V⁵⁺)	<ul style="list-style-type: none"> • <i>In vitro</i> studies demonstrated its pro-osteogenic function without significant cytotoxicity. [210,217,218] • Known to be more highly concentrated in bone tissue <i>in vivo</i>, suggesting that it has a role in osteogenesis; enhanced angiogenesis and chondrogenesis, and promoted mineralization 3–4 weeks post fracture in male Wistar rats.
Zinc (Zn²⁺)	<ul style="list-style-type: none"> • Increases proliferation, expression of type I collagen, Runx-2, BSP, and OCN, ALP activity in enhanced. [219–226] • Increases bone formation, BMD, bone mineral content growth, osseointegration, peri-implant osteogenesis, bone-to-implant contact. However, it can also unfavorably increase bone resorption.

Table I-2. Summary of the effects of various ions on bone regeneration.

Calcium has a variety of roles in cells and living systems, from intracellular molecular signalling to macroscale structural properties. This ion is especially important in bone tissue, because it is one of the two most essential components of mineralized bone matrix, along with phosphate. Moreover, the hydroxyapatite that forms the inorganic phase of bone tissue contains approximately 99% of the calcium in the body, acting as a storage reservoir for the mineral. Calcium can be leached from, or deposited into, existing bone matrix to maintain calcium homeostasis in the body. This bone calcification system is important in the formation of mature bone and during bone repair. Therefore, it is imperative to maintain the extracellular concentration of calcium in bone tissue.^[227] Furthermore, cellular calcium signalling

Introduction

is a key process in the formation and repair of bone. Calcium can stimulate the proliferation of mesenchymal precursor cells, as well as mature bone cells,^[228] through a process dependent on the production of nitric oxide (NO). This allows for appropriate numbers of bone growth precursor cells to be generated and recruited to the injury site in the context of bone tissue regeneration. In the context of bone regeneration applications, the calcium ion is of great importance. *In vitro* studies have shown that moderate extracellular calcium concentrations are optimal for osteoblast proliferation and extracellular matrix (ECM) mineralization.^[229] Furthermore, recent research has demonstrated that loading of calcium into bone repair scaffolds promotes the adhesion, proliferation, and differentiation of osteoblast-like MG63 cells *in vitro*.^[188] This observation, keeping in mind the general importance of calcium in bone formation and cellular signaling, gives support to the idea of using calcium ions to promote bone regeneration in medical applications.

Magnesium is the fourth-most abundant element in the human body, of which approximately half is stored in bone tissue. ^[230] It is an essential cation for many physiological functions, including enzymatic reactions involved in energy metabolism and synthesis of proteins, lipids, and nucleic acids.^[184] Numerous studies have shown a correlation between magnesium deficiency and osteoporosis.^[210] Pure magnesium corrodes too quickly in physiological pH and produces excessive hydrogen gas; therefore, efforts to use the metal itself in orthopaedic applications have been impeded.^[230] However, there have been several studies focused on complementing biomaterials with Mg²⁺ that have shown Mg²⁺ supplementation to increase cellular adhesion via an integrin-mediated mechanism, spreading, proliferation, ALP activity, matrix mineralization, and osteogenic differentiation *in vitro* as well as enhance osseointegration *in vivo*.^[203,204,231]

Silicon, commonly existing as the silicate ion (Si⁴⁻) *in vivo*, has an essential role in bone-forming metabolic processes. Silicon concentrations are elevated during early bone calcification, inducing hydroxyapatite precipitation into the matrix.^[183] Si ions have been widely used to modify hydroxyapatite, which is also a used biomaterial for bone replacement. In addition, the presence of Si ions speeds the remodeling. Silicon also has a role in modulating the homeostasis of collagen and other ECM proteins in bone matrix; the ion induces osteoblast differentiation as well as

collagen I production in human osteoblast cells.^[232] In addition, silicon is able to induce angiogenesis and vascularization.^[147]

Zinc is an essential trace element required for many cellular catalytic, structural, and regulatory processes and is critical for normal growth, immunological functions, and neurological health.^[233,234] Zinc is further recognized as an antioxidant and anti-inflammatory agent that might have significant therapeutic benefits against several chronic diseases, such as cancer, neurodegeneration, atherosclerosis, and immunological disorders. It has long been known that zinc is required for bone growth and development and that its deficiency can lead to many kinds of skeletal abnormality in fetal and postnatal development, including bone growth retardation, abnormal mineralization, and osteoporosis.^[234,235] At a cellular level, zinc exerts a dual mode of action by supporting both osteoblastogenesis and suppressing osteoclastogenesis. Zinc can enhance osteogenesis through inducing collagen synthesis, ALP activity, and mineralization of bone nodules. In osteoblast-like MC3T3-E1 cells, this is mediated by *Runx2* expression, the master gene of osteogenesis and, in mesenchymal stem cells.^[219,220,236]

Strontium is structurally, physically, and chemically similar to calcium and, thus, has been studied extensively in the context of bone regeneration. Strontium is a strong bone-seeking trace element, of which approximately 98% is localized in human bone tissue.^[237] In recent years, strontium has been recognized as a treatment for osteoporosis in the form of strontium ranelate. *In vitro*, the drug as a dual mode of action, by both decreasing bone resorption and increasing bone formation.^[238] Over time, this has shown to translate into an increase in osteoblast surfaces, mineral apposition rate, trabecular and cortical bone formation, bone mineral density (BMD), and ultimately, lower risk of fracture.^[239]

Strontium itself promotes osteogenic differentiation of MSCs by upregulating the expression of osteoblast marker genes, such as *Runx2*, *OCN*, osteopontin (*OPN*), bone sialoprotein (*BSP*), and type 1 collagen, and increasing ALP activity and matrix mineralization.^[212] Strontium also upregulates the expression of endogenous BMP-2;^[213] however, when used in conjugation with free rhBMP-2, a Sr-rhBMP-2 complex is rapidly formed that undermines the binding capability of rhBMP-2 to its receptor. As a result, the BMP/Smad signaling pathway is suppressed, decreasing the

Introduction

efficiency of *in vitro* and *in vivo* rhBMP-2 induced osteogenesis.^[182] Strontium has also widely been used to enrich biomaterials such as various kinds of calcium phosphate, bioactive glass, bone cement, and metallic implant. The presence of Sr²⁺ in these structures enhanced the proliferation and osteogenic differentiation in osteoblastic cells, and inhibited osteoclast activity *in vitro*.^[214,240] *In vivo*, Sr²⁺ incorporation promotes bone formation, remodeling and osseointegration. Studies have shown Sr²⁺ to lead to an increase in the bone-to-implant contact, peri-implant bone volume, and push-out force.^[204,241] Additionally, a recent study investigated the potential benefits of a combined ionic therapy using a cobalt- and strontium-doped bioglass, making use of the osteogenic effect of strontium and the angiogenic effect of cobalt, in the regeneration of functional bone tissue.^[241] This highlights the potential therapeutic applications of combining multiple ions into bone tissue regeneration implants to exploit the different actions of different ions.

Shi *et al.* have shown that strontium can be incorporated into the titanium implant surfaces to subsequently release the bioactive ion and enhance implant osseointegration.^[242] High surface of MTF coatings enable high interaction surface of the implant with the surrounding. Importantly, it is possible to incorporate strontium or calcium into the MTF during the synthesis process simply by adding ionic salts to the sol.^[243] By this way the ions will be incorporated to the titania matrix forming titanates with an enhanced biological activity. As for now the incorporation of $0.2 \times 10^{-3} : 1$ of Sr : Ti relation in moles has been achieved.^[243]

II. AIM AND OBJECTIVES OF THE THESIS

This PhD dissertation aims at the design and fabrication of mesoporous titania thin films with controlled pore size and chemical functionalization for potential use as coating in titanium implants. Mesoporous coatings offer the advantage that they display pores that can be filled with drugs and molecules promoting cell growth and with antibacterial properties that can be beneficial for the bone regeneration. In addition, in mesoporous materials the active surface of the coating is largely increased due to their porosity. Pores will be used here for the encapsulation and sustainable release of antibiotics. The large surface area of the porous materials will provide a means to enhance the delivery of bioactive ions. In addition, the mesoporous coatings will be engineered with bioactive molecules and self-assembled films of antibiotics.

The general aim comprises the following specific objectives:

Objective 1

To design and fabricate functional mesoporous titania films (MTFs) loaded with antibiotic molecules such as gentamicin and its subsequent controlled release. Drug release will be assessed through fluorescent emission measurements at different time periods. The impact of the antibiotic release will be evaluated by studies of *S. aureus* proliferation on top of the film. In addition, recombinant human Bone Morphogenetic Protein 2 (rhBMP-2) will be assembled on top of the MTFs. The impact of rhBMP-2 on MC3T3-E1 pre-osteoblastic cell line proliferation and differentiation will be evaluated.

Objective 2

To fabricate a multilayer coating through the layer-by-layer technique using as building blocks poly-L-lysine (PLL) and complexes of gentamicin and poly (acrylic acid) (PAA) to achieve a stable film capable of releasing gentamicin in a time window of weeks. Optimal gentamicin concentrations and ionic strength/pH conditions will be found to obtain stable complexes with the highest possible loading of gentamicin. The release of antibiotics and effectiveness of the PEM will be evaluated studying the proliferation of *S. aureus* on top of the film.

Objective 3

To synthesize mesoporous films comprising strontium titanates and evaluate their potential for enhancing osseointegration. A new fabrication method will be evaluated that comprises the film formation from a heterogeneous precursor mixture containing titanium precursor and strontium chloride as well as a structure directing agent. By spin coating and taking advantage of the evaporation induced self-assembly (EISA) method SrTiO₃ mesoporous films will be fabricated. The release of strontium ions from the film will be studied and their capability to promote MC3T3-E1 pre-osteoblast cell proliferation and differentiation for the improvement of osseointegration of titanium implants will be evaluated.

Objective 4

To fabricate mesoporous titania films functionalized with carboxylic groups capable of complexing and releasing Sr⁺² for enhanced osseointegration. A one step co-condensation approach will be developed to synthesize mesoporous silica films with carboxylic groups, and then the synthesis will be extended to the functionalization of titania films. A two-step synthetic pathway is followed to obtain a versatile titania mesoporous system that can be functionalized with different bioactive ions. The presence of carboxylic groups will be evaluated by selective complexation of bioactive ions; lead and strontium for silica and titania films, respectively. The main purpose of this chapter is to enhance cell osseointegration in implants by means of the release of strontium ions complexed to carboxylates in the pore walls of the coating.

III. MATERIALS AND METHODS

Materials

All the mesoporous films based on titania are prepared in glass coverslips of 14 mm in diameter and 0.13 - 0.16 mm of thickness from Thermo Scientific through spin coating. Silica based mesoporous films are prepared in glass slides of 0.8 - 1 mm of thickness from Thermo Scientific through dip coating.

For the titania film synthesis Titanium (IV) Chloride ($\geq 99.0\%$, TiCl_4), tetraethoxysilane (TEOS, 98 %), Brij 58 and Pluronic F127[®] were purchased from Sigma Aldrich (Madrid, Spain) and Absolute Ethanol ($\geq 99\%$, EtOH) from Scharlau. For chemical and biomolecular functionalization of the mesoporous films Mercaptosuccinic acid (MSA, 97 %), Mercaptoacetic acid (MAA, 97 %), Vinylmethoxysilane (VTMS, 98 %), Benzophenone (Ph_2CO , 99 %), Strontium chloride hexahydrate ($\text{SrCl}_2 \times 6\text{H}_2\text{O}$), recombinant human Bone Morphogenetic Protein -2 (rhBMP-2) and Gentamicin Sulphate were also purchased from Sigma Aldrich (Madrid, Spain). $\text{Pb}(\text{NO}_3)_2$ and methanol were purchased from Merck.

For LbL coatings Poly (acrylic acid) solution $M_w = 100$ kDa and Poly - L -lysine 0.01 % with $M_w = 150 - 300$ kDa were also purchased from Sigma Aldrich (Madrid, Spain).

To study the gentamicin release 2 - mercaptoethanol, Boric Acid and *O* - phtaldehyde were purchased from Sigma Aldrich and the 2 - propanol was purchased from Fisher Scientific.

Phosphate buffered saline (PBS) in tablets, Sodium dodecadocyl sulphate (SDS), Nitric acid (HNO_3) and Sodium hydroxide (NaOH) were purchased from Sigma Aldrich. Sodium chloride (NaCl), Calcium nitrate ($\text{Ca}(\text{NO}_3)_2$) and hydrochloric acid (HCl) were purchased from Fisher Scientific.

All the buffers and solutions were filtered through the 0.2 μm filters (Fisher, Madrid, Spain) and degassed in bath sonicator prior to its use. The Falcon polystyrene tissue culture plates were purchased from Fisher Scientific (Madrid, Spain). Nanopure water used in preparation of all the dilutions and buffers was produced with a Diamond UV water purification system (Branstead International, IA, Iowa, USA).

Methods

The main techniques and methods used are described below, and more specific methods are presented in the experimental part of each chapter.

Spin coating and dip coating

The spin coating technique uses centrifugal forces created by a spinning substrate to spread a coating solution over the desired surface to cover. It is important the amount of liquid used and it should be dispensed in the proper location with the help of a syringe or a pipette used manually or with an automated pumping system.^[244]

The setup consists of a sample holder or a stage, a motor and a controller used to spin the sample at a specific velocity and for a determined time. The solution is dispensed just at the beginning of the spinning process while the spin speed starts to accelerate to spread the liquid over the surface to cover it. During the spin time the solution is spread across the substrate and the excess will be forced off. The spin velocity will determine the coating thickness because while the spin speed decreases, the lower amount of solution would be forced off.^[244]

For the mesoporous films synthesized by spin coating for this research work, 30 μL are dispensed in the glass substrates. The acceleration time is set at 0 to reach the velocity of 68 rpm as soon as possible and the sample is spinning at this velocity for 30 seconds. The SCC-200 spin coater from Novocontrol Technologies is used.

In dip coating technique, the substrate where the glass slide is withdrawn vertically to the sol.^[245] Thickness and uniformity are sensitive to the conditions the substrate is withdrawn, and the faster the velocity the thicker is the film deposited.^[246]

A withdrawal speed of 3 mm s^{-1} is used to deposit the films synthesized by dip coating onto glass slides.

X-Ray photoelectron spectroscopy (XPS)

X-Ray photoelectron spectroscopy is a surface analysis technique. It is used to measure the elemental composition, the empirical formula and chemical and electronic state of the elements within a material.^[247] The basic principle of XPS lays in photoelectric effect described by Einstein.^[248] In XPS experiment, kinetic energy is measured from electrons that are emitted from the surface as schematically shown in **Figure III-1**. A soft X-ray irradiation is used to excite the core electrons. A

bound electron adsorbs the photon, converting some of its energy into kinetic energy (KE). The electron leaves the atom and some of its energy is used to overcome the Coulomb attraction of the nucleus, reducing its KE by its initial state binding energy (BE). At the same time the outer orbitals readjust, lowering the energy of the final state that is being created and giving this additional energy to the outgoing electron. XPS is very surface sensitive technique as atoms emit photons from few top atomic layers. A photoelectron spectrum is recorded by counting ejected electrons over a range of electron kinetic energies. Peaks appear in the spectrum from atoms emitting electrons of a particular characteristic energy.

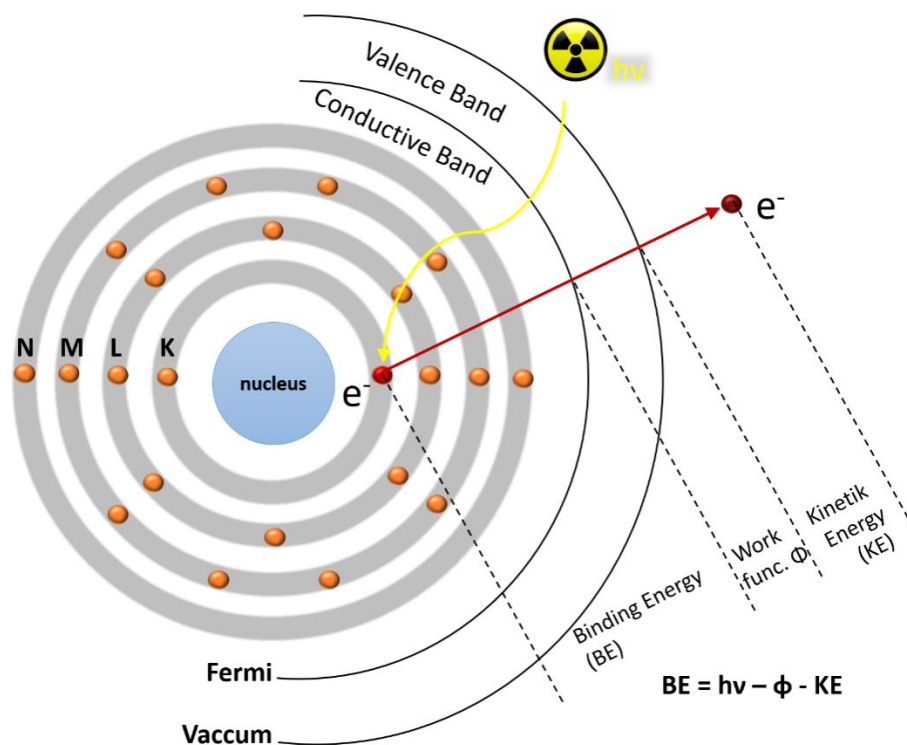


Figure III-1. Schematic representation of XPS. A core electron is excited with X-ray source, a photoelectron is ejected from the atom for a value of the binding energy, the kinetic energy and the work function of the spectrometer.

Experiments were performed with a SPECS Sage HR 100 spectrometer equipped with a 100 mm mean radius PHOIBOS analyzer and a nonmonochromatic X-ray source (Mg K α line of 1253.6 eV energy and 250 W), placed perpendicular to the analyzer axis and calibrated using the 3d_{5/2} line of Ag, with a full width at half maximum of 1.1 eV. The selected resolution for high resolution spectra was 15 eV of pass energy and 0.15 eV per step. All measurements are made in an ultrahigh vacuum chamber at a pressure of around 8×10^{-8} mbar. An electron flood gun is used to neutralize the charging. Measurements are conducted directly on the films,

which are previously washed with absolute ethanol and cut into samples of 1 cm × 1 cm. The analysis of spectra is done with CasaXPS 2.3.15dev87 software. Satellite removal and Shirley background subtraction are applied. Binding energies were calibrated assigning to the C 1s C–C peak 285 eV, and peaks were fitted with Gaussian–Lorentzian line shapes to determine the atomic percentages of elements present in the films.

Atomic force microscopy (AFM)

Atomic force microscopy is a high resolution scanning technique used to measure local properties of a surface using a probe. A cantilever with a sharp tip at its end is used for the scanning. When the tip is brought into proximity of a sample surface, forces between the tip and the sample lead to a deflection of the cantilever according to Hooke's law. In most cases a feedback mechanism is employed to adjust the tip-to-sample distance to maintain a constant force between the tip and the sample.^[249]

There are two imaging modes; static or contact mode and a variety of non-contact or “tapping” modes, where the cantilever vibrates at given frequencies. In contact mode, the tip drags across the sample surface, and while the tip scans the surface, the topography of the surface induces a vertical deflection of the cantilever. A feedback loop maintains this deflection at a pre-set load force and uses the feedback response to generate a topographic image. Close to the surface of the sample, attractive forces can be quite strong, causing the tip to “snap-in” to the surface.

In tapping mode, AFM maps topography by lightly tapping the surface with an oscillating probe tip. The cantilever is driven to oscillate up and down at or near its resonance frequency by a small piezoelectric element mounted in the AFM. The interaction of forces acting on the cantilever when the tip comes close to the surface, Van der Waals forces, dipole-dipole forces or electrostatic forces, among others, cause a decrease in the oscillation amplitude as the tip gets closer to the sample. The height is adjusted to maintain the oscillation amplitude and scan over the sample.^[250]

Images are obtained using a Nanowizard II AFM (JPK, Berlin, Germany). Images are acquired in air. The tapping mode is used with the tip TESP-V2 (Bruker, AFM probes) which has a spring constant of 40 N m⁻¹ and a resonant frequency in the range 280 – 320 kHz. Average roughness R_a calculation, which gives the deviation

in height, is done by applying **Equation III-1**. \bar{z} is the arithmetic average height calculated from an image described as a matrix with N lines and M columns and each height value z is associated to an (x, y) coordinate.^[250]

$$R_a(N, M) = \frac{1}{N} \sum_{x=1}^N (z(x, y) - \bar{z}(N, M)) \quad \text{Equation III-1}$$

Phase images need to be obtained with the tapping mode of the AFM and they represent the phase lag of the oscillation frequency of the cantilever when interacts with the sample. The greater the phase lag is the brighter is going to be the pixel and the smaller the phase lag, the darker the pixel. Chemical and physical properties of the material such as viscoelasticity, friction or adhesion impact on the phase shift and the tip experiences attractive and repulsive forces when it interacts with the surface.^[250]

Nanoindentation

Nanomechanical tests were performed using a triboindenter (Hysitron –TI-950), equipped with a Berkovich tip and a 2D - axis transducer. Values of Hardness (H) and Elastic Modulus (Er) were extracted from nanoindentation tests. Measurements were performed 10 times using partial load-unload function and Oliver-Pharr method.^[251] Measurements were performed after 120 seconds of drift correction and shallow calibration (5-30 nm) of the indenter on commercially available fused quartz (69.6 GPa).

Small-angle X-ray scattering (SAXS)

Small-angle X-ray scattering is a small-angle scattering technique by which nanoscale electronic density differences in a sample can be quantified. This means that it can determine nanoparticle size distributions, resolve the size and shape of macromolecules, determine pore sizes and characterize distances of partially ordered materials. This is achieved by analysing the elastic scattering behaviour of X-rays when travelling through the material, recording their scattering at small angles, typically 0.1 - 10°. It belongs to the family of small-angle scattering (SAS) techniques along with small-angle neutron scattering, and is typically done using hard X-rays with a wavelength of 0.07 - 0.2 nm. Depending on the angular range in which a clear scattering signal can be recorded, SAXS is capable of delivering

structural information of dimensions between 1 and 100 nm, and of repeat distances in partially ordered systems of up to 150 nm.^[252]

In a SAXS instrument a monochromatic beam of X-rays is brought to a sample from which some of the X-rays scatter, while most simply go through the sample without interacting with it. The scattered X-rays form a scattering pattern which is then detected at a detector which is typically a 2-dimensional flat X-ray detector situated behind the sample perpendicular to the direction of the primary beam that initially hit the sample. The scattering pattern contains the information on the structure of the sample.

2D- Small angle X-Ray scattering (2D-SAXS) patterns were obtained at the Austrian SAXS beamline at the Elettra synchrotron (Trieste, Italy), using a 1.54 Å (8 keV) incidence X-ray beam. The sample was placed at 82.88 cm from a pixel detector (Pilatus1M) on a rotation stage, which allowed to set the glancing angle between the incident radiation and the sample to 3°.^[253] The samples were prepared onto coverslips to allow measurements in Laue geometry. The angular scale of the detector was calibrated with Ag-behenate as the reference pattern.

Confocal laser scanning microscopy (CLSM)

Confocal laser scanning microscopy is an optical imaging technique with increased resolution and depth selectivity. The key feature of confocal microscope is in ability to acquire in-focus images from selected depths. Images are acquired point-by-point and reconstructed with a computer, allowing three-dimensional reconstructions of topologically complex objects. The quality of the image is greatly enhanced over simple microscopy because image information from a confocal microscope is constructed as one depth level at a time. In effect, the CLSM achieves a controlled and highly limited depth of focus.^[254]

Fluorescence images of stained pre-osteoblasts presented in this thesis were acquired on a Zeiss LSM 510 confocal microscope (Carl Zeiss, Göttingen, Germany).

Scanning electron microscopy (SEM) and Transmission electron microscopy (TEM)

The base of the electron microscopy is the use of electrons to excite a sample and obtain an image. The SEM is used for surface imaging and with the TEM electrons are transmitted through the specimen to form an image. Incident electrons interact

with the sample and they can suffer different transformation, but we are focused on secondary electrons and transmitted electrons, detected by SEM and TEM, respectively. As secondary electrons have a low energy, only the electrons which are in the surface of the sample are able to get out from the sample, so these are the electrons we are going to measure. In the SEM, the electrons interact with atoms in the sample, producing signals that can be detected and contain information about the surface topography and composition. The electron beam is scanned in a raster scan pattern, and the beam's position is combined with the detected signal to produce an image. The most common SEM mode is detection of secondary electrons emitted by atoms excited by the electron beam.^[255]

Electrons are very small and can be deflected by hydrocarbons or gas molecules, in both cases, to avoid electron deviation a vacuum environment is needed to use the electron beam. The illumination source is an electron gun where a cathode (filament) is used as electron source generated by thermal emission. Electron microscope lenses are electromagnetic and a wrapping of copper wire makes up the magnetic field, which is the essence of the lens. The condenser lenses gather the electrons to focus the illumination onto the specimen and to reduce spherical aberrations. In the TEM, the objective lens is used to focus and magnify the image and the objective aperture is used to enhance the contrast of the image, and finally the projector lenses further magnify the image, which is projected into the phosphorous screen.^[256]

In **Chapter 1** and **Chapter 3** film surfaces were visualized with a Field Emission Scanning Electron Microscopy (FE SEM) Carl Zeiss NTS Supra 40 at the Advanced Microscopy Centre FCEN-UBA in second electron imaging (SEI) detection mode. In **Chapter 1**, to visualize film thickness and pores inside the film a transversal cut is done and images were taken with a Dual Beam SEM/FIB Helios 450S microscope (FEI, Netherlands) at 5 and 10 kV acceleration voltages. In **Chapter 3**, to visualize the synthesized polyelectrolyte multilayer (PEM), a SEM of type JEOL JSM-6490LV has been used. Sample has been cut with a diamond tip and Pt-Au has been sputtered in the preparation chamber GATAN ALTO1000.

TEM images were collected with TEM JEOL JEM-1400PLUS microscope equipped with a Gatan US1000 CCD camera. Films samples were prepared on copper grids

with a carbon film purchased from EM Resolutions. The films were scratched and a deposited on top of the grid with a 5 μL drop of ethanol. In **Chapter 3** and **Chapter 4** Energy Dispersive X-ray (EDX) measurements have been performed. A JEOL JEM-2100F UHR TEM operated at 200 kV in Scanning Transmission Scanning Microscope (STEM-BF) equipped with an EDX detector (EDXS, Oxford INCA systems) was used for the semi-quantitative analysis of the film composition at different areas on the surface. INCA and Origin 8.5 software were used for the analysis of the experimental data.

Inductively coupled plasma mass spectrometry (ICP-MS)

An Inductively coupled plasma mass spectrometry combines a high-temperature ICP source with a mass spectrometer. The ICP source converts the atoms of the elements in the sample to ions. These ions are then separated and detected by the mass spectrometer. Argon gas flows inside the concentric channels of the ICP torch. The RF load coil is connected to a radio-frequency (RF) generator. As power is supplied to the load coil from the generator, oscillating electric and magnetic fields are established at the end of the torch. When a spark is applied to the argon flowing through the ICP torch, electrons are stripped off of the argon atoms, forming argon ions. These ions are caught in the oscillating fields and collide with other argon atoms, forming an argon discharge or plasma.^[257]

The sample is typically introduced into the ICP plasma as an aerosol, either by aspirating a liquid or dissolved solid sample into a nebulizer or using a laser to directly convert solid samples into an aerosol. Once the sample aerosol is introduced into the ICP torch, it is completely desolvated and the elements in the aerosol are converted first into gaseous atoms and then ionized towards the end of the plasma.^[257] Once the ions enter the mass spectrometer, they are separated by their mass-to-charge ratio.^[257]

To measure the strontium amount released (**Chapter 3** and **4**) samples have been prepared in 5 % HNO_3 . Iridium (Ir) was used as internal standard to calibrate the equipment. To quantify the amount of strontium, SrCO_3 solutions have been prepared at 1, 5, 10, 25, 50, 100 and 200 ppb for the calibration curve using the Sr reagent for ICP from Inorganic Ventures. To get accurate results the curve was forced to the blank. The calibration curve for strontium is: $y = 1.01x - 0.85$, where y

is the measured intensity (a.u.) and x the strontium concentration (ppm) and has an R^2 of 0.999. Measurements have been performed at a ICP-MS iCAP Q from Thermo Fisher.

Quartz crystal microbalance with dissipation monitoring

Quartz Crystal Microbalance with Dissipation monitoring (QCM-D) is a real-time, nanoscale technique for thin film formation, interactions and reactions. A QCM sensor consists of a thin quartz disc between a pair of electrodes. The sensor can be excited to oscillate at its resonance frequency by the application of an alternating voltage. The resonance frequency depends on the total oscillating mass of the sensor and sensor surface adhering layers, including coupled water. The frequency decreases when a thin film is attached to the sensor. If the film is thin and rigid the decrease in frequency is proportional to the mass of the film.^[258]

QCM-D is used in **Chapter 3** of the thesis for the *In situ* monitoring of the poly-L-lysine (PLL) M_w 150-300 kDa and poly (acrylic acid) (PAA) M_w 100 kDa and gentamicin complex films assembly and to study the film stability. An E4 QCM-D from Q-Sense, Goteborg, Sweden was used. The LbL assembly was performed on QSX 303 SiO₂ quartz crystals (Q-sense) by alternating the PLL at a 1 mg mL⁻¹ and the complex (1 mg mL⁻¹ PAA and 0.3 mg mL⁻¹ gentamicin) at pH 4.5 in NaCl 500 mM monitoring the decrease of the resonance frequency. Once the frequency value stabilized, the polymer solution has been replaced by NaCl 500 mM (pH 4.5) til a plateau was reached. This procedure has been repeated til the desired number of layers were deposited.

Ellipsometry and environmental ellipsometric porosimetry (EEP)

Ellipsometry measures a change in polarization as light reflects or transmits from a material structure. The polarization change is represented as an amplitude ratio, Ψ , and the phase difference, Δ . The measured response depends on optical properties and thickness of individual materials. Thus, ellipsometry is primarily used to determine film thickness and optical constants.^[259]

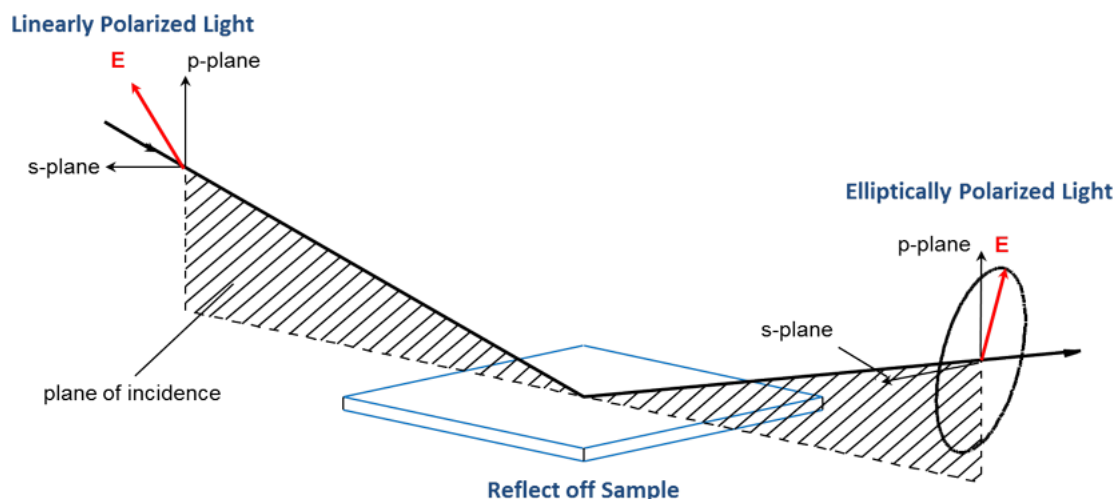


Figure III-2. Geometry of an Ellipsometric measurement.^[260]

Data analysis proceeds as follows: After a sample is measured, a model is constructed to describe the sample. The model is used to calculate the predicted response from Fresnel's equations which describe each material with thickness and optical constants. If these values are not known, an estimate is given for the purpose of the preliminary calculation. The calculated values are compared to experimental data. Any unknown material properties can then be varied to improve the match between experiment and calculation.^[259]

The film thickness is determined by interference between light reflecting from the surface and light traveling through the film. Depending on the relative phase of the re-joining light to the surface reflection, interference can be defined as constructive or destructive. The interference involves both amplitude and phase information. The film thickness affects the path length of light traveling through the film, but the index determines the light waves' velocity and refracted angle. Thus, both contribute to the delay between surface reflection and light traveling through the film. Both refractive index n and dielectric constant k must be known or determined along with the thickness to get the correct results from an optical measurement.^[259]

EEP measures the change of the optical properties and thickness of the materials during adsorption and desorption of volatile specie. The amount of adsorptive inside of pores is calculated from the measured change of the optical characteristics of the porous film during the vapour adsorption/desorption. There are several

methods for performing these calculations based on various equations (Lorentz–Lorenz, Newton–Laplace, Bragg–Pippard, etc). The optical characteristics of the dense part of the porous media and of the liquid adsorptive are used in these calculations. The various equations give similar results, however, the Lorentz–Lorenz equation is more widely used.^[259]

The technique is based on analysis of the hysteresis loops that appear due to the processes of capillary condensation and desorption of a vapour out of porous adsorbents. The hysteresis loops appear because the effective radius of curvature of condensed liquid meniscus is different during the adsorption and desorption processes. The adsorptive vapour condenses in pores even if the vapour pressure P is less than the equilibrium pressure of a flat liquid surface P_0 . Dependence of the relative pressure P/P_0 on the meniscus curvature is described by the Kelvin equation

$$\frac{1}{r_1} + \frac{1}{r_2} = - \frac{RT}{Y V_L} \ln \left(\frac{P}{P_0} \right) \quad \text{Equation III-2}$$

where Y and V_L are surface tension and molar volume of the liquid adsorptive, respectively. The principal curvature radii r_1 and r_2 define pore sizes. In the case of cylindrical pores, $r_1 = r_2$ and

$$\left(\frac{1}{r_1} + \frac{1}{r_2} \right) = \frac{2}{r_k} \quad \text{Equation III-3}$$

The radius r_k is often termed the Kelvin radius. If the radius of a cylindrical pore is r_p , then $r_p = r_k + t$, where t is the thickness of the layer already adsorbed on the pore walls. Values of t are obtained from the data for the adsorption of the same adsorptive on a nonporous sample having a similar surface.^[261]

Ellipsometry allows us to measure both the refractive index and the film thickness d . In this case the adsorptive volume in pores can be calculated as

$$V_{ads} = \frac{V_m}{\alpha_{ads} \cdot d_t} (B_1 d_1 - B_0 d_0) \quad \text{Equation III-4}$$

where V_{ads} is the volume of the liquid adsorptive in the pores, B_0 and B_1 are the volume polarizability of the film before and after adsorption, d_0 and d_1 are the film

thickness before and after adsorption, respectively, V_m is the molecular volume of the adsorptive and α_{ads} is the polarizability of the adsorptive molecule.^[261]

For titania films in all chapters the measurements were performed in a M2000 VASE from Woollam ellipsometer. Ellipsometric and EEP measurements of mesoporous silica films in **Chapter 4** were performed in a SOPRA GES5A ellipsometer, using samples previously washed with absolute ethanol and dried. Film thickness and refractive index values were obtained from the ellipsometric parameters Ψ and Δ under dry air flux containing variable water vapour pressure P ; P/P_0 was varied from 0 to 1 (P_0 being the saturation water vapour pressure at 25 °C). Water volume adsorbed at each value P/P_0 was determined by modelling the obtained refractive index according to a three-component (water–air–oxide) Bruggeman effective medium approximation. Adsorption–desorption isotherms were obtained by plotting the water volume adsorbed by the porous film at each P/P_0 . The pore size distribution was obtained from the isotherms using the Kelvin equation, taking into account the water contact angle in the film.^[262]

Contact angle goniometer

Contact angle goniometer measurements are essential for understanding the wetting characteristics of an analysed surface. The contact angle (CA) is defined as the angle made by a sessile drop of liquid (l) in contact with a solid (s) surface and is measured according the Young’s equation (**Equation III-5**) from the side of the liquid as seen in **Figure III-3**.^[263] Analysing the CA when a drop of water is placed on a surface information about the degree of hydrophobicity or hydrophilicity of almost any kind of surfaces can be obtained. ^[264]

$$\gamma_{sv} = \gamma_{sl} - \gamma_{lv} \cos\theta$$

Equation III-5

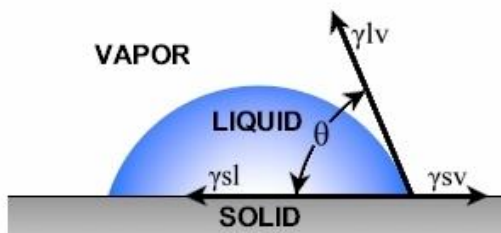


Figure III-3. Vector representations of Young’s equation on a sessile drop for measuring Young’s contact angle.^[265]

One of the most common techniques used to measure CA is by goniometry, where basically the CA is measured by an image of the drop adsorbed on the specimen's surface. After imaging, a tangent is drawn along the solid-liquid interface and the CA is measured from the drop profile. Young's model is applied only to systems with smooth and homogeneous surfaces. For rough and heterogeneous surfaces have been established modifications to the Young's model.

The Wilhelmy plate technique developed by Neumann is widely used to determine the advancing and receding contact angles and therefore the surface free energy of analysing surfaces.^[266] Contact angle measurements were performed in a Drop Shape Analyser – DSA100 from Kruss and a Ramé-Hart 190 CA equipment.

Dynamic light scattering (DLS)

Dynamic light scattering is a powerful technique for probing soft matter particles mainly at the sub-micron region. DLS is based on the time-resolved measurement of the scattered intensity, $I(t)$ produced by particles suspended in a liquid undergoing the Brownian motion. The Brownian motion is correlated with the scattered light therefore the larger the particle, the slower the Brownian motion will be; the diffusion due to Brownian motion of the particles is obtained by recording the rate at of fluctuation of the intensity of the scattered light. Subsequently small particles display more rapid scattered light intensity fluctuation in contrast with large particles. Further information about the random fluctuations in a time-resolved manner is provided by the autocorrelation function (**Equation III-6**).

$$g(t) = \frac{\langle I(t+t_0) \times I(t_0) \rangle}{\langle I \rangle^2} \quad \text{Equation III-6}$$

For large particles the correlation of the signal takes more time to decay while for small particles the correlation decreases rapidly as a consequence of the movement of the particles.

$$D = \frac{k_B T}{6\pi\eta R_H} \quad \text{Equation III-7}$$

According to Stokes-Einstein equation (**Equation III-7**) the particle size is given in terms of hydrodynamic radius which is defined by the diameter of a sphere that has the same translational diffusion coefficient as the particle⁸. Where D is the diffusion

coefficient, k_B is Boltzmann's constant, T is the temperature, η is the viscosity of the medium and R_H is the hydrodynamic radius of the analysed particle.^[267]

Measurements were performed in a Zetasizer Nano ZS from Malvern.

Gentamicin detection

One of the major problems related to the use of gentamicin, and all aminoglycoside antibiotics, in the laboratory is the limited means of quantifying the drug. Since gentamicin absorbs ultraviolet and visible light poorly and the molecule lacks fluorophores, no direct spectrophotometric or fluorometric method can be applied. Therefore, its detection often requires derivatisation.^[268]

Boric acid (0.4 M) is dissolved in distilled water; the pH is adjusted to 10.4 with potassium hydroxide solution. *O*-phthaldialdehyde (OPA) reagent is prepared according to following procedure: 0.2 g of OPA is dissolved in 1 mL of methanol and the solution is mixed with 19 mL of a 0.4M boric buffer. Then, 0.4 mL of 2-mercaptoethanole is added and the pH was adjusted to 10.4 with the potassium hydroxide solution. This reagent is kept in the dark at 4 °C until its use the following day. The samples and the 2-propanol are mixed in 1:1 proportion in volume and vortexed. Then, the OPA reagent is added in the same proportion and the solution is vortexed again.^[268,269] For 15 min, prior to measurement, the solutions are heated at 60 °C to catalyze the reaction. All the reagents were purchased from Sigma Aldrich, except the 2-propanol, which is from Fisher.

The formed fluorescent complex has its maximum absorption at 340 nm and the emission at 455 nm was collected at a Thermo Scientific™ Varioskan™ Flash Multimode Reader.

The gentamicin calibration curve was performed from 0 to 4 $\mu\text{g mL}^{-1}$ containing 7 points, prepared by triplicate. The calibration curve can be described with the following equation; $y = 6.49 + 21.26x$ where y is the emission of the OPA-gentamicin complex at 455 nm and x is the gentamicin concentration in $\mu\text{g mL}^{-1}$ and has an R^2 of 0.997.

Diffuse Reflectance Infrared Fourier Transform Spectroscopy (DRIFT)

A Fourier Transform Infrared (FTIR) Spectrometer is an instrument which acquires broadband near Infrared (NIR) to far Infrared (FIR) spectra. A FTIR is a

method of obtaining infrared spectra by first collecting an interferogram of a sample signal using an interferometer, and then performing a Fourier Transform (FT) on the interferogram to obtain the spectrum.^[270]

An FTIR is typically based on The Michelson Interferometer Experimental Set. The interferometer consists of a beam splitter, a fixed mirror, and a mirror that translates back and forth, very precisely. The beam splitter is made of a special material that transmits half of the radiation striking it and reflects the other half. Radiation from the source strikes the beam splitter and separates into two beams. One beam is transmitted through the beam splitter to the fixed mirror and the second is reflected off the beam splitter to the moving mirror. The fixed and moving mirrors reflect the radiation back to the beamsplitter. Again, half of this reflected radiation is transmitted and half is reflected at the beam splitter, resulting in one beam passing to the detector and the second back to the source.^[271]

DRIFT is a surface localized FTIR spectroscopy, since it can provide both chemical and structural information for all types of solid surfaces. When infrared radiation reaches a sample surface, one or several processes can occur: light can be adsorbed, reflected from the surface, or it can penetrate the sample before being scattered. If scattering centers, which are fibers in the case of ACM, are randomly oriented, the phenomenon is isotropic and generates a diffuse reflectance. The scattered light is then collected and relayed to the IR detector, where the absorption by chemical groups is revealed.^[272]

Optical Path Difference (OPD) is the difference between the two beams travelling through the two arms of an interferometer. Interferogram is the name of the signal format acquired by an FT-IR spectrometer. It is usually significantly more complex than a single sinusoid, which would be expected if only a single wavelength of light was present. The X-axis of the interferogram represents the optical path difference. Each individual spectral component contributes a single sinusoid with a frequency inversely proportional to its wavelength to this signal. This leads us to the definition of the unit of spectral measurement: the wavenumber (cm^{-1}), denoted as ν . A wavenumber represents the number of full waves of a particular wavelength per cm of length (typically in vacuum, where the

index of refraction $n=1$). The advantage of defining the spectrum in wavenumbers is that they are directly related to energy levels. A spectral feature at $4,000\text{ cm}^{-1}$ spectral location represents a transition between two molecular levels separated by twice the energy of a transition with spectral signature at $2,000\text{ cm}^{-1}$.^[270]

Once an interferogram is collected, it needs to be translated into a spectrum (emission, absorption, transmission, etc.). The process of conversion is through the Fast Fourier Transform algorithm.^[270]

In this work FTIR and DRIFT spectroscopy measurements were performed in a Nicolet Magna 560 instrument, equipped with a liquid N₂-cooled MCT-A detector.

X-Ray Reflectometry (XRR)

XRR studies allow determining porosity of porous films.^[273] Measurements were performed on a Panalytical Empyrean X-ray diffractometer with an incident beam of Cu K α radiation at 1.54 \AA and an incident angle of 1° . A divergence slit of 0.38 mm and a mask of 10 mm were used for the measurements. Film thickness was determined from the Kiessigfringes in the reflectogram. The reflectivity critical angle θ_c (the angle at which the reflected intensity is half the total external reflection) allows determining the electronic density (ρ_e) of the film by using **Equation III-8**;

$$\rho_e = \frac{\pi}{\lambda^2 r_e} \theta_c^2 \quad \text{Equation III-8}$$

where r_e is the classical radius of the electron ($2.813 \times 10^{-6}\text{ nm}$). Taking into account **Equation III-8**, the films porosity can be estimated from XRR data by measuring the change in the critical angle (and thus, in the thin film density) when the relative humidity (RH) changes from $\sim 5\%$ (*i.e.* the pores are full of air) to $\sim 90\%$ (*i.e.* the pores are filled with water). For that purpose, XRR measurements were made with the films placed inside a controlled humidity chamber. Considering that the increase in film density is only due to the presence of water, the water volume fraction ($F_v(H_2O)$) within the film was determined from the measured electronic densities using **Equation III-9**. In this case, the $F_v(H_2O)$ calculated is equivalent to the porosity (P) of the material.

$$P = F_v(H_2O) = \frac{\rho_e(\text{film} + H_2O) - \rho_e(\text{film})}{\rho_e(H_2O)} \quad \text{Equation III-9}$$

where $\rho_e(\text{film} + H_2O)$ is the electronic density of water-filled film (measured at high RH), $\rho_e(\text{film})$ is the electronic density of the film (measured at low RH) and the $\rho_e(H_2O)$ is the water electronic density.

Cell culture and assays

In this part, the cell culture methods and several assays to determine the osseointegration and antibacterial capacity of the substrates are explained.

MC3T3-E1 pre-osteoblastic cell line

The MC3T3 cell line comes from mouse (*Mus musculus*) calvaria bone. They are adherent pre-osteoblasts with fibroblastic morphology and with the ability to differentiate to osteoblasts. For the experiments the MC3T3-E1 cell line from Sigma Aldrich is used.

MC3T3-E1 cell culture

Cells are preserved in cryotubes with culture medium containing 10% glycerine at liquid N₂ at 196 °C. They are defrozen in 37 °C water bath, transferred to a centrifuge tube containing full culturing medium and centrifuged at 150 x g for 5 minutes. The cell pellet is resuspended in the full medium and dispensed in a culture flask. They are cultured in supplemented α -Minimum Essential Medium (α -MEM, Sigma Aldrich) with 10 % Fetal Bovine Serum (FBS, Sigma Aldrich) and 1 % of antibiotics (Penicillin-Streptomycin, Sigma Aldrich), referred as full culturing medium. They are kept at 37 °C and in a 5 % CO₂ atmosphere.

When cells reach 80 % confluence they are replicated. Using trypsin cells are detached from the culture bottle and around the 15-20 % of the detached cells are transferred to a new bottle. In this way, cells are always kept in the exponential growth phase. Cells are used for experiments til 15 passages to keep the genetic integrity of the cell line.

Actin cytoskeleton and focal adhesion staining

The actin cytoskeleton is composed of actin polymers and various associated proteins. It mediates a diversity of essential biological functions in eukaryotic cells.

The organization of the actin cytoskeleton is tightly regulated both temporally and spatially. Actin polymers are super organized into a filamentous network that is mediated by actin side binding or cross-linking proteins. A disruption of normal regulation may lead to cell transformations that have been shown to contain less F-actin and exhibit atypical coordination of F-actin levels to the cell cycle.^[274]

Focal adhesion and adherent junctions are membrane-associated complexes that serve as nucleation sites for actin filaments and as cross-linkers between the cell exterior, plasma membrane and actin cytoskeleton. The function of focal adhesions is structural, linking the ECM on the outside to the actin cytoskeleton on the inside. Focal adhesions consist of integrin-type receptors that are attached to the extracellular matrix and are intracellularly associated with protein complexes containing vinculin (universal focal adhesion marker), talin, α -actinin, paxillin, tensin, zyxin and focal adhesion kinase (FAK).

To confirm cell adhesion to the substrates Confocal Laser Scanning Microscopy (Zeiss LSM510) observations were performed after F-actin, focal adhesions and nucleus labeling with actin cytoskeleton and focal adhesion staining kit (FAK100, Millipore). Briefly, after reaching the 80% confluence, cells are trypsinized and resuspended in fresh medium to a final cell density of 3×10^4 cells mL⁻¹. 1 mL of cell suspension is added into each well of 24 multi well cell culture plates. After culturing for 2, 24 and 48 h, cells are first permeabilized with 0.1 % Triton-X100 (Sigma-Aldrich) for 4 min at room temperature. Then, cells are incubated in dilute anti-vinculin primary antibody for 1 h at room temperature, followed by three times wash for 5–10 min each with wash buffer (PBS with 0.05% Tween-20 (Sigma Aldrich)), followed by 1 h further incubation with a fluorescein isothiocyanate (FITC)-conjugated secondary antibody and tetramethylrhodamine (TRITC)-conjugated Phalloidin at room temperature. After three times rinsing with wash buffer, cells are incubated with 4,6-diamidino-2-phenylindole (DAPI) for 3 min at room temperature, followed by a three times wash.

MC3T3-E1 cell proliferation

After reaching 80 % confluence, cells are trypsinized and resuspended in fresh medium to a final cell density of $2.5-3 \times 10^4$ cells mL⁻¹. 1 mL of cell suspension is added into each well of 24 well cell culture plates. A cell proliferation colorimetric

assay is conducted with the Cell Counting Kit-8 (CCK-8) (Sigma Aldrich) containing WST-8[2-(2-methoxy-4-nitrophenyl)-3-(4-nitrophenyl)-5-(2,4-disulfophenyl)-2H-tetrazolium, monosodium salt], a nontoxic dye used for continuous cell culturing. Colorimetric analysis is performed at a certain time periods of cell culturing, in days scale, as noted in each of chapter. For this assay, the cells cultured on the samples are refreshed with 10 % v/v of CCK-8 containing medium. After 2 hours of incubation at 37 °C, aliquot of 150 µL is placed into 96 well cell plate. Optical density of reaction solution was acquired using a plate reader (GENios Pro, Tecan) equipped with a 450 nm filter. The statistical ANOVA analysis was done in Origin 8.5 software. Fisher's tests were performed to determine statistically significant differences with a $p < 0.05$.

MC3T3-E1 cell differentiation

MC3T3-E1 cell line behaves similar to primary calvarial osteoblasts and exhibit high levels of osteoblast differentiation after growth in ascorbic acid and inorganic phosphate. They form a well mineralized extracellular matrix (ECM) after 10 days of osteogenic culture.^[275]

For cell differentiation the full medium is additionally supplemented with 50 µg mL⁻¹ of L- ascorbic acid and 2mM of β-glycerophosphate, both purchased from Sigma Aldrich.

Alkaline phosphatase activity

Alkaline phosphatase (AP) is an important component in hard tissue formation, highly expressed in mineralized tissue cells. The AP in hard tissue formation serves as a marker for osteogenic activity has and it occurs at an early step in the mineralization process. Proliferating osteoblasts show AP activity in the stage of extracellular matrix maturation, being greatly enhanced during in vitro bone formation. AP activity is therefore a feasible marker for differentiating and mineralizing osteoblastic formation.^[276]

For AP quantification cells are seeded with a density of 5 x 10⁴ cell mL⁻¹ in a 24 multiwell dish. After 4 days of growth cells are cultured in osteogenic medium for 20 days following the differentiation during time.

Materials and Methods

The AP is quantified with the StemTAG™ Alkaline Phosphatase Activity Assay Kit from Cell Biolabs Inc. The AP catalyzes the conversion of p-Nitrophenyl Phosphate (pNPP) to p-Nitrophenol (pN). p -Nitrophenol is a bright yellow-colored compound which has maximum absorbance at 405 nm. The rate of increase in absorbance from pNPP (colorless) to pN (color) is directly proportional to the AP enzyme activity in the serum sample. Following the indications of the fabricant, a calibration curve with pN at concentrations ranging from 0.5 mM to 0.9766 μM is performed. The calibration curve to know the total amount of pN is obtained from 10 points ranging from and is $y = 0.04 + 7.51 x$ where y is the absorbance at 405 nm and x is the pN in mM with an R^2 of 0.999.

Cells are cleaned twice with PBS and lysated with 250 μL lysis buffer for 10 minutes at 4 °C. The solution has to be spin down at 12.000 g for 10 minutes and the supernatant must be kept. 1 : 1 relation in volume of cell lysate and pNPP are incubated for 15 minutes at 37 °C. To stop the reaction the same proportion in volume of 1 X stop solution is added and shaken for 30 seconds.

A Bradford assay is performed to quantify the protein quantity in the lysate and normalize the results. 1 part of protein sample is mixed with 30 parts of the Bradford Reagent, which consists of a dye, Brilliant Blue G that forms a complex with proteins, shifting the absorption maximum from 465 to 595 nm. Bovine serum albumin (BSA), from Sigma, is used as protein standard, and a calibration curve is performed with 5 points ranging from 1 to 2 mg mL⁻¹ of BSA. The calibration curve is $y = 0.37 + 0.13 x$ where y is the absorbance at 595 nm and x is the total amount of protein in mg mL⁻¹ with an R^2 of 0.983.

The absorbance measurements were performed at a Thermo Scientific™ Varioskan™ Flash Multimode Reader and the statistical ANOVA analysis was done in Origin 8.5 software. Fisher's tests were performed to determine statistically significant differences with a $p < 0.05$.

Staphilococcus aureus

Staphilococcus aureus is by far the most common pathogen found in surgical wounds, which can cause surgical site infections.^[277] Is a gram positive spherical bacteria belonging to the Staphylococci group.

The used *S. aureus* strain RN4220 is from Iñigo Lasa's Laboratory at Instituto de Agrobiotecnología, UPNA-CSIC Gobierno de Navarra. This strain is resistant to erythromycin.

***S. aureus* culture**

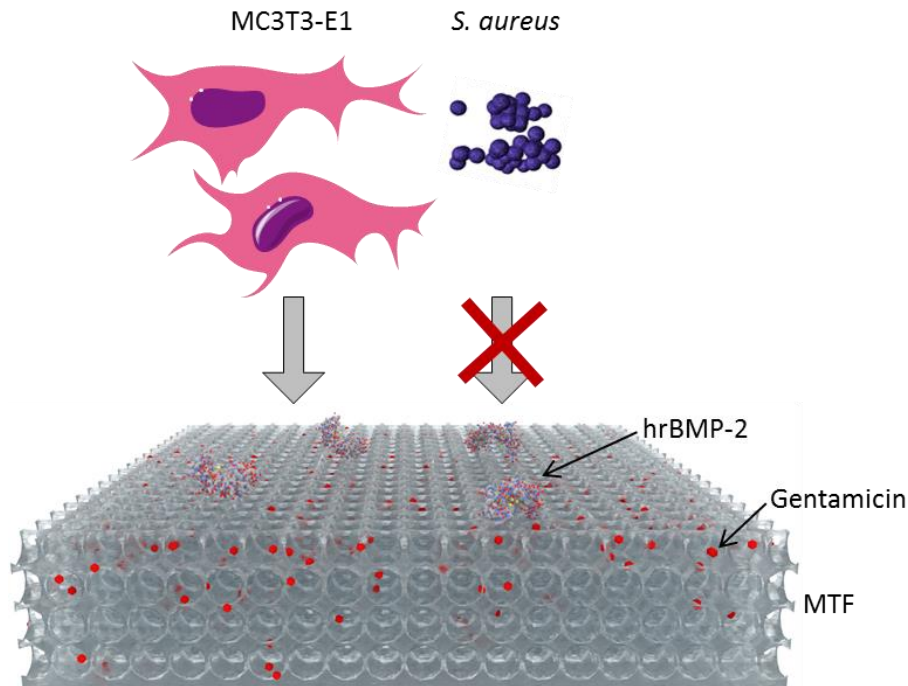
S. aureus is cultured in Luria-Bertani (LB) broth from Lennox with 10 µg mL⁻¹ erythromycin (Sigma Aldrich) overnight at 37 °C under constant shaking at 200 rpm.

***S. aureus* growth on surfaces**

After 24 h of growth in LB Broth, the bacteria are centrifuged at 2,500 rpm for 5 minutes and washed in 10 mM PBS with 150 mM NaCl (pH 7.4) three times. The optical density is adjusted to 0.257 at 600 nm with an UV-VIS Varian Cary 50 spectrophotometer, estimated to give 3 x 10⁸ CFU mL⁻¹. The bacteria solution is diluted in LB Broth with 10 µg mL⁻¹ erythromycin (Sigma Aldrich) at a concentration of 1,000 CFU mL⁻¹ and 1 mL is seeded onto the substrates placed each of them in a well of a 24 well dish. Bacteria is cultured for 24 h at 37 °C and then rinsed three times with 10 mM PBS to remove non-attached bacteria. After incubation, images are taken in the transmission mode in a Cell Axio Observer Microscope. To detach the adhered bacteria, samples are vortexed at 30,000 rpm for 1 minute inside sterile 50 mL centrifuge tubes with 10 mL of 10 mM PBS. Dilutions are done in PBS to culture 100 µL onto sterile LB Agar (Lennox) with 10 µg mL⁻¹ erythromycin. The plates are placed into an incubator at 37 °C to allow colonies to grow until visual counting is possible (approximately 18 hours).

IV. CHAPTER 1

MTFs with embedded Gentamicin and surface modified with rhBMP-2



1.1. Motivation

Since bone and joint inflammatory problems account for 50 % of chronic diseases in developed countries,^[19] there is an urgent demand for mechanically-resistant and bone-compatible orthopaedic implants.^[278-280] Implants often fail, requiring additional surgery and implant replacement, which is costly and compromises the health of the patient. A major reason for the failure of implants is the development of bacterial infections at the site of implant. During bone surgery, the surface of the implants is susceptible to bacterial infections that can lead to the formation of a biofilm and to a compromised immune response at the site of the implant. Aseptic loosening of the implants following surgery can result in the premature failure of the implant due to poor osseointegration.^[281,282] *Staphylococcus aureus* is among the most common bacteria causing implant associated infections and is considered to be a major, virulent pathogen that colonizes and infects both hospitalized patients with decreased immunity and healthy immunocompetent people.^[283,284] Skin and

mucous membranes are excellent barriers against local tissue invasion by *S. aureus*, but if any of them is breached due to trauma or surgery, bacteria can enter the underlying tissue, creating its characteristic local abscess lesion.^[285,286] Antibiotics are normally locally administered at the implant site, which effectively avoids the formation of bacterial colonies during surgery. However, there is a risk of bacterial colonization during the time bone tissue is being regenerated, which last several weeks, until the protective capsule is formed and especially after surgery when the osseointegration processes has started. To ensure the successful implant adaptation, the rational supply of antibiotics is needed and can be achieved by coating the implant surface with antibiotics-loaded polymer coatings such as polyelectrolyte multilayers, brushes or hydrogels.^[287-290] However, the main challenge is to obtain a localized supply of the antibiotics with a two-phase release profile. An initial burst release at short times is highly desirable as during surgery and at the initial phase of bone formation the risk of bacterial infection is larger, but at the same time a slow release lasting weeks is also required while the capsule is getting regenerated.

Coating the implant surface with mesoporous film is an attractive method to improve biocompatibility of Ti implants, as rougher surfaces promote bone and implant interlocking.^[291-293] Mesoporous materials have an ordered, homogenous distribution of interconnected pores whose diameters are in the 2–50 nm range.^[131,294-300] Titania can be synthesized as a mesoporous material without compromising its mechanical properties,^[301] which are fundamental for bone replacement. Mesoporous titania can be used for drug loading by soaking mesoporous in a drug solution and once drugs are entrapped their release is slowed by the necks that interconnect the mesopores.^[302,303] Atefyekta *et al.*^[304] have studied the loading and release of gentamicin, vancomycin and daptomycin from mesoporous titania films (MTFs) of pore sizes ranging from 4 to 7 nm, but the release of the antibiotics from the MTFs has been shown to occur within the first 80 minutes, which is not desirable for implants, where an initial burst release followed by a prolonged one is needed.^[304]

This chapter shows that the loading of mesoporous titania film with antibiotics and its surface functionalization with growth factors improve the antibacterial properties of the titania and promote the pre-osteoblasts proliferation and differentiation. Gentamicin was used to load mesoporous titania films of 80 nm in thickness and 5.7 nm in pore diameter, prepared by spin coating through the evaporation-induced self-assembly method. In contrast to previous studies, while 36 % of the gentamicin is released within the first 6 hours gentamicin release prolongs over 35 days. The antibacterial properties of the mesoporous titania were further enhanced by immobilizing a growth factor - the recombinant human bone morphogenetic protein 2 (rhBMP-2) - on the surface of the film, favouring cell attachment and growth. While the antibacterial action of the gentamicin-loaded MTF was tested against *S. aureus*, the proliferation, adhesion, and differentiation assays were performed with the MC3T3-E1 pre-osteoblastic cell line.

1.2. Experimental section

1.2.1. MTF synthesis and characterization

For the sol preparation Titanium (IV) Chloride, Ethanol Absolute, Pluronic F127® and nanopure water (H₂O) were mixed in a molar proportion of TiCl₄ : EtOH : F-127 : H₂O = 1 : 40 : 0.005 : 10. The titania precursor is prepared first, adding the TiCl₄ to the EtOH under vigorous stirring and leave till drops to room temperature. The F-127 is homogenized under stirring in water and then the titania precursor is added. The sol is left stirring for 10 minutes to obtain a homogenous solution. Ti dense films, without pores, are also synthesized, simply by mixing the same reagents in the same order except the surfactant. 30 μL previously mixed with EtOH in a volume proportion of sol : EtOH = 2 : 1, are spin coated and then placed for 30 minutes in an humidity chamber with a controlled relative humidity of 50 %, obtained with saturated Calcium Nitrate, Ca(NO₃)₂, solution in water. They are afterwards subjected to a thermal treatment: 30 minutes at 60 °C and another 30 minutes at 130 °C. Finally, they are calcinated; first, heating up with a ramp of 1 °C min⁻¹ and then, keeping them at 350 °C for 2 h. Ti dense films are treated in the same way.

The porous structure was confirmed through TEM imaging and after performing a transversal cut of the film, the inner part of the film was observed with the SEM. Films thickness and pore size are calculated and analysing the 2D-SAXS pattern the

ordering of the mesoporous structure is evaluated. The value of the Elastic Modulus (E_r) is extracted from nanoindentation tests.

1.2.2. rhBMP-2 and Gentamicin functionalization and characterization

A drop of 100 μL of rhBMP-2 (pI 9.15) at concentrations of 10 $\mu\text{g mL}^{-1}$ and 100 $\mu\text{g mL}^{-1}$ in PBS 10 mM was adsorbed for 1 hour on top of MTFs previously cleaned by immersing in absolute ethanol for 30 minutes, 15 minutes in distilled water, dried with N_2 gun and sterilized for 1h under UV light. After rhBMP-2 adsorption films were immersed in gentamicin sulfate solution at 0.2 mg mL^{-1} in distilled water for 24 hours and prior to its use films were immersed once in water and left to dry in air.

Water contact angles were measured for different rhBMP-2 concentrations adsorbed on MTFs. Three different films at different rhBMP-2 concentrations and with/without gentamicin were measured. The presence of sulphur was confirmed by XPS atomic composition analysis. AFM images were obtained for samples without any functionalization, with rhBMP-2 100 mg mL^{-1} and films with rhBMP-2 100 mg mL^{-1} and gentamicin.

1.2.3. Gentamicin release study

MTFs were immersed for 24 h in 0.2 mg mL^{-1} gentamicin in water. Then they were immersed in water once to remove the exceed of gentamicin and left to dry in air. Samples were placed in a well of a 24 multiwell dish. 1 mL of PBS 10 mM was added to each well containing the samples and the PBS was removed and replaced for each measurement. The release was measured at 30 minutes, 1, 2 and 6 hours and 2, 3, 6, 7, 10, 21, 28 and 35 days. Experiment was performed in triplicate.

1.2.4. MC3T3-E1 cell bioactivity experiments

Cell adhesion was evaluated in MTFs, films functionalized with gentamicin, 10 and 100 ng mL^{-1} rhBMP-2 and films dually functionalized. Cell adhesion was evaluated after 2 h, 1 and 2 days after cells were seeded onto samples.

Cell proliferation was followed for 2 h, 1, 2 and 4 days on top of glass, Ti dense substrates, MTFs and MTFs with 10 and 100 ng mL^{-1} rhBMP-2 and dually functionalized films.

AP was quantified at 2, 5, 10 and 20 days of cell culture in osteogenic medium, the differentiation was evaluated for MTFs, MTFs with 100 ng mL⁻¹ rhBMP-2 and dually functionalized films.

All samples were prepared under sterile conditions and dried in air prior to its use. Samples are prepared in triplicate.

1.2.5. Antibacterial study

MTFs were functionalized with gentamicin and dually functionalized MTFs were prepared with 100 ng mL⁻¹ rhBMP-2 and gentamicin. As control MTFs were used. Samples were prepared in triplicate for the experiment. Films were dried in air and placed in wells of 24 multiwell dishes.

Detached bacteria were diluted in 10 mM PBS; for samples with gentamicin the dilutions were 1/1, 1/10 and 1/100, and for MTFs 1/10,000, 1/100,000 and 1/1,000,000.

1.3. Results and discussion

1.3.1. MTF synthesis and functionalization with rhBMP-2 and gentamicin

The porous structure of the MTFs was confirmed by TEM and SEM characterization (**Figure IV-1a and IV-1b**). The insert in **Figure IV-1a** shows the SAXS pattern of the MTF. The elliptic shape of the pattern suggests the presence of multiple domains of locally ordered pores.^[138] Calculated interplanar distances show an interpore distance of 11.5 nm and 3.9 in the (-110) and (110) planes, respectively. The contraction due to the calcination process at 350 °C is of 65 %, as calculated from differences in the interpore distances at (-110) and (110) planes.^[305] From the analysis of water adsorption-desorption isotherms (**Figure IV-1d**) obtained by Environmental Ellipsometric Porosimetry (EEP), it can be concluded that the MTF has a porosity of 30.7 %, and a pore size of 5.7 nm in diameter connected by necks of 4.2 nm in diameter. The calculated film thickness from the EEP measurements is of 80 nm, a value which is in agreement with the thickness of around 90 nm obtained from the SEM image of the transversal cut of the MTF (**Figure IV-1c**).

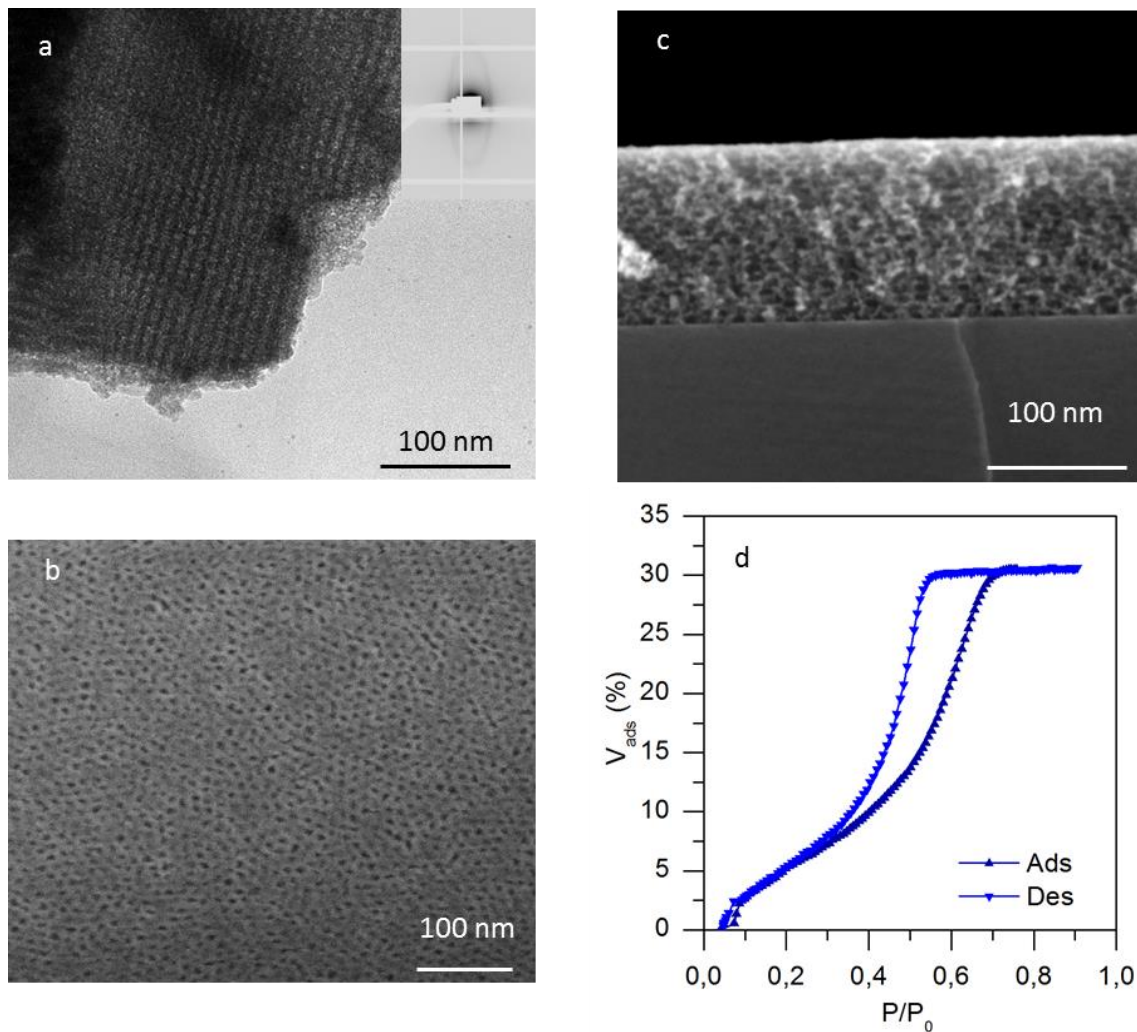


Figure IV-1. Mesoporous titania film (MTF) structural characterization by electron microscopy, 2D-SAXS and EEP. a) TEM image, insert; 2D-SAXS pattern, b) SEM image of the surface, c) SEM image of a transversal cut and d) EEP of water vapour adsorption and desorption.

Nanoindentation measurements, **Figure IV-2**, show an elastic modulus of 25 ± 5 GPa, smaller than the elastic modulus for dense titanium surfaces, which is ranged between 100 and 120 Gpa.^[31] Nevertheless, this value is in agreement with the range of elastic modulus for bone, which lays between 4 and 30 GPa depending on bone type,^[23] and also with the values previously reported for porous titania films.^[306]

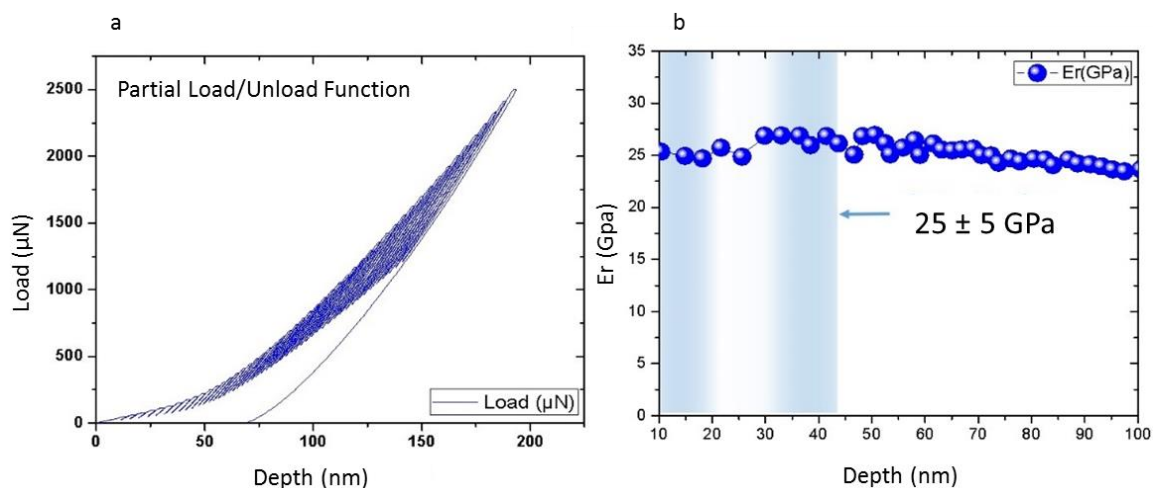


Figure IV-2. Nanoindentation studies performed on mesoporous titania films. a) Shows the partial-load/unload vs displacement curve used for the tests and b) the results of the analysis of each unload section for Elastic modulus (E_r).

MTFs are functionalized with rhBMP-2 and loaded with gentamicin. The 3D structure of the BMP-2 has a size of around 7 nm x 3.5 nm x 2.5 nm,^[307] which does not allow the molecule to enter inside the mesoporous structure and it will remain in the surface of the films. To confirm the presence of both rhBMP-2 and gentamicin, the atomic percentage of S/Ti is obtained through high resolution XPS spectra in the spectral range of Sulphur (S) and Titanium (Ti) (**Figure IV-3**). As gentamicin sulphate is used, the S is used as an indirect marker to ensure the presence of gentamicin. The peak corresponding to S 2p_{3/2} is more pronounced in the MTF loaded with antibiotic, coated with protein or both loaded and coated, as compared to the bare MTF. Because first the rhBMP-2 is adsorbed on top of the MTF and then the film is immersed in gentamicin for a day, it could be the case that the rhBMP-2 desorbs from the titania surface during the loading. Although there is no S in the bare MTF, a S/Ti atomic relative percentage of 0.41 ± 0.09 % is obtained, which corresponds to the noise of the equipment. When the MTF is loaded with gentamicin the S/Ti relative percentage increases to 2.03 ± 0.09 %. If the MTF is functionalized with rhBMP-2 without gentamicin loading the S/Ti increases to 3.44 ± 0.99 %. The S/Ti ratio for the MTFs functionalized with rhBMP-2 and loaded with gentamicin is the lowest: 1.48 ± 0.32 %. The loss in S content could be a consequence of the incorporation of gentamicin after the rhBMP-2 is adsorbed on top of the MTF; however, the calculated standard error is high. Additional proof of the loading and functionalization were obtained from contact angle measurements. **Figure IV-4** shows the changes in contact angle of water following rhBMP-2 functionalization

and gentamicin loading. Bare MTF has a contact angle of $13.4 \pm 0.30^\circ$ (**Figure IV-4a**). When the MTF is loaded with gentamicin or functionalized with rhBMP-2 the contact angle changes to $73.15 \pm 1.07^\circ$ (**Figure IV-4b**) and $72.47 \pm 2.60^\circ$ (**Figure IV-4c**), respectively. For the MTF functionalized with rhBMP-2 and loaded with gentamicin the contact angle increases to $90.95 \pm 2.19^\circ$ (**Figure IV-4d**). Moreover, gentamicin loading was proven by release experiments and by measuring the antibacterial properties of the MTF after loading.

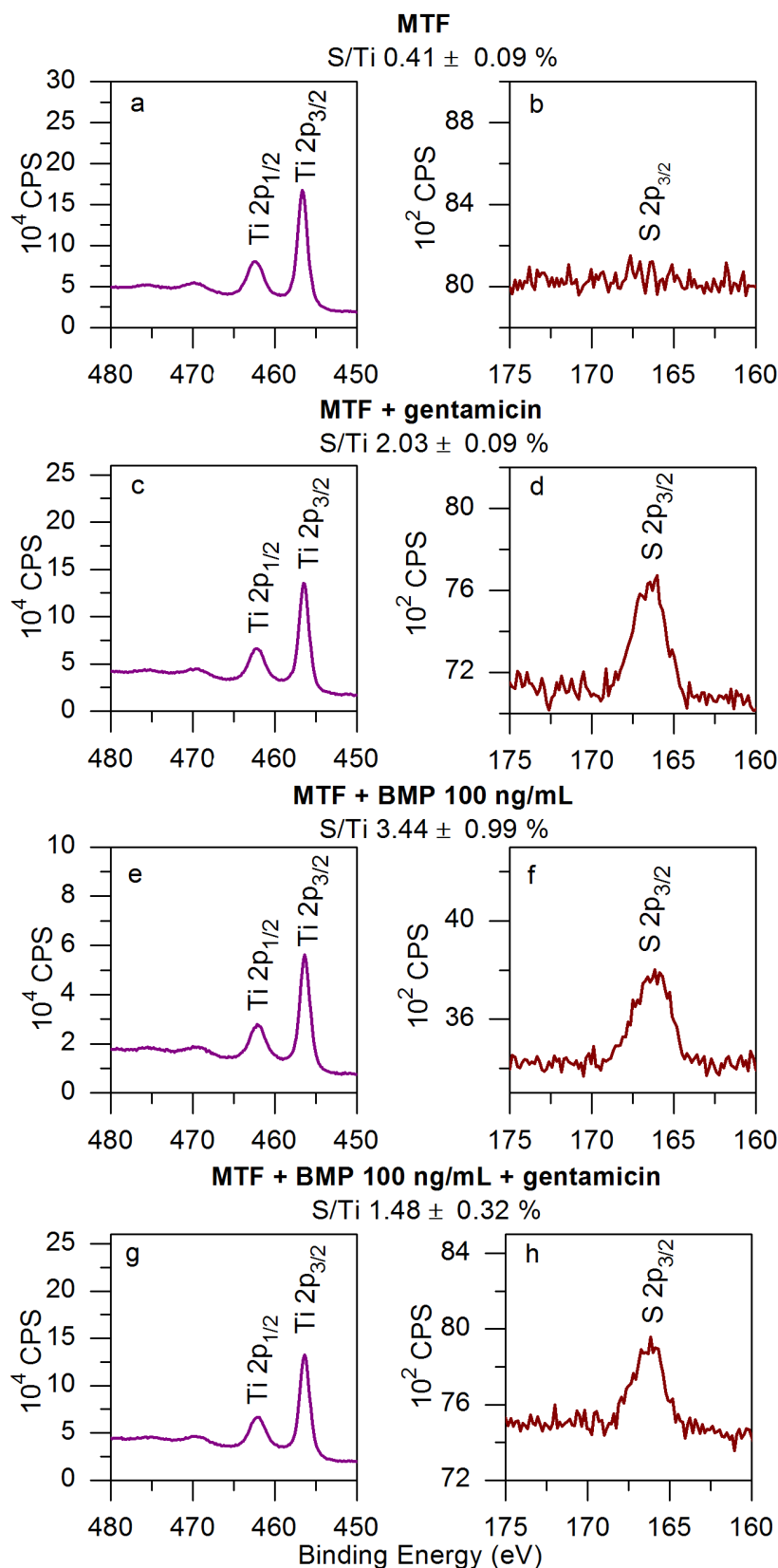


Figure IV-3. XPS high resolution spectra of Titanium (Ti) and Sulphur (S) and S/Ti atomic percentage calculation on top of each graph for each film. a) Ti and b) S of MTF, c) Ti and d) S of MTF with gentamicin, e) Ti and f) S of MTF with 100 ng mL^{-1} rhBMP-2 and g) Ti and h) S of MTF with 100 ng mL^{-1} rhBMP-2 and gentamicin substrates.

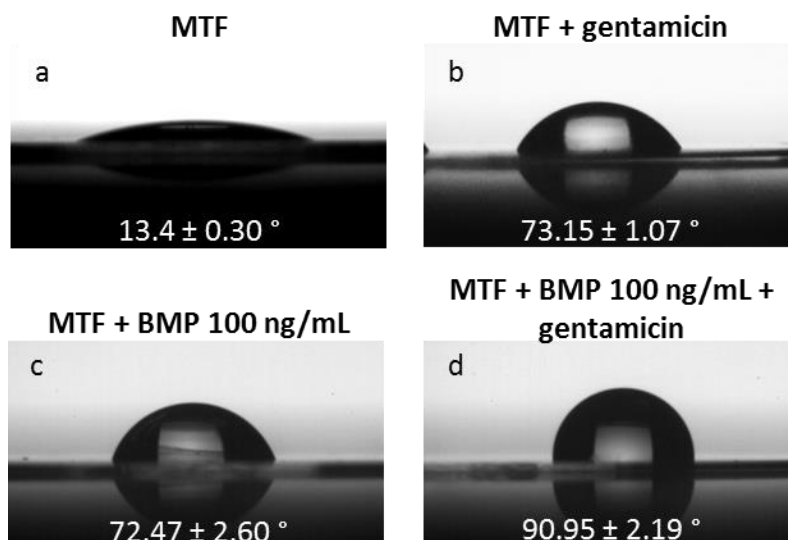


Figure IV-4. Contact angle measurements. a) Bare MTF b) MTF with gentamicin, c) MTF with 100 ng mL^{-1} rhBMP-2 and d) MTF with 100 ng mL^{-1} rhBMP-2 and gentamicin.

MTFs show a smooth topography as confirmed by AFM imaging (**Figure IV-5a, IV-5b** and **IV-5c**), with a roughness of around 190 pm. When the protein is deposited on top of the MTF, the roughness increases to 250 pm, meaning that the surface loses homogeneity and confirming the presence of rhBMP-2 (**Figure IV-5f**). The height profile shows singularities with a few nm in thickness, which are not observed in the bare MTF. Phase image also confirms the presence of a different material on top of the MTF (**Figure IV-5e**); when the height changes also a phase shift is detected. When the MTF functionalized with rhBMP-2 is loaded with gentamicin some rhBMP-2 is loosed from the surface (**Figure IV-5g**) and the roughness decreases to 210 pm (**Figure IV-5i**). The presence of proteins is indicated in the image by blue arrows.

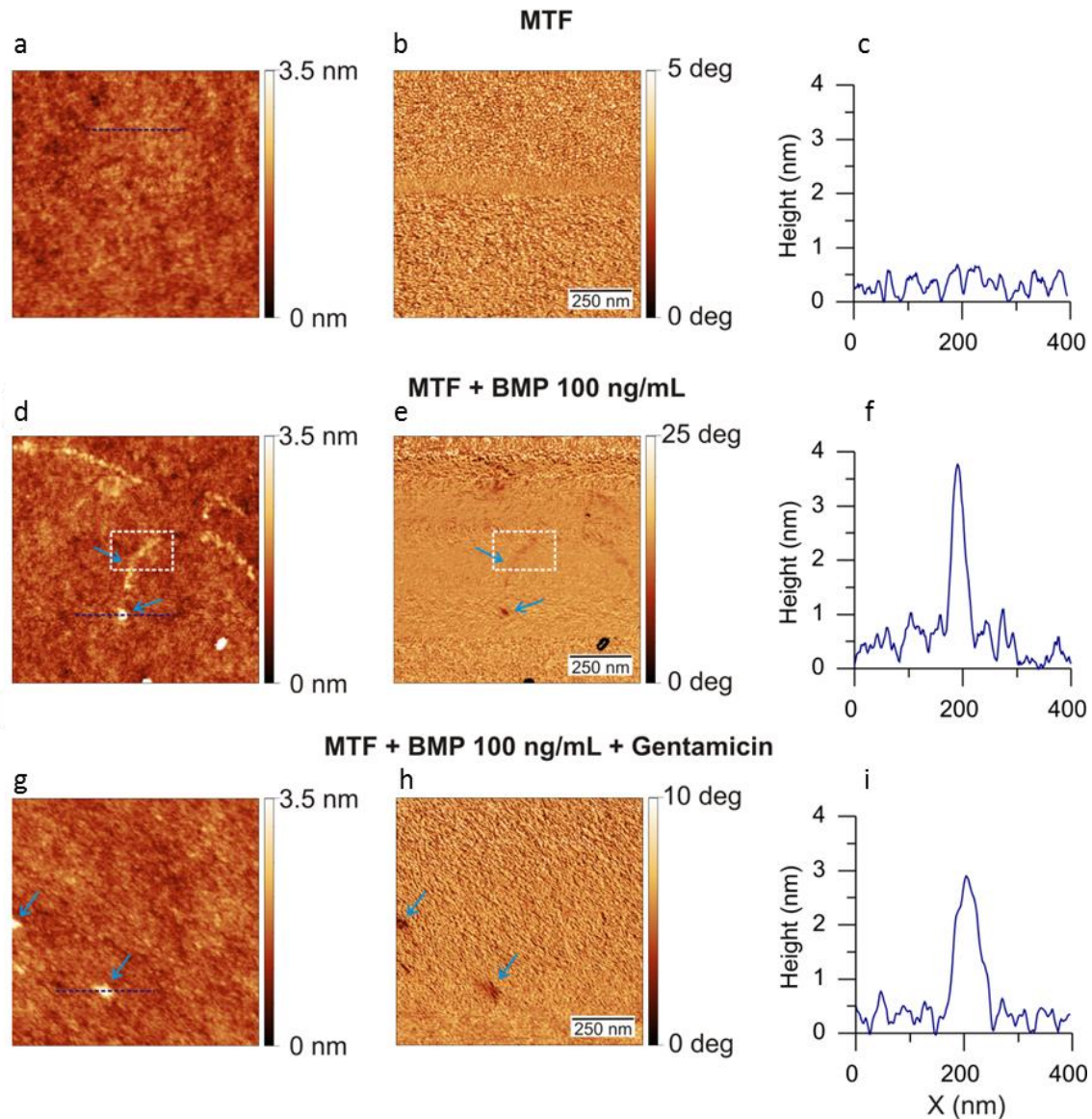


Figure IV-5. AFM images (height, phase and height section) of MTF, MTF with 100 ng mL⁻¹ rhBMP-2 and MTF with 100 ng mL⁻¹ rhBMP-2 and loaded gentamicin. a) height, b) phase and c) section of MTF substrates, d) height, e) phase, f) section of MTF with 100 ng mL⁻¹ rhBMP-2 substrate, showing an increase in the height, and g) height, similar to MTF with 100 ng mL⁻¹ rhBMP-2 sample, h) height and i) section image of MTF with 100 ng mL⁻¹ rhBMP-2 and loaded with gentamicin.

1.3.2. Gentamicin release from MTFs

The release profile of the gentamicin is plotted in **Figure IV-6**. There is a fast release at initial times; within the first 6 h around the 36 % of the total gentamicin liberated is released. This initial burst release is required to avoid bacteria adhering and infecting the implant during surgery, which is known to be the riskiest period for infection. After the burst release a second slower and prolonged release takes place. Release is evaluated up to 35 days, where a plateau is reached and this second release profile is within the time frame required for the implant to be integrated in

the tissue and for the formation of the protective fibrous capsule.^[308] This second release step suggests that gentamicin is retained inside the pores interacting with the titania surface. Angelomé *et al.*^[309] have shown that hydroxyl groups in dialcohols can be incorporated into MTFs by complexation of Ti(IV) centers present in the pore surface.^[309] Moreover, they have demonstrated that the dialcohols can be released in aqueous solution at specific pH values. Thus, gentamicin can be anchored to the titania surface through oxo bridges due to the presence of three hydroxyl groups in the molecule, which would explain the slow release of gentamicin from the MTF.

The obtained results on gentamicin liberation are significantly different from Atefyekta *et al.*^[304], where a fast release of gentamicin takes place in around 80 min from mesoporous titania with pore sizes similar to ours. However, their mesoporous titania films are less ordered and 200 nm thick, twice as thick as the ones presented in this chapter. It is possible that the pores in the synthesized MTFs are more interconnected and with narrowed necks and this causes that only the 36 % of gentamicin is released fast as gentamicin is more difficulted to leave the pore mesh. In the work by Atefyekta *et al.*^[304] the authors have recognized that the release was fast and the methodology that they used to measure the antibiotic release could also be a reason for the differences observed in the present chapter. Atefyekta *et al.*^[304] have measured gentamicin loading and release by Quartz Crystal Microbalance with Dissipation (QCM-D) from MTF deposited on top of a QCM-D crystal. Both upload and release were measured from variations in the frequency of the crystal and for the release studies the authors apply a continuous flow of PBS at a flux of 50 mL min⁻¹, which is a relatively high flux and should trigger a faster liberation of gentamicin. Besides, in this work, the release was performed in static conditions.

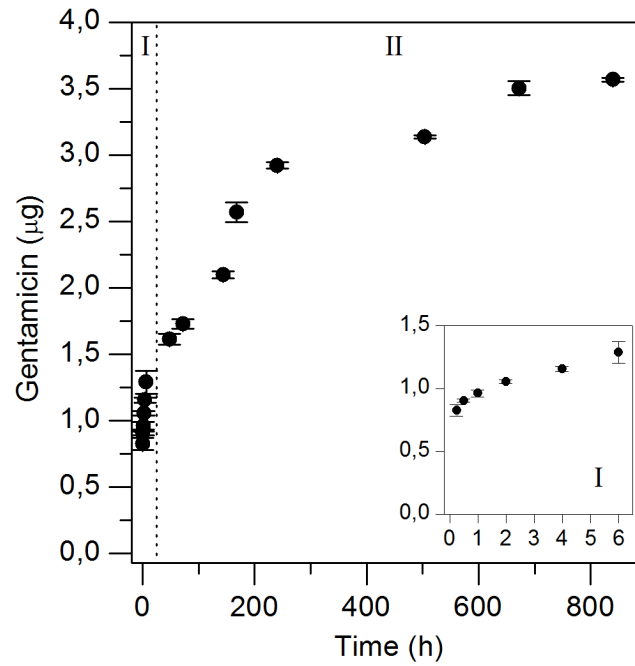


Figure IV-6. Release profile of gentamicin from MTF. Region I shows the burst release (the insert is a zoom of region I) and region II the sustainable release. The release is followed up to 35 days by emission measurements at 455 nm.

1.3.3. Biocompatibility and bioactivity evaluation

Initial cell adhesion on biomaterials plays a key role on cell proliferation, migration and differentiation. The focal adhesions (FA) and extracellular matrix (ECM) interactions involve integrins that bind different ECM proteins with the external end and cytoskeleton *via* adapter proteins such as talin, α -actinin, filamin and vinculin. FAs are based on this integrin-adapter protein–cytoskeleton complex. Osteoblasts anchor on a substrate *via* integrin receptors, which are involved in processes named as “outside-in-signaling” and “inside-out-signaling” between the ECM and the cell. These pathways involving integrins can regulate subsequent cell adhesion, migration, proliferation, and differentiation.^[310,311]

The MC3T3-E1 osteoblast precursor cell line is used to evaluate adhesion to the functionalized MTFs. **Figure IV-7**, **IV-8** and **IV-9** show confocal laser scanning microscope images of the cells cultured on the bare MTFs, MTFs functionalized with rhBMP-2 and MTFs functionalized with rhBMP-2 and gentamicin, respectively. The actin filaments (F-actin) are stained with phalloidin, red fluorescence in the second row and vinculin is stained with FITC, green fluorescence in the first row. The nucleus is stained with DAPI and is represented in blue in the merge images (third row), where all the labeled cell parts are shown. From the F-actin images can be seen that cultured cells in the three substrates exhibit a similar size and a well-arranged cytoskeleton with distinctive stress fibers inside the cytoplasm, especially at the border of the cells. However, cell shape is different after 48 h of culture (third column). When the MTF was modified with rhBMP-2 (**Figure IV-8**) cell shape was more elongated if compared with cells cultured 48 h on the bare MTFs (**Figure IV-7**) or rhBMP-2 and gentamicin (**Figure IV-9**). This cell shape and higher filopodia^[312] means that cells were interacting better when rhBMP-2 is present on the surface. FA allow cells to interact with the surrounding environment; vinculin can interconnect signals in the focal adhesions and is a key regulator.^[313,314] In the images of vinculin staining (first row) in all substrates lots of green spots can be found. After 2 h of cell incubation on the substrates (first column) focal adhesions can also be perfectly distinguished, meaning that cells adhere well to the substrates from initial times, which will later improve cell proliferation.^[310,313]

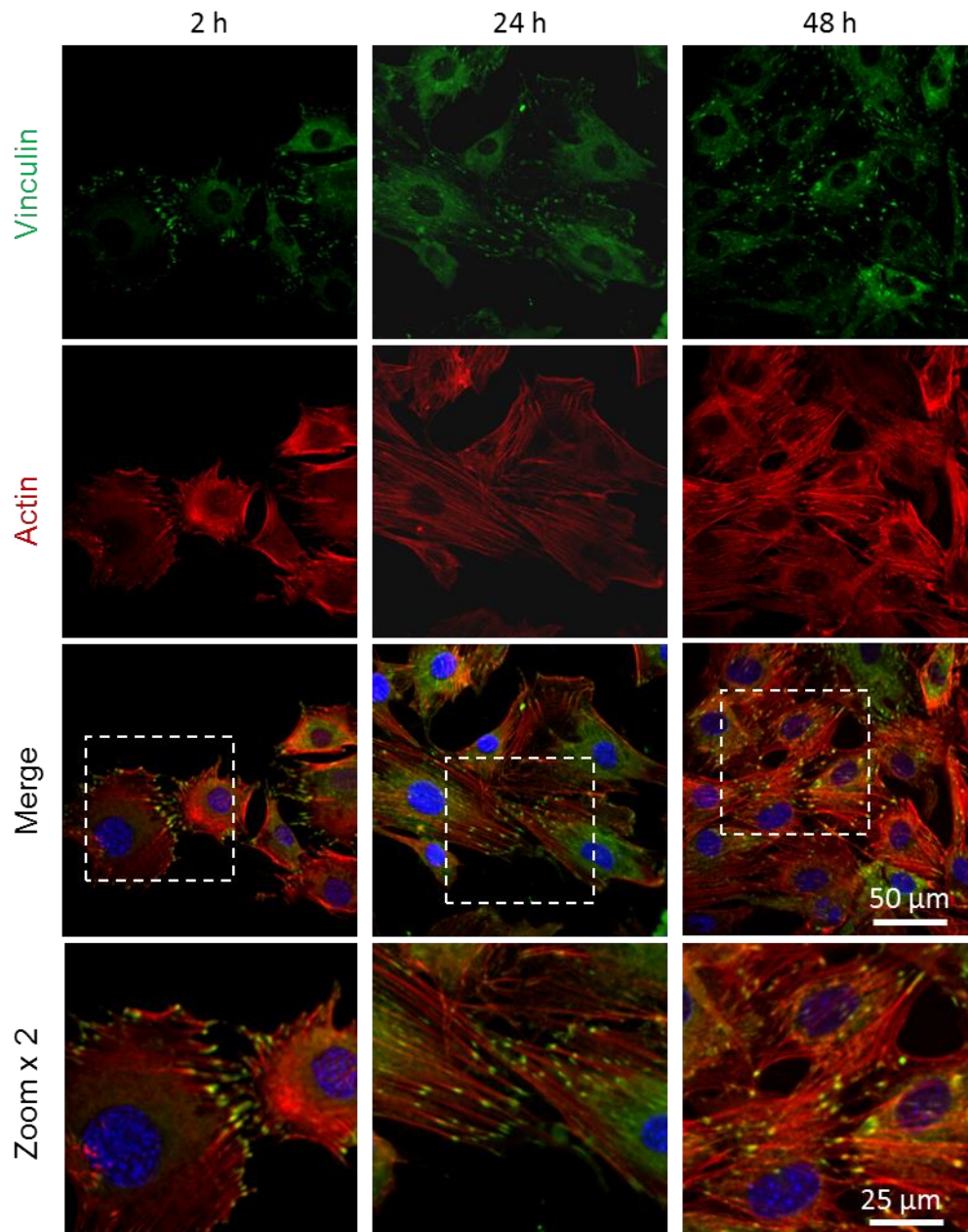


Figure IV-7. CLSM images of vinculin (first row), actin (second row), the merge of the actin, the vinculin and the nucleus (third row) and the zoom of the merge image (fourth row) at 2h (first column), 24h (second column) and 48h (third column) of growth of MC3T3-E1 cell line on MTFs substrates at 63x.

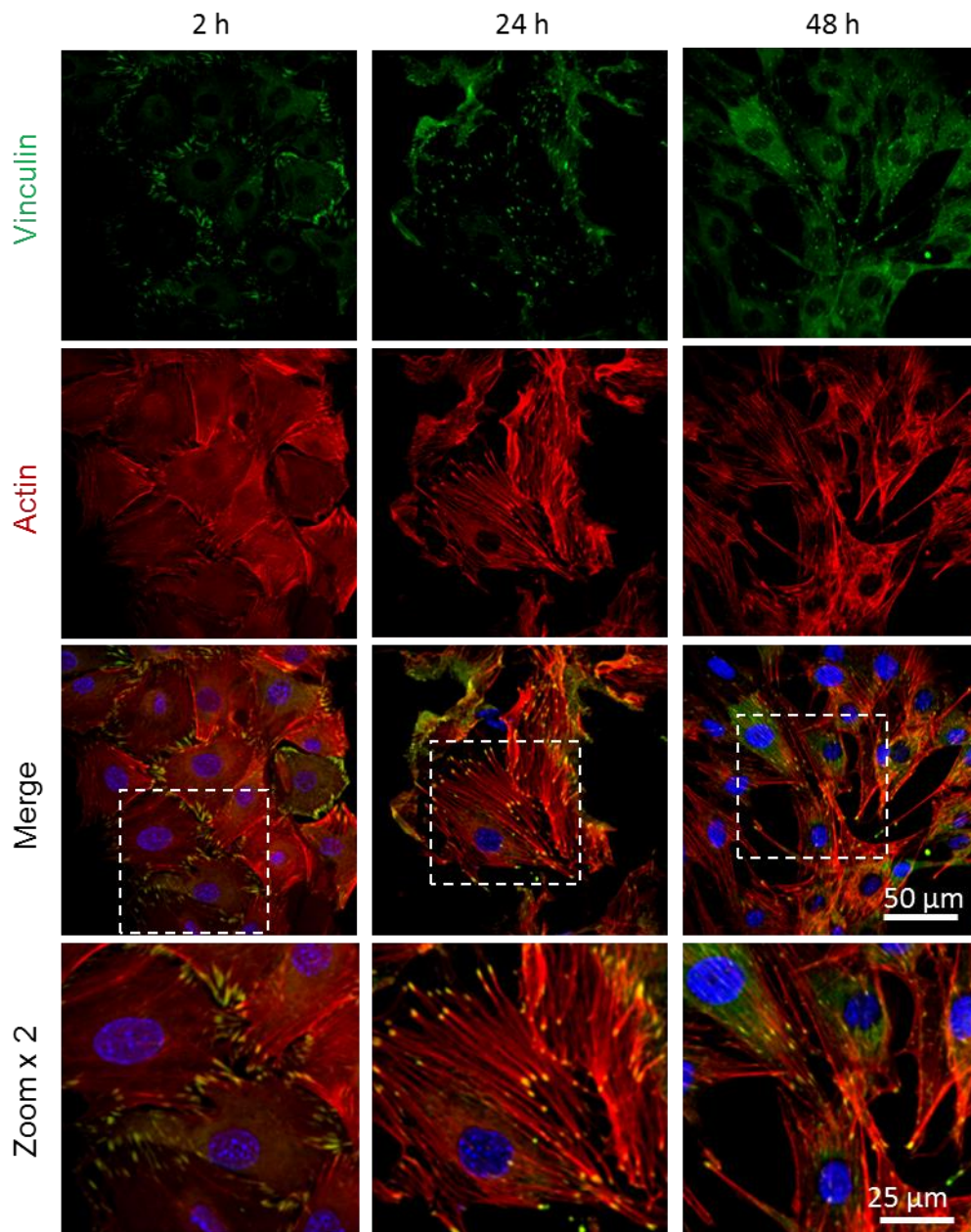


Figure IV-8. CLSM images of vinculin (first row), actin (second row), the merge of the actin, the vinculin and the nucleus (third row) and the zoom of the merge image (fourth row) at 2h (first column), 24h (second column) and 48h (third column) of growth of MC3T3-E1 cell line on MTF with 100 ng mL^{-1} rhBMP-2 substrates at 63x.

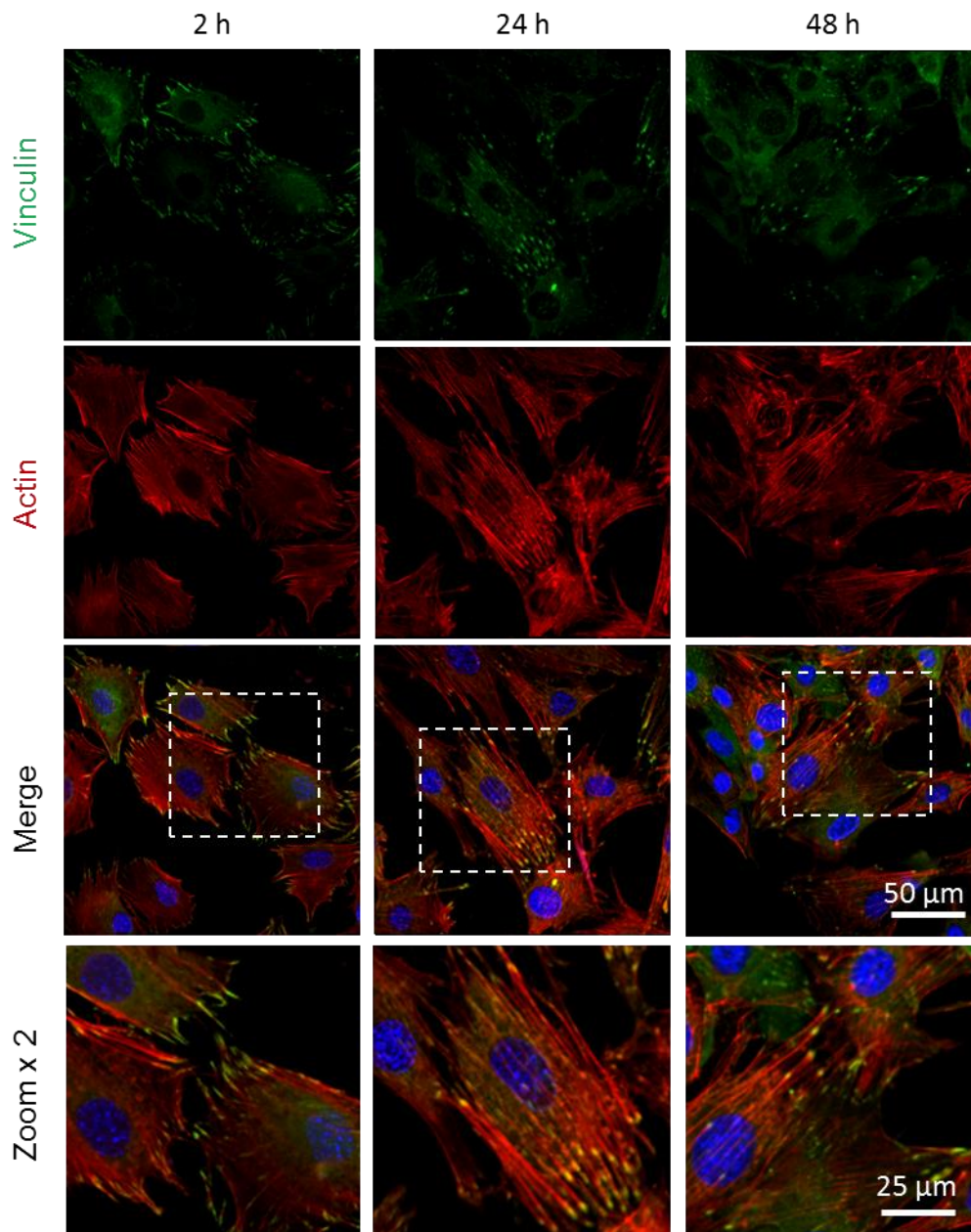


Figure IV-9. CLSM images of vinculin (first row), actin (second row), the merge of the actin, the vinculin and the nucleus (third row) and the zoom of the merge image (fourth row) at 2h (first column), 24h (second column) and 48h (third column) of growth of MC3T3-E1 cell line on MTF with 100 ng mL^{-1} rhBMP-2 and gentamicin substrates at 63x.

During the thesis glass substrates, dense titanium substrates or MTFs are used indistinctly as controls for experiments with cells. In **Figure IV-10** is shown that any of them is suitable for MC3T3-E1 pre-osteoblast proliferation. MC3T3-E1 pre-osteoblasts are cultured for 1, 2 and 7 days on glass, dense titanium and MTF substrates. As seen there is no significant difference on cell density for the evaluated time periods and any of the three substrates are used as controls from now on.

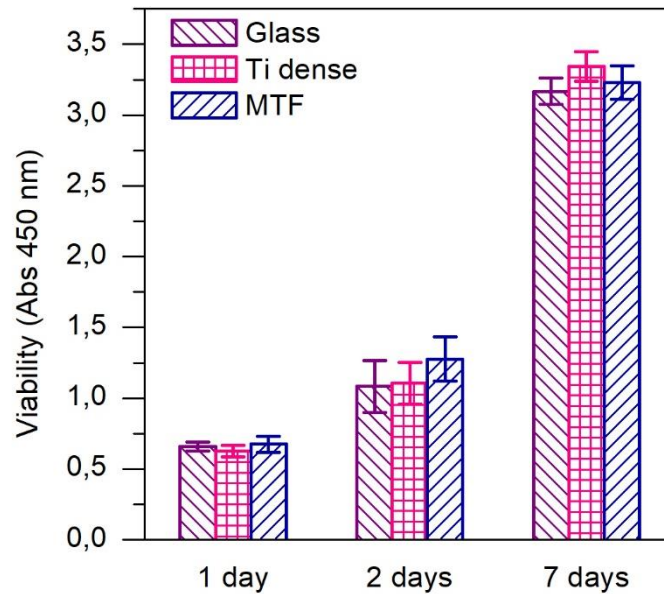


Figure IV-10. Proliferation of MC3T3-E1 pre-osteoblasts cultured on Glass, Ti dense and MTF substrates for 1, 2 and 3 days.

To study the influence of the rhBMP-2 on cell proliferation, cells are cultured in substrates coated with rhBMP-2. The deposition of rhBMP-2 on the MTF was performed from solutions with 10 and 100 ng mL⁻¹ rhBMP-2 concentration. Results are plotted in **Figure IV-11**. After 7 days, the culture is confluent, meaning that the surface is completely covered by cells forming a monolayer, and no difference can be distinguished between the MTF functionalized with rhBMP-2 and the bare MTF control. Within the first day cells proliferate at the same rate and cell density is the same for the three evaluated substrates. After 2 days of culture, substrates with 100 ng mL⁻¹ of rhBMP-2 show an enhanced cell proliferation rate if compared with cells cultured on MTFs and MTF with 10 ng mL⁻¹ rhBMP-2 ($p < 0.05$). After 4 days of culture, same differences are maintained, but cell density is also higher when rhBMP-2 concentration is low (10 ng mL⁻¹) if compared with MTFs. As previously seen in **Figure IV-8**, cells are more expanded and showing higher filopodia in presence of rhBMP-2. When the interaction of cells with a substrate is better it is

known that proliferation is also improved.^[310,313] If MTFs are loaded with gentamicin and functionalized with rhBMP-2, differences are observed regarding the proliferation rates of MC3T3-E1 cells on films only functionalized with rhBMP-2. At day 2, between samples with rhBMP-2 or samples with rhBMP-2 and loaded with gentamicin there is no difference on cell density and in both cases the density is higher if compared with cell density on bare MTFs. If cells are cultured for 4 days, there is a difference between samples without and with gentamicin. After 4 days of cell culture, for the MTF with rhBMP-2 loaded gentamicin, the cell proliferation rate is not as high as without gentamicin, and the proliferation rate decreases in a 46 % with a value comparable to bare MTFs.

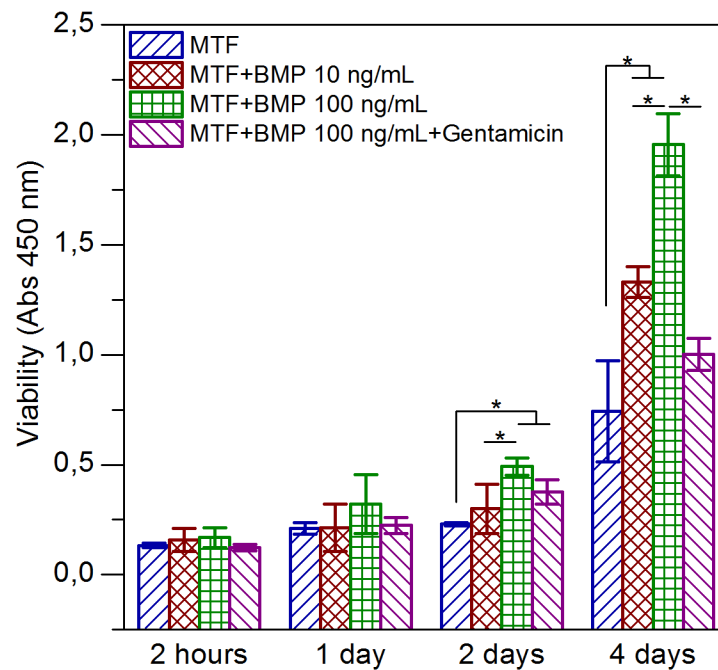


Figure IV-11. Proliferation of MC3T3-E1 pre-osteoblasts cultured on MTF, MTF with 10 mL⁻¹ rhBMP-2, with 100 ng mL⁻¹ rhBMP-2 and with 100 ng mL⁻¹ rhBMP-2 and gentamicin substrates for 2 h, 1, 2 and 4 days. * means that the difference is statistically significant ($p < 0.05$)

Alkaline phosphatase is one of the gene markers in the early stage of osteogenic differentiation.^[162] **Figure IV-12** shows the AP activity of cells cultured on the MTFs, MTFs with rhBMP-2 and MTFs with rhBMP-2 and gentamicin. After cells reach confluence, they are differentiated for 20 days and AP activity is measured at different steps to evaluate differences in differentiation rates. At day 2 and day 5 of differentiation there is no difference between the evaluated substrates and at day 20 all cells are differentiated and is not possible to see any difference among

substrates as well. Only at day 10 of cell culture in osteogenic medium differences can be seen. For MTF coated with rhBMP-2, with or without gentamicin, the differentiation is more than the double of the differentiation on bare MTFs. This result was expected as the effectiveness of rhBMP-2 in promoting pre-osteoblast differentiation has been demonstrated in a large number of works.^[168,315-317]

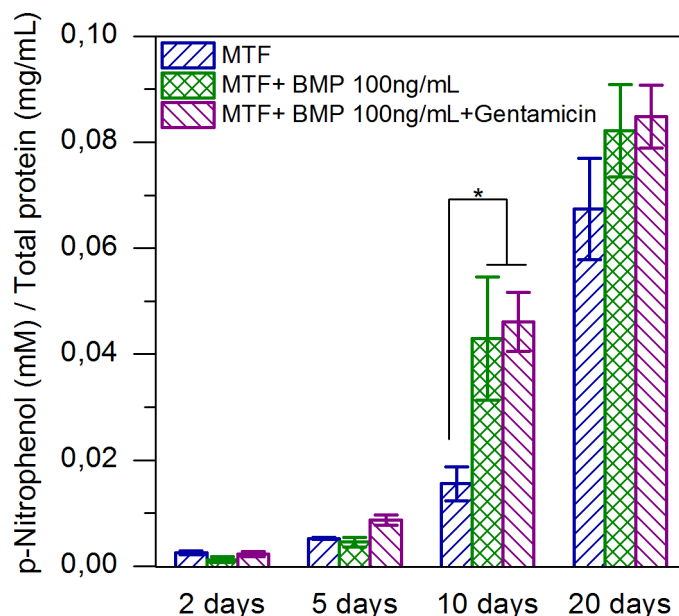


Figure IV-12. Alkaline phosphatase activity after 2, 5 10 and 20 days of MC3T3-E1 pre-osteoblastic cell culture in osteogenic medium on MTF, MTF with 100 ng mL⁻¹ rhBMP-2 and MTF with gentamicin and 100 ng mL⁻¹ rhBMP-2 substrates. * means the difference is statistically significant (p < 0.05)

1.3.4. Evaluation of the antibacterial properties of the rhBMP-2 and gentamicin functionalized MTFs

The evaluation of the antibacterial capacity of MTF loaded with gentamicin and rhBMP-2 functionalized is performed by incubating *S. aureus* for 24 h on top of the films. **Figure IV-13a** shows CFU grown on the LB agar plates. Green ticks mean bacteria have grown on the agar plates and CFU counting is possible and red crosses means that *S. aureus* has not grown. $4.75 \times 10^6 \pm 5.8 \times 10^5$ CFU are counted for MTF, in **Figure IV-13b** a zoom of CFU grown on agar plates after growing in MTF is shown. However, when the MTF contains gentamicin, with or without rhBMP-2, bacteria are not grown, as can be seen in the zoom in **Figure IV-13c**. **Figure IV-13d** and **IV-13e** show a cell observer image of *S. aureus* grown for 24 h on top of the MTF and the MTF functionalized with rhBMP-2 and loaded with gentamicin, respectively. The bare MTF surface is completely covered by the bacteria; the image shows black dots which are the coccus. The surface of the gentamicin loaded film shows very few dots,

so some bacteria attach but are not alive, as seen in the agar plate culture, where no CFU are found.

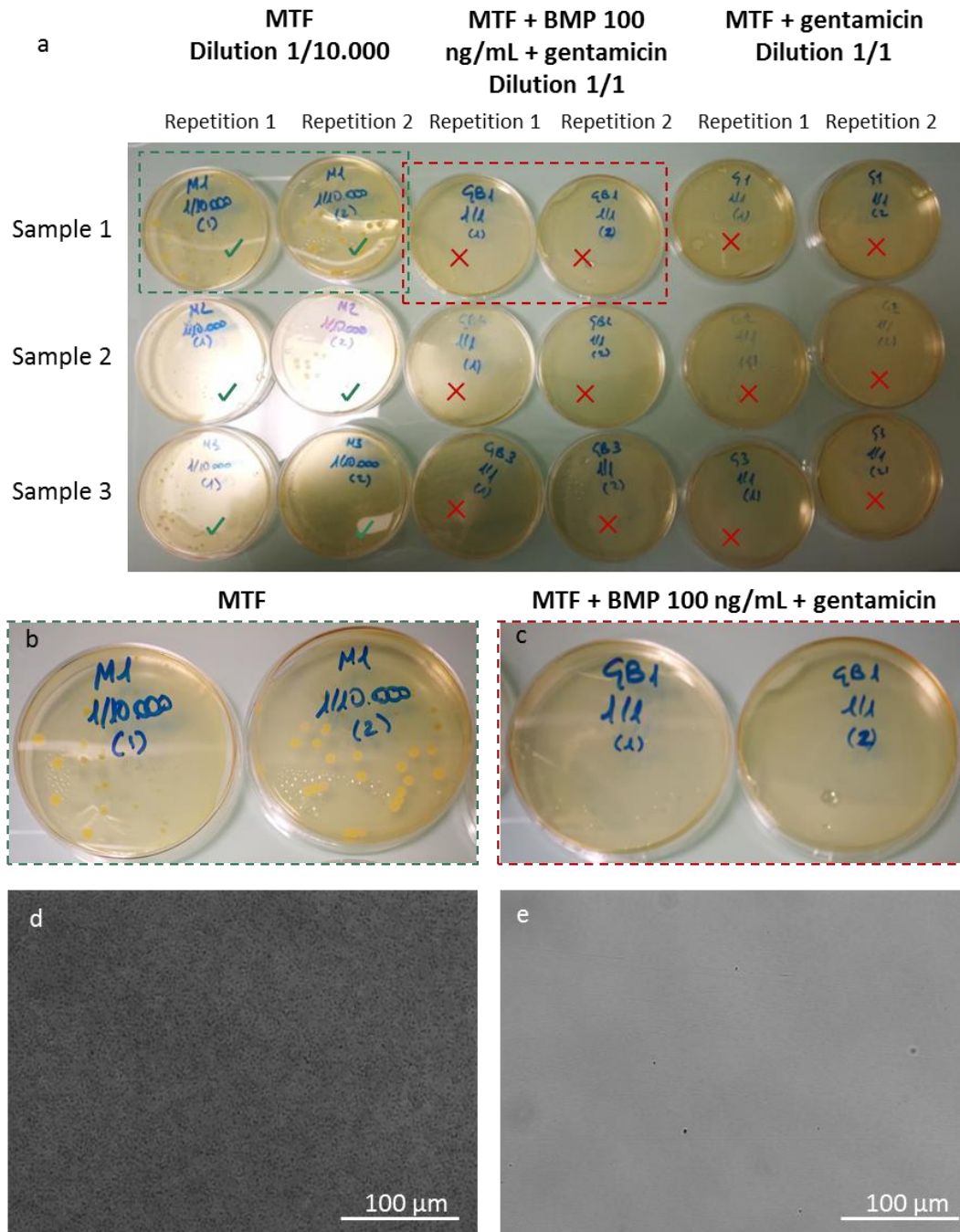


Figure IV-13. CFU counting after *S. aureus* growth on agar plates for 24h and cell observer images of *S. aureus* growth on MTF and MTF functionalized with rhBMP-2 and gentamicin. a) Three samples with cultured *S. aureus* for 24 h on LB agar plates. *S. aureus* cultured in 1/10,000 dilution for MTF and 1/1 dilution for MTF with 100 ng mL⁻¹ rhBMP-2 and gentamicin and MTF with gentamicin. b) Zoom of Sample 1 of agar plates with cultured *S. aureus* on MTF, c) Zoom of Sample 1 of agar plates with cultured *S. aureus* on MTF with rhBMP-2 and gentamicin and cell observer images of 24 h of growth of *S. aureus* on d) MTF and d) MTF with rhBMP-2 and gentamicin substrates.

1.4. Conclusions and perspectives

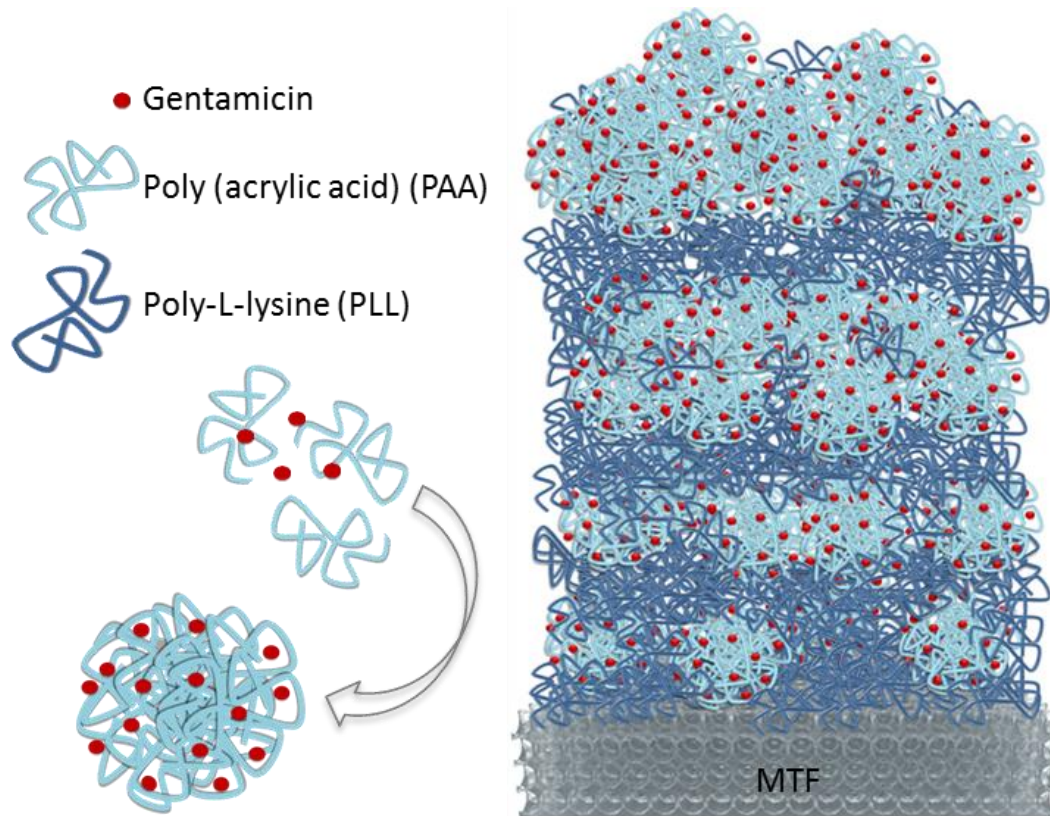
Highly mesoporous titania films with a 30.7 % porous volume have been shown here to encapsulate gentamicin in the porous matrix to an extent that the films display antibacterial properties. At physiological pH, the release of gentamicin in 10 mM PBS shows a two-step release profile. The porous structure of the titania results in an initial burst release of gentamicin within the first 6 h with a liberation of around the 36 % of the total released gentamicin. The burst release is followed by a slow release of the remaining gentamicin that lasts over weeks. This release profile fits with the initial requirements of avoiding the formation of bacteria colonies on the implant while surgery is conducted, releasing most of the gentamicin during first hours, while the rest of the gentamicin is released in lower doses for a period lasting weeks avoiding infection while the tissue is being reconstituted.

MTFs functionalized with rhBMP-2 improve MC3T3-E1 cell adhesion and proliferation. However, when the MTF is also loaded with gentamicin, proliferation rate is diminished but still is comparable to the proliferation rate for bare MTFs. Cell differentiation is not affected by the presence of gentamicin, and when MTFs are functionalized with rhBMP-2 the differentiation rate increases at day 10 to the double of the rate of cells cultured onto MTFs.

The efficacy of the functionalized substrates against *S. aureus* bacterial infection is shown seeding 1,000 CFU of bacteria on the gentamicin loaded MTFs. Bacteria do not proliferate, hinting the potential of the gentamicin loaded MTF for avoiding *S. aureus* infections.

Overall, this chapter shows the potential of mesoporous titania for antibiotic loading and delivery for avoiding bacterial infection. The release profile of gentamicin matches with the requirements of a burst release during operation and immediately after followed by a sustainable release of gentamicin until the bone tissue is reconstituted. The additional modification of the MTF with rhBMP-2 has a positive effect on proliferation and cell adhesion that seems to overcome negative effects from gentamicin on pre-osteoblasts. The versatility of the mesoporous substrates has been shown; it is possible to tune the mesoporous structure by changing the surfactant used for the synthesis, and film thickness can also be tuned in order to modify the number of loaded molecules inside the film. Also, many different types

of molecules can be entrapped inside the film or adsorbed on the top, giving different functionalities to the substrate.

V. CHAPTER 2**Antibacterial PEMs based on PLL and PAA-gentamicin complexes****2.1. Motivation**

The widespread nature of bacterial infections and their increasing resistance to antibiotics has led to the development of antibacterial coatings in multiple medical settings, especially on bone implants.^[70] The surface of implants is susceptible to numerous bacterial infections mainly because of the formation of a surface biofilm and the compromised immune response at the implant/tissue interface.^[318] Once a biofilm is formed, it protects adherent bacteria from the host defence system and bactericidal agents via several mechanisms.^[47,319,320] The biofilm becomes a source of pathogens and infections, being the cause of so called nosocomial infections.^[48,124,321] Nosocomial infections are secondary to the main condition of the patient, and can have lethal consequences following operations such as bone replacement or open heart surgery.^[322-324] Because biofilms can form on almost any

material present in a surgery room, prevention of their formation can be fundamental for patient survival.

The encapsulation of antibiotics in polymer matrixes is an attractive approach for the fabrication of antibacterial coatings. These coatings are usually made out of hydrogels, layer-by-layer (LbL) assemblies, polymer brushes or porous polymer scaffolds.^[70,223,325-333] A major drawback of the encapsulation of antibiotics in polymer films is the difficulty in achieving a slow release of antibiotics. In addition, often the coating degrades accompanied by liberation of the antibiotics all at once, or at a rate faster than required.^[70,334]

The LbL technique has been used for the engineering of scaffolds and implants to assemble growth factors and other molecules that facilitate tissue regeneration or enhance cell adhesion.^[335-341] Molecular complexes, stable colloidal aggregates of molecules bound by weak interactions, have also been employed as building blocks for the fabrication of PEMs. For example, Romero *et al.*^[342] have shown that complexes of alginate and the antiTNF- α antibody can be assembled in LbL, while the direct assembly of the antibody does not result in stable layers because of the weak charge of antiTNF- α .

Recently, Moskowitz *et al.*^[124] proposed an antibacterial coating with an initial burst release of gentamicin followed by slow release. The coating was formed by a tetralayer unit containing gentamicin sulphate, poly acrylic acid (PAA) and a synthetic poly(β -amino ester) (Poly 1), combined as PAA/Poly 1/PAA/Gentamicin. Gentamicin is a frequently used antibiotic, an aminoglycan displaying three primary amine groups, which can interact with PAA through electrostatic interactions and hydrogen bonding. The entire film comprised 200 tetralayers, achieved over 5 days using an automated fabrication method.^[124]

In this chapter, a simple method for the fabrication of antibacterial coatings employing the LbL technique is proposed (**Figure V-1**). Using PAA-gentamicin complexes as building blocks with poly-L-lysine (PLL), a coating in just a few assembly steps with enough gentamicin loading to exhibit antibacterial properties is assembled. The obtained results are particularly appealing for the development of antibacterial coatings to prevent acquisition of nosocomial infections in various medical settings.

2.2. Experimental section

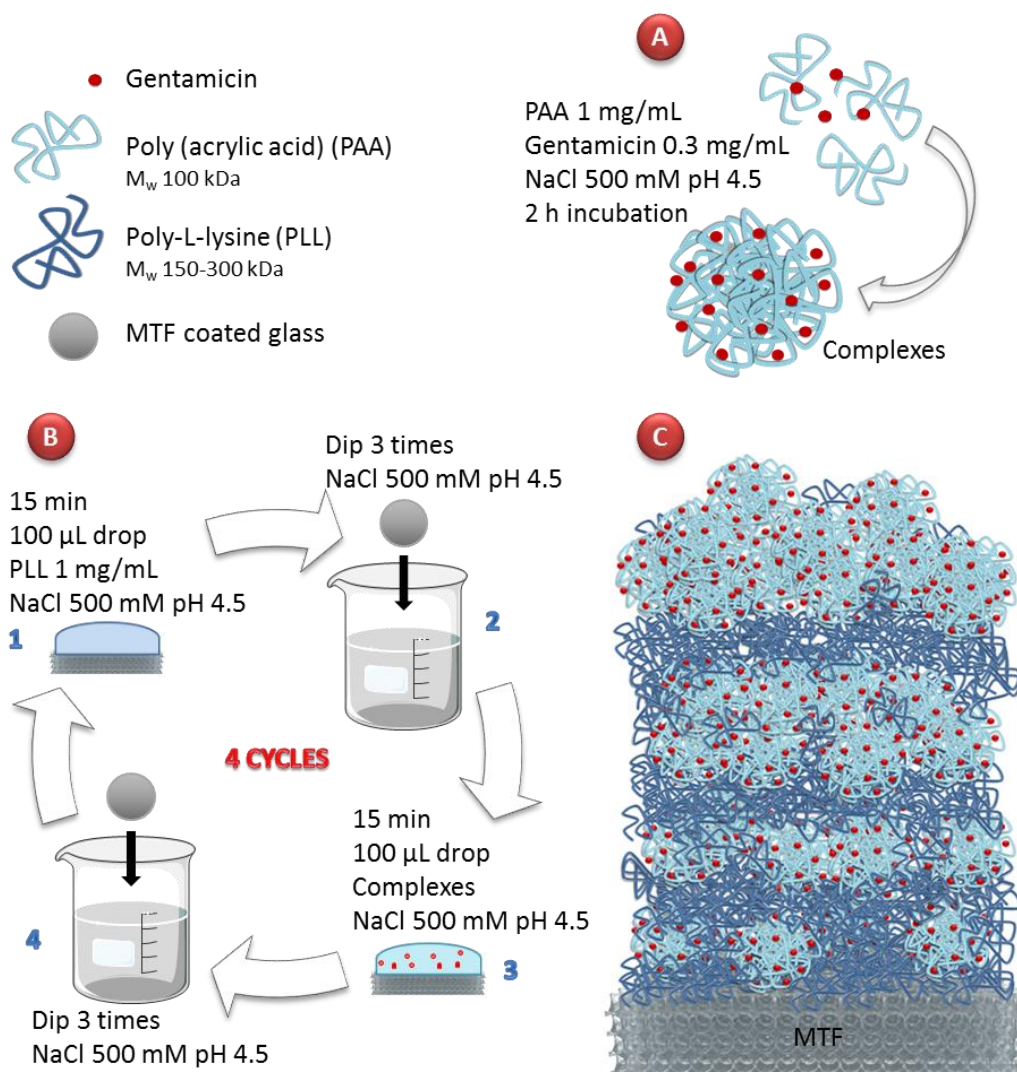


Figure V-1. A) Scheme of the formation of gentamicin and PAA complexes in 500 mM NaCl at pH 4.5. B) LbL assembly of PLL and PAA-gentamicin complexes. The LbL assembly was performed in 500 mM NaCl at pH 4.5 in 4 steps: 1) 15 min incubation of 100 μ L drop of 1 mg mL⁻¹ PLL, 2) removal of the PLL that has not been adsorbed by dipping the substrate in 500 mM NaCl pH 4.5, 3) 15 min incubation of 100 μ L drop of PAA-gentamicin complexes and 4) removal of the complexes that have not been adsorbed by dipping the substrate in 500 mM NaCl pH 4.5. This cycle is repeated 4 times. C) Scheme of PEMs showing 4 bilayers of PLL/PAA-gentamicin complexes grown on top of titania films.

2.2.1. Poly (acrylic acid) and gentamicin complex preparation and characterization

PAA and gentamicin complexes were prepared by mixing PAA and gentamicin sulfate at different ionic strengths: 2 M, 500 mM and 10 mM NaCl and H₂O. Complexes were prepared with PAA 1 mg mL⁻¹ and with different concentrations of gentamicin, preparing complexes with 0.1, 0.25, 0.3 and 0.45 mg mL⁻¹ of gentamicin. The growth of the complexes was followed measuring the size by dynamic light

scattering immediately after complex preparation, after 2 h and after 4 h. In all cases measurements were repeated 10 times. For TEM imaging, a drop of 5 μL of the complexes was deposited on a TEM grid, left for 5 min on the grid to ensure that the complexes were deposited, cleaned 3 times with drops of distilled water and incubated for 5 min with a 5 μL drop of ammonium molybdate ($(\text{NH}_4)_2\text{MoO}_4$, Sigma Aldrich) at 20 ng mL^{-1} pH 6.7, finally the grid was cleaned three times with water drops.

2.2.2. Poly (acrylic acid) and gentamicin complexes and poly-L-lysine multilayer preparation and characterization

PEMs have been fabricated by means of the LbL technique on top of MTFs (synthesis described in **Chapter 1**). The titania was first cleaned with absolute ethanol and dried at 100 °C. The PAA-gentamicin complexes and PLL solutions were prepared in 500 mM NaCl at a pH of 4.5. A drop of 100 μL with PLL 1 mg mL^{-1} was left incubating on titania for 15 min at room temperature, then it has been removed and rinsed 3 times with 500 mM NaCl pH 4.5. Then, the same volume of PAA-gentamicin complex was deposited on the surface left 15 min, removed and the surface rinsed again 3 times as before. The alternating assembly of PLL and the complexes has been repeated 4 times to obtain a multilayer of 8 layers. Films were synthesized in sterile conditions to study their antibacterial capacity. Samples were dried in air for AFM measurements and previous to their use for the experiments on gentamicin release. To visualize the PEM, SEM images of a transversal cut have been taken and by AFM imaging surface roughness was calculated. PEMs were washed with with nanopure water and left to dry at room temperature.

2.2.3. QCM-D Measurements

The assembly of PLL/PAA-gentamicin complexes multilayers was monitored via QCM-D, Q-Sense E4 system. The LbL assembly was performed on QSX 303 SiO_2 quartz crystals. The PLL and the complexes are injected to the 4-sensor chamber with the help of a peristaltic pump and left under incubation for at least 10 min. For each deposition the solution was fluxed until frequency was stabilized, then a rinsing step of at least 10 min with NaCl 500 M (pH 4.5) took place. Experiments were conducted at 23 °C and the flux velocity of the solution was 100 $\mu\text{L min}^{-1}$.

To study the stability of the multilayer under different pH conditions the multilayers were exposed in the QCMD chamber to NaCl 500 mM solutions with pHs ranging from 5 to 13. The solutions were fluxed at $5.77 \mu\text{L min}^{-1}$. Fluxing solutions have been changed once frequency reaches a plateau.

2.2.4. Gentamicin release study

Gentamicin release was studied by placing the samples in a 24 multiwell dish. 1 mL of 10 mM PBS was added to the wells with the sample. The release has been measured at 30 min, 1, 2, 6, 28, 55 h and 3, 6, 7, 10, 21, 28 and 35 days. The PBS was removed for each measurement from the well and replaced with fresh PBS solution.

2.2.5. Antibacterial study

PEMs were dried in air and placed in 24 multiwell dishes. Round coverslips of 16 mm of diameter were immersed for 24h in gentamicin 0.3 mg mL^{-1} in water and cleaned by immersing the samples one time in distilled water, this samples were used as control. Samples were prepared in triplicate. Dilutions were made in PBS; for samples with the PEM coating the dilutions were 1/1 and 1/10, and for glass controls 1/1,000 and 1/10,000. 10 μL of each dilution was placed in LB Agar plates for overnight incubation. Visual counting of the CFU has been performed and an average and the standard error were calculated.

2.3. Results and discussion

2.3.1. PAA-gentamicin complex synthesis and characterization

PAA-gentamicin complexes were prepared by mixing PAA and gentamicin solutions (**Figure V-1A**) at different gentamicin and NaCl concentrations at pH 4.5. At this pH the amines of gentamicin are largely protonated and positively charged since the pKa for amino groups in gentamicin are in the range of 5.5 and 9. It can also be expected that carboxylate groups from PAA are to a large extent deprotonated and negatively charged as the pKa for PAA is 3.9.^[74,119] It is found that a pH of 4.5 is optimal to favour the formation of complexes of PAA and gentamicin. Salt concentration is tuned to obtain the most stable complexes with the highest gentamicin concentration. As observed by Dynamic Light Scattering measurements, DLS, (**Figure V-2**), without salt (**Figure V-2a**) or with 10 mM NaCl (**Figure V-2b**), complexes start to form with 0.1 mg mL⁻¹ of gentamicin, but they do not show a stable size when the concentration of gentamicin is 0.25 mg mL⁻¹ or higher. In both cases the size of the complexes increases by more than 100 % after 4 h. In water, for 0.45 mg mL⁻¹ gentamicin, complexes start to precipitate after 4 h. However, DLS also shows smaller complexes present in solution that do not precipitate. With 500 mM NaCl, complexes start to form with at least 0.3 mg mL⁻¹ of gentamicin, but if the concentration of gentamicin is increased to 0.45 mg mL⁻¹ the size of the complexes is not stable, changing with time (**Figure V-2c**). After 4 h the size of the complexes is 3 times larger than their size measured immediately after preparation. At high salt concentration (2 M) the formation of complexes is suppressed (**Figure V-2d**).

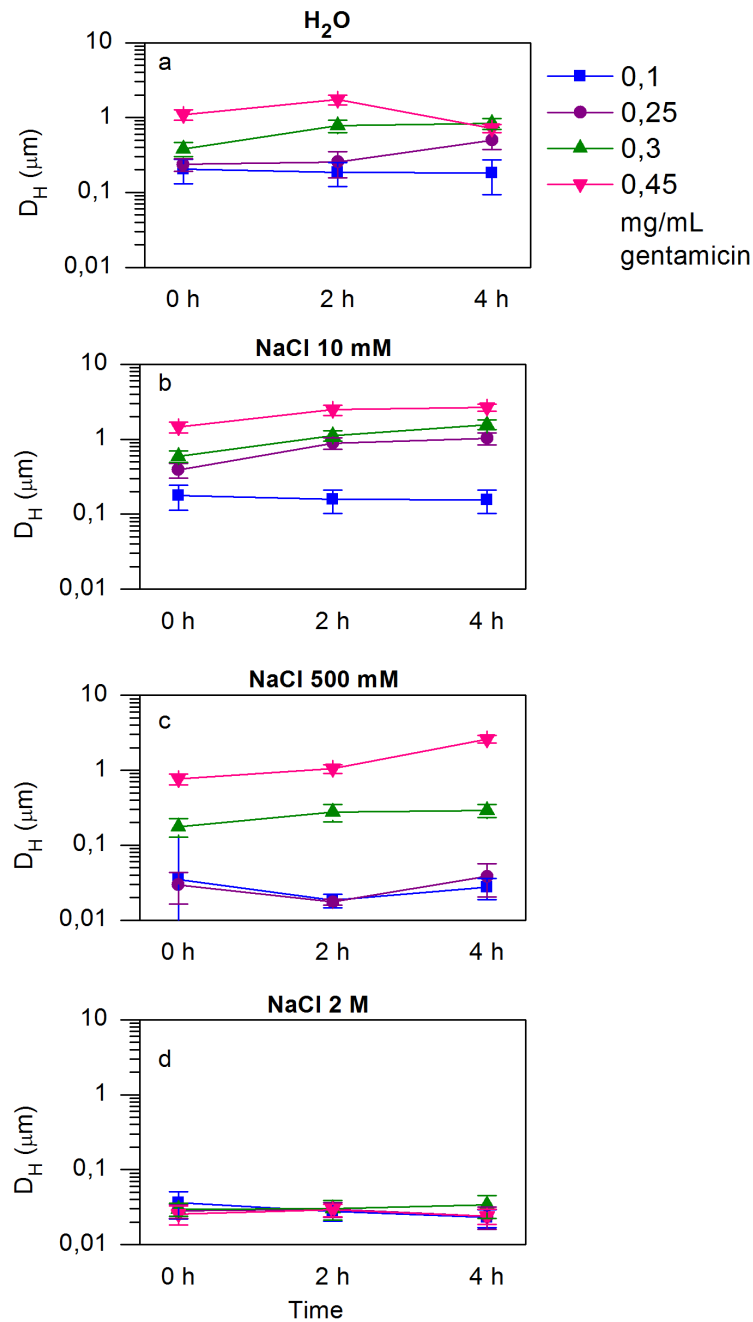


Figure V-2. Changes in the hydrodynamic diameter of PAA-gentamicin complexes over time for different NaCl and gentamicin concentrations at pH 4.5. DLS measurements of complexes measured immediately after being prepared, and at 2 and 4 h after preparation. Complexes were prepared with 0.1, 0.25, 0.3 and 0.45 mg mL^{-1} gentamicin in a) H_2O , b) 10 mM, c) 500 mM and d) 2 M NaCl.

Antibacterial activity of the coating can be enhanced with larger gentamicin content and larger gentamicin concentration leads to larger and more unstable complex size.

The largest gentamicin concentration that leads to complexes with relatively stable size within the 2 hours that the layer-by-layer assembly lasts has been proved to be 0.3 mg mL^{-1} . The evolution of the hydrodynamic diameter of the complexes over time has been monitored using constant gentamicin concentration (0.3 mg mL^{-1}) and varying salt concentration (0 – 2 M) (**Table V-1**). At high salt concentration (2 M), the formation of complexes is suppressed. The resulting hydrodynamic diameter of $\sim 30 \text{ nm}$ corresponds to free PAA of 100 kDa under the same NaCl and pH conditions. At low salt concentration (10 mM), the size of the complexes is relatively large, $>1500 \text{ nm}$, leading to the precipitation after 4 hours. It has been found that at 500 mM of NaCl the complexes maintained their size (120-300 nm), during the first 4 hours after formation. More detailed analysis of size distributions revealed the presence of two peaks of 25 and 180 nm, just after mixing both components (**Figure V-3a**). After 2 h the smallest peak disappears while the second peak shifts to higher values and is narrower, meaning that the larger complexes increase their size at the expense of the smaller ones. At 4 h, the peak is slightly shifted to higher sizes and seems to continue to narrow, but it is considered that the size distribution has practically not changed from 2 to 4 h after assembly of the complexes, which is the time when the PEM is assembled. On contrary to DLS analysis, TEM characterization of the sample two hours after mixing shows the presence of small and large complexes ranging from 60 to 350 nm in diameter (**Figure V-3b**), suggesting that the scattering intensity of the small complexes at 2 h is shielded by the much larger scattering of the large complexes. Overall, for the further experiments the complexes that were prepared with 0.3 mg mL^{-1} gentamicin and 500 mM of NaCl were selected.

Ionic Strength	Hydrodynamic diameter (\pm SD)		
	0 h	2 h	4 h
H ₂ O	382.1 \pm 80.8 nm	774 \pm 147 nm	831.6 \pm 143.6 nm
NaCl 10 mM	596.3 \pm 102.6 nm	1121 \pm 171.1 nm	1570 \pm 229.3 nm
NaCl 500 mM	177.7 \pm 48.7 nm	276.3 \pm 72.5 nm	293 \pm 59.3 nm
NaCl 2 M	29.67 \pm 5.8 nm	30.13 \pm 8.8 nm	33.74 \pm 11.5 nm

Table V-1. Time evolution of the hydrodynamic diameter of PAA-gentamicin complexes prepared with 0.3 mg mL⁻¹ gentamicin and different NaCl concentrations at pH 4.5. DLS measurements of complexes were conducted immediately after preparation, and 2 h and 4 h after complex preparation. Complexes were prepared with 0.3 mg mL⁻¹ of gentamicin in water and 10 mM, 500 mM and 2 M NaCl. The standard deviation calculated from three replicates is shown.

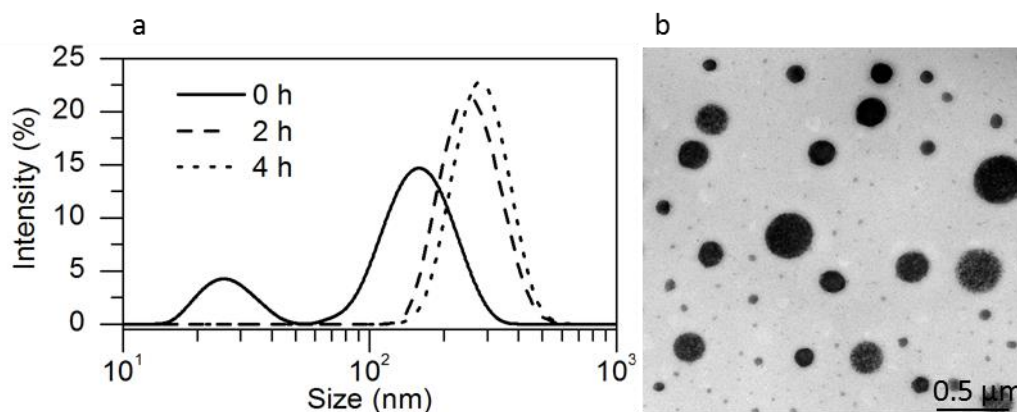


Figure V-3. a) Intensity plot of size distribution at different times after complex formation for PAA-gentamicin complexes prepared in 500 mM NaCl at pH 4.5 with 0.3 mg mL⁻¹ gentamicin. b) TEM image of complexes 2 h after preparation.

2.3.2. Layer-by-Layer assembly of PLL/PAA-gentamicin complexes

PLL and PAA-gentamicin complexes were alternately deposited on titania films, as depicted in **Figure V-1B**. The complexes are left for 2 h to form, and then are used for the PEM assembly and as seen in DLS measurements of the hydrodynamic diameter (**Table V-1**) the size after 2 h keeps constant for the following 2 h at around 300 nm in diameter. The assembly of the 4 bilayers of PLL and complexes was monitored by the Quartz Crystal Microbalance with dissipation technique (QCM-D) (**Figure V-4a**). With the increase of a material on top of QCM-D sensor the frequency shifts to lower values.^[343] The deposition of each layer of PLL and complexes causes the increase of frequency in the following order 8, 11, 51, 73 Hz and 34, 57, 85 and 191 Hz, respectively. Observed frequency changes suggest that the LbL assembly follows exponential growth (**Figure V-4b**).^{[34],[46-48]} Data is fitted to the exponential function $y = y_0 + A \cdot e^{R_0 \cdot x}$, where y_0 is the offset with a value of -34.71, A is the initial value (42.42) and R_0 the rate 0.67. y corresponds to $-\Delta f$ and x to each bilayer, the obtained R^2 is 0.999. The exponential growth implies an increase in the amount of PLL and PAA-gentamicin complexes per layer as the number of assembled layers increases. Since complexes can be considered as spherical nanoparticle of ~100 nm the deposition of each layer results in an increase in the area available for assembly of the next PLL layer. The increase in available free area allows for the deposition of more PLL than on a planar surface. This situation repeats as the assembly proceeds. Consequently, the top layer will contain more complexes and more gentamicin than the layers below, as depicted in **Figure V-1C**. To evaluate the chemical stability of the film, the PEMs immobilized to QCM-D sensor was exposed to an alkaline environment (pH 13), showing that the multilayer film is highly stable in such conditions (**Figure V-4c**) and thereby suitable for biomedical applications.^[347]

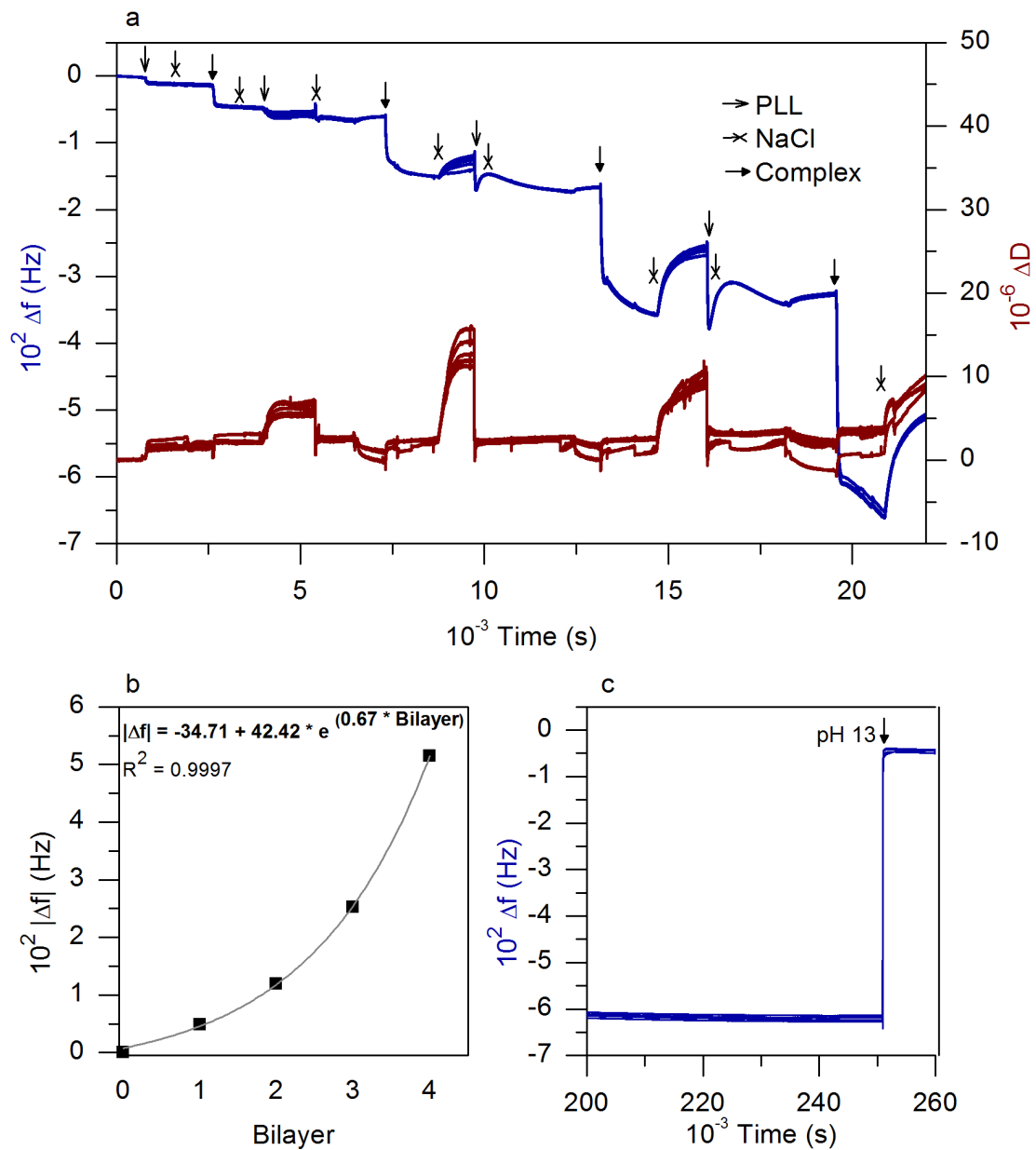


Figure V-4. QCM-D monitoring of layer-by-layer assembly of PLL and PAA-gentamicin complexes prepared with 0.3 mg mL^{-1} gentamicin and film degradation. a) LbL assembly of 4 bilayers of PLL and PAA-gentamicin (0.3 mg mL^{-1}) complexes in 500 mM NaCl and pH 4.5, b) plot of frequency changes after each bilayer is deposited, and c) film degradation in 500 mM NaCl at pH 13.

Detailed SEM analysis PEM cross-section (**Figure V-5**) revealed an irregular topology with the highest measured around 2 μm in height, correlating thus the high frequency changes monitored by QCM-D. The surface inhomogeneity was further confirmed by AFM analysis. **Figure V-6** shows AFM images of height (**a, d, e** and **h**), phase (**b** and **f**) and height profile (**c** and **g**) of PLL/PAA-gentamicin complex PEMs. The roughness calculated from the height images of the PEM coating is 13.9 and 7.9 nm for the 15 x 15 μm (**Figure V-6a**) and 5 x 5 μm (**Figure V-6e**) scans, respectively. The discrepancy in the roughness between the two images from the same sample confirms the data obtained from SEM (**Figure V-5**), that the surface of the PEMs is rather inhomogeneous.^[348] The inhomogeneity on the surfaces is probably the result of the large size dispersion shown by the complexes as observed by TEM and DLS. Phase images (**Figure V-6b** and **f**) show that the lag in the phase remains constant over all scanned regions, suggesting that the LbL assembly is continuous without uncovered regions. From the height profile peaks of more than 100 nm can be distinguished, as well as regions with peaks of only a few nm and intermediate peaks with heights of around 50 nm can also be identified (**Figure V-6c** and **g**). These images together with the QCM-D monitoring leads to associate the exponential growth of the PLL-complex PEM to the 'Island Model'. This model proposes that the first component is adsorbed in the surface forming "islands" and after several deposition steps the height and radius of the islands increases making the surface more and more heterogeneous and increasing the amount of material adsorbed.^[110,349,350]

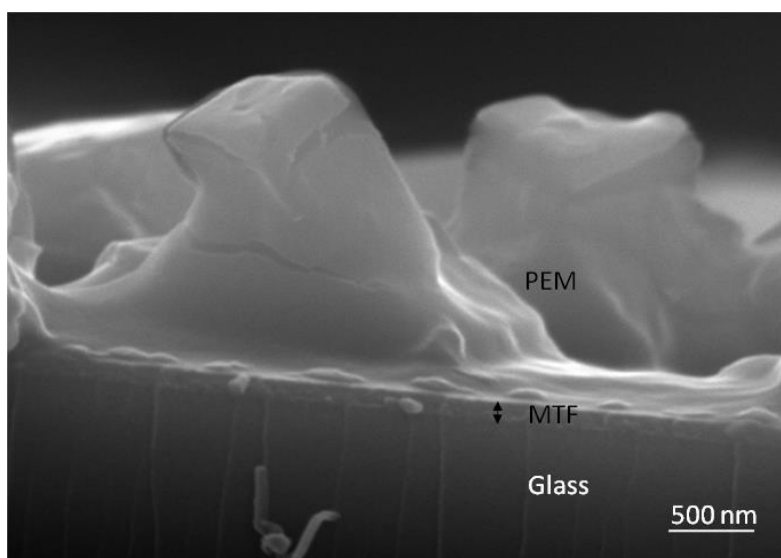


Figure V-5. SEM cross-sectional image of the PEM deposited on top of the MTF. The glass and the MTF can be distinguished, as well as the PEM grown on top.

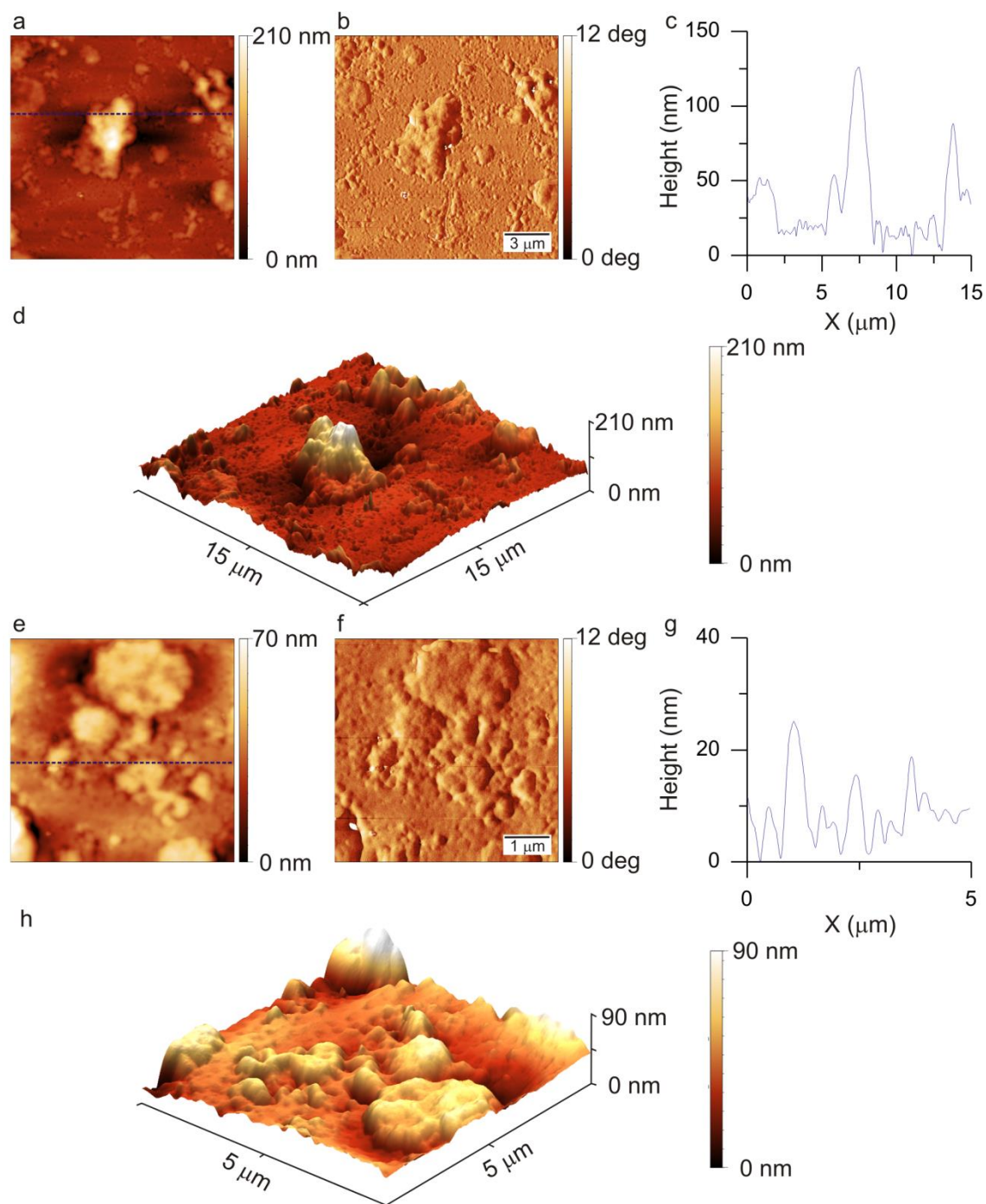


Figure V-6. AFM images of the assembly of 4 PLL/PAA-gentamicin (0.3 mg mL^{-1}) complex bilayers. a) Height, b) phase, c) height of section in a and d) 3D graph of the height of $15 \mu\text{m} \times 15 \mu\text{m}$ image and e) height, f) phase, g) height of section in a and h) 3D graph of the height of $5 \mu\text{m} \times 5 \mu\text{m}$ image.

2.3.3. Gentamicin release from PEMs

The advantage of encapsulating antibiotics close to the implant-tissue interface is the effective antibiotic release that leads to the side effects minimization.^[351] Despite the PEMs being stable at physiological pH, it is observed a release of gentamicin from the films. At physiological pH (7.4), gentamicin is less protonated than at pH 4.5, the pH at which the complexes were prepared. The deprotonation of gentamicin should weaken the interaction of the antibiotic with PAA, which should trigger gentamicin release. On the contrary, PAA has a larger charge at higher pHs. PAA and PLL multilayers fabricated with free PAA are stable at physiological pH. Since the stability of the film is largely due to the interaction of PLL with PAA, a stable film releasing gentamicin is possible. The amount of gentamicin released from the films can be monitored by measuring the fluorescence emission at 455 nm of the complex formed by gentamicin and the OPA reagent. There is a burst release of gentamicin within the first 6 hours, which liberates around 48 % of the total gentamicin (insert in **Figure V-7**). Then, after the burst release, a prolonged release takes place. Gentamicin is slowly released in a period from 6 hours to 35 days, after which a plateau is reached. This release profile of gentamicin encapsulated in the PEM has the characteristics required to avoid infections after a replacement surgery: (1) during the critical short-term post-implantation period, which lasts several hours, a burst release of gentamicin takes place. This burst release is needed to inhibit the initial adhesion of bacteria during the surgery, where there is the largest risk for infection as the body is opened and exposed. (2) A continued and slow release takes place beyond the initial first hours lasting weeks to avoid bacterial infection during the formation of a protective fibrous capsule and tissue integration on the implant.^[308]

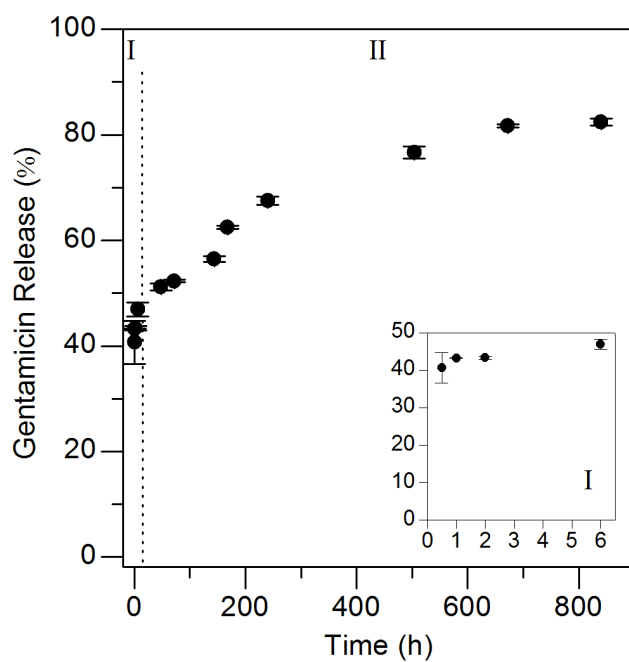


Figure V-7. Release profile of gentamicin from PEMs formed of 4 bilayers of PLL/PAA-gentamicin complex on top of titania thin films. Region I shows the burst release (the insert is a zoom of region I) and region II the sustainable release. The release is followed up to 35 days using emission measurements at 455 nm.

2.3.4. Evaluation of the antibacterial properties of the PEMs

To demonstrate the antibacterial activity of the films, an *S. aureus* strain was seeded on top of the PLL/PAA-gentamicin PEMs. Samples were prepared under sterile conditions and a glass immersed in gentamicin was used as a control. Approximately 1,000 CFU of *S. aureus* were seeded at 37 °C for 24 h on three replicates for each sample. Transmission images show very few bacteria adhering to the surface of the film, while a larger number of bacteria are observed on the control (**Figure V-8a and b**). This result suggests that the PEM has antibacterial properties. When bacteria were detached and incubated for 24 h on agar plates, the CFU for bacteria grown on control surfaces was 3 orders of magnitude higher than that for bacteria grown on the PEMs (**Figure V-8c**). Bacteria were detached from the surfaces and incubated for 24 h on agar plates before counting.

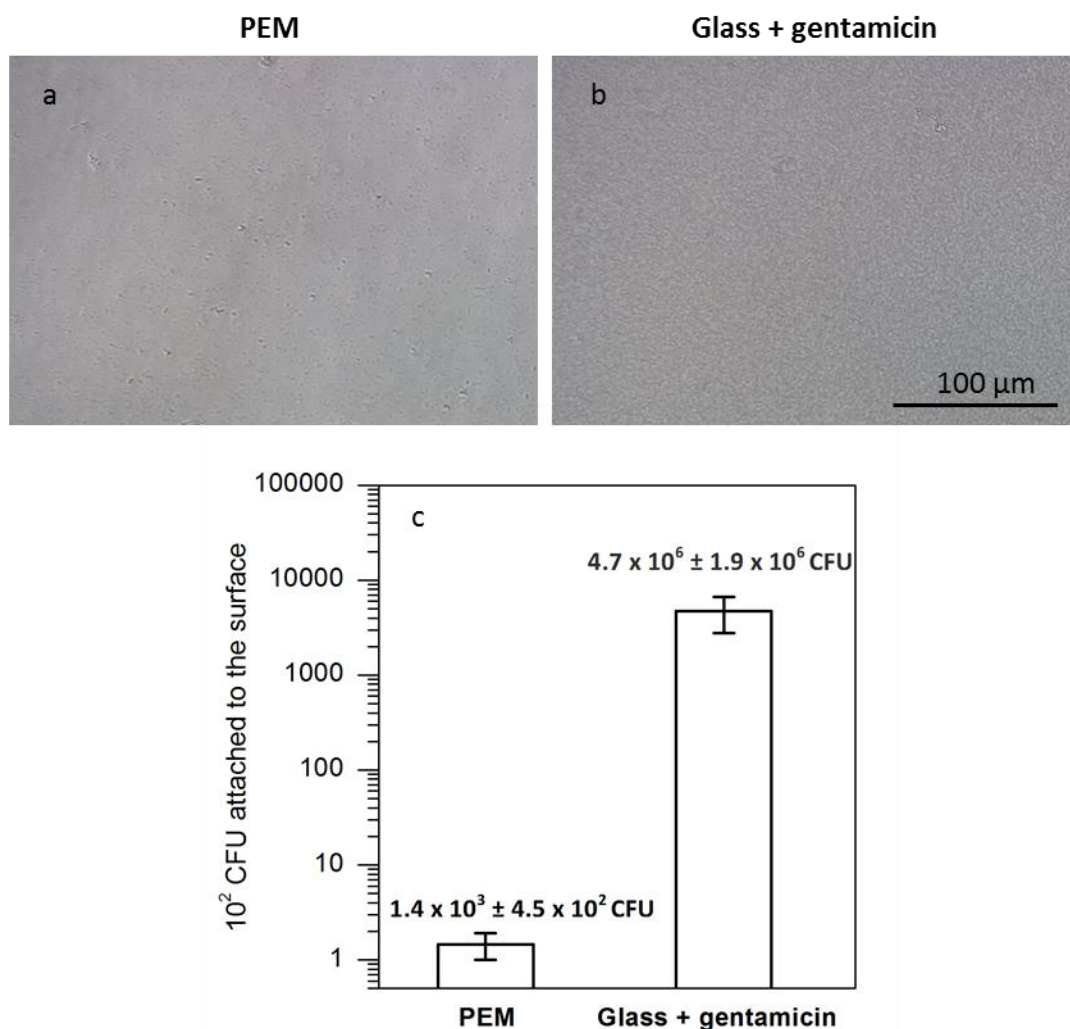


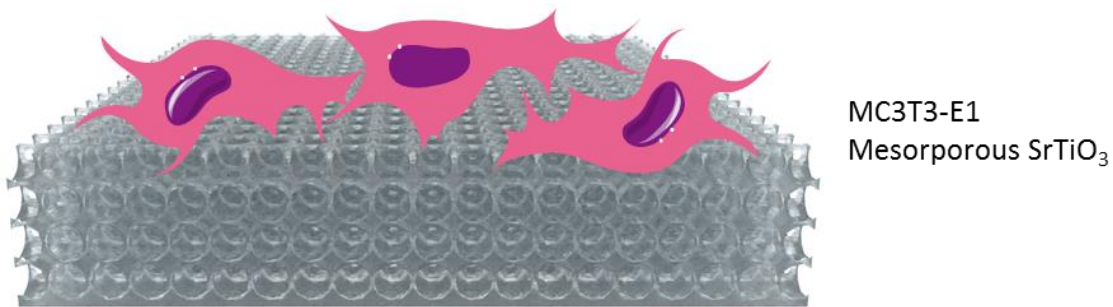
Figure V-8. *S. aureus* growth on PAA-gentamicin PEM coatings and on glass substrates immersed in gentamicin. Cell observer images following 24 h of incubation of *S. aureus* on a) PEM coating on top of titania films and b) glass immersed in gentamicin. c) CFU of the adhered bacteria on the PEM and glass with gentamicin.

2.4. Conclusions and perspectives

Stable PAA-gentamicin complexes were synthesized by mixing 0.3 mg mL^{-1} gentamicin and 1 mg mL^{-1} PAA in 500 mM NaCl at $\text{pH } 4.5$. Complexes display a hydrodynamic diameter ranging from 160 to 300 nm and are stable within 4 hours. PEMs were constructed by alternating PLL and PAA-gentamicin complexes by adsorption on top of titania up to 4 bilayers. The assembly of the PAA-gentamicin complexes with PLL shows an exponential growth and a large number of PAA-gentamicin complexes are deposited with only a few assembled layers.

The PLL/PAA-gentamicin PEMs are stable until $\text{pH } 13$. However, PEMs release gentamicin at physiological pH values. Release studies in 10 mM PBS showed an initial burst release within the first 6 h followed by a slow release of gentamicin lasting up to 5 weeks. The antibacterial properties of the PEMs were tested by seeding an *S. aureus* strain on the LbL films. The CFU counts for bacteria grown on the PEMs after 24 h is 3 orders of magnitude smaller than those grown on a glass control immersed in gentamicin. It is important to note that only 4 bilayers of PLL and the complex are required to achieve a film with antibacterial properties.

During surgery and while the body is exposed to the environment, a fast release of gentamicin can be crucial for avoiding the attachment of bacteria. At the same time, a continuous supply of gentamicin in lower doses is required during the osseointegration process until the tissue is reconstituted to ensure that bacteria do not attach and proliferate at the site of the implant. The initial burst release of gentamicin followed by a long-lasting slow release over weeks makes the PAA-gentamicin PEMs especially attractive as an antibacterial coating for implants, and highlights the potential of these films to prevent nosocomial infections following implant surgery.

VI. CHAPTER 3**SrTiO₃ mesoporous coating for enhanced osseointegration****3.1. Motivation**

Since the role of an implant is the replacement of the bone, it needs to mimic the biological environment and mechanical properties of the bone. Several strategies have been proposed to improve interaction between titanium implants and the regenerating bone tissue.^[79,125,352-354] Topography plays an important role on the osseointegration process with cells adhering better to rougher surfaces. Indeed, titania with nanoscale surface features has been shown to favour osseointegration.^[126,127] To increase the bioactivity of titania, growth factors can be deposited on top of the implant or the titania can be doped with bioactive ions.^[352,355-357]

Several ions present in the human bone mineral apatites like calcium (Ca²⁺), magnesium (Mg²⁺), niobium (Nb⁵⁺), phosphate (PO₄³⁻), silicate (Si⁴⁻), strontium (Sr²⁺), and zinc (Zn²⁺) are known to promote osteoblastic precursor cell differentiation.^[182,185,194,197,199,205,216,218,236,358] The incorporation of some of these bioactive ions in titania, in particular strontium, has been shown to induce growth factor signaling pathways to osteoblastic precursor cell differentiation.^[182]

Approximately 98 % of the strontium present in our body is localized in bone tissue.^[237] Strontium has a beneficial effect on the bone metabolism due to its anabolic and antiresorptive activity^[359] and has been shown to be a promising therapeutic agent to heal bone disease, as example, strontium ranelate has been

used in clinics for long time.^[360] As oral medicament it has been proved to act on both the desorption and formation of bone,^[361] but currently is not recommended due to the side effects it has when is administered orally.^[362] Besides, the side effects are suppressed when the drug is administered locally.^[363] Strontium itself promotes osteogenic differentiation of mesenchymal stem cells by up-regulating the expression of osteoblast marker genes, such as *Runx2*, osteocalcin (*OCN*), osteopontin (*OPN*), bone sialoprotein (*BSP*), and type 1 collagen, and increasing Alkaline Phosphatase (AP) activity and matrix mineralization.^[212]

Strontium incorporated in titania has been shown to lead to an enhanced osseointegration and an improved differentiation of pre-osteoblastic cells.^[352,364-366] The strontium incorporated in titania, however, must be released in the environment of the regenerating tissue for a positive action. Besides the amount of Sr incorporated in the titania the area available for ion exchange plays an important role in the release of Sr as it will only be delivered in the media when it is located on the surface.^[352,367] Rougher titania surfaces for example have been shown to deliver Sr more effectively than plain titania as a consequence of the larger available surface.^[182,352,364] A possible mean to increase the surface area for ion delivery is the use of mesoporous titania. Mesoporous materials have an ordered, homogenous array of pores with highly controlled diameters in the 2-10 nm range.^[294] Titania can be synthesized as a mesoporous material without compromising its mechanical properties,^[301] which is fundamental for bone replacement. Moreover, a mesoporous titania film (MTF) can be easily synthesized on top of non-porous titania with the same biocompatibility properties as the non-porous titania.

A large surface is available in mesoporous films that can be used for the delivery of Sr or other bioactive element present in the formulation of the mesoporous material.^[262] The larger surface results in a larger amount of Sr potentially available for delivery in the media if compared with non-porous titania with the same content of Sr. Moreover, the mesoporous material can be designed to present interconnected pores linked by narrow necks. Once the Sr is released from the surface of the pore it will have to escape through the pores, retarding its release from the film. Importantly, it is possible to incorporate strontium or calcium into the MTF during the synthesis process simply by adding ionic salts to the sol, as demonstrated by

Grandfield *et al.*^[243] By this way the ions will be incorporated to the titania matrix, up to 0.01 : 1 of Sr : Ti relation in moles.^[243] Strontium salts are not very soluble,^[368-370] and depending on the synthetic pathway applied to obtain the mesoporous films and the solvents used, the concentration of the strontium salt that can be incorporated during the synthesis varies. Grosso *et al.*^[371] also incorporated Sr in MTFs and found a 1 : 1 Sr : Ti relation but only in nanocrystals located in the walls of the mesoporous structure, being Sr not homogeneously distributed.^[371]

In this chapter strontium titanate mesoporous films (SrTiMFs) are prepared by sol-gel chemistry employing the evaporation induced self-assembly method (EISA). Pore and neck size of the films are measured by Environmental Ellipsometric Porosimetry (EEP). Film thickness and surface are visualized by Scanning Electron Microscopy (SEM), and pores by Transmission Electron Microscopy (TEM). Small-angle X-Ray Scattering (SAXS) patterns are obtained to determine the pore ordering and mechanical properties of the SrTiMFs are examined by nanoindentation. Sr concentration and molar relation to Ti is determined by X-ray Photoelectron Spectroscopy (XPS). To assure the Sr is homogeneously distributed in the Ti mesoporous structure Energy Dispersive X-Ray (EDX) analysis is performed in different points of the film. Sr release is followed by Induced Coupled Mass Spectroscopy (ICP-MS). TEM imaging is also performed after the release study to evaluate film stability. Cell attachment, proliferation and differentiation studies are performed with the MC3T3-E1 pre-osteoblastic cell line showing the enhanced bioactivity of the SrTiMFs.

3.2. Experimental section

3.2.1. SrTiMF synthesis and characterization

For the sol preparation Titanium (IV) Chloride ($\geq 99.0\%$, TiCl₄), Strontium chloride hexahydrate (SrCl₂ x 6 H₂O), Ethanol Absolute (Synthesis grade, EtOH), Pluronic F127[®] and nanopure water (H₂O) were mixed in a molar proportion of TiCl₄ : EtOH : SrCl₂ : F-127 : H₂O = 1 : 40 : 0.2 : 0.0056 : 10. The titania precursor was prepared first, adding TiCl₄ to the EtOH under vigorous stirring and leaving it till drops to room temperature. SrCl₂ was homogenized under stirring in water, then the F-127 was added under stirring and finally the titania precursor is added. The sol is left stirring for 10 minutes to obtain a homogenous solution.

For the films preparation, 30 μL of the sol were mixed with EtOH in a volume proportion of sol : EtOH 2 : 1 and spin coated at 68 rpm for 30 seconds on glass slices. Films are placed for 30 minutes in a humidity chamber with a relative humidity of 50 % and then they are subjected to a thermal treatment: 30 minutes at 60 °C and another 30 minutes at 130 °C. Finally, films are calcinated; first, heating up with a ramp of 1 °C min^{-1} and then, keeping them at 350 °C for 2 h. As control MTFs were synthesized following the same procedure described in **Chapter 1**.

Pores were visualized through TEM imaging and field topology was analysed through FE-SEM. Ellipsometric and EEP measurements were performed to measure film thickness and pore and bottleneck diameters. 2D-SAXS patterns were analysed to study pore ordering. The value of the elastic modulus (E_r) is extracted from nanoindentation tests.

3.2.2. Strontium detection and release study

The presence of strontium was confirmed by XPS atomic composition analysis. To ensure the strontium was homogeneously distributed in the mesoporous titania a Scanning Transmission Scanning Microscope with Energy Dispersive X-Ray detector (STEM-EDX) was used for the semi-quantitative analysis of the film composition at different positions on the surface.

To measure the total amount of Sr in the SrTiMF, films were immersed in 5 mL HNO_3 > 99.5 % puriss overnight (around 18 h) to complete dissolution of the film, then distilled water was added till 5 % concentration of HNO_3 was obtained for ICP-MS measurements. As control, MTFs were also dissolved following the same procedure. 3 samples for each film type were evaluated.

To study the release of the strontium, samples were placed in wells of 12 multiwell dishes with 2 mL 10 mM PBS and the strontium released was measured at 5, 15, 30 min, 1, 2, 6 h and 1, 2 and 7 days. Samples were prepared in triplicate. TEM images were acquired on samples previously immersed in 10 mM PBS for 24 h.

3.2.3. MC3T3-E1 cell bioactivity experiments

To confirm cell adhesion to the substrates CLSM images were taken after F-actin, focal adhesions and nucleus labelling. Cell proliferation was evaluated by

colorimetric analysis. Measurements were done by triplicate at 2 h, 1, 2 and 3 days. Alkaline phosphatase activity was measured after 5, 10, 15 and 20 days of cell culture in osteogenic medium.

3.3. Results and discussion

3.3.1. SrTiMF synthesis and functionalization

SrTiMFs are synthesized by sol-gel chemistry applying the EISA process. The block co-polymer Pluronic F127[®] was used to generate the mesoporous structure. TEM and SEM imaging confirmed the porous structure (**Figure VI-1a** and **b**); the pores are seen as white spots in TEM and darker spots in SEM images. The pore ordering is not well defined, some regions present disordered pores, while other seem to present well-ordered pores, with an array compatible with the typical body centered cubic array of mesopores typical of F127 templated oxides. The insert in **Figure VI-1a** refers to the 2D-SAXS pattern of the SrTiMF, taken at 90°: a circular pattern is observed, compatible with mesoporous thin films in which pores in the *xy* plane are polyoriented, matching what it is observed by electron microscopy.^[138] The calculated interplanar (-110) distance from the SAXS pattern is 11.1 nm, typical of F127 templated mesoporous oxides.^[305] From the water adsorption and desorption isotherms (**Figure VI-1c**) a porous volume of 30 % and a pore diameter of 5.5 nm is determined. The bottlenecks connecting the pores have a diameter of 3.2 nm. The SrTiMFs film thickness is 85 nm. These results also confirm that the inner porous volume of the film is accessible to water. In these conditions Sr present in the walls could get in contact with cell media and be released. Due to the high porous volume of the film the surface area largely increases if compared with non-mesoporous titania films.^[372] Then, a larger surface will be in contact with the media allowing higher release of Sr from the surface. Sangle *et al.*^[373] have synthesized a mesoporous SrTiO₃ film by pulse laser deposition and obtained rod-like mesoporous structure of 20 nm with a wall thickness of 5 – 7 nm. When films are around 100 nm in thickness the surface, compared to a non porous surface of same area, is increased in a 2,500 %.^[373]

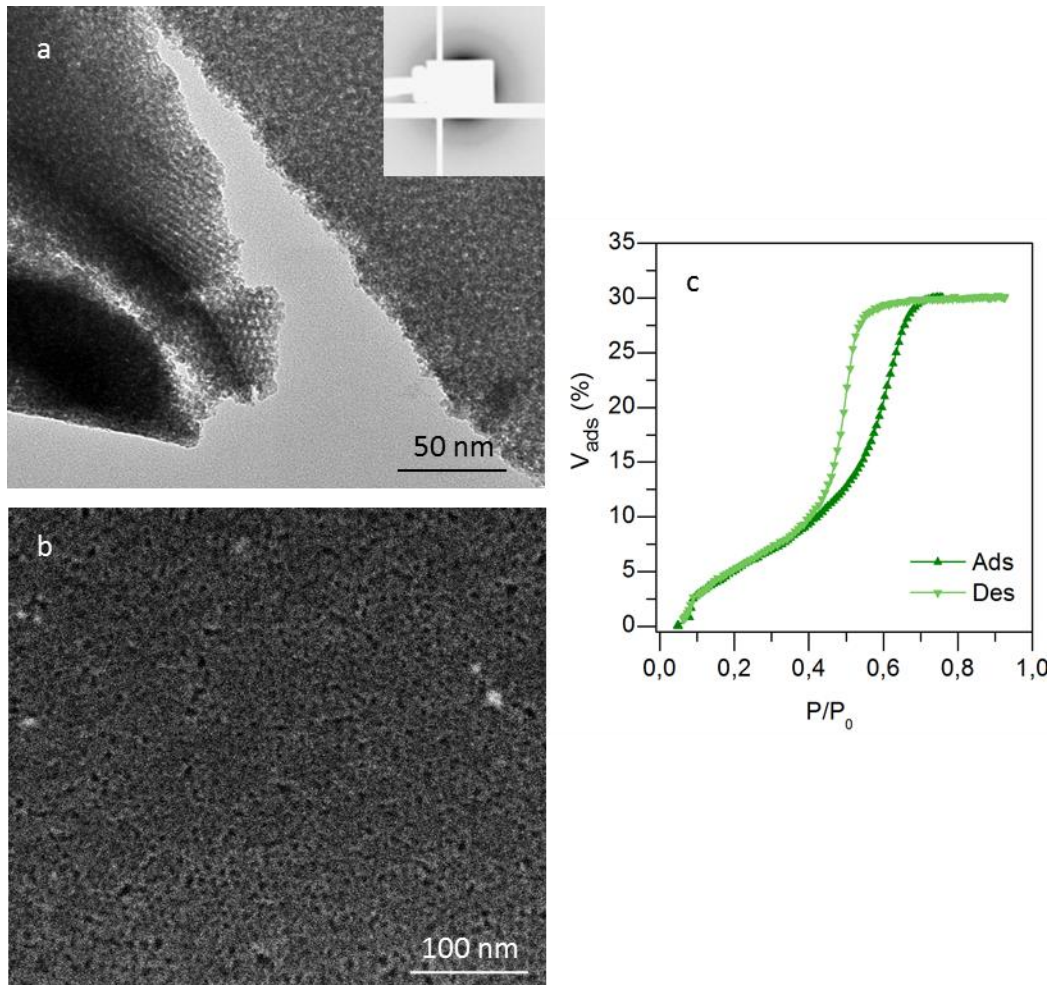


Figure VI-1. SrTiMF structural characterization by electron microscopy, SAXS and EEP. a) TEM image, insert 2D-SAXS pattern taken at 90°, b) SEM image of the surface and c) water adsorption-desorption isotherm, obtained by EEP.

Nanoindentation measurements showed an elastic modulus of 25 ± 5 GPa for the MTF (**Figure IV-2** in **Chapter 1**) and 35 ± 7 GPa for the SrTiMF (**Figure VI-2**). The incorporation of strontium to the mesoporous structure does not affect the Elastic modulus of the films; moreover the Elastic module is improved compared with plain MTF. However, in any case the value is smaller than for dense titanium surfaces, which ranges between 100 and 120 GPa,^[31] but at the same time the Elastic modulus of SrTiMF is in agreement with the range of elasticity of bone, which lays between 4 and 30 GPa depending on bone type.^[23]

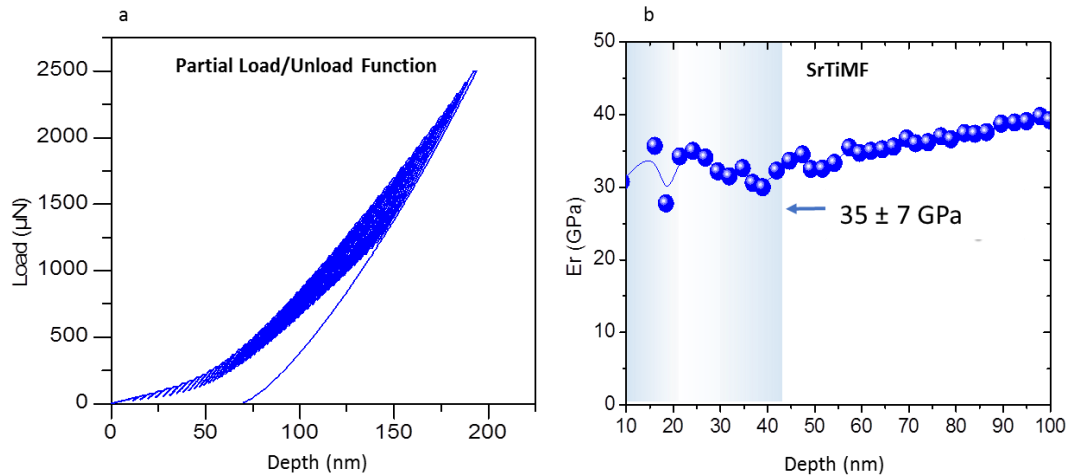


Figure VI-2. Nanoindentation study a) Shows the partial-load/unload vs displacement curve used for the tests and the results of the analysis of each unload section for Elastic modulus (E_r) of b) the SrTiMF.

The Sr : Ti molar relation in the films synthesis was 0.2 : 1. This relation has been the highest possible to obtain an optimal solution for synthesis, since if the concentration of SrCl₂ was augmented it started to precipitate resulting in an inhomogeneous solution. XPS measurements have confirmed that this relation is kept after film synthesis, where the resulting relative Sr/Ti atomic percentage is around $20.8 \pm 0.4 \%$. Compared with Grandfield *et al.*^[243] that obtained a 0.01 : 1 of Sr : Ti molar relation, the synthesized MTFs have incorporated 20 times more strontium in the film, and very importantly in an homogeneous distribution.

Figure VI-3a shows the XPS spectra of a SrTiMF, and **Figure VI-3b** and **VI-3c** show the high resolution spectra of Ti and Sr, respectively. It must be noticed that chlorine, which should appear at 199 cm^{-1} , is not detected in the XPS spectra confirming that strontium is integrated in the titanium network and not forming SrCl₂ crystals. By means of ICP-MS the total strontium amount is obtained once the film is digested. The total amount of strontium in the SrTiMF resulting from the measurement of 3 samples is $2.29 \pm 0.53 \mu\text{g}$.

Figure VI-4 shows representative STEM and EDX spectra at different spots of the SrMTFs. **Figure VI-4a** and **VI-4b** correspond to STEM micrographs taken of different parts of the film. The spectra shown (**Figure VI-4c**) are obtained in three spots from same region. There are no regions where Ti or Sr bands are missing,

meaning that the mesoporous network has a homogeneous distribution of the elements and no phase segregation occurs in the mesoporous oxide.

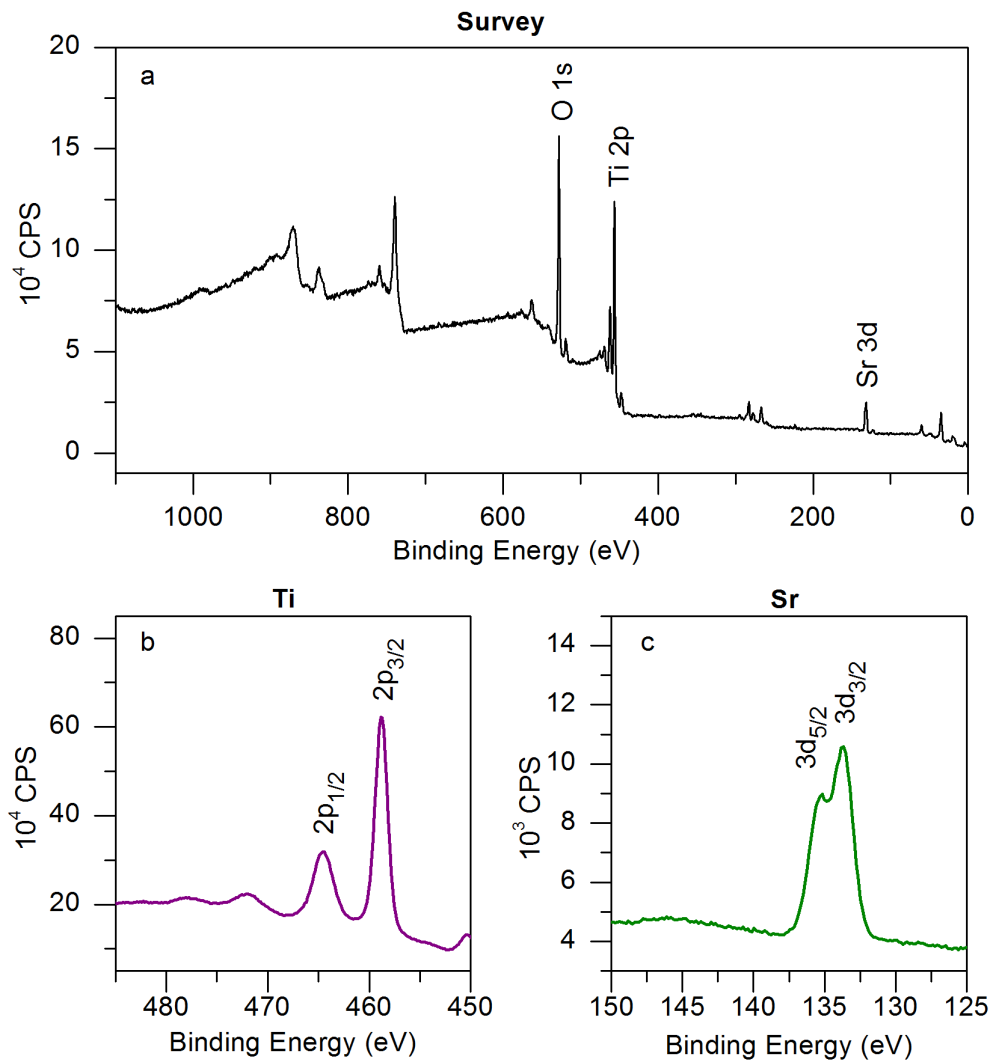


Figure VI-3. XPS a) Survey spectra and high resolution b) Ti and c) Sr spectra from SrTiMF.

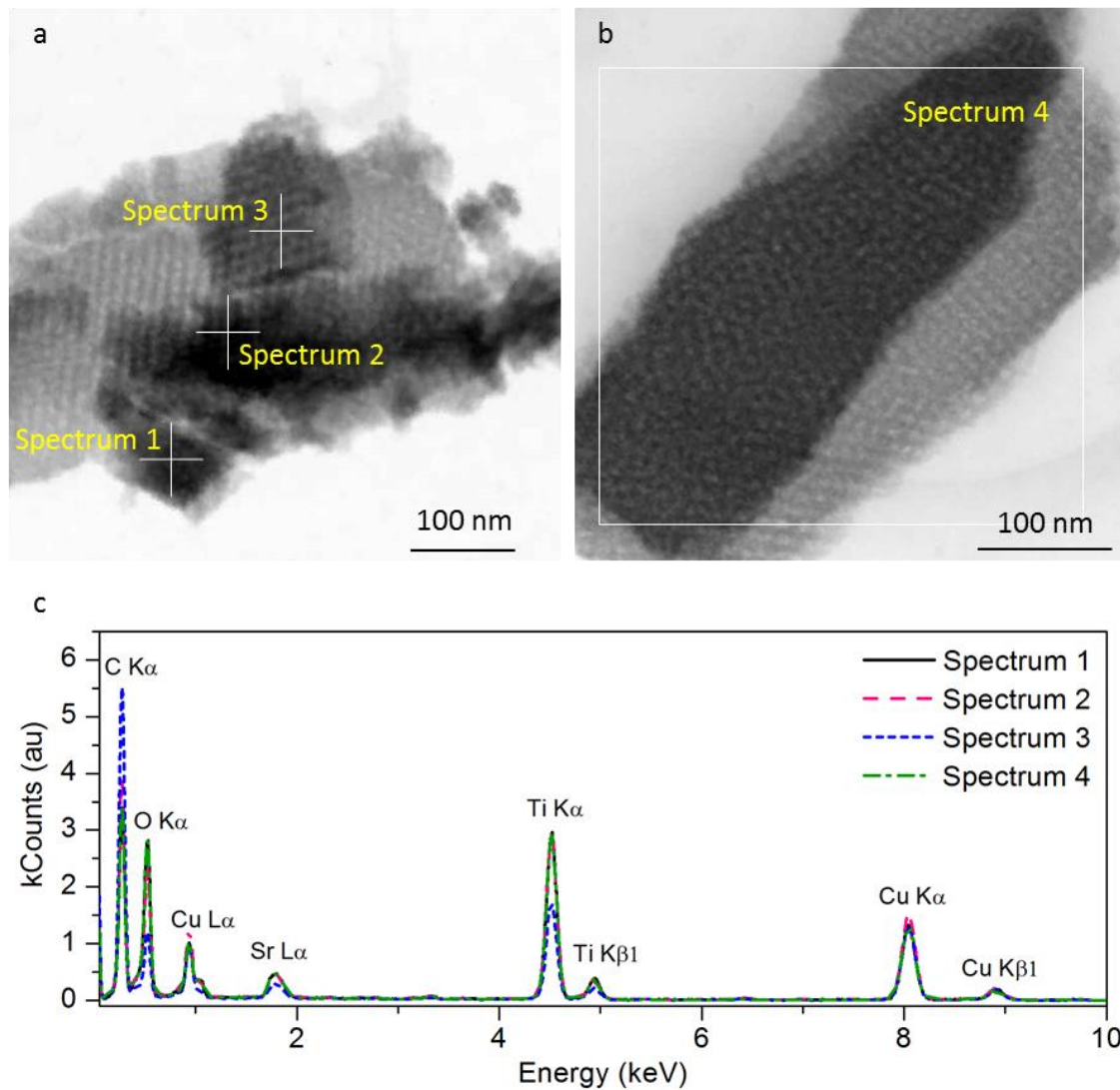


Figure VI-4. a) and b) STEM images of SrTiMF and c) EDX analysis of the points in image a (white crosses) and area in image b (white rectangle).

3.3.2. Strontium release

Figure VI-5 shows the release profile of Sr measured by ICP-MS. After 1 h, 38.58 ± 1.77 % of Sr is released and after 8 h the percentage of released Sr is 43.76 ± 7.99 %. The next measurements at 24 h show a 44.41 ± 6.61 % of Sr released. The release curve shows a fast release within the first 8 h, where the maximum release is reached. Then, the release is very slow but continuous. The release characteristics of the mesoporous could be further tuned by modifying pore size, porous structure or film thickness.^[372] The larger the surface area and thickness of the SrTiMF the higher the concentration of ions available for release will be.^[372,374] **Figure VI-6** is a representative TEM image of the SrTiMF after being immersed for 24 h in 10 mM PBS for the release experiment. As can be seen, the films do not suffer any noticeable

dissolution and the porous structure is maintained without any appreciable changes.

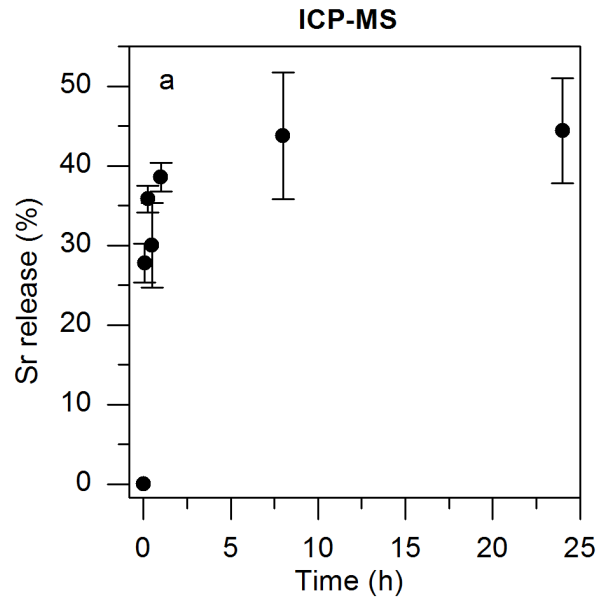


Figure VI-5. Percentage of strontium loss from SrTiMF over time measured with ICP-MS.

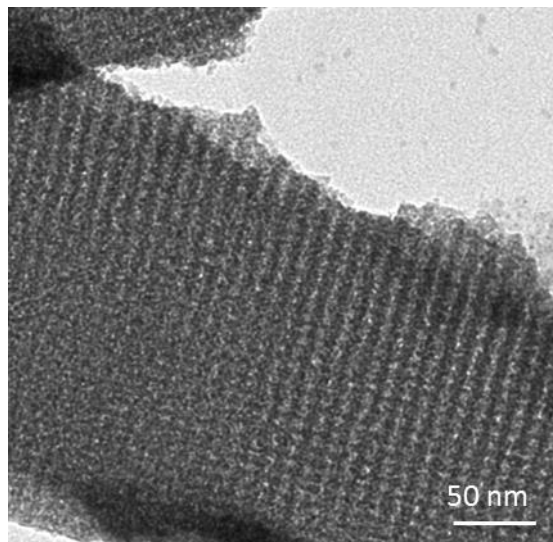


Figure VI-6. TEM representative micrograph of SrTiMTF after being immersed 24 h in 10 mM PBS.

3.3.3. Biocompatibility and bioactivity evaluation

The MC3T3-E1 osteoblast precursor cell line is used to evaluate adhesion to the MTFs (In **Chapter 1**) and SrTiMFs. **Figure IV-7** and **VI-8** show CLSM images of the cells cultured on the MTFs and SrTiMFs, respectively. The actin filaments (F-actin) are stained with phalloidin, which can be appreciated as red fluorescence in the images displayed in the second row of the figure. Vinculin is stained with FITC, and the staining is shown in green in the first row of images. The nucleus is stained with DAPI and is represented in blue in the Merge images (third row), where all the labeled cell parts are shown. In the F-actin images it can be seen that cultured cells on SrTiMF exhibit a similar size as when cells are grown on MTF and an arranged cytoskeleton with distinctive stress fibers inside the cytoplasm, especially at the border of the cells. However, cell shape is different after 48 h of culture (third column). Compared to cells cultured on top of MTFs, when strontium is incorporated in the MTF the cell shape is more elongated and cells show higher filopodia.^[312] This means that cells are better interacting with the surface in presence of strontium and that they are well attached to the surface.

Vinculin interconnects signals in the focal adhesions and is a key regulator in the environment sensing.^[313,314] The first row of images in **Figure VI-7** shows the vinculin staining in the green channel. Green dots can be distinguished at the end of the actin filaments of cells cultured on SrTiMFs. After 2 h of cell incubation on the substrates (first column) focal adhesions can be perfectly distinguished, meaning cells adhere well to the substrates already at initial times and adhesion will later improve cell proliferation.^[310,313]

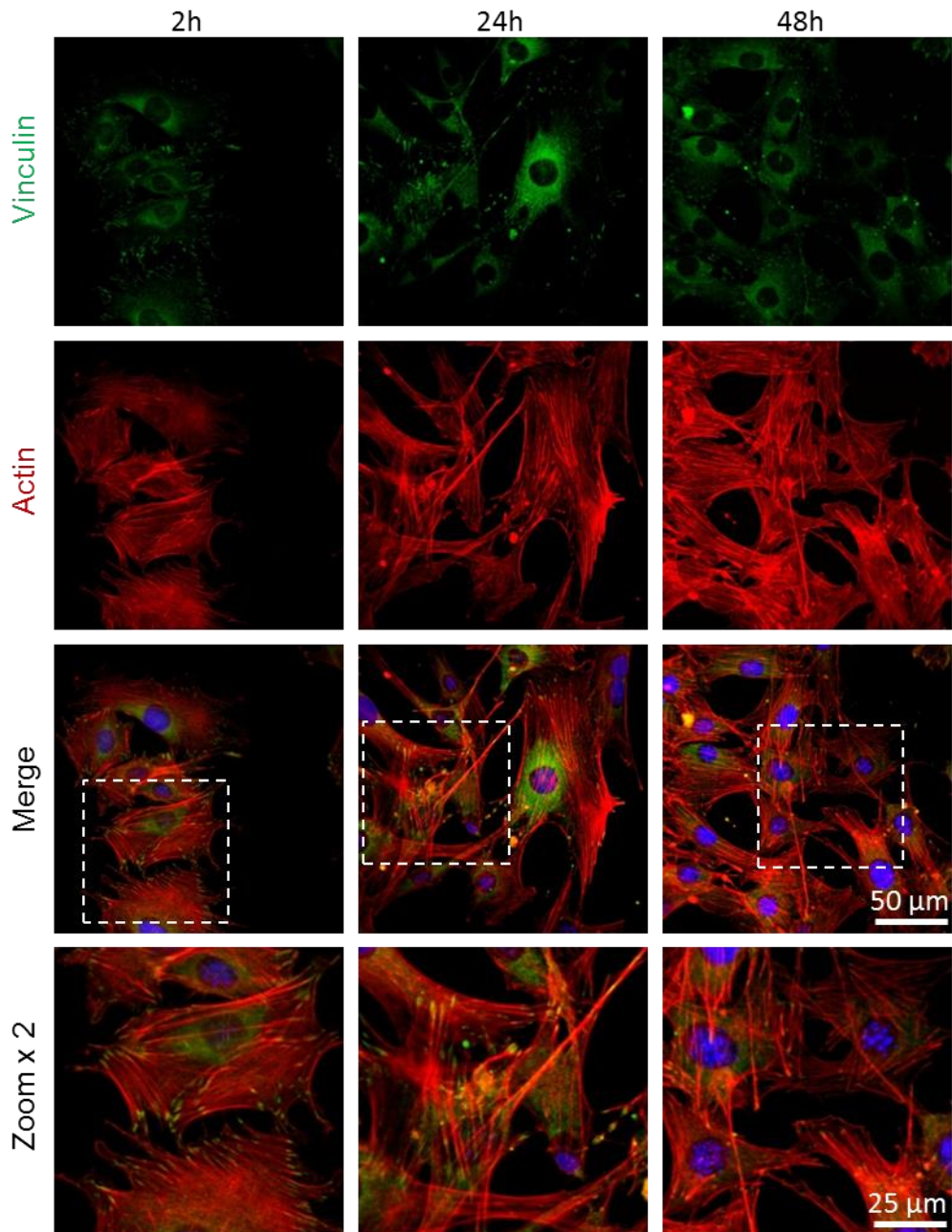


Figure VI-7. CLSM images of vinculin (first row), actin (second row), the merge of the actin, the vinculin and the nucleus (third row) and the zoom of the merge image (fourth row) at 2h (first column), 24h (second column) and 48h (third column) of growth of MC3T3-E1 cell line on SrTiMF substrates at 63x.

Figure VI-8 shows results on cell proliferation for MC3T3-E1 cells cultured on top of MTFs and SrTiMFs. After 7 days the culture is confluent, meaning that the surface is completely full of cells forming a monolayer, and no difference can be distinguished between samples. Within the first day cells proliferate at the same rate and cell density is the same for both substrates. After 2 days of culture on SrTiMFs cell proliferation rate is enhanced if compared with cells cultured on MTFs ($p < 0.05$). At day 2, the proliferation on MTF containing Sr is a 64 % higher if compared with plane MTFs, and after 3 days of culture the difference is of 52 %. As previously seen in **Figure VI-8**, cells are more expanded and showing higher filopodia, as the interaction is better, it is known that proliferation is also improved.^[310,313] These results confirm as expected that, strontium enhances pre-osteoblastic cell proliferation,^[375-377] but more importantly how the Sr is released from the mesoporous structure makes the substrate a good candidate to enhance cell attachment and proliferation at initial times after the implant is placed in the human body.

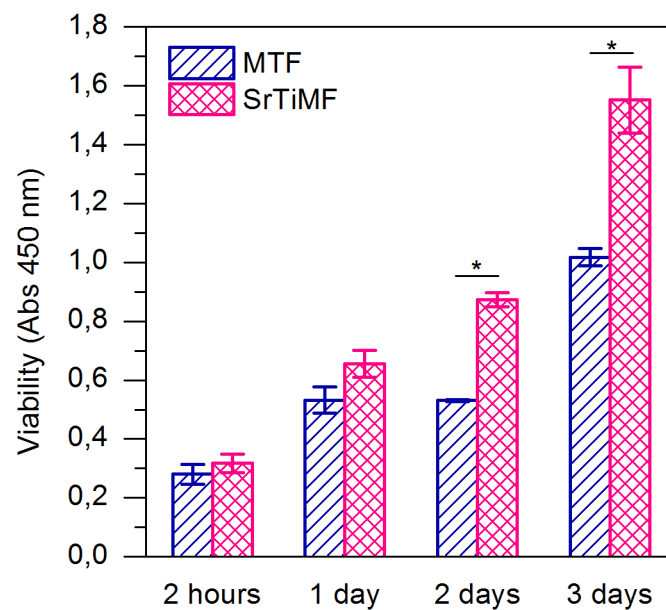


Figure VI-8. Proliferation of MC3T3-E1 pre-osteoblasts cultured on MTF and SiTiMF substrates for 2 h, 1, 2 and 3 days. * means the difference is statistically significant ($p < 0.05$).

Alkaline phosphatase (AP) is one of the gene markers in the early stage of osteogenic differentiation^[162] and his activity has also been evaluated. **Figure VI-9** shows AP activity of the cells cultured on the MTFs and SrTiMFs. After cells reach confluence, they are differentiated for 20 days and the AP activity is measured at different differentiation times to evaluate differences in the degree of differentiation. Differences between both types of substrates ($p < 0.05$) are observed just after cells are cultured in osteogenic medium. Only 5 days after cells are cultured on top of the substrates, the AP activity is more than the double on SrTiMFs compared to MTFs. Following measurements at 10, 15 and 20 days also confirm enhanced cell differentiation on SrTiMF.^[375-377]

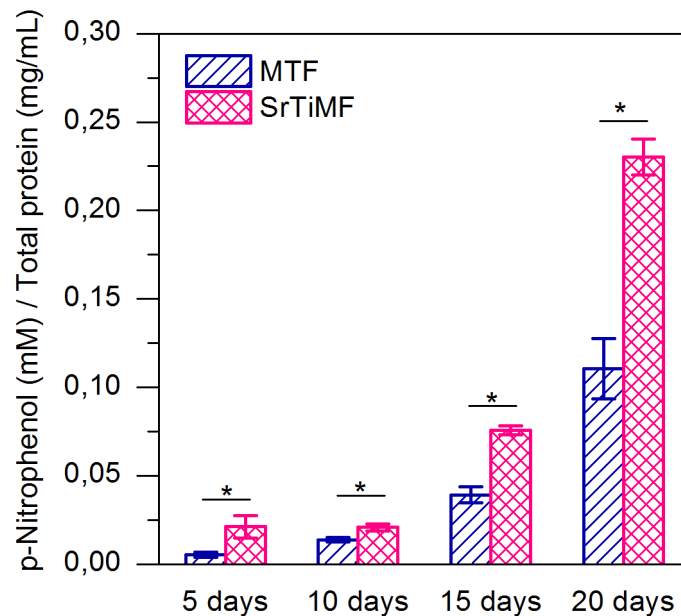


Figure VI-9. Alkaline phosphatase activity after 5, 10, 15 and 20 days of MC3T3-E1 pre-osteoblastic cell culture in osteogenic medium on MTF and SrTiMF. * means the difference is statistically significant ($p < 0.05$).

3.4. Conclusions and perspectives

SrTiMFs display a porous and accessible mesoporous structure. Around 20 % of strontium has been incorporated in the MTFs, which is the highest value for Sr in mesoporous titania reported. Moreover, Sr and Ti are homogeneously distributed in the mesoporous structure without any phase segregation.

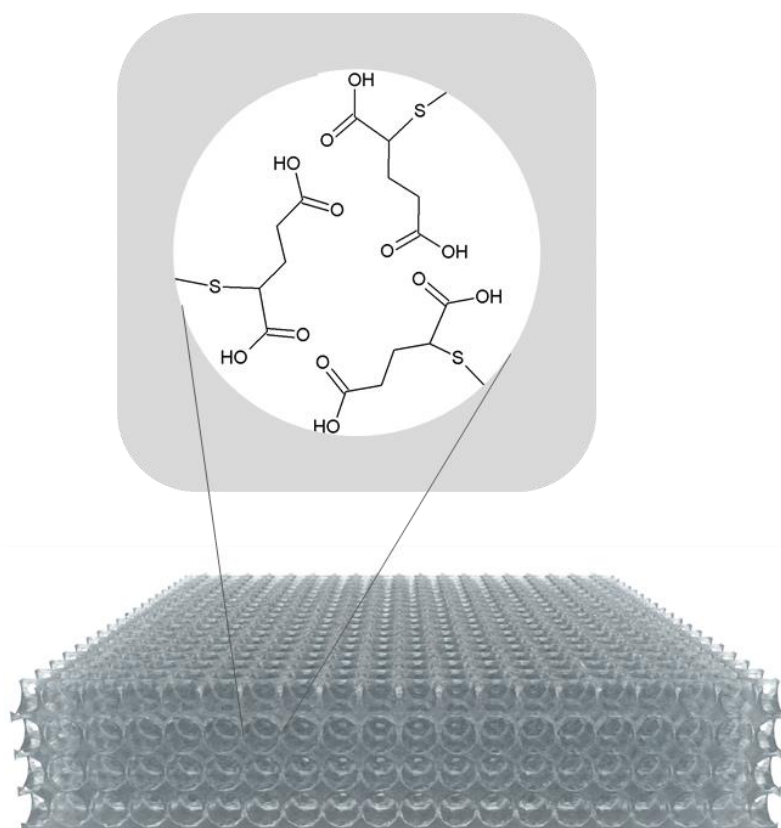
The high porous volume of around 30 % results in a large interface for strontium exchange with the media since pores are accessible for water as demonstrated by EEP measurements. At physiological pH in 10 mM PBS 44 % of the strontium present in the films is released within 8 h.

SrTiMFs improve MC3T3-E1 cell adhesion and proliferation if compared with MTFs resulting in more elongated cells with more defined stress fibers and focal points. Cell differentiation is enhanced in a 100 % after 3 days if strontium is present in the mesoporous structure.

This chapter shows that it is possible to synthesize doped mesoporous titania films with a high concentration of bioactive ions such as strontium and with a large surface area for ion exchange, due the mesoporous structure. Films display mechanical properties compatible with bone and can be easily assembled on top of titania implants with high potential for increasing osseointegration, specially at early stages after implant surgery.

VII. CHAPTER 4

COOH-functionalized Si and Ti mesoporous films to complex metallic ions



4.1. Motivation

Oxide-based mesoporous hybrid materials (MHMs) display the large surface areas and tunable pore sizes of mesoporous materials, the mechanical and thermal stabilities of an inorganic support, and are chemically functionalized with organic moieties. Organic molecules included within the oxide provide a mean to tailor the pore surface properties, such as hydrophobicity, polarity, catalytic activity as well as optical and electronic features. Thus, MHMs carry the potential for many applications in catalysis, chemical sensing, adsorption, contaminant immobilization, and drug or gene delivery.^[137,378,379] MHMs in the form of thin films are particularly interesting because they can be easily removed from reaction media and they are easily processable, allowing facile production of devices.^[380]

The incorporation of organic functionalities within porous oxides has attracted the increasing attention of the scientific community since the early development in mesoporous materials' synthesis. Two grafting routes are commonly used for organic fabrication: post-grafting (post-functionalization) or co-condensation (one-step approach).^[137,380] In the first case, the functionality is grafted to the material after consolidation of the mesostructure through vapour deposition or solution impregnation. The modification is established through the generation of new bonds between Si–OH or M–OH surface groups and the functionalization agent. The co-condensation method involves the mixing of inorganic precursors with a precursor that bears the organic functionality in the presence of the template; organosilanes are generally used for this approach. Because the meso-structuration and functionalization take place simultaneously, a portion of the introduced organic groups remains trapped inside the network, thus hindering their accessibility to the medium. The benefit of the co-condensation method is that it involves a reduced number of processing steps, provides homogeneous distribution of functional groups within the inorganic network, and induces minimal pore clogging.

In this chapter the functionalization of mesoporous titania with organosilanes displaying carboxylic groups that can complex Sr has been explored, producing an alternative to the incorporation of Sr in the titania matrix presented in **Chapter 3**. In this new approach Sr has been complexed through carboxylates that have been anchored to the porous walls through post-functionalization. Again, taking advantage of the large surface displayed by the mesoporous films compared to the non mesoporous titania, the loading of the Sr is increased in a similar way. The design of titania with organosilanes displaying carboxylic groups is not direct and requires a significant optimization of fabrication protocols.

Initial work was performed with mesoporous silica films; carboxylated silanes were used for functionalization of mesoporous silica films. However, when using titania the carboxylic groups are capable to complex titania, and this complicates the one-step synthesis of films based on titania.^[381,382] Therefore, an alternative fabrication route was founded in which the vinylmethoxysilane (VTMS) was first included in the mesoporous titania network and modified after film synthesis with carboxylate groups through a photoreaction with the silanol.

The synthesis of mesoporous silica films functionalized with covalently bonded carboxylic groups by co-condensation is shown first. Carboxylic derivatized alkoxysilanes are obtained by photochemical radical thiol-ene addition (PRTEA), produced by clicking mercaptosuccinic (MSA) or mercaptoacetic thioacids (MAA). Different amount of organosilanes are used for the film synthesis. Electron microscopy, porosimetry measurements and Small Angle X-ray Scattering with two-dimensional detection (2D-SAXS) are used for the structural characterization of the film and to relate the degree of mesoporous phase ordering and the amount of organosilane added to the film. The incorporation of the functional groups is shown by X-Ray Photoelectron Spectroscopy (XPS) and Diffuse Reflectance Infrared Fourier Transform Spectroscopy (DRIFTS). The availability of the COOH groups for further chemical modification is demonstrated by DRIFTS following the changes in the typical carbonyl IR bands during proton exchange and Pb^{2+} metal complexation. This simple methodology generates COOH-modified silica thin films in one step, without the need of hard reaction conditions or deprotection steps. Functionalization with carboxyl groups brings a pH-dependent switch-ability to the pore surface that can be used for multifunctional mesoporous materials design.

Titania based mesoporous films grafted with carboxylates cannot be synthesized in one step due to the complexation of the titanium by carboxylic groups, which will impact on the mesoporous structure and eventually limit the availability of carboxylates.^[381,382] VTMS is co-condensed with titanium tetrachloride in order to obtain vinyl-functionalized Ti-Si hybrid mesoporous films. By post-grafting the MSA is anchored through PRTEA to the vinyl groups functionalizing the surface with carboxylic groups. Same methodology is used to study the structure of the films and show the incorporation of the functional groups. Sr^{2+} complexation is assessed by XPS and DRIFTS measurements.

Strontium release is followed by Inductively Coupled Plasma Mass Spectrometry (ICP-MS). Cell proliferation and differentiation experiments are carried out using MC3T3-E1 pre-osteoblastic cell line, the CCK-8 dehydrogenase activity assay and by measuring the alkaline phosphatase (AP) activity at different time periods. Actin filaments and vinculin are labelled using the FAK-100 kit.

4.2. Experimental section

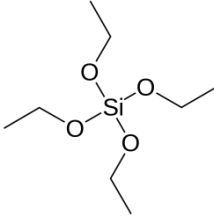
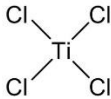
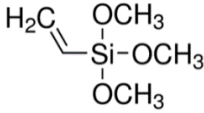
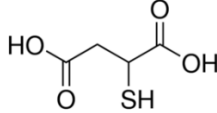
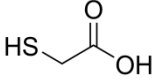
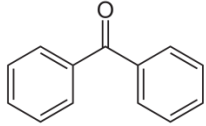
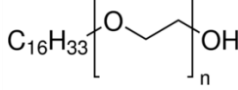
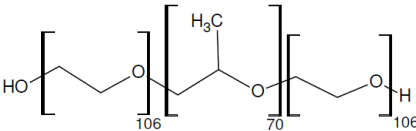
Reagents	Name	Abbreviation	Chemical structure
Si precursor	Tetraethyl orthosilicate	TEOS	
Ti precursor	Titanium tetrachloride	TiCl ₄	
Si-Vinyl precursor	Vinylmethoxysilane	VTMS	
Carboxylic Acids	Mercaptosuccinic acid	MSA	
	Mercaptoacetic acid	MAA	
Photoinitiator	Benzophenone	Ph ₂ CO	
	Brij 58	B	
Templates	Pluronic F127	F	

Table VII-1. Reagents used for the synthesis of mesoporous silica and mesoporous titania films functionalized with carboxylic groups.

4.2.1. COOH-functionalized mesoporous silica film synthesis

To synthesize COOH-functionalized mesoporous silica films the carboxylic trialkoxysilane precursors were prepared first. 2-((2-(Trimethoxysilyl)ethyl)

thio)succinic acid, $(\text{MeO})_3\text{Si-MSA}$, and 2-((2-(trimethoxysilyl)ethyl)thio)acetic acid, $(\text{MeO})_3\text{Si-MAA}$, precursors were prepared as reported by Bordoni *et al.*^[143] Briefly, 1 equivalent of vinylmethoxysilane (VTMS) was added to a vial containing methanol solution of the desired amount of MSA or MAA (chosen according to the desired proportion of organic functions in the final material) and 0.15 equivalents of benzophenone (Ph_2CO) as photoinitiator. Reaction solutions were then irradiated under gentle stirring for 16 hours, using a 15 W, 18" long black-light lamp ($\lambda_{\text{max}} = 352 \text{ nm}$). The precursor's reaction mixture was used in the preparation of the sols without any further treatment.

The sols to produce the functionalized mesoporous silica films were prepared in three steps: (1) TEOS, ethanol, and the template (Brij 58 or Pluronic F127) were mixed; (2) the reaction mixture of thio-ene addition was added drop wise under stirring, the carboxylated precursor added was varied from 5 % up to 20 % in molar proportion; and (3) HCl solution was added drop wise under stirring. The films synthesized with Pluronic F127® or Brij 58 will be referred as SiF and SiB, respectively. The chosen order allows the correct co-condensation reaction between the two silanes. The theoretical molar proportions of the sols were TEOS : Si-R : template : HCl : EtOH : H₂O = $1 - x : x : s : 0.28 : 24 : 5.2$, with $0 \leq x \leq 0.2$, R = MSA or MAA, and $s = 0.005$ for F127 or $s = 0.05$ for Brij 58. After its preparation, the sol was aged for different times in the 1–24 h range. **Table VII-2** shows the complete information about the studied systems.

Carboxylic acid	Template	Nominal % of functional silane	Aging time
MSA	F127	5	1 h
			5 h
			24 h
		12.5	1 h
			24 h
			24 h
	Brij 58	5	1 h
			24 h
			24 h
		12.5	1 h
			24 h
			24 h
MAA	F127	5	1 h
			5 h
			24 h
		12.5	1 h
			24 h
			24 h
	Brij 58	5	1 h
			24 h
			24 h
		12.5	1 h
			24 h
			24 h

Table VII-2. Description of explored systems regarding type of carboxylate function, surfactant, percentage of silane in the material and sample aging

Hybrid mesoporous $\text{Si}_{1-x}(\text{SiR})_x\text{O}_2$ films were synthesized by dip coating, applying the EISA approach. A withdrawal speed of 3 mm/s was used to deposit the films onto glass slides. Immediately after synthesis, the films were placed in a humidity-controlled chamber at 50% relative humidity (obtained with a saturated $\text{Ca}(\text{NO}_3)_2$ solution in water) and kept there for 24 h. Afterwards, films were exposed to a gentle thermal treatment: 24 h at 60 °C, 24 h at 130 °C, and 2 h at 200 °C. Finally, the template was extracted by immersing the films for 2 days in pure grade ethanol.

4.2.2. COOH-functionalized mesoporous titania film synthesis

Mesoporous titania films (MTFs) were functionalized with carboxylic groups by post-grafting. The films were first synthesized with VTMS and then the carboxylic moiety was anchored to the films through the vinyl groups by click-chemistry. As a template Pluronic F127[®] was used. The fabrication of functionalized hybrid Ti-Si films with vinyl groups required the preparation of sols solution in three step process: (1) addition of TiCl₄ to EtOH (TiCl₄ : EtOH = 1 : 40 mol) under vigorous stirring at room temperature; (2) mix the TiCl₄ solution with ethanol and Pluronic F127; and (3) addition of VTMS to H₂O under stirring. The theoretical molar proportions of the sols were TiCl₄ : VTMS : F127 : EtOH : H₂O = 1-x : x : 0.005 : 40 : 10 with x₁ = 0.1 and x₂ = 0.2. Films with the vinyl group with x₁ = 0.1 and x₂ = 0.2 are referred as V10 and V20, respectively.

Hybrid mesoporous Ti_{1-x}(Si-Vinyl)_xO₂ films were synthesized by spin coating. Films were prepared in round glass coverslips. A drop of 30 μL of the sol was spin coated at 68 rpm for 30 seconds on glass slices. Immediately after synthesis, the films were placed in a humidity-controlled chamber at 50% relative humidity (obtained with a saturated Ca(NO₃)₂ solution in water) and kept there for 24 h. Then, they were subjected to a thermal treatment: 30 minutes at 60 °C, another 30 minutes at 130 °C and 2 h at 200 °C. Finally, the template was extracted by immersing the films for at least 2 days in pure grade ethanol.

To anchor the carboxylic group by click chemistry, the films are immersed in pure ethanol solution containing MSA 23.3 mM (C1) and 33.3 mM (C2) and Ph₂CO as photoinitiator in 0.15 equivalents in moles to MSA. Reaction was performed for 1 h under irradiation with a 15 W, 18" long black-light lamp (λ_{max} = 352 nm). After the reaction films were cleaned by immersing them 1 h in pure grade ethanol, 30 minutes in distilled water and 1 h in pH 3 aqueous solution adjusted with HCl.

4.2.3. Films characterization

Pores were visualized by TEM and 2D-SAXS patterns were obtained at an angle between the incident radiation and the sample of 3°. The atomic composition of the films was determined by XPS, to calculate the atomic ratio between Sulphur and Silicon, three different films for each sample were measured. Ellipsometric and EEP measurements gave information about films thickness and pore and bottleneck

diameters. Film porosity was obtained from the XRR data. STEM-EDX measurements determined Si/Ti relation in films based on titania with Si-Vonyl.

4.2.4. Pb²⁺ complexation study

For metal coordination studies in COOH-functionalized mesoporous silica films, the films were put in contact with a 0.4 mM Pb(NO₃)₂ aqueous solution for 5 min, washed with water and ethanol, dried, and then scratched. DRIFTS measurements were performed by depositing scratched films onto a KBr-filled sample holder. To observe the speciation and accessibility of the COOH group in the inorganic network, the films were dried for 10 min in a 130 °C oven and immediately after scratched; the spectrum was taken immediately to minimize the water adsorption from the environment. In the case of acidic treatment, films were set for 10 min in a chamber saturated with HCl vapour. Then, films were dried and scratched in a similar way, as with the untreated films.

4.2.5. Sr²⁺ complexation and release studies

To complex Sr ions to the titania films bearing carboxylate groups, 100 mM and 500 mM aqueous solutions of SrCl₂ were prepared by film immersion for 3 h. After one immersion in distilled water films were left to dry in air for XPS measurements. As controls MTF and hybrid films prior to the photoreaction to attach the organic functionalization were used, also immersed in SrCl₂ for 3 h. Samples were prepared by triplicate. The amount of strontium complexed and adsorbed was measured by XPS and atomic composition analysis. To assess ion complexation DRIFTS measurements were performed; films were dried at 60 °C after Sr²⁺ complexation.

The strontium release was studied by ICP-MS. Briefly, samples were cleaned immersing in ethanol, then in water and left to dry in air. They were placed in wells of 12 multiwell dishes with 2 mL PBS 10 mM and the strontium release was measured at 5, 15, 30 min, 1, 2, 6 h and 1, 2 and 7 days. As controls the release of Sr from MTFs was also studied. The released Sr in PBS is diluted to 5 mL in distilled water in 5 % HNO₃ for ICP-MS measurements. To measure the total amount of strontium, films were immersed in 2 mL HNO₃ overnight and then distilled water has been added til 5 % concentration of HNO₃ was obtained for ICP-MS measurements.

4.2.6. MC3T3-E1 cell biactivity experiments

Cell experiments were performed in COOH-functionalized hybrid films with complexed Sr. As control MTFs and MTFs filled with Sr were used. F-actin, nuclei and focal adhesions of the cells were labeled and visualized by CLSM to study cell adherence to the substrates. Alkaline Phosphatase Activity Assay Kit and the Bradford assay for total protein quantification were performed to study cell differentiation process at 5, 10, 15 and 20 days. All samples were evaluated in triplicate.

4.3. Results and discussion

4.3.1. COOH-functionalized Si mesoporous films

Two different alkoxy silane bearing carboxylic moieties, one with a short alkyl chain and one dicarboxylate, are synthesized by PRTEA; the reaction pathway is presented in **Figure VII-1**.

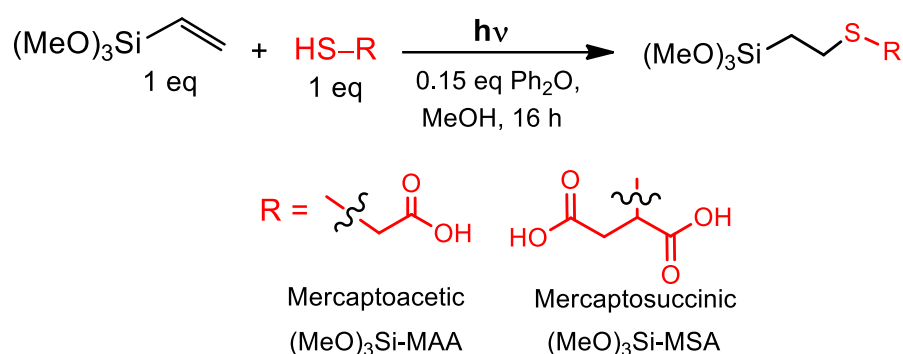


Figure VII-1. Scheme of the synthetic pathway to obtain alkoxy silanes with MAA and MSA.

In all tested conditions, the obtained materials were porous, as can be seen in the TEM images (**Figure VII-2** and **VII-3**). However, only the oxides with lower concentration of organic silane showed a high degree of order, as corroborated by TEM and 2D-SAXS. In fact, for all samples containing 5 % of organic moiety, 2D-SAXS patterns can be assigned to a body centered cubic $Im3m$ pore array, oriented with the (110) plane parallel to the substrate. This structure is obtained with F127 and Brij 58 as templates, and is similar to the structures obtained without organic functional groups.^[383] In two cases with 12.5 % of nominal organic silane, the same structure is obtained for both SiB MSA and SiF MAA. Further increase in the amount of COOH-modified silane to 12.5 % and 20 % impacts on the pore order. For F127 templated oxides, the 2D-SAXS patterns are ellipses, which correspond to locally

ordered (*wormlike*) arrays of mesopores. For Brij 58 templated samples, no pattern is observed, meaning that pores are not ordered. These observations agrees with previous studies,^[384] that showed that the presence of the organic functional groups generally limits the organic/metal molar ratio in which order is obtained, being 20 % the most usual limit.^[137,139,140] Aging the film for 24 h has no effect on the behaviour of the final structure .^[142]

Regarding the plane's distances obtained from 2D-SAXS patterns, it is interesting to note that the d_{-110} distance, the distance between the pores for the cubic structure in the xy plane, decreases when the amount of organic material in the film is increased, as can be seen for the SiF-MSA (**Table VII-3**).

Nominal % of organosilane	Aging	
	1h	24 h
0	14.8	
5	13.3	13.5
12.5	12.6	12.6
20	11.2	11.4

Table VII-3. d_{-110} interplanar distances (in nm) obtained from 2D-SAXS patterns for the SiF-MSA system.

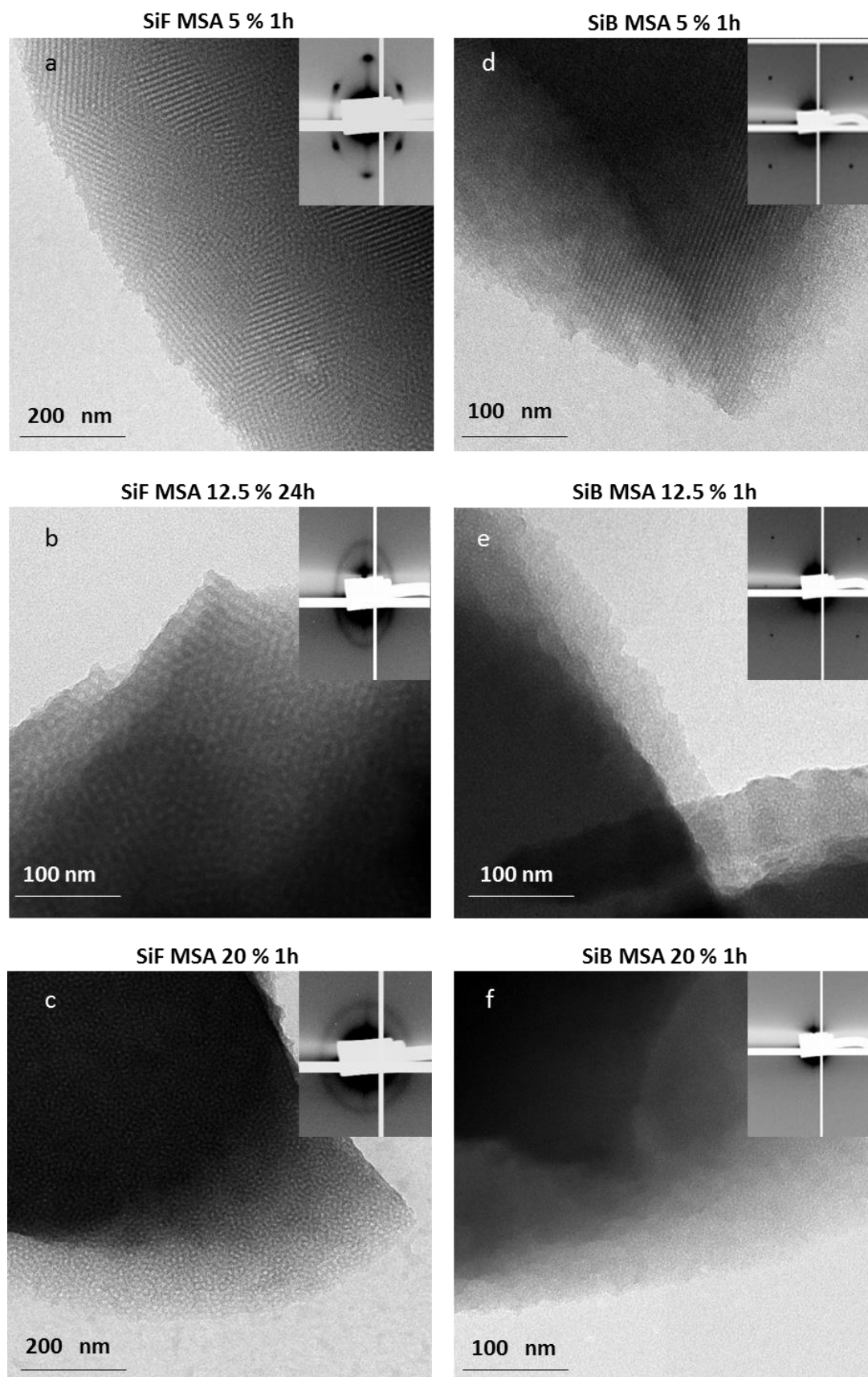


Figure VII-2. TEM micrographs and 2D-SAXS patterns of: a) SiF MSA 5 % 1 h, b) SiF MSA 12.5 % 24 h, c) SiF MSA 20 % 1 h, d) SiB MSA 5% 1 h, e) SiB MSA 12.5 % 1 h and f) SiB MSA 20 % 1 h.

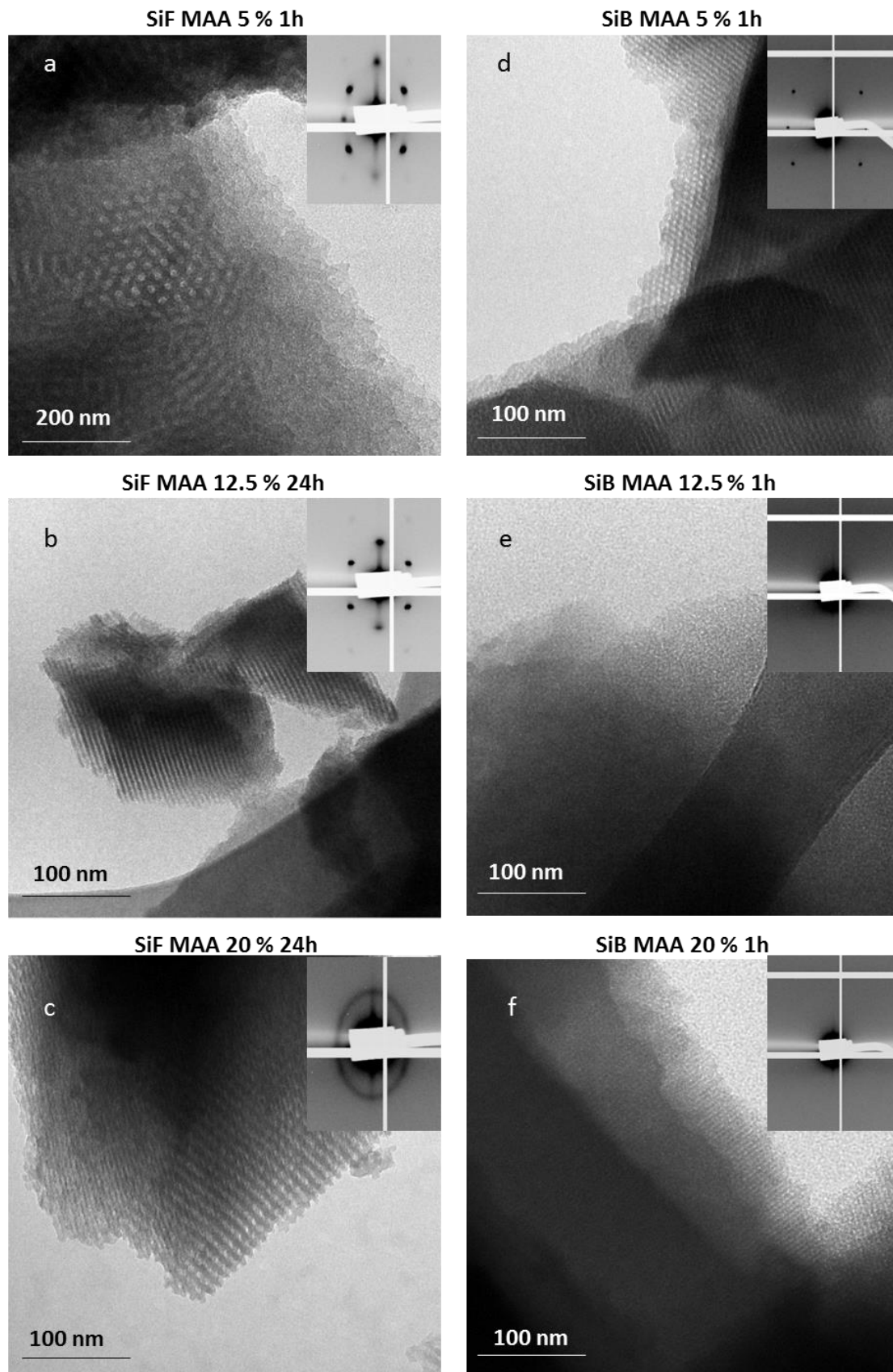


Figure VII-3. TEM micrographs and 2D-SAXS patterns of: a) SiF MAA 5 % 1 h, b) SiF MAA 12.5 % 24 h, c) SiF MAA 20 % 24 h, d) SiB MAA 5 % 1 h, e) SiB MAA 12.5 % 1 h and f) SiB MAA 20 % 1 h.

These results indicate that the diameter of micelles decreases with the increase of the concentration of the organic functionalities resulting in smaller interpore distances. This tendency suggests concentration-dependent interaction of templates and the organic moiety, affecting the size of the micelles and ultimately the pores size. A possible explanation is that the COOH moieties interact with the hydrophilic part of the templates diminishing the hydration of the formed micelles and decreasing their size.^[385]

Adsorption and desorption isotherms for SiF and SiB MSA 20% with 1 and 24 h of sol aging are shown in **Figure VII-4** and show the typical hysteresis loop for mesoporous materials. From the analyzed isotherms,^[262] results shown in **Table VII-4**, it can be concluded that the films presented an accessible porosity of around 20 % and pore diameters of around 4 nm and 2 nm for F127 and Brij 58, respectively. These values are in good agreement with previously obtained results for mesoporous thin films that were treated at moderate temperatures, followed by template extraction using organic solvents. This kind of treatment results in less deformed and interconnected pores than in the case of calcination, with smaller pore sizes and lower porosity.^[386,387]

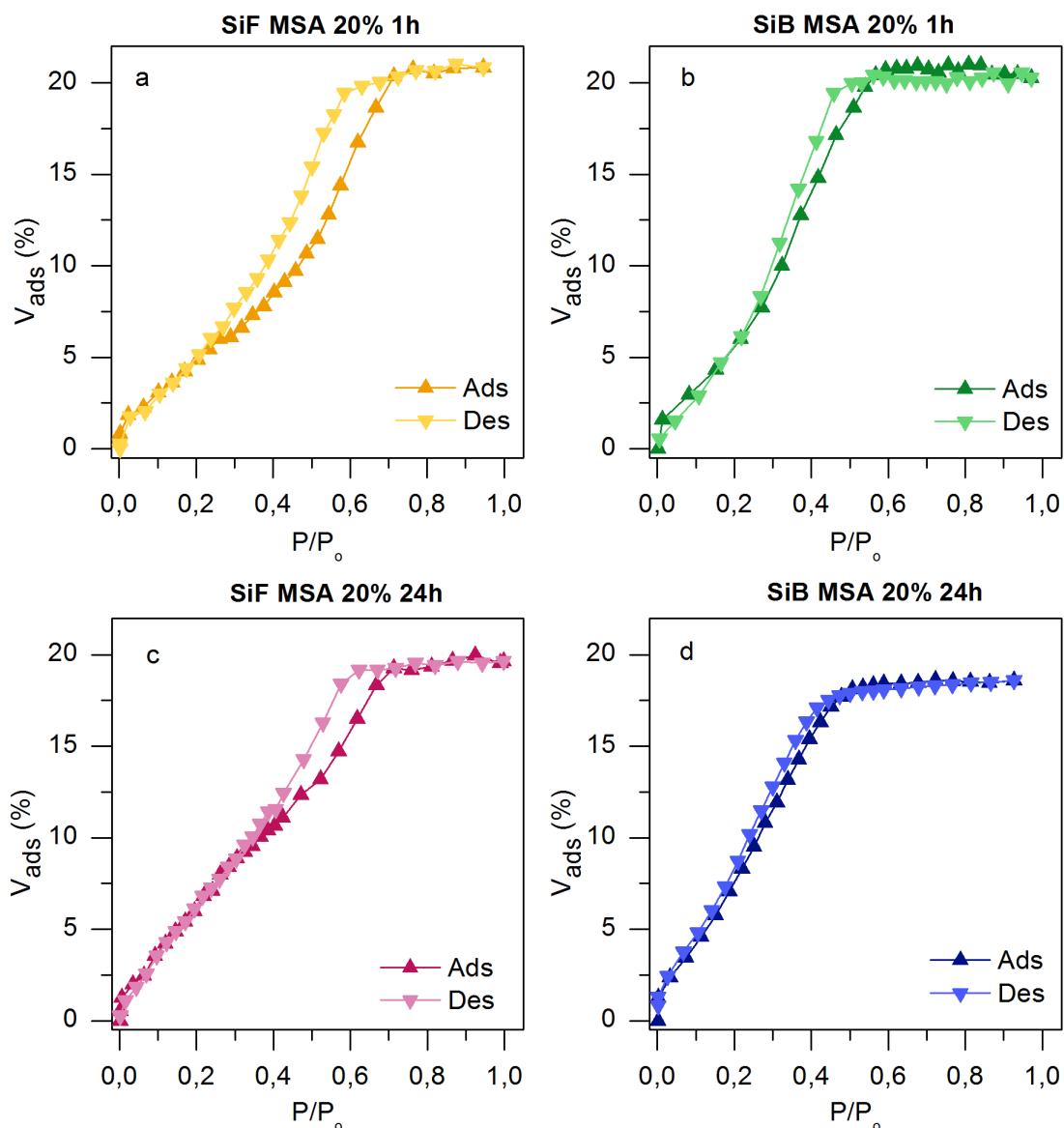


Figure VII-4. EEP results for a) SiF-MSA 20 % 1 h, b) SiB-MSA 20 % 1 h, c) SiF-MSA 20 % 24 h and d) SiB-MSA 20 % 24 h thin films.

Sample	Thickness (nm)	Porosity (%)	Pore diameter (nm)
SiB-MSA 20 % 1 h	254	20	2.7
SiB-MSA 20 % 24 h	225	19	2.1
SiF-MSA 20 % 1 h	285	21	3.9
SiF-MSA 20 % 24 h	295	20	4.7

Table VII-4. Data obtained from EEP measurements of thickness (nm), porosity (%) and pore diameter (nm).

The EEP confirms that the obtained films present an accessible porosity of around 20 % and pore sizes of 4 nm for F127 templated films and 2 nm for Brij 58. These values are in good agreement with results for mesoporous thin films treated at moderate temperature followed by template extraction using solvents.^[386,387]

To understand the final properties and potentialities of the materials one needs to understand chemical composition and speciation of the organic groups incorporated within the hybrid films. These results are particularly important for the case of mesoporous hybrid materials prepared with the co-condensation methodology, since it is highly probable that the organic functionalities will degrade due to thermal treatment. The XPS technique is used to characterize the chemistry of the film surface. Since the carboxylated precursors used for the hybrid films' synthesis contain thioether bonds, the incorporation of the functionalizing agent into the films was quantified by tracking the signal of Sulphur 2p and compared to the Silicon 2p signal. **Figure VII-5** shows representative XPS spectra of the hybrid films, all hybrid films analyzed confirm the presence of Si, O, C, and S, indicating the successful incorporation of carboxylated silanes.

Figure VII-6 and **Figure VII-7** show, the high resolution scan spectra for S and Si of the SiB-MSA 5, 12.5 and 20 % mesoporous systems of 1 and 24 h of sol aging, respectively. All spectra show the Si 2p signal around 103 eV. From the high resolution spectra, it can be seen that the samples containing 12.5 and 20 % of the carboxylated silanes show the presence of two peaks at 164.2 and 168.6 eV (**Figure VII-6c** and **e** and **Figure VII-7c** and **e**), whereas the films with 5 % show a single peak at 168.6 eV (**Figure VII-6a** and **Figure VII-7a**). The binding energy at around 164.2 can be assigned to $-C-S-$ and the one at around 168.6 eV can be associated to the oxidized Sulphur species $-C-SO_x-C-$.^[388] The oxidation of S was observed for every sample. Oxidation could be due to the thermal treatment performed in the presence of oxygen.

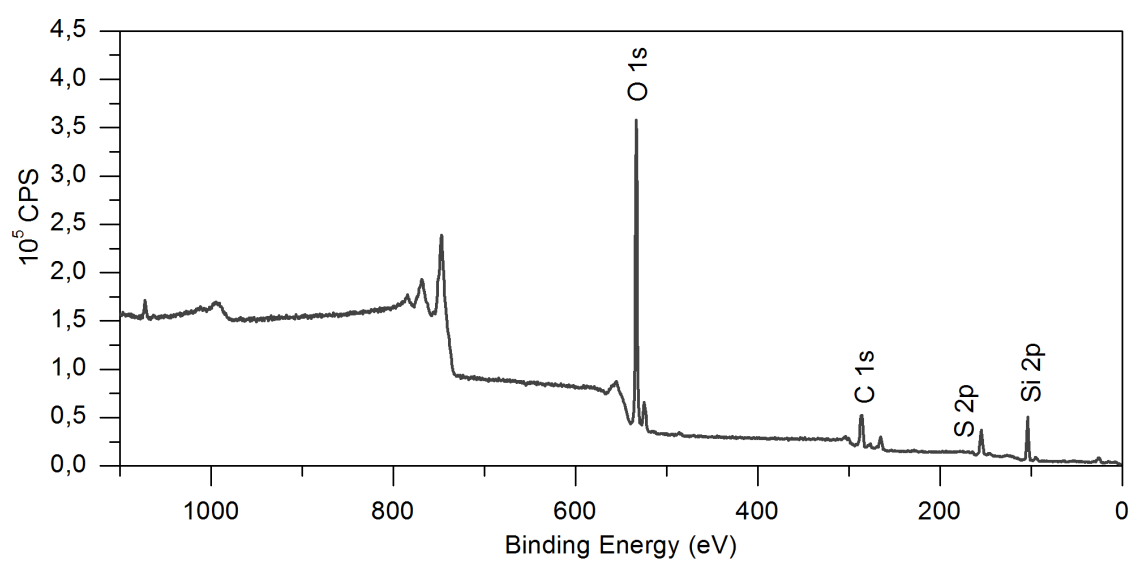


Figure VII-5. XPS spectra wide scan for SiB-MSA 20% 1 h system.

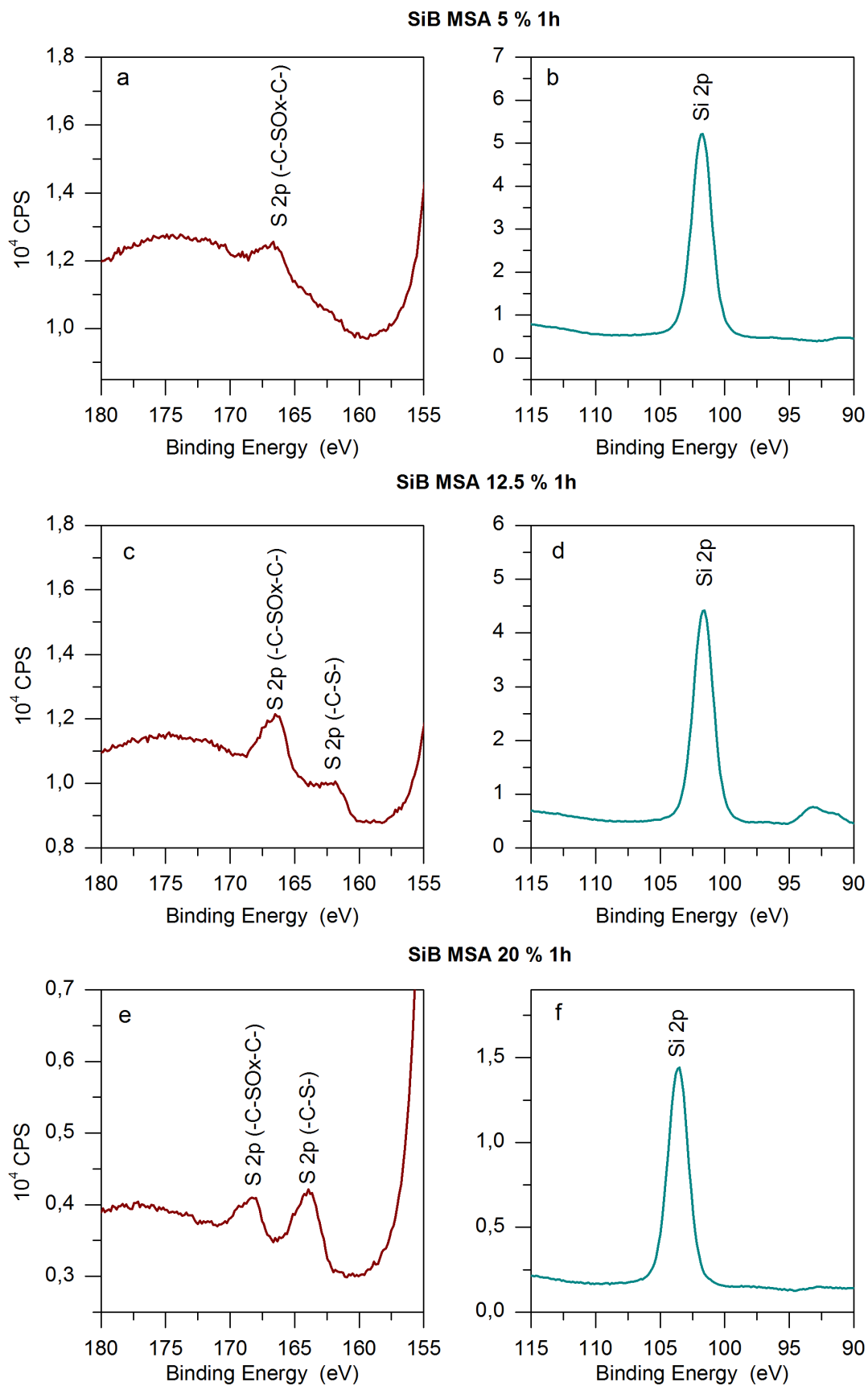


Figure VII-6. High resolution spectra of a) S of SiB MSA 5 %, b) Si of SiB MSA 5 %, c) S of SiB MSA 12.5 %, d) Si of SiB MSA 12.5 %, e) S of SiB MSA 5 % and f) Si of SiB MSA 5 % of films prepared with 1h aged sols.

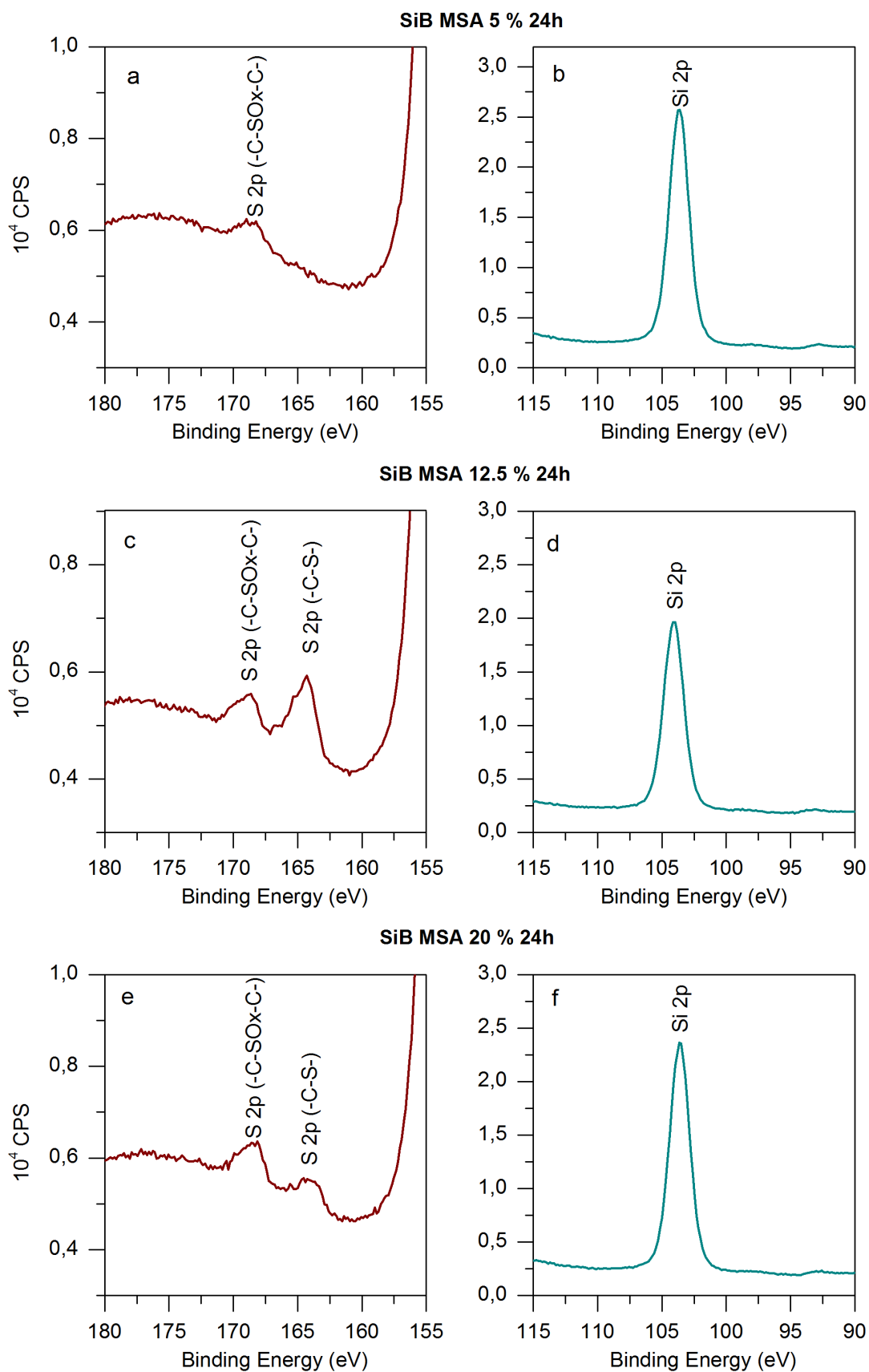


Figure VII-7. High resolution spectra of a) S of SiB MSA 5 %, b) Si of SiB MSA 5 %, c) S of SiB MSA 12.5 %, d) Si of SiB MSA 12.5 %, e) S of SiB MSA 20 % and f) Si of SiB MSA 20 % of films prepared with 24 h aged sols.

The XPS survey also provides the atomic percentage of S and Si in the samples, which can be related to the proportion of carboxylated organosilane incorporated into the films. Because each carboxylated silane molecule contains one Sulphur atom per Silicon the percentage of incorporated silanes can be equalled to the percentage of Sulphur. As shown in **Table VII-5**, increasing the fraction of functionalized silanes during film preparation, results in an increase in the final amount of Sulphur in the hybrid film. In addition, regardless of the sample considered, the final composition of the functionalizing agent in the film corresponds to around the 30 % of the nominal composition in the solution. This is presumably due to the degradation of the silanes during the thermal treatment at 200 °C and/or the template extraction in ethanol. The effect of sol aging is ruled out as a potential cause of degradation, because the binding energy for the Sulphur species and the incorporation of functional silanes in the final material is equivalent for different aging times, indicating that the silane remains stable for at least 24 h.

Sample	S/Si (%)	Sample	S/Si (%)
SiF-MSA 20% 1h	6.0 ± 0.4	SiF-MSA 20% 24 h	6.0 ± 0.7
SiF-MSA 12.5% 1h	4.5 ± 0.3	SiF-MSA 12.5% 24 h	4.8 ± 0.4
SiF-MSA 5% 1h	1.7 ± 0.5	SiF-MSA 5% 24 h	2.0 ± 0.1
SiB-MSA 20% 1h	6.0 ± 0.3	SiB-MSA 20% 24 h	6.2 ± 0.5
SiB-MSA 12.5% 1h	5.0 ± 0.6	SiB-MSA 12.5% 24 h	4.2 ± 0.5
SiB-MSA 5% 1h	0.1 ± 0.1	SiB-MSA 5% 24 h	1.3 ± 0.2

Table VII-5. Atomic Percentages for S and Si and S/Si Relation calculated from XPS spectra of the different systems containing the MSA moiety.

4.3.2. Pb²⁺ complexation study

Infrared spectroscopy was used to qualitatively analyze the presence and reactivity of COOH groups. **Figure VII-8** shows DRIFTS spectra of selected MSA modified samples after template extraction, compared to the spectra of unmodified films. The IR spectrum of SiF MSA 20 % 1 h (**Figure VI--8b**) shows the presence of characteristic signals of the carbonyl group, which is absent in the SiF film (**Figure VII-8a**): a shoulder band at 1716 cm⁻¹, associated to the carbonyl group's asymmetric mode of the carboxylic acid ($\nu_{C=O}$) protonated form, and another band at lower wavenumber (~ 1578 cm⁻¹).^[389] Both bands superimpose with the band of adsorbed water (scissoring of OH groups). The lower wavenumber band can be

attributed to C=O stretching of the acidic groups that interact by hydrogen bonding with chemical species on the oxide surface, as Tsai *et al.*^[390] have previously observed in powders by magic angle spinning NMR,^[390] or to the ionized form of the carboxylic acid.^[391] Besides the bands associated to COOH groups, the spectra shows the characteristics bands corresponding to the O–Si–O stretching (TO, TO₂, and TO₃ modes) of the silica network at 1300–950 and 800 cm⁻¹ zones and the Si–OH band at 850 cm⁻¹.^[392] Also, the stretching vibration bands corresponding to the aliphatic skeleton of silane and some residue of the template (ν_{C-H}) are exhibited at 2954, 2927, and 2858 cm⁻¹. The shift and intensity of C=O bands can be used to evaluate the reactivity of COOH/COO⁻ groups toward simple reactions, such as acid–base or metal complexation. Note, however, that as the films were obtained by the co-condensation method, not all carboxylic groups were available on the pore surface. When SiF-MSA 20 % film was exposed to HCl vapours (**Figure VII-8c**), the intensity of the band located at 1716 cm⁻¹ increased with the concomitant disappearance of the band located at around 1578 cm⁻¹, indicating that a fraction of the COOH groups are involved in acid–base equilibrium.^[389] Immediately after, this film was immersed in 0.4 mM Pb²⁺ aqueous solution. The spectrum (**Figure VII-8d**) shows a decrease in the intensity of the band located at 1716 cm⁻¹ and the appearance of a distinctive band at 1550 cm⁻¹ that is associated with coordinated carboxylic groups.^[389,391] Moreover, it can be seen that the 850 cm⁻¹ band associated with Si–OH does not suffer any changes after contact with acidic or Pb(II) solutions (**Figure VII-8c** and **d**). This indicates, as expected on the basis of previous results,^[143] that the acidity and ion exchange due to the bare silica matrix are negligible when compared to those due to the COOH groups, under these experimental conditions. Thus, these simple acid–base and coordination experiments show that the included carboxylic groups are available for simple chemical reactions such as proton interchange or Pb(II) ion trapping.

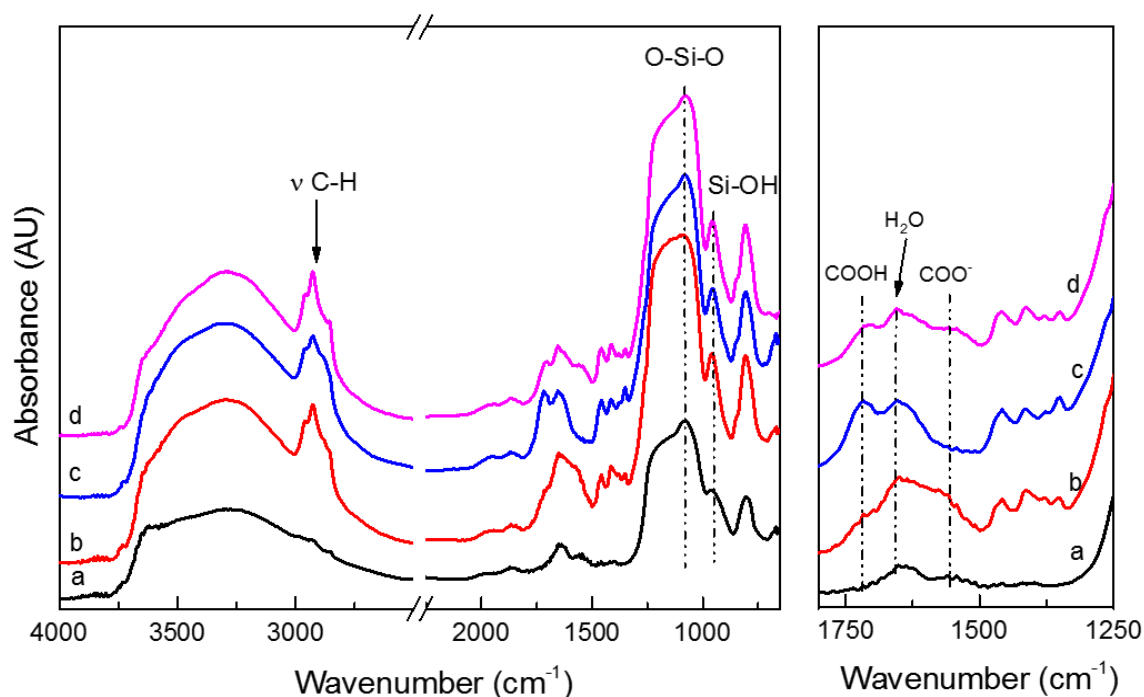


Figure VII-8. DRIFTS spectra of scratched films after extraction: a) SiF, b) SiF-MSA 20 % 1 h; c) SiF- MSA 20 % 1 h after contact with HCl and d) SiF-MSA 20 % 1 h after contact with Pb^{2+} . Left: wide spectra. Right: enlargement of the COOH region.

4.3.3. COOH-functionalized Ti based mesoporous films

As previously mentioned, if the COOH-grafted mesoporous film is based on titania, is not possible to synthesize the films through the same procedure followed to synthesize silica based mesoporous thin films grafted with carboxylic groups in one step, through co-condensation. Titanium is complexed by the carboxylic groups, which would not be available to complex other ions and they would lose their functionality.^[381,382] Therefore, a different approach was followed. Silanes were incorporated in the film during fabrication as before but bearing a vinyl group. Once mesoporous titania films are prepared with vinyl silanes in the pores, the MSA reacts with the vinyl groups gifting the pore surface with carboxylic moieties through post-functionalization in a two-step synthesis. The synthetic pathway is depicted in **Figure VII-9**.

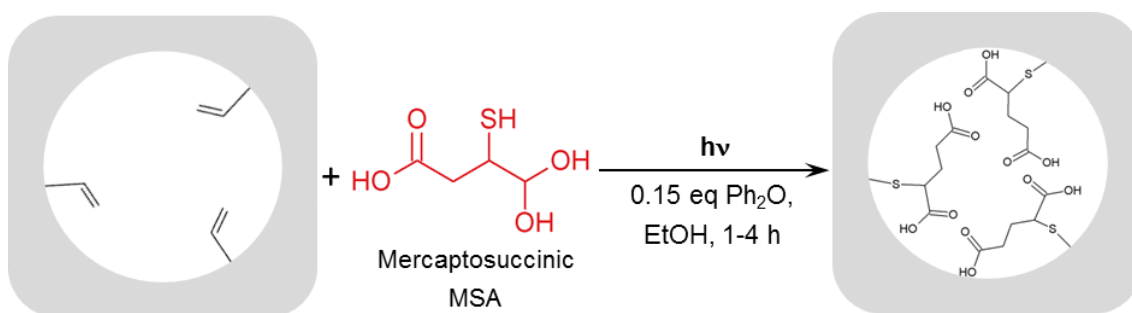


Figure VII-9. Scheme of the synthetic pathway to attach MSA to the vinyl groups present in the Ti-Si hybrid mesoporous films.

Samples are prepared with two concentrations of organosilane at concentrations of 10 and 20 % in moles to the total amount of titanium. **Figure VII-10** show two high resolution TEM (HRTEM) images and the EDX spectra. The Ti and Si can be detected, and as expected, the Si amount present in the film with 20 % of Si-Vinyl (~ 22.09 %) is the double of the Si in films with 10 % (~ 9.52 %). Then, reactions are performed with two concentrations of MSA (C1 = 23.3 mM and C2 = 33.3 mM). **Figure VII-11** shows the high resolutions spectra of Titanium and Sulphur, used to calculate the S/Ti molar relations shown in **Table VII-6**. S/Ti relation is the same in the 4 different samples, meaning that the amount of MSA, which reacts with the vinyl group, remains constant even if the concentration of vinyl groups is increased to the double in the mesoporous film. This suggests that the amount of vinyl groups available for reaction with MSA is similar regardless the amount of added VTMS. Therefore, the films containing 10 % of VTMS are selected for further experiments. In the same line, S/Ti ratio remains constant regardless MSA concentration.

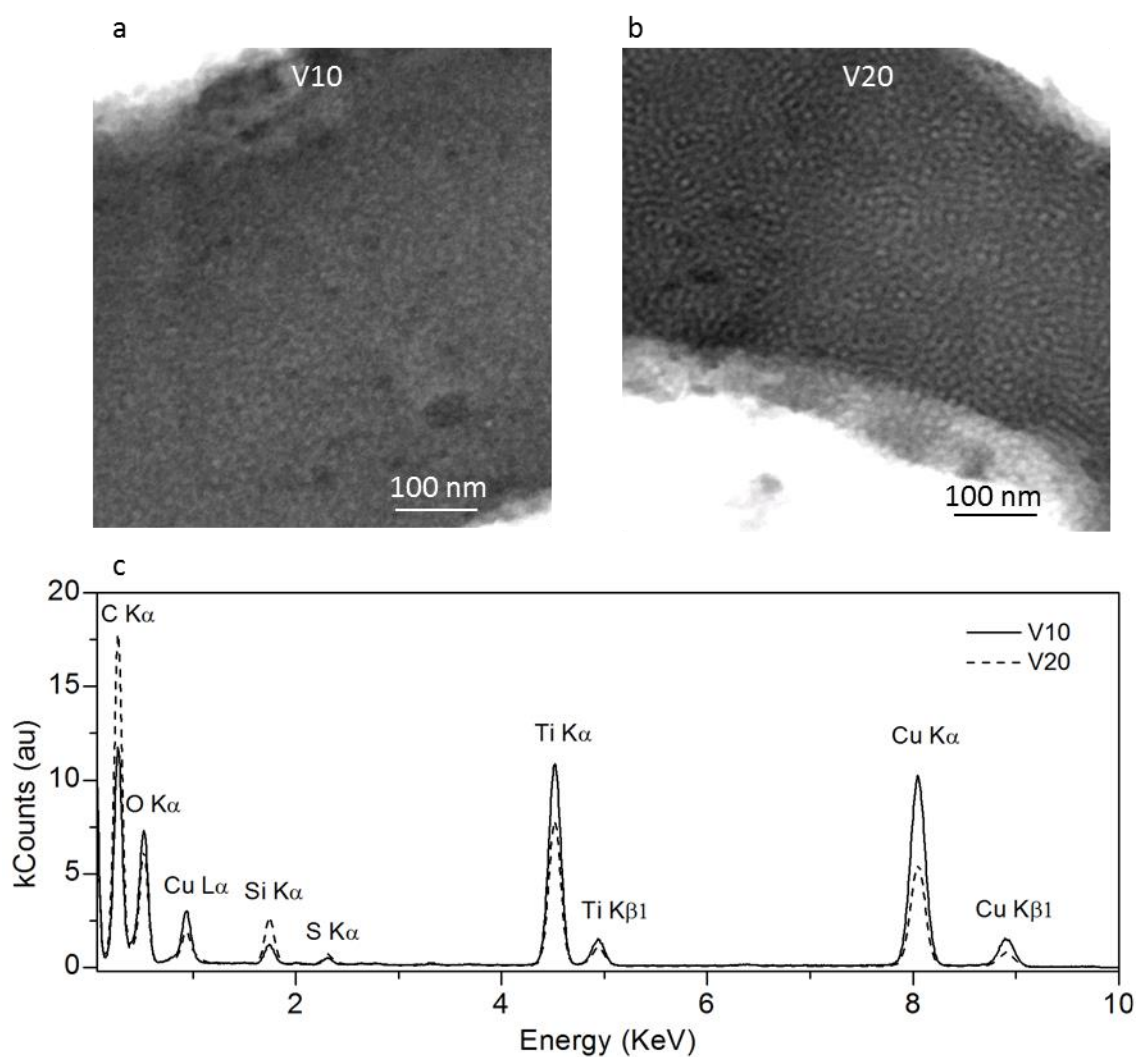


Figure VII-10. STEM images of MTF with a) 10 % and b) 20 % of Si -Vinyl and c) EDX analysis of the images.

Sample	S/Ti (%)
10 % Si-Vinyl C1	9.89 ± 0.43
10 % Si-Vinyl C2	7.97 ± 1.36
20 % Si-Vinyl C1	6.47 ± 1.79
20 % Si-Vinyl C2	10.05 ± 2.30

Table VII-6. S/Ti atomic relative percentages of mesoporous titania films with 10 % and 20 % of Si-Vinyl reacted with C1 and C2 of MSA obtained from XPS measurements.

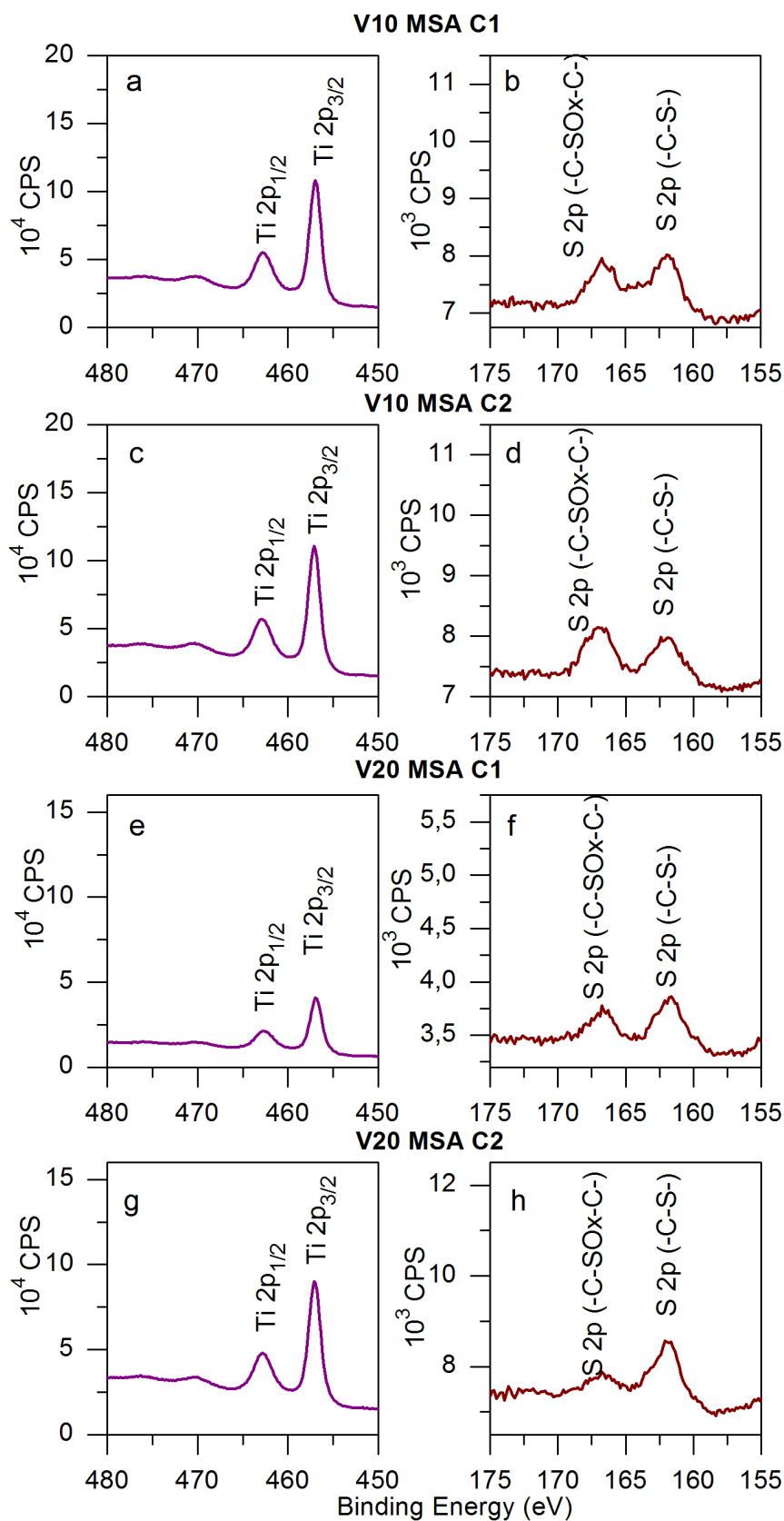


Figure VII-11. XPS high resolution spectra of a) Ti and b) S of MTF with 10 % of Si-Vinyl reacted with C1 MSA, c) Ti and d) S of MTF with 10 % of Si-Vinyl reacted with C2 MSA, e) Ti

and f) S of MTF with 20 % of Si-Vinyl reacted with C1 MSA and g) Ti and h) S of MTF with 20 % of Si-Vinyl reacted with C2 MSA.

4.3.4. Sr²⁺ complexation study

The incorporation of Sr within MTF containing 10 % Si-Vinyl and C1 MSA is the double than Sr in bare MTFs (**Table VII-7**). **Figure VII-12, VII-13** and **VII-14** show high resolution spectra of Ti and Sr with 100 and 500 mM of SrCl₂ of MTFs, MTF with 10 % Si-Vinyl and MTF with 10 % Si-Vinyl and C1 MSA, respectively. The initial concentration of Sr precursor (100 or 500 mM SrCl₂) has no effect on the final ratio of Sr to Ti in the films. However, the films functionalized with vinyl groups allowed for higher incorporation of Sr as compared to MTFs; the Sr/Ti ratio is around 10 and 15 %, respectively. As calculated in **Chapter 2**, the porosity of the MTFs is of 33 %, lower than the porosity of the MTF with Si-Vinyl, which could be the reason for a longer amount of Sr incorporated in the second type of substrates. What is more, if the films with Si-Vinyl are subjected to the photoreaction and the COOH groups are incorporated, the Sr amount increases by 33 %, and that is due to the complexation with carboxylic groups. Changes in the DRIFTS peaks (**Figure VII-15**) also confirm the Sr²⁺ complexation with carboxylic groups. In the presence of MSA bands appear at of 1610 – 1515 cm⁻¹ and 1495 – 1345 cm⁻¹, which correspond to asymmetric and symmetric vibrational modes of the coordinated carboxyl groups of the carboxylic acid ($\nu_{C=O}$).^[389,393] As mentioned, carboxylates can complex Ti, which could be the reason for the appearance of these bands.^[381,382] When the films are immersed in Sr, the maximum peak and the intensities of the asymmetric and symmetric mode of the coordinated carboxyl bands change, meaning that the complex is formed.²⁷ The band ranging from 950 to 650 cm⁻¹ is assigned to Ti-O bonds with a peak at around 800 cm⁻¹, confirming that the material is formed of titania.^[394,395]

Sample	Sr/Ti (%)
MTF 100 mM SrCl ₂	9.3 ± 0.6
MTF 500 mM SrCl ₂	11.9 ± 0.4
10 % Si-Vinyl 100 mM SrCl ₂	16 ± 4
10 % Si-Vinyl 500 mM SrCl ₂	15.2 ± 1.3
10 % Si-Vinyl C1 100 mM SrCl ₂	19.5 ± 1.1
10 % Si-Vinyl C1 500 mM SrCl ₂	19.4 ± 1.3

Table VII-7. Sr/Ti atomic relative percentages of MTF with 100 and 500 mM SrCl₂, MTF with 10 % of Si-Vinyl with 100 and 500 mM SrCl₂ and MTF with 10 % of Si-Vinyl reacted with C1 MSA with 100 and 500 mM SrCl₂ obtained from XPS measurements.

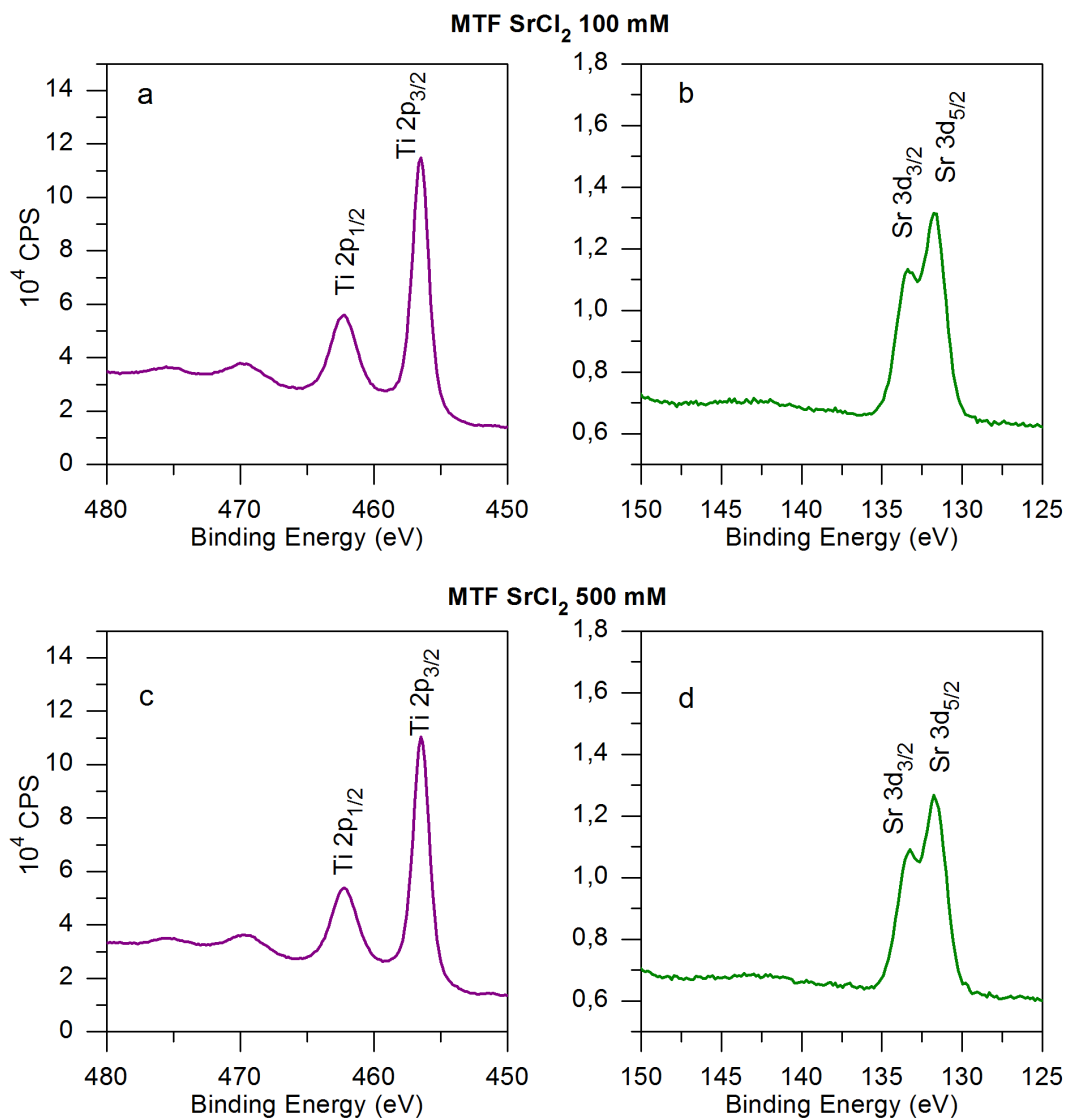


Figure VII-12. XPS high resolution spectra of a) Ti and b) Sr of MTF with 100 mM SrCl₂ and c) Ti and b) Sr of MTF with 500 mM SrCl₂.

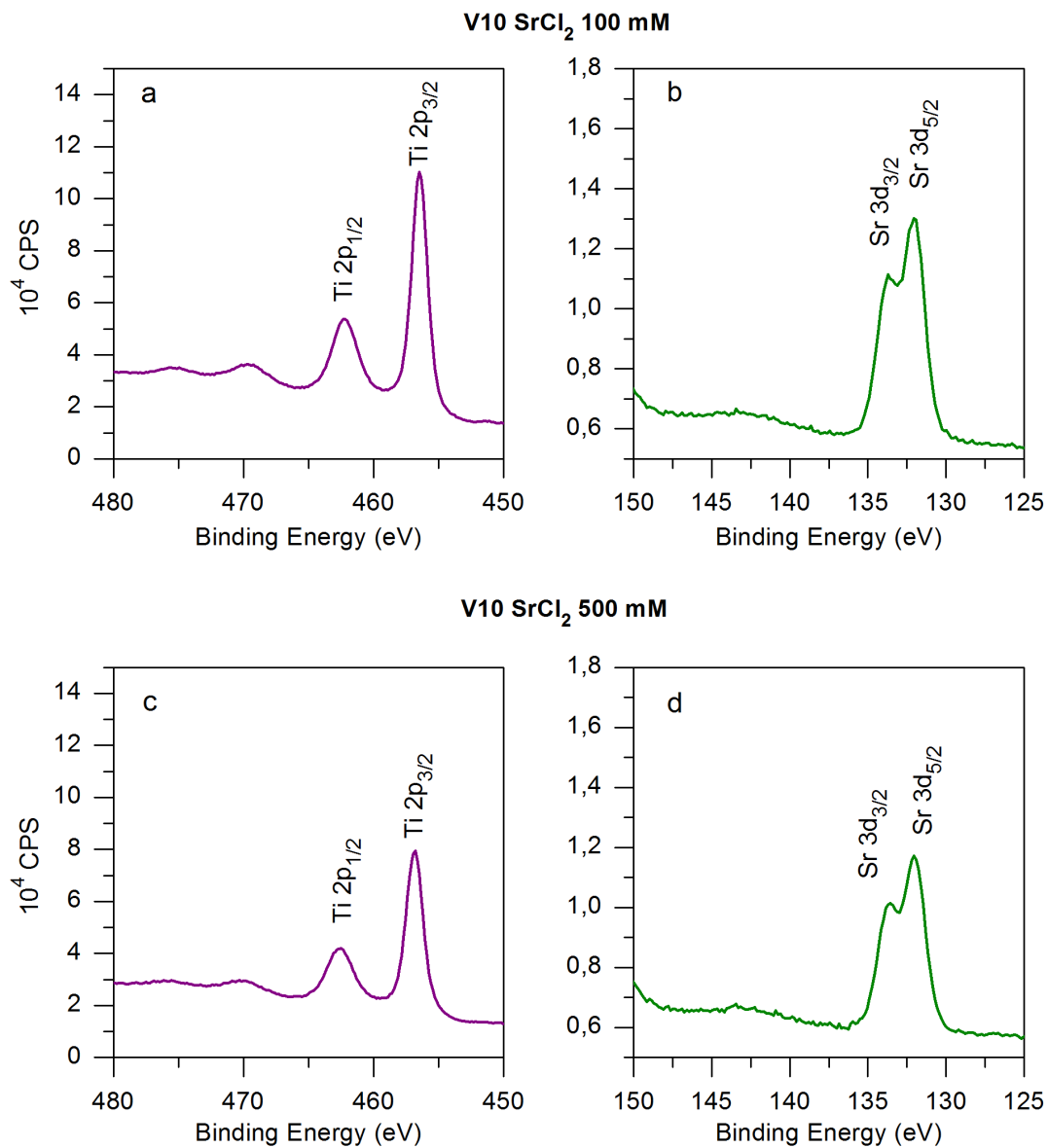


Figure VII-13. XPS high resolution spectra of a) Ti and b) Sr of MTF with 10 % of Si-Vinyl with 100 mM SrCl₂ and c) Ti and d) Sr of MTF with 10 % of Si-Vinyl with 500 mM SrCl₂.

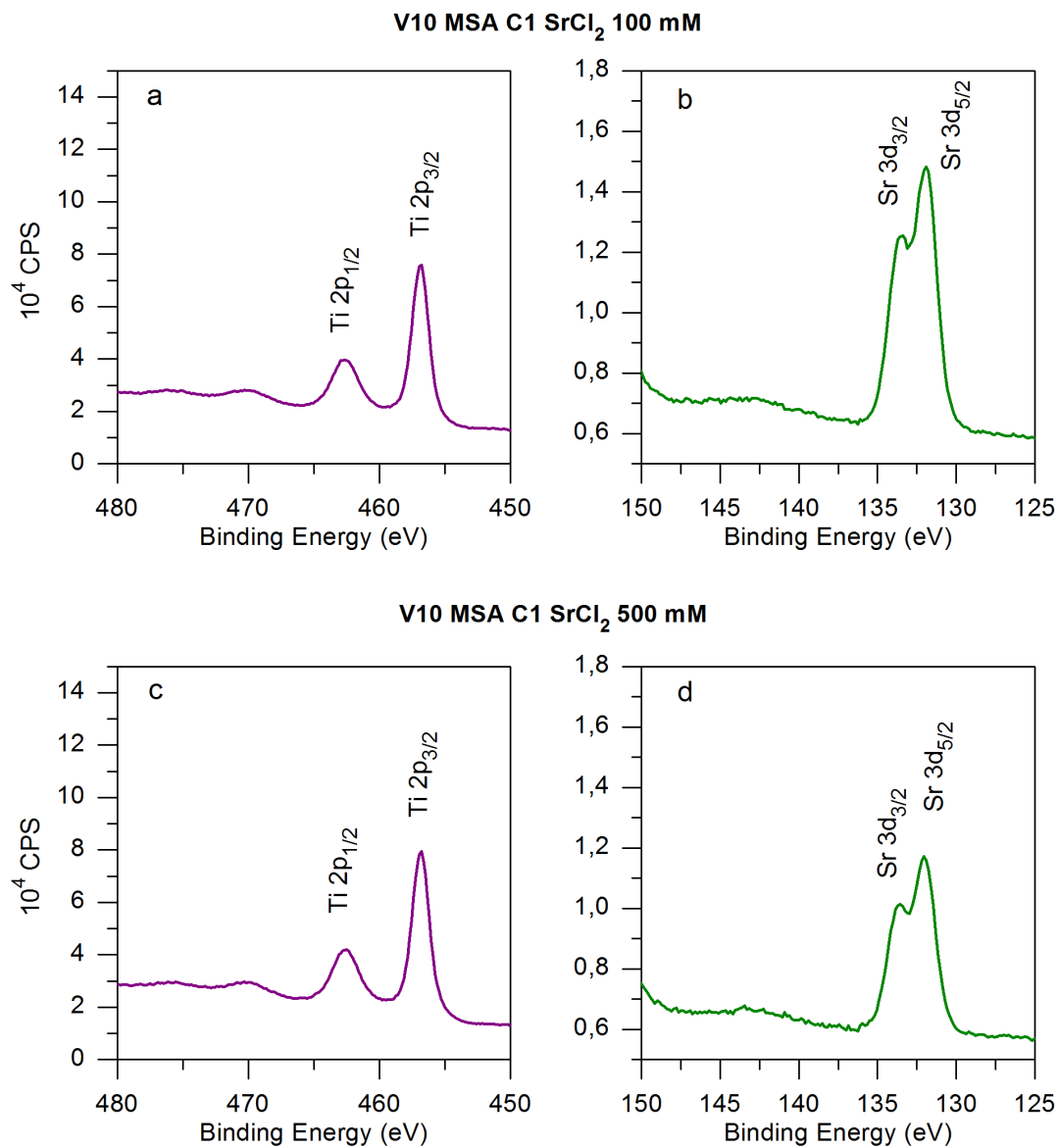


Figure VII-14. XPS high resolution spectra of a) Ti and b) Sr of MTF with 10 % of Si-vinyl reacted with C1 MSA with 100 mM SrCl₂ and c) Ti and d) Sr of MTF with 10 % of Si-vinyl reacted with C1 MSA with 500 mM SrCl₂.

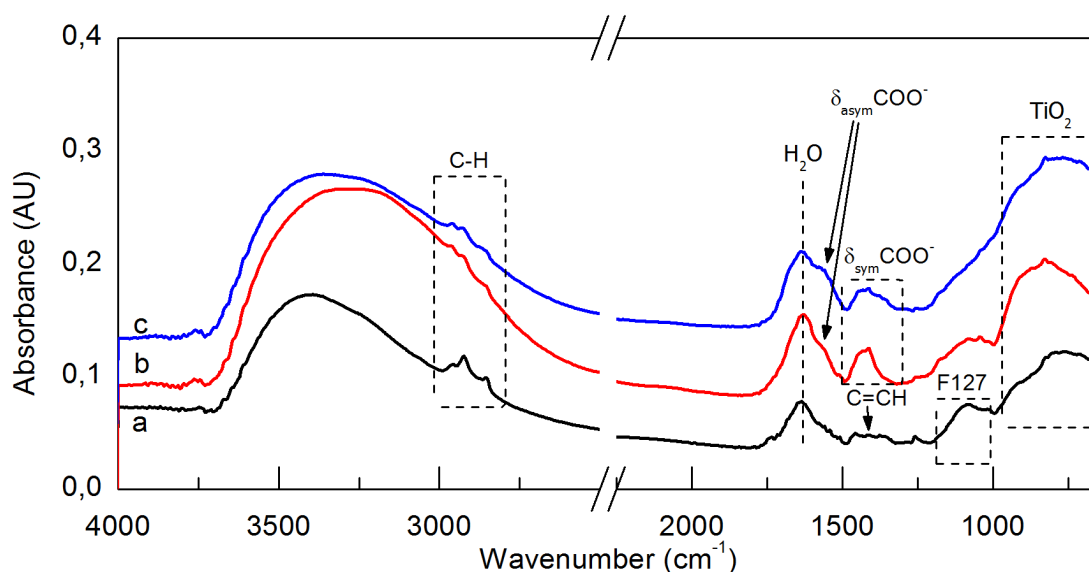


Figure VII-15. DRIFTS spectra of scratched films: a) MTF with 10 % Si-Vinyl, b) MTF with 10 % Si-Vinyl and C1 MSA and c) MTF with 10 % Si-Vinyl and C1 MSA after contact with Sr^{2+} .

Figure VII-16 shows TEM images of the MTF with 10 % of Si-Vinyl (**Figure VII-16a**), after the reaction with MSA (**Figure 16c**) and once the Strontium is complexed (**Figure VII-16e**). The structure and porosity of the films remain unaffected. The X-Ray Reflectometry (XRR) measurements (**Figure VII-16b, d** and **f**) confirmed the porosity of 42 % for the three samples, meaning there are no changes in the structure of the films. On the other hand, the SAXS pattern of the MTF with 10 % of Si-Vinyl (Insert **Figure VII-16a**) showed a halo without defined dots. The elliptic shape of the pattern suggests the presence of multiple domains of locally ordered pores.^[138] After the photoreaction with UV light, where functionalization of mesoporous surface with carboxylic groups takes place, characteristic dots are observed (Insert **Figure VII-16c**).

The Pluronic F127® template is removed by immersing the film in ethanol. Although it is generally agreed that this method is not as efficient as the calcination, it could not be applied here because of the possibility of losing the vinyl groups. It is possible therefore that not all the surfactant molecules are removed from the mesoporous if the ethanol extraction method is used. Besides, during the reaction to attach the MSA to the vinyl groups, the film is exposed to UV light, which is another technique to remove surfactants from mesoporous films.^[396–398] Thus, the appearance of dots in the SAXS pattern after the photoreaction may be due to the removal of remaining

surfactant upon extraction with ethanol. In **Figure VII-15** the C-O-C stretch ($1200 - 1000 \text{ cm}^{-1}$)^[394] is identified for the MTF with 10 % of Si-Vinyl, and after the photoreaction the intensity of the peaks are reduced. Calculated interplanar distances for MTF with 10 % of Si-Vinyl show an interpore distance of 15.12 nm and 9 in the (-110) and (110) planes, meaning there is a 40.5 % volume contraction after the soft thermal process up to 200 °C.^[305] After the click reaction the interpore distance decreases to 13.26 (-110 plane) and 7.92 nm (110 plane). No differences in the structure of the film are observed after this is exposed to the photoreaction or after the complexation with strontium.

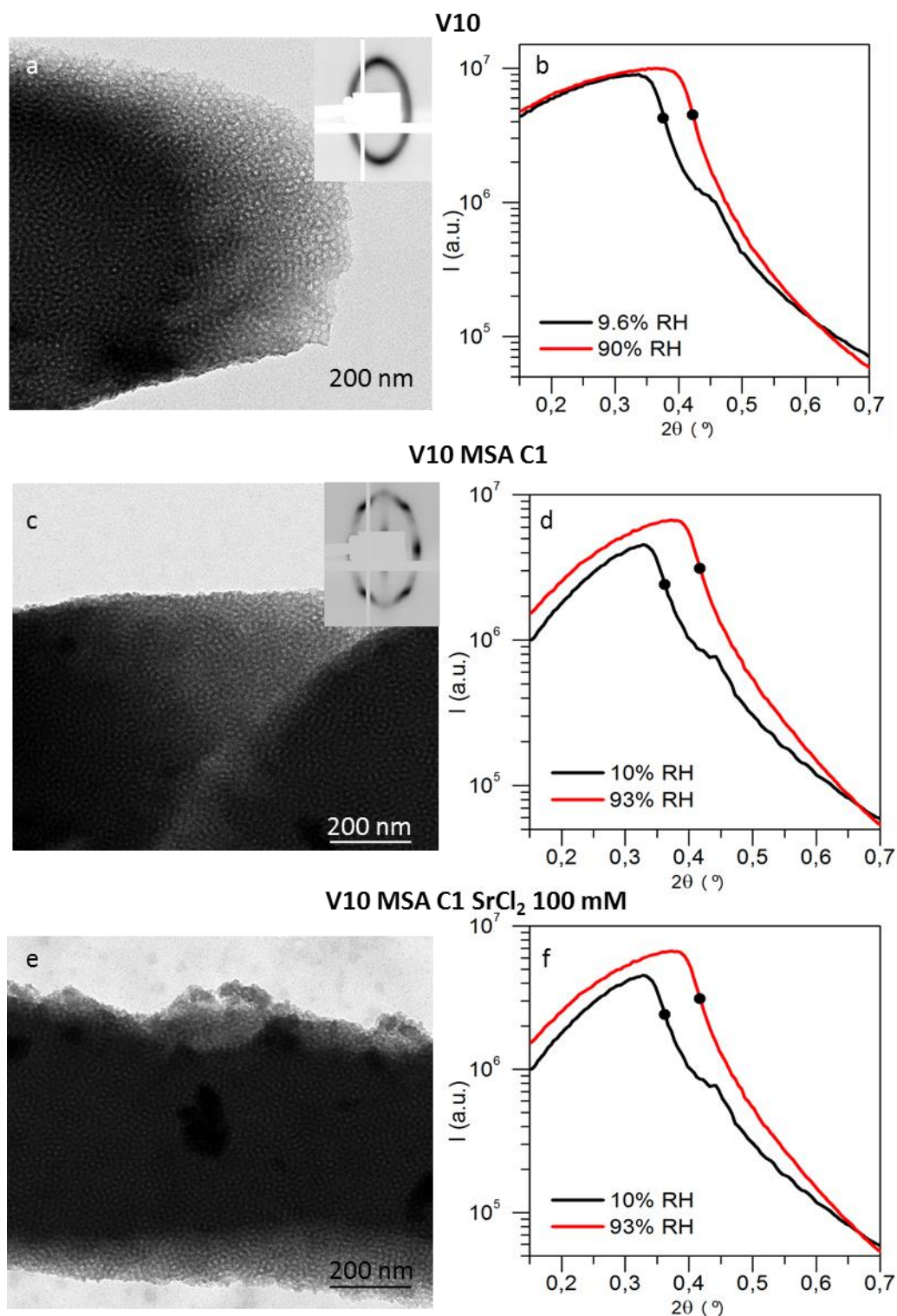


Figure VII-16. Characterization of MTF with 10 % Si-Vinyl, reacted with C1 MSA and then with 100 mM SrCl₂. Characterization through TEM (a, c and e), 2D-SAXS patterns (insert in a and c) and XRR (b, d and f).

4.3.5. Sr²⁺ release study

After 3h of reaction with 100 mM SrCl₂, the total amount of Sr is calculated in MTF and MTF with 10 % of Si-Vinyl and MSA C1, which is of 6.06 ± 0.82 µg and 10.99 ± 0.52 µg, respectively. The release of Strontium in PBS was monitored by ICP-MS (Table VII-9, Figure VII-17), showing fast release of the Sr from MTF (Figure VII-17a). After 2h a plateau is reached at 70 - 80 % of the total Strontium inside the MTF being released. Importantly, the Sr release from the COOH-functionalized film is more progressive (Figure VII-17b). Initially a fast release takes place (2 hours) which is probably due to uncomplexed Sr, followed by a second phase that is much slower and over a week time, where a plateau in concentration is reached. The amount of Sr that is released after 7 days corresponds to 42 % of the initial Sr within the film.

Time	MTF		V10 MSA C1	
	Sr in the films (µg)	Released Sr (%)	Sr in the films (µg)	Released Sr (%)
0	6.06 ± 0.82		10.99 ± 0.52	
15 min	3.80 ± 0.91	62.63 ± 11.58	8.63 ± 0.22	21.45 ± 1.98
2 h	4.74 ± 0.21	78.24 ± 3.51	8.11 ± 0.15	26.17 ± 1.32
8 h	4.63 ± 0.32	76.35 ± 5.20	7.89 ± 0.55	28.54 ± 4.96
2 days	4.75 ± 0.33	78.45 ± 5.47	7.31 ± 0.40	33.52 ± 3.61
7 days	4.61 ± 0.15	76.01 ± 2.50	6.30 ± 0.35	42.66 ± 3.16
10 days	4.33 ± 0.52	71.43 ± 8.58	6.33 ± 0.50	42.37 ± 4.51

Table VII-8. Total amount of Sr present in the substrates and the percentage of released Sr over time from MTFs and MTFs with 10 % of Si-Vinyl reacted with C1 MSA previously immersed in 100 mM SrCl₂ for 3 hours measured by ICP-MS.

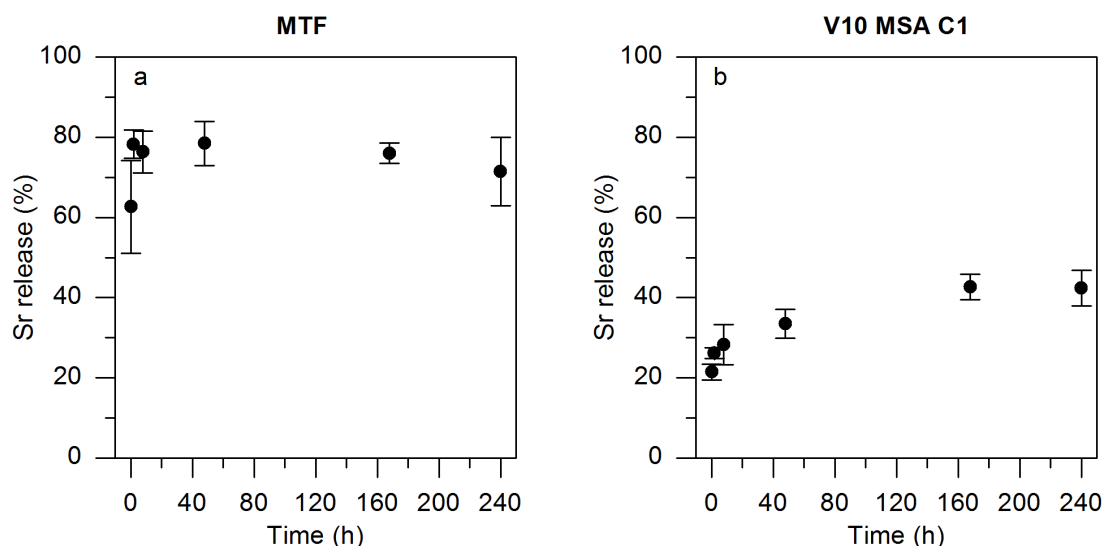


Figure VII-17. Released strontium percentage over time from a) MTFs and b) MTFs with 10 % of Si-Vinyl reacted with C1 MSA, previously immersed in 100 mM SrCl₂ for 3 hours measured by ICP-MS.

4.3.6. Biocompatibility and bioactivity evaluation

Next, cell adhesion on MTFs was evaluated. The degree of initial adhesion of cells determines how fast the proliferation, migration and differentiation will proceed. **Figure VII-18** and **Figure VII-19** show Confocal Laser Scanning Microscopy (CLSM) images of MC3T3-E1 pre-osteoblastic cells cultured on MTFs with Sr and MTFs with 10 % Si-Vinyl and C1 MSA with Sr, respectively. The vinculin is an adapter protein that is involved in the interactions between the focal adhesions (FA) of the cells and the extracellular matrix (ECM).^[310,311,313,314] While, actin filaments (F-actin) are stained with phalloidin (shown in red), vinculin is stained with FITC (shown in green). The nucleus is stained with DAPI as shown in the merged images. Detailed inspection of F-actin filaments suggests that cells have a similar size when cultured on different substrates (compare second row in **Figure VII-18** and **Figure VII-19**) even if they are compared with cells grown on MTF substrates (**Figure IV-7** from **Chapter 1**). It must be noticed that **Figure VII-18** and **Figure VII-19** show cells with higher filopodia,^[312] as compared to the cells grown on MTF substrates, although there is no significant difference in cell adhesion. The higher filopodia could be a consequence of the presence of Sr in the films. It is known that a good interaction of cell with a substrate leads to improved proliferation.^[310,313] MC3T3-E1 pre-osteoblastic cell proliferation experiments (**Figure VII-20**) shows an increased proliferation rate after 2 days of cell incubation between the glass substrates and

the MTF and MTF with 10 % Si-Vinyl and C1 MSA, both with Sr. After 3 days, there is no significant difference ($p > 0.05$) between the cell proliferation rate on MTFs substrates and MTFs with Sr. However, MTF with 10 % Si-Vinyl C1 MSA and Sr show a higher proliferation rate of cells ($p < 0.05$), as the amount of Sr released from the COOH-functionalized film is higher (**Table VII-8**). After one week, cells reach confluence, so, no differences are observed (**Figure VII-20**).

AP activity after 5 days remains constant for the three substrates (**Figure VII-21**), but after 10 days, the substrates containing Sr exhibited larger number of differentiated cell. After 15 days of culturing in osteogenic medium the differences between Sr-doped MTF and MTF with 10 % Si-Vinyl and C1 MSA with Sr are more pronounced, which is due to higher amount of Sr released from the second substrates that also occurs in a more progressive manner. As expected, after 20 days, the difference between the two substrates containing Sr is no longer appreciable

[399-402]

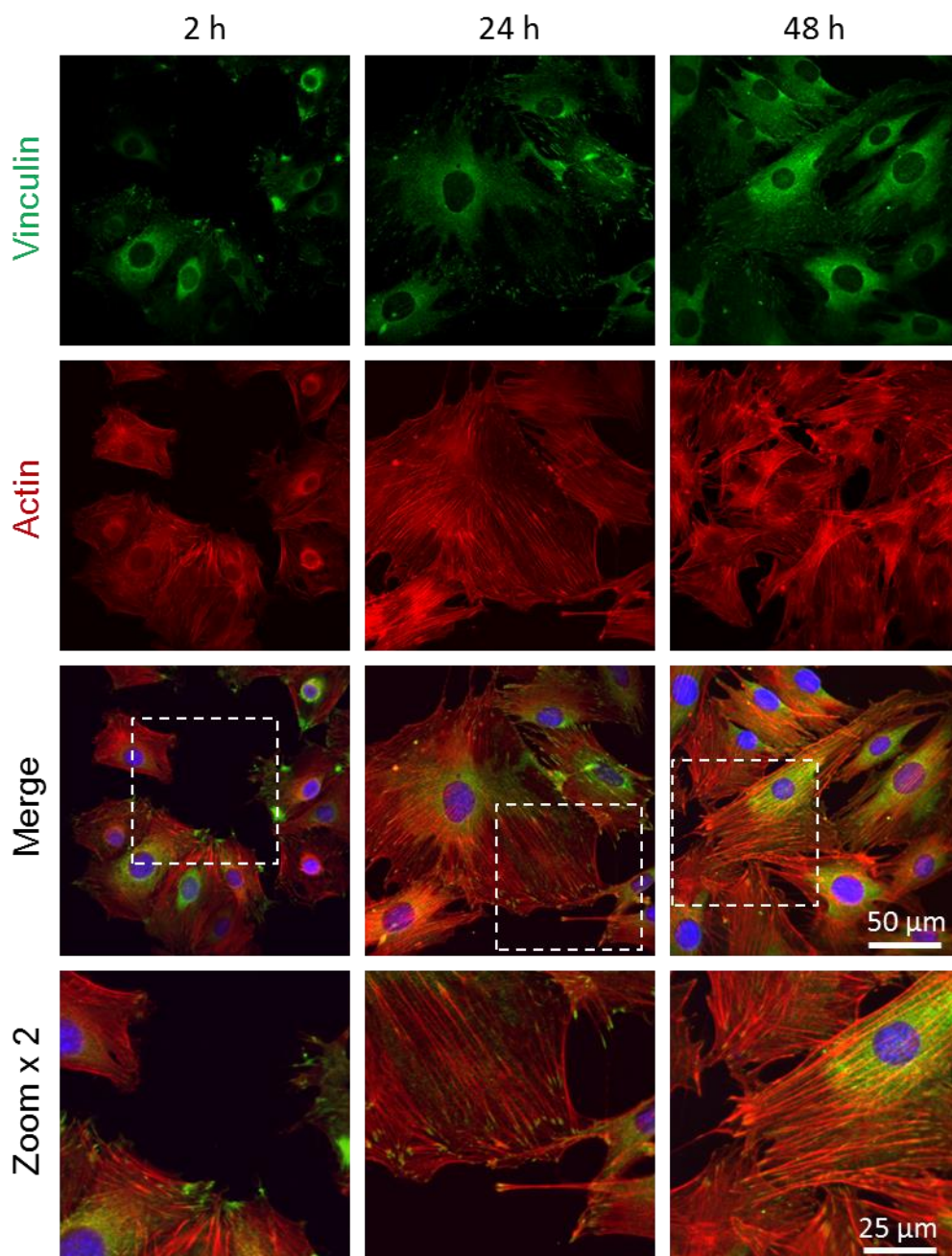


Figure VII-18. CLSM images of vinculin (first row), actin (second row), the merge of the actin, the vinculin and the nucleus (third row) and the zoom of the merge image (fourth row) at 2 h (first column), 24 h (second column) and 48 h (third column) of growth of MC3T3-E1 cell line on MTF with 100 mM SrCl₂ substrates at 63x.

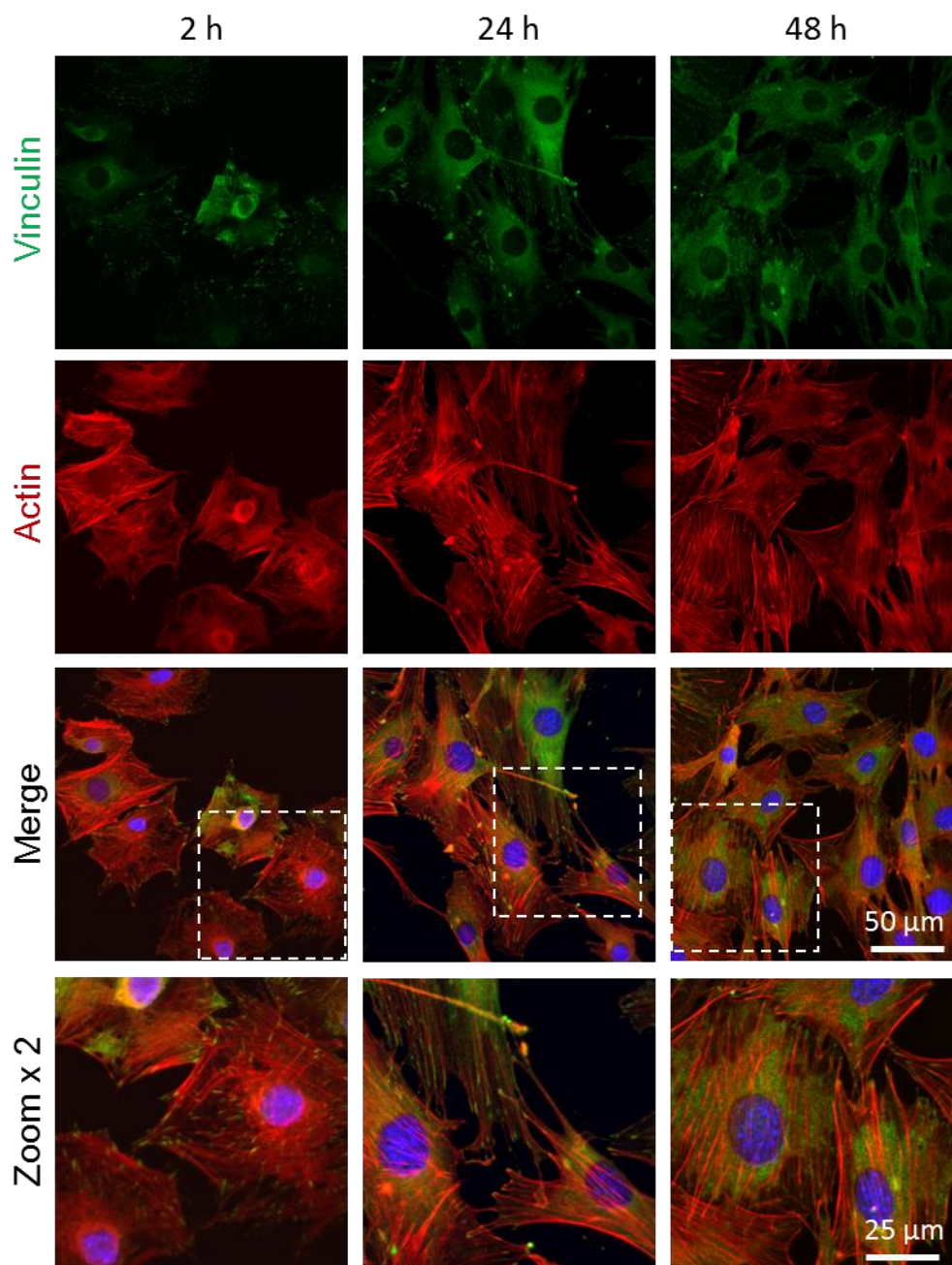


Figure VII-19. CLSM images of vinculin (first row), actin (second row), the merge of the actin, the vinculin and the nucleus (third row) and the zoom of the merge image (fourth row) at 2 h (first column), 24 h (second column) and 48 h (third column) of growth of MC3T3-E1 cell line on MTF with 10 % of Si-Vinyl reacted with C1 MSA with 100 mM SrCl₂ substrates at 63x.

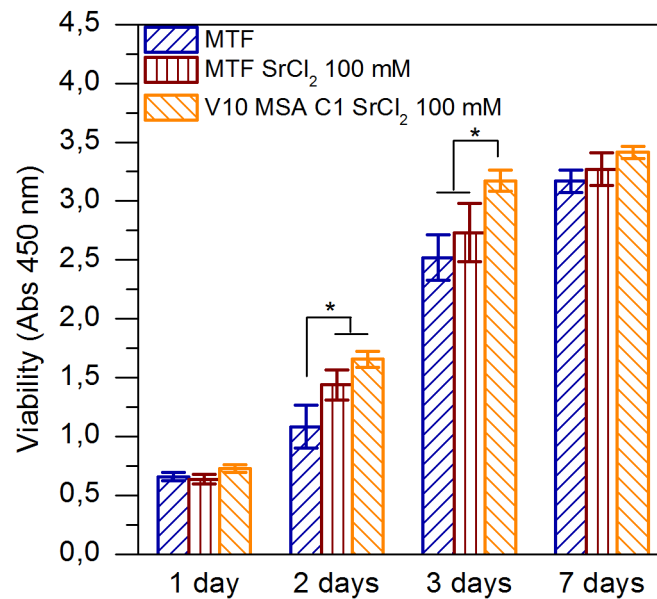


Figure VII-20. Proliferation of MC3T3-E1 pre-osteoblasts cultured on MTF, MTF with 100 mM SrCl₂ and MTFs with 10 % of Si-Vinyl reacted with C1 MSA with 100 mM SrCl₂ substrates for 1, 2, 3 and 7 days. * means the difference is statistically significant.

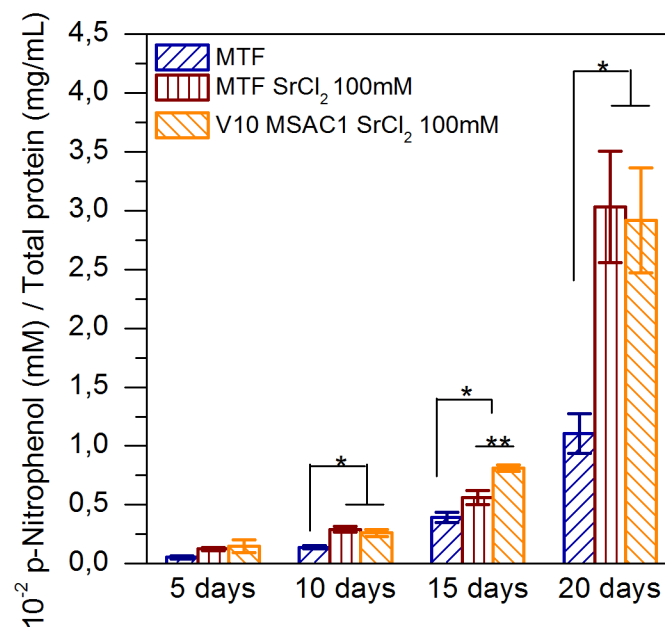


Figure VII-21. Alkaline phosphatase activity after 5, 10, 15 and 20 days of MC3T3-E1 pre-osteoblastic cell culture in osteogenic medium on MTF with 100 mM SrCl₂ and MTFs with 10 % of Si-Vinyl reacted with C1 MSA with 100 mM SrCl₂ substrates. * and ** mean the differences are statistically significant.

4.4. Conclusions and perspectives

In this chapter, direct incorporation of readily available COOH groups to mesoporous silica and titania thin films was demonstrated. Two different carboxylated organosilanes obtained by PRTEA were used, demonstrating the easiness of this reaction and the versatility of the chosen protocol to incorporate organic functions. Moreover, the two templates (F127 and Brij 58) used in the process showed identical successful results. Structural characterization demonstrated the generation of mesoporous phases whose degree of ordering depends on the amount of added organosilanes. In particular, low organosilane concentrations result in a body-centered cubic mesoporous ordering, whereas higher concentrations generate locally ordered structures. The incorporation of functional silanes was clearly demonstrated by XPS, showing that around 30 % of the nominal organosilane concentration is incorporated within the films.

The presence of COOH groups on the pore surface is confirmed by infrared spectroscopy alongside with its availability for further chemical modification. Clear changes in the typical carbonyl signals during proton interchange and metal complexation experiments were observed, indicating that chemical reactions can be performed on the modified mesoporous structure.

The proposed simple methodology allows for the synthesis of COOH-modified silica thin films in one step, without the need of harsh reaction conditions or deprotection steps. Moreover, as the material is obtained as a thin film, it can be easily incorporated in reaction media and/or integrated into devices. As COOH groups are expected to serve as binding sites for more complex molecules, such as proteins, enzymes, or ions, the presented results pave the way toward applications of such COOH-modified films, for example, as sensors or drug-delivery devices.

The synthetic pathway is extended to the functionalization with carboxylic groups of mesoporous titania films. A two-step synthesis is followed, with a pre-functionalization through co-condensation with VTMS, functionalizing the mesoporous films with vinyl groups. Films containing 10 and 20 % of organosilane have been synthesized. After the click reaction with MSA it has been demonstrated that the incorporation of COOH groups is the same for films containing a 10 or a 20

% of VTMS, so further experiments were performed with the first ones. Films have been shown to have locally ordered mesoporous structure.

Sr²⁺ complexation studies have shown that the amount of Sr embedded in the films containing COOH groups is the double than in bare MTFs. Moreover, and more importantly, the release profile of the Sr is more prolonged during time, which helps in the differentiation process. The release also shows an initial burst release which would help to enhance pre-osteoblast cell attachment and proliferation processes. Even if there are no appreciable differences in cell attachment if results are compared with MTFs with Sr, the proliferation rate is improved in the 3rd day of culture and the differentiation is also enhanced at day 15.

If the obtained results are compared to the ones obtained in **Chapter 3** for SrTiMFs, it can be concluded that this new approach offers a coating with higher Sr amount; 10.99 µg vs. 2.29 µg. Besides, the synthetic approach followed to obtain SrTiMFs is simpler than the one to synthesize COOH-functionalized titania films.

This chapter shows the possibility to complex bioactive ions in MTFs containing larger surface areas than titania surfaces to increase the interaction surface with the media and enhance ion release to obtain more effective results in pre-osteoblast proliferation and differentiation.

VIII. GENERAL CONCLUSIONS

Overall the research conducted in this thesis is focused on the functionalization of mesoporous titania films combining the use of antibiotics, growth factors and bioactive ions. Mesoporous films containing strontium and available carboxylic groups have been synthesized through spin coating and the EISA method. These films charged with antibiotics have demonstrated to be effective against *S. aureus* colonization and have been proven to promote implant osseointegration through pre-osteoblastic MC3T3-E1 cell proliferation and differentiation enhancement. Summing up the results from each chapter, the following conclusions can be drawn:

In **Chapter 1**, mesoporous titania films with a porous volume of 30.7 % were synthesized. They were used for the encapsulation of gentamicin and surface functionalized with rhBMP-2. Due to the porous structure of the film the gentamicin undergoes a progressive release; within the first 6 h the 36 % of the gentamicin was released, but then a second release phase lasting weeks took place. This gentamicin release kinetics is optimal for antibiotic administration after a surgery; moreover, the localized release of gentamicin avoids the problems from a low drug concentration at the implant site when antibiotics are administered orally.

The presence of the gentamicin and rhBMP-2 has been demonstrated with XPS and contact angle measurements. The combination of both resulted in an optimal coating for titanium implants. The release of gentamicin prevents *S. aureus* proliferation on the film surface, and the rhBMP-2 can enhance implant osseointegration and counteract negative side effects of gentamicin on cell proliferation.

In **Chapter 2**, a PEM based on PLL and PAA-gentamicin complexes has been assembled on top MTFs. The complex synthesis has been optimized in order to obtain complexes with stable size while the LbL assembly is conducted. Complexes for the PEM assembly were prepared in 500 mM NaCl at pH 4.5 by mixing 0.3 mg mL⁻¹ gentamicin and 1 mg mL⁻¹ PAA. These complexes were assembled alternatively on top of MTFs with PLL. In total 4 bilayers were deposited. The PEM showed an exponential growth, which can be related to the 'island model' of growth of PEMs described in previous works. The PEM is stable till pH 13, but at physiological pH

progressively releases the gentamicin. The release mechanism shows an initial burst release followed by a progressive release lasting weeks.

The PEM was effective against *S. aureus* infection, compared to the control, which consisted of a glass coverslip immersed in gentamicin, 3 orders of magnitude less of bacteria were able to form colonies.

In **Chapter 3**, hybrid mesoporous films have been prepared by incorporation of strontium chloride to the solution used for the synthesis of MTFs. The resulting SrTiMTFs had a 20 % of Sr, which was homogeneously distributed in the film structure. Due to the presence of pores, the surface area available for the interchange of ions is larger, thus, a high amount of Sr can be released to the media in contact with the film. The 44 % of the Sr present in the films is released after 8 h, and this enhanced MC3T3-E1 pre-osteoblastic cell adhesion to the surface. Cells resulted to show higher filopodia with more defined stress fibers, moreover, cell differentiation is increased in a 100% compared to cells grown on top of MTFs.

This chapter demonstrated the possibility to incorporate bioactive ions in the mesoporous structure and the effectiveness they have in promoting cellular processes.

In **Chapter 4**, the surface of pores in MTFs has been functionalized with carboxylate groups for complexing and delivering Sr. First, mesoporous silica films containing available COOH groups have been synthesized in one-step synthesis. Carboxylated organosilanes have been prepared by PRTEA, and have been incorporated to the solution containing the silica precursor and the structure directing agent. The incorporation of the silanes in the silica films has been demonstrated by XPS measurements and the presence of the carboxylates through IR measurements. Pb²⁺ has been proven to be complexed by changes in the carbonyl band signal.

Then, mesoporous titania films functionalized with COOH groups on the pore surface are synthesized in two-step synthesis. VTMS is co-condensed with the Ti precursor, and then, after film synthesis, through post-grafting, MSA reacts with the vinyl groups by click chemistry. Sr²⁺ complexation studies and the presence of COOH groups have been conducted by IR and XPS measurements. The release of Sr has also been followed. The release profile shows an initial burst release at initial times, followed by a prolonged release. The release helps in the initial cell adhesion to the

implant surface, followed by an enhanced proliferation rate, which is higher compared to cells cultured on top of MTF from day 3. This methodology allows the synthesis of COOH-modified mesoporous titania films. This COOH groups can serve as binding sites for ions or more complex molecules, such as drugs or proteins.

Overall, the versatility of mesoporous substrates has been demonstrated. It is possible to tune the mesoporous structure and pore orientation by changing the structure directing agent. Also the thickness can be modified by changing the spinning or dipping settings, and lastly, is also possible to synthesize hybrid mesoporous films to endow the films with a wide range variety of functionalities. By tuning the synthesis of the mesoporous films different amount of molecules can be entrapped inside the pore structure and the inner surface area can be enhanced to obtain a larger interchangeable surface.

To conclude, this thesis has highlighted the potential of mesoporous titania films functionalized through different approaches to induce a good osseointegration of implants and prevent bacterial infections.

IX. REFERENCES

- [1] S. Ramakrishna, J. Mayer, E. Wintermantel, K. W. Leong, *Composites science and technology*; Elsevier Applied Science Publishers, 1985; Vol. 9.
- [2] J. P. Ley, A. N. Cranin, M. Katzap, In *Biomaterials Engineering and Devices: Human Applications*; Humana Press: Totowa, NJ, 2000; pp. 3–24.
- [3] J. D. Bronzino, J. B. Park, *Biomaterials principles and applications*; CRC Press, 2002.
- [4] D. L. Wise, *Biomaterials engineering and devices*; Humana Press, 2000.
- [5] D. L. (Donald L. Wise, *Orthopedic, dental, and bone grafting applications*; Humana Press, 2000.
- [6] R. Dimitriou, E. Jones, D. McGonagle, P. V Giannoudis, *BMC Med.* **2011**, 9, 66.
- [7] V. Campana, G. Milano, E. Pagano, M. Barba, C. Cicione, G. Salonna, W. Lattanzi, G. Logroscino, *J. Mater. Sci. Mater. Med.* **2014**, 25, 2445.
- [8] T. W. Bauer, G. F. Muschler, *Clin. Orthop. Relat. Res.* **2000**, 371, 10.
- [9] W. Wang, K. W. K. Yeung, *Bioact. Mater.* **2017**, 2, 224.
- [10] M. Rang, *Br. J. Surg.* **1966**, 53, 483.
- [11] J. F. Baker, M. H. Vioreanu, H. A. Khan, *J Bone Jt. Surg [Br]* **2011**, 9393, 1285.
- [12] S. Kovač, V. Pišot, R. Trebše, A. Rotter, *J. Arthroplasty* **2004**, 19, 664.
- [13] J. Hettfleisch, R. Wissenbach, *J. Bone Joint Surg. Br.* **1994**, 76, 671.
- [14] R. Judet, J. Judet, *J. Bone Joint Surg. Br.* **1952**, 34–B, 173.
- [15] W. Waugh, *John Charnley : the Man and the Hip*; Springer London, 1990.
- [16] S. Affatato, *Wear of orthopaedic implants and artificial joints.*; Woodhead Pub, 2012.
- [17] R. Trebše, A. Mihelič, In *Infected Total Joint Arthroplasty*; Springer London: London, 2012; pp. 7–11.
- [18] L. C. Jones, L. D. Timmie Topoleski, A. K. Tsao, In *Mechanical Testing of Orthopaedic Implants*; Elsevier, 2017; pp. 17–32.
- [19] M. Navarro, A. Michiardi, O. Castano, J. . Planell, *J. R. Soc. Interface* **2008**, 5, 1137.
- [20] M. Geetha, A. K. Singh, R. Asokamani, A. K. Gogia, *Prog. Mater. Sci.* **2009**, 54, 397.
- [21] M. Saini, Y. Singh, P. Arora, V. Arora, K. Jain Monika Saini, K. Jain, *World J Clin Cases* **2015**, 3.
- [22] M. Cross, J. Spycher, In *Joint Replacement Technology*; Elsevier, 2008; pp. 190–211.
- [23] J. Lawrence Katz, *Nature* **1980**, 288, 196.
- [24] C. E. Misch, *Contemporary implant dentistry*; Mosby Elsevier, 2008.

References

- [25] A. Wennerberg, T. Albrektsson, *Int. J. Oral Maxillofac. Implants* **2010**, *25*, 63.
- [26] T. P. Chaturvedi, *Indian J. Dent. Res.* **2009**, *20*, 91.
- [27] N. J. Hallab, S. Anderson, T. Stafford, T. Glant, J. J. Jacobs, *J. Orthop. Res.* **2005**, *23*, 384.
- [28] A. S. Wong, A. M. R. New, G. Isaacs, M. Taylor, *Proc. Inst. Mech. Eng. Part H J. Eng. Med.* **2005**, *219*, 265.
- [29] H. Tschernitschek, L. Borchers, W. Geurtsen, *Quintessence Int. (Berl)*. **2005**, *36*, 523.
- [30] K. Karthik, Sivakumar, Sivaraj, V. Thangaswamy, *J. Pharm. Bioallied Sci.* **2013**, *5*, S117.
- [31] C. N. Elias, J. H. C. Lima, R. Valiev, M. A. Meyers, *JOM*. **2008**, *60*, 46.
- [32] V. Vijayaraghavan, A. V Sabane, K. Tejas, *J. Indian Prosthodont. Soc.* **2012**, *12*, 201.
- [33] B. D. Ratner, *Biomaterials science: an introduction to materials in medicine*; Academic Press, 2013.
- [34] Arthritis of the Knee - Total Knee Replacement (Arthroplasty) and Other Treatments at HSS. *2010*.
- [35] J. J. Jacobs, J. L. Gilbert, R. M. Urban, *J. Bone Joint Surg. Am.* **1998**, *80*, 268.
- [36] K. G. Neoh, X. Hu, D. Zheng, E. T. Kang, *Biomaterials* **2012**, *33*, 2813.
- [37] X. Zhu, J. Chen, L. Scheideler, R. Reichl, J. Geis-Gerstorfer, *Biomaterials* **2004**, *25*, 4087.
- [38] F. Ory, J. L. Fraysse, In *Titanium in Medical and Dental Applications*; Elsevier, 2018; pp. 65–91.
- [39] G. Ma, S. Gong, G. Lin, L. Zhang, G. Sun, *Applied surface science.*; North-Holland, 1985; Vol. 258.
- [40] M. Fedel, A. Motta, D. Maniglio, C. Migliaresi, *J. Biomed. Mater. Res. Part B Appl. Biomater.* **2008**, *90B*, 338.
- [41] L. Zhao, P. K. Chu, Y. Zhang, Z. Wu, *J. Biomed. Mater. Res. Part B Appl. Biomater.* **2009**, *91B*, 470.
- [42] L. Pulido, E. Ghanem, A. Joshi, J. J. Purtill, J. Parvizi, *Clin. Orthop. Relat. Res.* **2008**, *466*, 1710.
- [43] A. W. Blom, J. Brown, A. H. Taylor, G. Pattison, S. Whitehouse, G. C. Bannister, *J. Bone Joint Surg. Br.* **2004**, *86*, 688.
- [44] S. M. Kurtz, K. L. Ong, E. Lau, K. J. Bozic, D. Berry, J. Parvizi, *Clin. Orthop. Relat. Res.* **2010**, *468*, 52.
- [45] P. I. Brånemark, R. Adell, U. Breine, B. O. Hansson, J. Lindström, A. Ohlsson, *Scand. J. Plast. Reconstr. Surg.* **1969**, *3*, 81.
- [46] E. M. Hetrick, M. H. Schoenfisch, *Chem. Soc. Rev.* **2006**, *35*, 780.
- [47] W. M. Dunne, *Clin. Microbiol. Rev.* **2002**, *15*, 155.

- [48] J. W. Costerton, P. S. Stewart, E. P. Greenberg, *Science* **1999**, *284*, 1318.
- [49] W. Zimmerli, A. Trampuz, P. E. Ochsner, *N. Engl. J. Med.* **2004**, *351*, 1645.
- [50] J. L. Del Pozo, R. Patel, *N. Engl. J. Med.* **2009**, *361*, 787.
- [51] M. Ribeiro, F. J. Monteiro, M. P. Ferraz, *Biomatter* **2012**, *2*, 176.
- [52] H. A. Khan, F. K. Baig, R. Mehboob, *Asian Pac. J. Trop. Biomed.* **2017**, *7*, 478.
- [53] M. C. Hudson, W. K. Ramp, K. P. Frankenburg, *FEMS Microbiol. Lett.* **1999**, *173*, 279.
- [54] C. R. Arciola, D. Campoccia, S. Gamberini, M. E. Donati, L. Montanaro, *Biomaterials* **2004**, *25*, 4825.
- [55] L. G. Harris, R. G. Richards, *Injury* **2006**, *37*, S3.
- [56] S. J. Kalita, S. Verma, *Mater. Sci. Eng. C* **2010**, *30*, 295.
- [57] M. Stigter, K. de Groot, P. Layrolle, *Biomaterials* **2002**, *23*, 4143.
- [58] M. Stigter, J. Bezemer, K. de Groot, P. Layrolle, *J. Control. Release* **2004**, *99*, 127.
- [59] S. Radin, J. T. Campbell, P. Ducheyne, J. M. Cuckler, *Biomaterials* **1997**, *18*, 777.
- [60] V. Alt, A. Bitschnau, J. Osterling, A. Sewing, C. Meyer, R. Kraus, S. Meissner, S. Wenisch, E. Domann, R. Schnettler, *Biomaterials* **2006**, *27*, 4627.
- [61] K.-U. Lewandrowski, G. Schollmeier, A. Ekkernkamp, H. J. Mankin, H. K. Uhthoff, W. W. Tomford, In *Biomaterials Engineering and Devices: Human Applications*; Humana Press: Totowa, NJ, 2000; pp. 111–132.
- [62] A. A. Campbell, L. Song, X. S. Li, B. J. Nelson, C. Bottoni, D. E. Brooks, E. S. DeJong, *J. Biomed. Mater. Res.* **2000**, *53*, 400.
- [63] M. Morra, C. Cassinelli, G. Cascardo, L. Mazzucco, P. Borzini, M. Fini, G. Giavaresi, R. Giardino, *J Biomed Mater Res* **2006**, *78*, 449.
- [64] A. Ewald, S. K. Glückermann, R. Thull, U. Gbureck, *Biomed. Eng. Online* **2006**, *5*, 22.
- [65] W. Chen, Y. Liu, H. . Courtney, M. Bettenga, C. M. Agrawal, J. D. Bumgardner, J. L. Ong, *Biomaterials* **2006**, *27*, 5512.
- [66] A. M. Gallardo-Moreno, M. A. Pacha-Olivenza, L. Saldaña, C. Pérez-Giraldo, J. M. Bruque, N. Vilaboa, M. L. González-Martín, *Acta Biomater.* **2009**, *5*, 181.
- [67] R. Muzzarelli, R. Tarsi, O. Filippini, E. Giovanetti, G. Biagini, P. E. Varaldo, *Antimicrob. Agents Chemother.* **1990**, *34*, 2019.
- [68] B. J. Nablo, M. H. Schoenfisch, *Biomaterials* **2005**, *26*, 4405.
- [69] E. M. Hetrick, M. H. Schoenfisch, *Biomaterials* **2007**, *28*, 1948.
- [70] M. Cloutier, D. Mantovani, F. Rosei, *Trends Biotechnol.* **2015**, *33*, 637.
- [71] F. Richards, C. McCall, C. Cox, *JAMA J. Am. Med. Assoc.* **1971**, *215*, 1297.
- [72] Y. Dubrovskaya, R. Tejada, J. Bosco, A. Stachel, D. Chen, M. Feng, A. Rosenberg, M. Phillips, *SAGE Open Med.* **2015**, *3*, 205031211561280.
- [73] K. T. Fitzgerald, K. L. Newquist, In *Small Animal Toxicology*; Elsevier, 2013; pp. 229–249.

References

- [74] P. Baudoux, N. Bles, S. Lemaire, M.-P. Mingeot-Leclercq, P. M. Tulkens, F. Van Bambeke, *J. Antimicrob. Chemother.* **2006**, *59*, 246.
- [75] BIOL 230 Lecture Guide - Flash Animation: Mode of Action of Aminoglycosides.
- [76] Gentamicin-Molecule – Science of Acne.
- [77] G. Decher, J. D. D. Hong, J. Schmitt, *Thin Solid Films* **1992**, 831.
- [78] G. Decher, M. Eckle, J. Schmitt, B. Struth, *Curr. Opin. Colloid Interface Sci.* **1998**, *3*, 32.
- [79] C. Holmes, J. Daoud, P. O. Bagnaninchi, M. Tabrizian, *Adv. Healthc. Mater.* **2014**, *3*, 572.
- [80] G. Decher, J. D. D. Hong, J. Schmitt, *Thin Solid Films* **1992**, 831.
- [81] J. B. Schlenoff, D. Laurent, H. Ly, J. Stepp, *Adv. Mater.* **1998**, *10*, 347.
- [82] Tarek R. Farhat, J. B. Schlenoff, *Langmuir* **2001**, *17*, 1184.
- [83] M. Bruening, D. Dotzauer, *Nat. Mater.* **2009**, *8*, 449.
- [84] O. Onitsuka, A. C. Fou, M. Ferreira, B. R. Hsieh, M. F. Rubner, *J. Appl. Phys.* **1998**, *80*, 4067.
- [85] L. Ouyang, R. Malaisamy, M. L. Bruening, *J. Memb. Sci.* **2008**, *310*, 76.
- [86] I. F. Patel, M. V. Kiryukhin, N. L. Yakovlev, H. S. Gupta, G. B. Sukhorukov, *J. Mater. Chem. B* **2015**, *3*, 4821.
- [87] Y. Lvov, K. Ariga, I. Ichinose, T. Kunitake, *J. Am. Chem. Soc.* **1995**, *117*, 6117.
- [88] D. Laurent, J. B. Schlenoff, *Langmuir* **1997**, *13*, 1552.
- [89] E. Donath, G. B. Sukhorukov, F. Caruso, S. A. Davis, H. Möhwald, *Angew. Chem. Int. Ed. Angew. Chem. Int. Ed* **1998**, *37*, 2201.
- [90] T. Krebs, H. L. Tan, G. Andersson, H. Morgner, P. Gregory Van Patten, *Phys. Chem. Chem. Phys.* **2006**, *8*, 5462.
- [91] S. S. Shiratori, M. F. Rubner, *Macromolecules* **2000**, *33*, 4213.
- [92] D. Gregurec, M. Olszyna, N. Politakos, L. Yate, L. Dahne, S. E. Moya, *Colloid Polym. Sci.* **2015**, *293*, 381.
- [93] G. Decher, J. Schmitt, In *Trends in Colloid and Interface Science VI*; Steinkopff: Darmstadt, 1992; pp. 160–164.
- [94] J. D. Mendelsohn, S. Y. Yang, J. Hiller, A. I. Hochbaum, M. F. Rubner, *Biomacromolecules* **2003**, *4*, 96.
- [95] G. Rydzek, J.-S. Thomann, N. Ben Ameer, L. Jierry, P. Mésini, A. Ponche, C. Contal, A. E. El Haitami, J.-C. Voegel, B. Senger, P. Schaaf, B. Frisch, F. Boulmedais, *Langmuir* **2010**, *26*, 2816.
- [96] L. Lee, F. Cavalieri, A. P. R. Johnston, F. Caruso, *Langmuir* **2010**, *26*, 3415.
- [97] B.-S. Kim, S. W. Park, P. T. Hammond, *ACS Nano* **2008**, *2*, 386.
- [98] Y. Lvov, G. Decher, G. Sukhorukov, *Macromolecules* **1993**, *26*, 5396.
- [99] G. Decher, *Science (80-.).* **1997**, *277*, 1232.

- [100] B. Thierry, F. M. Winnik, Y. Merhi, J. Silver, M. Tabrizian, *Biomacromolecules* **2003**, *4*, 1564.
- [101] J. Zhang, B. Senger, D. Vautier, C. Picart, P. Schaaf, J.-C. Voegel, P. Lavallo, *Biomaterials* **2005**, *26*, 3353.
- [102] D. L. Elbert, A. Curtis B. Herbert, J. A. Hubbell, *Langmuir* **1999**, *15*, 5355.
- [103] L. Richert, P. Lavallo, E. Payan, X. Z. Shu, G. D. Prestwich, J.-F. Stoltz, P. Schaaf, J.-C. Voegel, C. Picart, *Langmuir* **2004**, *20*, 448.
- [104] Alexei A. Antipov, Gleb B. Sukhorukov, A. Edwin Donath, H. Möhwald, *J. Phys. Chem. B* **2001**, *105*, 2281.
- [105] F. Caruso, H. Möhwald, *J. Am. Chem. Soc.* **1999**, *121*, 6039.
- [106] Y. M. Lvov, Z. Lu, J. B. Schenkman, A. Xiaolin Zu, J. F. Rusling, *J. Am. Chem. Soc.* **1998**, *120*, 4073.
- [107] P. Lavallo, C. Gergely, F. J. G. Cuisinier, G. Decher, P. Schaaf, A. J. C. Voegel, C. Picart, *Macromolecules* **2002**, *35*, 4458.
- [108] C. Picart, J. Mutterer, L. Richert, Y. Luo, G. D. Prestwich, P. Schaaf, J.-C. Voegel, P. Lavallo, *Proc. Natl. Acad. Sci. U. S. A.* **2002**, *99*, 12531.
- [109] Donald T. Haynie, Ling Zhang, Jai S. Rudra, Wanhua Zhao, A. Yang Zhong, N. Palath, *Biomacromolecules* **2005**, *6*, 2895.
- [110] D. T. Haynie, E. Cho, P. Waduge, *Langmuir* **2011**, *27*, 5700.
- [111] Z. Gu, *Bioinspired and biomimetic polymer systems for drug and gene delivery*; 2015.
- [112] C. Porcel, P. Lavallo, G. Decher, B. Senger, A. J.-C. Voegel, P. Schaaf, *Langmuir* **2007**, *23*, 1898.
- [113] C. Picart, P. Lavallo, P. Hubert, F. J. G. Cuisinier, G. Decher, A. P. Schaaf, J.-C. Voegel, *Langmuir* **2001**, *17*, 7414.
- [114] G. L. Whiting, T. Farhan, W. T. S. Huck, In *Polymer Brushes*; Wiley-VCH Verlag GmbH & Co. KGaA: Weinheim, FRG, 2005; pp. 371–380.
- [115] W. Senaratne, L. A. And, C. K. Ober, *Biomacromolecules* **2005**, *6*, 2427.
- [116] X. Liu, F. Han, P. Zhao, C. Lin, X. Wen, X. Ye, *Nanomedicine Nanotechnology, Biol. Med.* **2017**, *13*, 1423.
- [117] J. M. Garza, N. Jessel, G. Ladam, V. Dupray, S. Muller, J.-F. Stoltz, P. Schaaf, J.-C. Voegel, P. Lavallo, *Langmuir* **2005**, *21*, 12372.
- [118] Sigma-Aldrich, BioFiles 3.8 - Attachment and Matrix Factors 3.
- [119] A. Díez-Pascual, P. Shuttleworth, *Materials (Basel)*. **2014**, *7*, 7472.
- [120] D. Mazia, G. Schatten, W. Sale, *J. Cell Biol.* **1975**, *66*, 198.
- [121] Z. S. Nurkeeva, V. V. Khutoryanskiy, G. A. Mun, M. V. Sherbakova, A. T. Ivaschenko, N. A. Aitkhozhina, N. A. Aitkhozhina, *Eur. J. Pharm. Biopharm.* **2004**, *57*, 245.
- [122] P. T. Hammond, *Mater. Today* **2012**, *15*, 196.

References

- [123] H. F. Chuang, R. C. Smith, P. T. Hammond, *Biomacromolecules* **2008**, *9*, 1660.
- [124] J. S. Moskowitz, M. R. Blaisse, R. E. Samuel, H.-P. Hsu, M. B. Harris, S. D. Martin, J. C. Lee, M. Spector, P. T. Hammond, *Biomaterials* **2010**, *31*, 6019.
- [125] W. Xia, K. Grandfield, A. Hoess, A. Ballo, Y. Cai, H. Engqvist, *J. Biomed. Mater. Res. Part B Appl. Biomater.* **2012**, *100B*, 82.
- [126] X. Liu, P. Chu, C. Ding, *Mater. Sci. Eng. R Reports* **2004**, *47*, 49.
- [127] J. D. Bass, D. Grosso, C. Boissiere, E. Belamie, T. Coradin, C. Sanchez, *Chem. Mater.* **2007**, *19*, 4349.
- [128] Revision Arthroplasty of the Knee | eOrthopod.com.
- [129] Revision Arthroplasty of the Hip | eOrthopod.com.
- [130] Y. Yamauchi, N. Suzuki, L. Radhakrishnan, L. Wang, *Chem. Rec.* **2009**, *9*, 321.
- [131] J. L. Vivero-Escoto, Y.-D. Chiang, K. Wu, Y. Yamauchi, *Sci. Technol. Adv. Mater.* **2012**, *13*, 13003.
- [132] M. Ogawa, *Chem. Commun.* **1996**, *0*, 1149.
- [133] V. Valtchev, S. Mintova, M. Tsapatsis, *Ordered porous solids: recent advances and prospects*; Elsevier Science, 2009.
- [134] H. Yang, N. Coombs, I. Sokolov, G. A. Ozin, *Nature* **1996**, *381*, 589.
- [135] L. Mahoney, R. T. Koodali, *Materials (Basel)*. **2014**, *7*, 2697.
- [136] L. Nicole, C. Boissière, D. Grosso, A. Quach, C. Sanchez, *J. Mater. Chem.* **2005**, *15*, 3598.
- [137] C. Sanchez, C. Boissière, D. Grosso, C. Laberty, L. Nicole, *Chem. Mater.* **2008**, *20*, 682.
- [138] A. Escobar, L. Yate, M. Grzelczak, H. Amenitsch, S. E. Moya, A. V Bordonni, P. C. Angelome, *ACS Omega*. **2017**, *2*, 4548.
- [139] G. J. A. A. Soler-Illia, O. Azzaroni, *Chem. Soc. Rev.* **2011**, *40*, 1107.
- [140] F. Cagnol, D. Grosso, C. Sanchez, *Chem. Commun.* **2004**, *0*, 1742.
- [141] L. Han, O. Terasaki, S. Che, *J. Mater. Chem.* **2011**, *21*, 11033.
- [142] N. Liu, R. A. Assink, C. J. Brinker, *Chem. Commun.* **2003**, *0*, 370.
- [143] A. V. Bordonni, M. V. Lombardo, A. E. Regazzoni, G. J. A. A. Soler-Illia, A. Wolosiuk, *J. Colloid Interface Sci.* **2015**, *450*, 316.
- [144] A. V. Bordonni, M. V. Lombardo, A. Wolosiuk, *RSC Adv.* **2016**, *6*, 77410.
- [145] N. P. Lang, T. G. Wilson, E. F. Corbet, *Clin. Oral Implants Res.* **2000**, *11 Suppl 1*, 146.
- [146] R. Langer, N. A. Peppas, *AIChE J.* **2003**, *49*, 2990.
- [147] C. Wang, C. He, Z. Tong, X. Liu, B. Ren, F. Zeng, *Int. J. Pharm.* **2006**, *308*, 160.
- [148] M. Mohseni, K. Gilani, S. A. Mortazavi, *Iran. J. Pharm. Res. IJPR* **2015**, *14*, 27.
- [149] M. N. Singh, K. S. Y. Hemant, M. Ram, H. G. Shivakumar, *Res. Pharm. Sci.* **2010**, *5*, 65.

- [150] I. Brigger, C. Dubernet, P. Couvreur, *Adv. Drug Deliv. Rev.* **2002**, *54*, 631.
- [151] V. P. Torchilin, *Nat. Rev. Drug Discov.* **2005**, *4*, 145.
- [152] T. M. Allen, P. R. Cullis, *Science (80-.)*. **2004**, *303*, 1818.
- [153] M. P. Ginebra, T. Traykova, J. A. Planell, *J. Control. Release* **2006**, *113*, 102.
- [154] C. Charnay, S. Bégu, C. Tourné-Péteilh, L. Nicole, D. A. Lerner, J. M. Devoisselle, *Eur. J. Pharm. Biopharm.* **2004**, *57*, 533.
- [155] T. Gren, C. Bjerre, O. Camber, G. Ragnarsson, *Int. J. Pharm.* **1996**, *141*, 53.
- [156] E. Gultepe, D. Nagesha, S. Sridhar, M. Amiji, *Adv. Drug Deliv. Rev.* **2010**, *62*, 305.
- [157] L. Barnes, I. R. Cooper, Y. Achermann, *Biomaterials and medical device-associated infections*; 2014.
- [158] E. F. Eriksen, *Rev. Endocr. Metab. Disord.* **2010**, *11*, 219.
- [159] E. F. Eriksen, H. J. Gundersen, F. Melsen, L. Mosekilde, *Metab. Bone Dis. Relat. Res.* **1984**, *5*, 243.
- [160] E. F. Eriksen, L. Mosekilde, F. Melsen, *Bone* **1986**, *7*, 101.
- [161] T. Komori, H. Yagi, S. Nomura, A. Yamaguchi, K. Sasaki, K. Deguchi, Y. Shimizu, R. T. Bronson, Y. H. Gao, M. Inada, M. Sato, R. Okamoto, Y. Kitamura, S. Yoshiki, T. Kishimoto, *Cell* **1997**, *89*, 755.
- [162] M. Murshed, D. Harmey, J. L. Millán, M. D. McKee, G. Karsenty, *Genes Dev.* **2005**, *19*, 1093.
- [163] C. J. Bettinger, R. Langer, J. T. Borenstein, *Angew. Chemie Int. Ed.* **2009**, *48*, 5406.
- [164] L. E. McNamara, R. J. McMurray, M. J. P Biggs, F. Kantawong, R. O. C Oreffo, M. J. Dalby, *SAGE-Hindawi Access to Res. J. Tissue Eng.* **2010**.
- [165] H. S. Alghamdi, R. Bosco, J. J. J. P. van den Beucken, X. F. Walboomers, J. A. Jansen, *Biomaterials* **2013**, *34*, 3747.
- [166] R. Junker, A. Dimakis, M. Thoneick, J. A. Jansen, *Clin. Oral Implants Res.* **2009**, *20*, 185.
- [167] H. Alghamdi, *J. Funct. Biomater.* **2018**, *9*, 7.
- [168] E. Hunziker, J. Jovanovic, A. Horner, M. Keel, K. Lippuner, N. Shintani, *Eur. Cells Mater.* **2016**, *32*, 241.
- [169] T. Cundy, I. R. Reid, A. Grey, In *Clinical Biochemistry: Metabolic and Clinical Aspects*; Elsevier, 2014; pp. 604–635.
- [170] B. L. Hogan, *Genes Dev.* **1996**, *10*, 1580.
- [171] S. Knöchel, K. Dillinger, M. Köster, W. Knöchel, *Mech. Dev.* **2001**, *109*, 79.
- [172] A. Yamaguchi, T. Katagiri, T. Ikeda, J. M. Wozney, V. Rosen, E. A. Wang, A. J. Kahn, T. Suda, S. Yoshiki, *J. Cell Biol.* **1991**, *113*, 681.
- [173] H. Yamashita, P. ten Dijke, D. Huylebroeck, T. K. Sampath, M. Andries, J. C. Smith, C. H. Heldin, K. Miyazono, *J. Cell Biol.* **1995**, *130*, 217.
- [174] P. M. Eimon, R. M. Harland, *Dev. Biol.* **1999**, *216*, 29.

References

- [175] A. Daluiski, T. Engstrand, M. E. Bahamonde, L. W. Gamer, E. Agius, S. L. Stevenson, K. Cox, V. Rosen, K. M. Lyons, *Nat. Genet.* **2001**, *27*, 84.
- [176] P. ten Dijke, K. Miyazono, C. H. Heldin, *Curr. Opin. Cell Biol.* **1996**, *8*, 139.
- [177] B. B. Koenig, J. S. Cook, D. H. Wolsing, J. Ting, J. P. Tiesman, P. E. Correa, C. A. Olson, A. L. Pecquet, F. Ventura, R. A. Grant, *Mol. Cell. Biol.* **1994**, *14*, 5961.
- [178] P. ten Dijke, H. Yamashita, T. K. Sampath, A. H. Reddi, M. Estevez, D. L. Riddle, H. Ichijo, C. H. Heldin, K. Miyazono, *J. Biol. Chem.* **1994**, *269*, 16985.
- [179] M. Kawabata, T. Imamura, M. Takase, A. Nishihara, E. Oeda, J. Hanai, K. Miyazono, *Nature* **1997**, *389*, 622.
- [180] R. Derynck, Y. Zhang, X. H. Feng, *Cell* **1998**, *95*, 737.
- [181] R. N. Wang, J. Green, Z. Wang, Y. Deng, M. Qiao, M. Peabody, Q. Zhang, J. Ye, Z. Yan, S. Denduluri, O. Idowu, M. Li, C. Shen, A. Hu, R. C. Haydon, R. Kang, J. Mok, M. J. Lee, H. L. Luu, L. L. Shi, *Genes Dis.* **2014**, *1*, 87.
- [182] W. Zhang, G. Wang, Y. Liu, X. Zhao, D. Zou, C. Zhu, Y. Jin, Q. Huang, J. Sun, X. Liu, X. Jiang, H. Zreiqat, *Biomaterials* **2013**, *34*, 3184.
- [183] A. Hoppe, N. S. Güldal, A. R. Boccaccini, *Biomaterials* **2011**, *32*, 2757.
- [184] N. J. Lakhkar, I.-H. Lee, H.-W. Kim, V. Salih, I. B. Wall, J. C. Knowles, *Adv. Drug Deliv. Rev.* **2013**, *65*, 405.
- [185] A. Doğan, S. Demirci, Y. Bayir, Z. Halici, E. Karakus, A. Aydin, E. Cadirci, A. Albayrak, E. Demirci, A. Karaman, A. K. Ayan, C. Gundogdu, F. Şahin, *Mater. Sci. Eng. C* **2014**, *44*, 246.
- [186] Y. Zhang, X. Chen, R. Miron, Y. Zhao, Q. Zhang, C. Wu, S. Geng, *Int. J. Nanomedicine* **2015**, *10*, 839.
- [187] J. K. Foskett, C. White, K.-H. Cheung, D.-O. D. Mak, *Physiol. Rev.* **2007**, *87*, 593.
- [188] S. S. Lim, C. Y. Chai, H.-S. Loh, *Mater. Sci. Eng. C* **2017**, *76*, 144.
- [189] Y.-J. Seol, J. Y. Park, J. W. Jung, J. Jang, R. Girdhari, S. W. Kim, D.-W. Cho, *Tissue Eng. Part A* **2014**, *20*, 2840.
- [190] C. Wu, Y. Zhou, W. Fan, P. Han, J. Chang, J. Yuen, M. Zhang, Y. Xiao, *Biomaterials* **2012**, *33*, 2076.
- [191] R. A. Perez, J.-H. Kim, J. O. Buitrago, I. B. Wall, H.-W. Kim, *Acta Biomater.* **2015**, *23*, 295.
- [192] J. Bejarano, R. Detsch, A. R. Boccaccini, H. Palza, *J. Biomed. Mater. Res. Part A* **2017**, *105*, 746.
- [193] C. Gérard, L.-J. Bordeleau, J. Barralet, C. J. Doillon, *Biomaterials* **2010**, *31*, 824.
- [194] H. Wang, S. Zhao, J. Zhou, Y. Shen, W. Huang, C. Zhang, M. N. Rahaman, D. Wang, *J. Mater. Chem. B* **2014**, *2*, 8547.
- [195] S. D'Mello, S. Elangovan, L. Hong, R. D. Ross, D. R. Sumner, A. K. Salem, *J. Biomed. Mater. Res. Part B Appl. Biomater.* **2015**, *103*, 1044.
- [196] T. B. Zeinab, G. Nazli, M. Angad, V. B. Clemens, H. Pamela, *Front. Bioeng. Biotechnol.* **2016**, *4*.

- [197] W.-J. Qu, D.-B. Zhong, P.-F. Wu, J.-F. Wang, B. Han, *J. Bone Miner. Metab.* **2008**, *26*, 328.
- [198] M. Lee, K. Arikawa, F. Nagahama, *Biol. Trace Elem. Res.* **2017**, *178*, 283.
- [199] M. Arioka, F. Takahashi-Yanaga, M. Sasaki, T. Yoshihara, S. Morimoto, M. Hirata, Y. Mori, T. Sasaguri, *Biochem. Pharmacol.* **2014**, *90*, 397.
- [200] Z. Zhu, J. Yin, J. Guan, B. Hu, X. Niu, D. Jin, Y. Wang, C. Zhang, *FEBS J.* **2014**, *281*, 5371.
- [201] S. Yoshizawa, A. Brown, A. Barchowsky, C. Sfeir, *Acta Biomater.* **2014**, *10*, 2834.
- [202] H.-K. Kim, H.-S. Han, K.-S. Lee, D.-H. Lee, J. W. Lee, H. Jeon, S.-Y. Cho, H.-J. Roh, Y.-C. Kim, H.-K. Seok, *J. Tissue Eng. Regen. Med.* **2017**, *11*, 2710.
- [203] S. Galli, Y. Naito, J. Karlsson, W. He, I. Miyamoto, Y. Xue, M. Andersson, K. Mustafa, A. Wennerberg, R. Jimbo, *Acta Biomater.* **2014**, *10*, 5193.
- [204] Z.-S. Tao, W.-S. Zhou, X.-W. He, W. Liu, B.-L. Bai, Q. Zhou, Z.-L. Huang, K. Tu, H. Li, T. Sun, Y.-X. Lv, W. Cui, L. Yang, *Mater. Sci. Eng. C* **2016**, *62*, 226.
- [205] Y. Bai, Y. Deng, Y. Zheng, Y. Li, R. Zhang, Y. Lv, Q. Zhao, S. Wei, *Mater. Sci. Eng. C* **2016**, *59*, 565.
- [206] H. Tada, E. Nemoto, B. L. Foster, M. J. Somerman, H. Shimauchi, *Bone* **2011**, *48*, 1409.
- [207] M. Julien, S. Khoshniat, A. Lacreusette, M. Gatius, A. Bozec, E. F. Wagner, Y. Wittrant, M. Masson, P. Weiss, L. Beck, D. Magne, J. Guicheux, *J. Bone Miner. Res.* **2009**, *24*, 1856.
- [208] R. Zhang, Y. Lu, L. Ye, B. Yuan, S. Yu, C. Qin, Y. Xie, T. Gao, M. K. Drezner, L. F. Bonewald, J. Q. Feng, *J. Bone Miner. Res.* **2011**, *26*, 1047.
- [209] W. N. Addison, F. Azari, E. S. Sørensen, M. T. Kaartinen, M. D. McKee, *J. Biol. Chem.* **2007**, *282*, 15872.
- [210] S. Castiglioni, A. Cazzaniga, W. Albisetti, J. A. M. Maier, *Nutrients* **2013**, *5*, 3022.
- [211] T. Qing, M. Mahmood, Y. Zheng, A. S. Biris, L. Shi, D. A. Casciano, *J. Appl. Toxicol.* **2018**, *38*, 172.
- [212] F. Yang, D. Yang, J. Tu, Q. Zheng, L. Cai, L. Wang, *Stem Cells* **2011**, *29*, 981.
- [213] L. Zhao, H. Wang, K. Huo, X. Zhang, W. Wang, Y. Zhang, Z. Wu, P. K. Chu, *Biomaterials* **2013**, *34*, 19.
- [214] E. Gentleman, Y. C. Fredholm, G. Jell, N. Lotfibakhshaiesh, M. D. O'Donnell, R. G. Hill, M. M. Stevens, *Biomaterials* **2010**, *31*, 3949.
- [215] S. Peng, G. Zhou, K. D. K. Luk, K. M. C. Cheung, Z. Li, W. M. Lam, Z. Zhou, W. W. Lu, *Cell. Physiol. Biochem.* **2009**, *23*, 165.
- [216] Y. Li, Q. Li, S. Zhu, E. Luo, J. Li, G. Feng, Y. Liao, J. Hu, *Biomaterials* **2010**, *31*, 9006.
- [217] R. K. Rude, F. R. Singer, H. E. Gruber, *J. Am. Coll. Nutr.* **2009**, *28*, 131.
- [218] D. N. Paglia, A. Wey, A. G. Park, E. A. Breitbart, S. K. Mehta, J. D. Bogden, F. W.

References

- Kemp, J. Benevenia, J. P. O'Connor, S. S. Lin, *J. Orthop. Res.* **2012**, *30*, 1971.
- [219] M. Yamaguchi, M. N. Weitzmann, *Mol. Cell. Biochem.* **2011**, *355*, 179.
- [220] K. Huo, X. Zhang, H. Wang, L. Zhao, X. Liu, P. K. Chu, *Biomaterials* **2013**, *34*, 3467.
- [221] Y. Yamada, A. Ito, H. Kojima, M. Sakane, S. Miyakawa, T. Uemura, R. Z. LeGeros, *J. Biomed. Mater. Res. Part A* **2008**, *84A*, 344.
- [222] K. Yusa, O. Yamamoto, M. Iino, H. Takano, M. Fukuda, Z. Qiao, T. Sugiyama, *Arch. Oral Biol.* **2016**, *71*, 162.
- [223] J. A. Lemire, J. J. Harrison, R. J. Turner, *Nat. Rev. Microbiol.* **2013**, *11*, 371.
- [224] E. S. Thian, T. Konishi, Y. Kawanobe, P. N. Lim, C. Choong, B. Ho, M. Aizawa, *J. Mater. Sci. Mater. Med.* **2013**, *24*, 437.
- [225] H.-J. Seo, Y.-E. Cho, T. Kim, H.-I. Shin, I.-S. Kwun, *Nutr. Res. Pract.* **2010**, *4*, 356.
- [226] Y. Qiao, W. Zhang, P. Tian, F. Meng, H. Zhu, X. Jiang, X. Liu, P. K. Chu, *Biomaterials* **2014**, *35*, 6882.
- [227] M. Peacock, *Clin. J. Am. Soc. Nephrol.* **2010**, *5*, S23.
- [228] R. C. Riddle, A. F. Taylor, D. C. Genetos, H. J. Donahue, *Am. J. Physiol. Physiol.* **2006**, *290*, C776.
- [229] S. Maeno, Y. Niki, H. Matsumoto, H. Morioka, T. Yatabe, A. Funayama, Y. Toyama, T. Taguchi, J. Tanaka, *Biomaterials* **2005**, *26*, 4847.
- [230] J. Walker, S. Shadanbaz, T. B. F. Woodfield, M. P. Staiger, G. J. Dias, *J. Biomed. Mater. Res. Part B Appl. Biomater.* **2014**, *102*, 1316.
- [231] X. Jiang, G. Wang, J. Li, W. Zhang, L. Xu, H. Pan, J. Wen, X. Liu, Q. Wu, T. Jiao, W. She, *Int. J. Nanomedicine* **2014**, 2387.
- [232] A. E. Porter, N. Patel, J. N. Skepper, S. M. Best, W. Bonfield, *Biomaterials* **2004**, *25*, 3303.
- [233] C. T. Chasapis, A. C. Loutsidou, C. A. Spiliopoulou, M. E. Stefanidou, *Arch. Toxicol.* **2012**, *86*, 521.
- [234] A. S. Prasad, *Adv. Nutr.* **2013**, *4*, 176.
- [235] I.-S. Kwun, Y.-E. Cho, R.-A. R. Lomeda, H.-I. Shin, J.-Y. Choi, Y.-H. Kang, J. H. Beattie, *Bone* **2010**, *46*, 732.
- [236] G. Jin, H. Cao, Y. Qiao, F. Meng, H. Zhu, X. Liu, *Colloids Surf. B. Biointerfaces* **2014**, *117*, 158.
- [237] P. Habibovic, J. E. Barralet, *Acta Biomater.* **2011**, *7*, 3013.
- [238] E. Bonnelye, A. Chabadel, F. Saltel, P. Jurdic, *Bone* **2008**, *42*, 129.
- [239] J. Y. Reginster, O. Bruyère, A. Sawicki, A. Roces-Varela, P. Fardellone, A. Roberts, J. P. Devogelaer, *Bone* **2009**, *45*, 1059.
- [240] G. Molino, A. Bari, F. Baino, S. Fiorilli, C. Vitale-Brovarone, *J. Mater. Sci.* **2017**, *52*, 9103.
- [241] S. Kargozar, N. Lotfibakhshaesh, J. Ai, M. Mozafari, P. Brouki Milan, S.

- Hamzehlou, M. Barati, F. Baino, R. G. Hill, M. T. Joghataei, *Acta Biomater.* **2017**, *58*, 502.
- [242] J. Shi, Y. Li, Y. Gu, S. Qiao, X. Zhang, H. Lai, *Sci. Rep.* **2017**, *7*, 15563.
- [243] K. Grandfield, S. Pujari, M. Ott, H. Engqvist, W. Xia, *J. Biomater. Nanobiotechnol.* **2013**, *4*, 107.
- [244] J. F. Taylor, *Met. Finish.* **2001**, *99*, 16.
- [245] C. J. Brinker, G. C. Frye, A. J. Hurd, C. S. Ashley, *Thin Solid Films* **1991**, *201*, 97.
- [246] L. E. Scriven, *MRS Proc.* **1988**, *121*, 717.
- [247] S. Hüfner, *Photoelectron Spectroscopy; Advanced Texts in Physics*; Springer Berlin Heidelberg: Berlin, Heidelberg, 2003.
- [248] A. Einstein, *Ann. Phys.* **1905**, *322*, 132.
- [249] G. Binnig, C. F. Quate, C. Gerber, *Phys. Rev. Lett.* **1986**, *56*, 930.
- [250] N. A. Geisse, *Mater. Today* **2009**, *12*, 40.
- [251] W. C. Oliver, G. M. Pharr, *J. Mater. Res.* **1992**, *7*, 1564.
- [252] O. Glatter, O. Kratky, *Small angle x-ray scattering*; Academic Press: London ;;New York, 1982.
- [253] H. Amenitsch, S. Bernstorff, M. Kriechbaum, D. Lombardo, H. Mio, M. Rappolt, P. Laggner, *IUCr, J. Appl. Crystallogr.* **1997**, *30*, 872.
- [254] S. Inoué, In *Handbook Of Biological Confocal Microscopy*; Springer US: Boston, MA, 2006; pp. 1–19.
- [255] J. I. Goldstein, D. E. Newbury, P. Echlin, D. C. Joy, C. E. Lyman, E. Lifshin, L. Sawyer, J. R. Michael, In *Scanning Electron Microscopy and X-ray Microanalysis*; Springer US: Boston, MA, 2003; pp. 21–60.
- [256] D. B. Williams, C. B. Carter, In *Transmission Electron Microscopy*; Springer US: Boston, MA, 1996; pp. 3–17.
- [257] P. D. Ruth E. Wolf, *Introduction to ICP-MS* **2005**.
- [258] I. Reviakine, D. Johannsmann, R. P. Richter, *Anal. Chem.* **2011**, *83*, 8838.
- [259] H. G. Tompkins, E. A. Irene, *Handbook of ellipsometry*; William Andrew Pub., 2005.
- [260] What is Ellipsometry? - J.A. Woollam.
- [261] M. R. Baklanov, K. P. Mogilnikov, V. G. Polovinkin, F. N. Dultsev, *J. Vac. Sci. Technol. B Microelectron. Nanom. Struct. Process. Meas. Phenom.* **2000**, *18*, 1385.
- [262] C. Boissiere, D. Grosso, S. Lepoutre, L. Nicole, A. Aline Brunet Bruneau, C. Sanchez, *Langmuir.* **2005**, *21*, 12362.
- [263] T. Young, *Philos. Trans. R. Soc. London* **1805**, *95*, 65.
- [264] P. G. de Gennes, *Rev. Mod. Phys.* **1985**, *57*, 827.
- [265] P. Soo-Jin, S. Min-Kang, *Interface Sci. Technol.* **2011**, *18*, 147.
- [266] V. Ponec, *Recl. des Trav. Chim. des Pays-Bas* **2010**, *110*, 137.

References

- [267] M. Robins, A. Fillery-Travis, *J. Chem. Technol. Biotechnol.* **2007**, *54*, 201.
- [268] J. Gubernator, Z. Drulis-Kawa, A. Kozubek, *Int. J. Pharm.* **2006**, *327*, 104.
- [269] J. Krzek, H. Woltyńska, U. Hubicka, *Anal. Lett.* **2009**, *42*, 473.
- [270] C. Berthomieu, R. Hienerwadel, *Photosynth. Res.* **2009**, *101*, 157.
- [271] H. W. Siesler, Wiley InterScience (Online service), *Near-infrared spectroscopy : principles, instruments, applications*; Wiley-VCH, 2002.
- [272] G. Accardo, R. Cioffi, F. Colangelo, R. d'Angelo, L. De Stefano, F. Paglietti, *Materials (Basel)*. **2014**, *7*, 457.
- [273] M. M. Zalduendo, J. Langer, J. J. Giner-Casares, E. B. Halac, G. J. A. A. Soler-Illia, L. M. Liz-Marzán, P. C. Angelomé, *J. Phys. Chem. C* **2018**, *122*, 13095.
- [274] P. Defilippi, C. Olivo, M. Venturino, L. Dolce, L. Silengo, G. Tarone, *Microsc. Res. Tech.* **1999**, *47*, 67.
- [275] D. Wang, K. Christensen, K. Chawla, G. Xiao, P. H. Krebsbach, R. T. Franceschi, *J. Bone Miner. Res.* **1999**, *14*, 893.
- [276] M. Weinreb, D. Shinar, G. A. Rodan, *J. Bone Miner. Res.* **2009**, *5*, 831.
- [277] A. J. Mangram, T. C. Horan, M. L. Pearson, L. C. Silver, W. R. Jarvis, *Infect. Control Hosp. Epidemiol.* **1999**, *20*, 247.
- [278] K. R. Smith, T. R. Hunt, M. A. Asher, H. C. Anderson, W. L. Carson, R. G. Robinson, *J. Bone Joint Surg. Am.* **1991**, *73*, 115.
- [279] M. Z. Ibrahim, A. A. D. Sarhan, F. Yusuf, M. Hamdi, *J. Alloys Compd.* **2017**, *714*, 636.
- [280] L. C. Jones, L. D. Timmie Topoleski, A. K. Tsao, *Mech. Test. Orthop. Implant.* **2017**, *17*.
- [281] D. Campoccia, L. Montanaro, C. R. Arciola, *Biomaterials* **2006**, *27*, 2331.
- [282] Z. Song, L. Borgwardt, N. Høiby, H. Wu, T. S. Sørensen, A. Borgwardt, *Orthop. Rev. (Pavia)*. **2013**, *5*, 14.
- [283] E. Barth, Q. M. Myrvik, W. Wagner, A. G. Gristina, *Biomaterials* **1989**, *10*, 325.
- [284] C. von Eiff, R. A. Proctor, G. Peters, *Postgrad. Med.* **2001**, *110*, 63.
- [285] F. D. Lowy, *N. Engl. J. Med.* **1998**, *339*, 520.
- [286] S. D. ELEK, *Ann. N. Y. Acad. Sci.* **1956**, *65*, 85.
- [287] D. Li, P. Lv, L. Fan, Y. Huang, F. Yang, X. Mei, D. Wu, *Biomater. Sci.* **2017**, *5*, 2337.
- [288] L. Séon, P. Lavalley, P. Schaaf, F. Boulmedais, *Langmuir* **2015**, *31*, 12856.
- [289] K. Yang, Q. Han, B. Chen, Y. Zheng, K. Zhang, Q. Li, J. Wang, *Int. J. nanomedicine.* **2018**, *13*, 2217.
- [290] W. Zhou, Z. Jia, P. Xiong, J. Yan, M. Li, Y. Cheng, Y. Zheng, *Mater. Sci. Eng. C* **2018**, *90*, 693.
- [291] B. D. Boyan, E. M. Lotz, Z. Schwartz, *Tissue Eng. Part A.* **2017**, *23*, 1479.
- [292] F. Bayata, C. Yildiz, *Adv. Mater. Sci. Eng.* **2018**, *2018*, 1.

- [293] E. Avcu, Y. Yildiran Avcu, F. E. Baştan, M. A. U. Rehman, F. Üstel, A. R. Boccaccini, *Prog. Org. Coatings*. **2018**, *123*, 362.
- [294] M. Vallet-Regí, M. Manzano Garcia, M. Colilla, *Biomedical applications of mesoporous ceramics: drug delivery, smart materials, and bone tissue engineering*; 2012.
- [295] L. Zhou, X. Zheng, Z. Gu, W. Yin, X. Zhang, L. Ruan, Y. Yang, Z. Hu, Y. Zhao, *Biomaterials* **2014**, *35*, 7666.
- [296] M. Vallet-Regí, F. Balas, D. Arcos, *Angew. Chemie Int. Ed.* **2007**, *46*, 7548.
- [297] K. C.-W. Wu, Y. Yamauchi, *J. Mater. Chem.* **2012**, *22*, 1251.
- [298] Y. Yamauchi, *J. Ceram. Soc. Japan* **2013**, *121*, 831.
- [299] S. Chen, Y. Zhu, W. Li, W. Liu, L. Li, Z. Yang, C. Liu, W. Yao, X. Lu, X. Feng, *Chinese J. Catal.* **2010**, *31*, 605.
- [300] Z. Luo, Y. Hu, K. Cai, X. Ding, Q. Zhang, M. Li, X. Ma, B. Zhang, Y. Zeng, P. Li, J. Li, J. Liu, Y. Zhao, *Biomaterials* **2014**, *35*, 7951.
- [301] T. Rahman, R. Liu, E. Ortel, R. Kraehnert, A. Antoniou, *Appl. Phys. Lett.* **2014**, *104*, 241902.
- [302] H. Qu, S. Bhattacharyya, P. Ducheyne, *Sol-Gel Processed Oxide Controlled Release Materials*; 2011.
- [303] C. A. Stewart, Y. Finer, B. D. Hatton, *Sci. Rep.* **2018**, *8*, 895.
- [304] S. Atefyekta, B. Ercan, J. Karlsson, E. Taylor, S. Chung, T. J. Webster, M. Andersson, *Int. J. Nanomedicine* **2016**, *11*, 977.
- [305] D. F. Lionello, P. Y. Steinberg, M. M. Zalduendo, G. J. A. A. Soler-Illia, P. C. Angelomé, M. C. Fuertes, *J. Phys. Chem. C*. **2017**, *121*, 22576.
- [306] Y. Gaillard, V. J. Rico, E. Jimenez-Pique, A. R. González-Elipe, *J. Phys. D. Appl. Phys.* **2009**, *42*, 145305.
- [307] M. Laub, H. P. Jennissen, T. Seul, E. Schmachtenberg, *Materwiss. Werksttech.* **2001**, *32*, 926.
- [308] J. M. Anderson, *Annu. Rev. Mater. Res.* **2001**, *31*, 81.
- [309] P. C. Angelomé, G. J. de A. A. Soler-Illia, *Chem. Mater.* **2005**, *17*, 322.
- [310] K. Anselme, *Biomaterials*. **2000**, *21*, 667.
- [311] Z. Zhang, B. Gu, W. Zhu, L. Zhu, *Exp. Ther. Med.* **2013**, *6*, 707.
- [312] S. H. Gong, H. Lee, A. Pae, K. Noh, Y. M. Shin, J. H. Lee, Y. H. Woo, *J. Adv. Prosthodont.* **2013**, *5*, 416.
- [313] K. A. DeMali, *Trends Biochem. Sci.* **2004**, *29*, 565.
- [314] J. D. Humphries, P. Wang, C. Streuli, B. Geiger, M. J. Humphries, C. Ballestrem, *J. Cell Biol.* **2007**, *179*, 1043.
- [315] J. de Queiroz Fernandes, V. N. de Lima, J. P. Bonardi, O. M. Filho, S. B. F. Queiroz, *J. Maxillofac. Oral Surg.* **2018**, *17*, 13.
- [316] S. Sun, Y. Zhang, D. Zeng, S. Zhang, F. Zhang, W. Yu, *J. Mater. Sci. Mater. Med.*

- 2018**, 29, 141.
- [317] M. Lingner, R. Seidling, L. J. Lehmann, E. Mauermann, U. Obertacke, M. L. R. Schwarz, *J. Orthop. Surg. Res.* **2018**, 13, 219.
- [318] W. F. Oliveira, P. M. S. Silva, R. C. S. Silva, G. M. M. Silva, G. Machado, L. C. B. B. Coelho, M. T. S. Correia, *J. Hosp. Infect.* **2018**, 98, 111.
- [319] K. Lewis, *Antimicrob. Agents Chemother.* **2001**, 45, 999.
- [320] R. M. Donlan, J. W. Costerton, *Clin. Microbiol. Rev.* **2002**, 15, 167.
- [321] M. Butterworth, T. Payne, In *Complications in Foot and Ankle Surgery*; Springer International Publishing: Cham, 2017; pp. 69–87.
- [322] E. S. McBryde, L. C. Bradley, M. Whitby, D. L. S. McElwain, *J. Hosp. Infect.* **2004**, 58, 104.
- [323] K. Rutledge-Taylor, A. Matlow, D. Gravel, J. Embree, N. Le Saux, L. Johnston, K. Suh, J. Embil, E. Henderson, M. John, V. Roth, A. Wong, J. Shurgold, G. Taylor, Canadian Nosocomial Infection Surveillance Program, *Am. J. Infect. Control* **2012**, 40, 491.
- [324] R. M. Klevens, J. R. Edwards, C. L. Richards, T. C. Horan, R. P. Gaynes, D. A. Pollock, D. M. Cardo, *Public Health Rep.* **2007**, 122, 160.
- [325] Q. Yu, Z. Wu, H. Chen, *Acta Biomater.* **2015**, 16, 1.
- [326] J. Gallo, M. Holinka, C. S. Moucha, *Int. J. Mol. Sci.* **2014**, 15, 13849.
- [327] I. Kurtz, J. Schiffman, I. S. Kurtz, J. D. Schiffman, *Materials (Basel)*. **2018**, 11, 1059.
- [328] B. Hu, C. Owh, P. L. Chee, W. R. Leow, X. Liu, Y.-L. Wu, P. Guo, X. J. Loh, X. Chen, *Chem. Soc. Rev.* **2018**.
- [329] X. Ding, S. Duan, X. Ding, R. Liu, F.-J. Xu, *Adv. Funct. Mater.* **2018**, 1802140.
- [330] A. Idrees, P. Varela, F. Ruini, J. M. Vasquez, J. Salber, U. Greiser, W. Wang, S. McMahon, S. Sartori, G. Ciardelli, V. Chiono, V. Chiono, *Biomed. Sci. Eng.* **2018**, 2.
- [331] A. Bassegoda, K. Ivanova, E. Ramon, T. Tzanov, *Appl. Microbiol. Biotechnol.* **2018**, 102, 2075.
- [332] M. R. E. Santos, P. V. Mendonça, M. C. Almeida, R. Branco, A. C. Serra, P. V. Morais, J. F. J. Coelho, *Biomacromolecules* **2018**, acs.biomac.8b00685.
- [333] S. Li, S. Dong, W. Xu, S. Tu, L. Yan, C. Zhao, J. Ding, X. Chen, *Adv. Sci.* **2018**, 5, 1700527.
- [334] G. Baier, A. Cavallaro, K. Friedemann, B. Müller, G. Glasser, K. Vasilev, K. Landfester, *Nanomedicine Nanotechnology, Biol. Med.* **2014**, 10, 131.
- [335] J. J. Richardson, M. Bjornmalm, F. Caruso, *Science (80-.)*. **2015**, 348, aaa2491.
- [336] N. J. Shah, M. L. Macdonald, Y. M. Beben, R. F. Padera, R. E. Samuel, P. T. Hammond, *Biomaterials* **2011**, 32, 6183.
- [337] J. Min, R. D. Braatz, P. T. Hammond, *Biomaterials* **2014**, 35, 2507.
- [338] M. L. Macdonald, R. E. Samuel, N. J. Shah, R. F. Padera, Y. M. Beben, P. T.

- Hammond, *Biomaterials* **2011**, *32*, 1446.
- [339] D. Choi, M. Komeda, J. Heo, J. Hong, M. Matsusaki, M. Akashi, *ACS Biomater. Sci. Eng.* **2018**, *4*, 1833.
- [340] S. Zhang, M. Xing, B. Li, S. Zhang, M. Xing, B. Li, *Int. J. Mol. Sci.* **2018**, *19*, 1641.
- [341] S. B. Goodman, Z. Yao, M. Keeney, F. Yang, *Biomaterials* **2013**, *34*, 3174.
- [342] G. Romero, O. Ochoteco, D. J. Sanz, I. Estrela-Lopis, E. Donath, S. E. Moya, *Macromol. Biosci.* **2013**, *13*, 903.
- [343] M. C. Dixon, *J. Biomol. Tech.* **2008**, *19*, 151.
- [344] E. Guzmán, A. Mateos-Maroto, M. Ruano, F. Ortega, R. G. Rubio, *Adv. Colloid Interface Sci.* **2017**, *249*, 290.
- [345] L. Peng, F. Cheng, Y. Zheng, Z. Shi, W. He, *Langmuir* **2018**, *34*, 10748.
- [346] C. Su, J. Sun, X. Zhang, D. Shen, S. Yang, C. Su, J. Sun, X. Zhang, D. Shen, S. Yang, *Polymers (Basel)*. **2017**, *9*, 363.
- [347] J. M. Anderson, A. Rodriguez, D. T. Chang, *Semin. Immunol.* **2008**, *20*, 86.
- [348] A. Bonyár, *Micron* **2016**, *87*, 1.
- [349] V. I. Kulikouskaya, M. E. Lazouskaya, A. N. Kraskouski, V. E. Agabekov, *Russ. J. Phys. Chem. A* **2018**, *92*, 146.
- [350] V. I. Kulikouskaya, S. V. Pinchuk, K. S. Hileuskaya, A. N. Kraskouski, I. B. Vasilevich, K. A. Matievski, V. E. Agabekov, I. D. Volotovskii, *J. Biomed. Mater. Res. Part A* **2018**, *106*, 2093.
- [351] M. Arruebo, N. Vilaboa, J. Santamaria, *Expert Opin. Drug Deliv.* **2010**, *7*, 589.
- [352] X. Song, W. Tang, D. Gregurec, L. Yate, S. E. Moya, G. Wang, *Appl. Surf. Sci.* **2018**, *436*, 653.
- [353] M. Echeverry-Rendón, O. Galvis, R. Aguirre, S. Robledo, J. G. Castaño, F. Echeverría, *J. Mater. Sci. Mater. Med.* **2017**, *28*, 169.
- [354] W. Chen, X. Shen, Y. Hu, K. Xu, Q. Ran, Y. Yu, L. Dai, Z. Yuan, L. Huang, T. Shen, K. Cai, *Biomaterials* **2017**, *114*, 82.
- [355] Z. Xu, H. Lu, J. Lu, C. Lv, X. Zhao, G. Wang, *RSC Adv.* **2018**, *8*, 3051.
- [356] J. Park, S. Bauer, A. Pittrof, M. S. Killian, P. Schmuki, K. von der Mark, *Small* **2012**, *8*, 98.
- [357] X. Hu, K.-G. Neoh, Z. Shi, E.-T. Kang, C. Poh, W. Wang, *Biomaterials* **2010**, *31*, 8854.
- [358] E. O'Neill, G. Awale, L. Daneshmandi, O. Umerah, K. W.-H. Lo, *Drug Discov. Today* **2018**, *23*, 879.
- [359] P. J. Marie, P. Ammann, G. Boivin, C. Rey, *Calcif. Tissue Int.* **2001**, *69*, 121.
- [360] A. L.-J. Liu, P.-W. Shen, P.-J. Chen, *Clin. Cases Miner. Bone Metab.* **2013**, *10*, 206.
- [361] L. Maïmoun, T. C. Brennan, I. Badoud, V. Dubois-Ferriere, R. Rizzoli, P. Ammann, *Bone* **2010**, *46*, 1436.
- [362] M. J. Bolland, A. Grey, *BMJ* **2016**, *354*, i5109.

References

- [363] V. Offermanns, O. Z. Andersen, G. Riede, M. Sillassen, C. S. Jeppesen, K. P. Almtoft, H. Talasz, C. Öhman-Mägi, B. Lethaus, R. Tolba, F. Kloss, M. Foss, *Acta Biomater.* **2018**, *69*, 385.
- [364] C. Zhou, A. Xu, D. Wang, G. Lin, T. Liu, F. He, *Biomater. Sci.* **2018**, *6*, 1946.
- [365] Y. Li, Y. Qi, Q. Gao, Q. Niu, M. Shen, Q. Fu, K. Hu, L. Kong, *Int. J. Nanomedicine* **2015**, *10*, 4549.
- [366] W. Zhang, H. Cao, X. Zhang, G. Li, Q. Chang, J. Zhao, Y. Qiao, X. Ding, G. Yang, X. Liu, X. Jiang, *Nanoscale* **2016**, *8*, 5291.
- [367] N. Li, L. Zhang, Y. Chen, M. Fang, J. Zhang, H. Wang, *Adv. Funct. Mater.* **2012**, *22*, 835.
- [368] E. Nielsen, K. Greve, O. Ladefoged, *Strontium, inorganic and soluble salts Evaluation of health hazards and proposal of health based quality criteria for drinking water*; 2013.
- [369] D. F. Jacques, B. I. Bourland, *Soc. Pet. Eng. J.* **1983**, *23*, 292.
- [370] C. Christgau, H. Hansen, J. Nilsson, S. Andersen, Water-soluble strontium salts for use in treatment of cartilage and/or bone conditions **2003**.
- [371] D. Grosso, C. Boissière, B. Smarsly, T. Brezesinski, N. Pinna, P. A. Albouy, H. Amenitsch, M. Antonietti, C. Sanchez, *Nat. Mater.* **2004**, *3*, 787.
- [372] J. L. Vivero-Escoto, Y.-D. Chiang, K. Wu, Y. Yamauchi, *Sci. Technol. Adv. Mater.* **2012**, *13*, 13003.
- [373] A. L. Sangle, S. Singh, J. Jian, S. R. Bajpe, H. Wang, N. Khare, J. L. MacManus-Driscoll, *Nano Lett.* **2016**, *16*, 7338.
- [374] M. G. Bellino, S. Golbert, M. C. De Marzi, G. J. A. A. Soler-, *Biomater. Sci.* **2013**, *1*, 186.
- [375] J. Shi, Y. Li, Y. Gu, S. Qiao, X. Zhang, H. Lai, *Sci. Rep.* **2017**, *7*, 15563.
- [376] E. M. Brown, *Osteoporos. Int.* **2003**, *14*, 25.
- [377] N. Chattopadhyay, S. J. Quinn, O. Kifor, C. Ye, E. M. Brown, *Biochem. Pharmacol.* **2007**, *74*, 438.
- [378] C. Sanchez, C. Boissiere, S. Cassaignon, C. Chaneac, O. Durupthy, M. Faustini, D. Grosso, C. Laberty-Robert, L. Nicole, D. Portehault, F. Ribot, L. Rozes, C. Sassoie, *Chem. Mater.* **2014**, *26*, 221.
- [379] G. J. A. A. Soler-Illia, P. Innocenzi, *Chem. - A Eur. J.* **2006**, *12*, 4478.
- [380] P. Innocenzi, L. Malfatti, *Chem. Soc. Rev.* **2013**, *42*, 4198.
- [381] P. C. Angelomé, S. Aldabe-Bilmes, M. E. Calvo, E. L. Crepaldi, D. Grosso, C. Sanchez, G. J. A. A. Soler-Illia, *New J. Chem.* **2005**, *29*, 59.
- [382] K. D. Dobson, A. J. McQuillan, *Spectrochim. Acta Part A Mol. Biomol. Spectrosc.* **1999**, *55*, 1395.
- [383] P. C. Angelomé, M. C. Fuertes, G. J. A. A. Soler-Illia, *Adv. Mater.* **2006**, *18*, 2397.
- [384] L. Nicole, C. Boissière, D. Grosso, P. Hesemann, J. Moreau, C. Sanchez, *Chem. Commun.* **2004**, *0*, 2312.

- [385] D. A. Doshi, A. Gibaud, N. Liu, D. Sturmayer, A. P. Malanoski, Darren R. Dunphy, H. Chen, S. Narayanan, A. MacPhee, J. Wang, S. T. Reed, A. J. Hurd, A. Frank van Swol, C. J. Brinker, **2003**.
- [386] I. L. Violi, M. D. Perez, M. C. Fuertes, G. J. A. A. Soler-Illia, *ACS Appl. Mater. Interfaces* **2012**, *4*, 4320.
- [387] F. Twaiq, M. S. Nasser, S. A. Onaizi, *Front. Chem. Sci. Eng.* **2014**, *8*, 488.
- [388] Y. Qiao, M. Ma, Y. Liu, S. Li, Z. Lu, H. Yue, H. Dong, Z. Cao, Y. Yin, S. Yang, *J. Mater. Chem. A* **2016**, *4*, 15565.
- [389] A. Fitch, S. Dragan, *J. Chem. Educ.* **1998**, *75*, 1018.
- [390] H. H. G. Tsai, G. L. Jheng, H. M. Kao, *J. Am. Chem. Soc.* **2008**, *130*, 11566.
- [391] R. M. Silverstein, G. C. Bassler, T. C. Morrill, *Spectrometric identification of organic compounds*; Wiley, 1991.
- [392] P. Innocenzi, *J. Non. Cryst. Solids* **2003**, *316*, 309.
- [393] A. Piccolo, F. J. Stevenson, *Geoderma* **1982**, *27*, 195.
- [394] P. Innocenzi, L. Malfatti, M. Piccinini, A. Marcelli, *J. Phys. Chem. A* **2010**, *114*, 304.
- [395] C. Pecharromán, F. Gracia, J. P. Holgado, M. Ocaña, A. R. González-Elipe, J. Bassas, J. Santiso, A. Figueras, *J. Appl. Phys.* **2003**, *93*, 4634.
- [396] A. Hozumi, H. Sugimura, K. Hiraku, T. Kameyama, O. Takai, *Chem. Mater.* **2000**, *12*, 3842.
- [397] A. M. Dattelbaum, M. L. Amweg, J. D. Ruiz, L. E. Ecke, A. P. Shreve, A. N. Parikh, *J. Phys. Chem. B* **2005**, *109*, 14551.
- [398] M. T. J. Keene, R. Denoyel, P. L. Llewellyn, *Chem. Commun.* **1998**, *0*, 2203.
- [399] G. A. B. Silva, B. M. Bertassoli, C. A. Sousa, J. D. Albergaria, R. S. de Paula, E. C. Jorge, *J. Bone Miner. Metab.* **2018**, *36*, 73.
- [400] Z. Mao, Z. Fang, Y. Yang, X. Chen, Y. Wang, J. Kang, X. Qu, W. Yuan, K. Dai, *RSC Adv.* **2017**, *7*, 24607.
- [401] A. Bakhit, N. Kawashima, K. Hashimoto, S. Noda, K. Nara, M. Kuramoto, K. Tazawa, T. Okiji, *Sci. Rep.* **2018**, *8*, 9224.
- [402] P. Naruphontjirakul, A. E. Porter, J. R. Jones, *Acta Biomater.* **2018**, *66*, 67.

List of Publications

- (1) Ciganda, R.; Gu, H.; Hernandez, R.; **Escobar, A.**; Martínez, A.; Yates, L.; Moya, S.; Ruiz, J.; Astruc, D. Electrostatic Assembly of Functional and Macromolecular Ferricinium Chloride-Stabilized Gold Nanoparticles. *Inorg. Chem.* **2017**, *56* (5), 2784–2791.
- (2) Fu, F.; Martinez, A.; Wang, C.; Ciganda, R.; Yate, L.; **Escobar, A.**; Moya, S.; Fouquet, E.; Ruiz, J.; Astruc, D. Exposure to Air Boosts CuAAC Reactions Catalyzed by PEG-Stabilized Cu Nanoparticles. *Chem. Commun.* **2017**, *53* (39), 5384–5387.
- (3) **Escobar, A.**; Yate, L.; Grzelczak, M.; Amenitsch, H.; Moya, S. E.; Bordoni, A. V.; Angelome, P. C. One-Step Synthesis of Mesoporous Silica Thin Films Containing Available COOH Groups. *ACS Omega.* **2017**, *2* (8), 4548–4555.
- (4) Fu, F.; Martinez-Villacorta, A. M.; **Escobar, A.**; Irigoyen, J.; Moya, S.; Fouquet, E.; Ruiz, J.; Astruc, D. Synthesis of Late Transition-Metal Nanoparticles by Na Naphthalenide Reduction of Salts and Their Catalytic Efficiency. *Inorg. Chem. Front.* **2017**, *4* (12), 2037–2044.
- (5) Andreozzi, P.; Diamanti, E.; Py-Daniel, K. R.; Cáceres-Vélez, P. R.; Martinelli, C.; Politakos, N.; **Escobar, A.**; Muzi-Falconi, M.; Azevedo, R.; Moya, S. E. Exploring the pH Sensitivity of Poly(allylamine) Phosphate Supramolecular Nanocarriers for Intracellular siRNA Delivery. *ACS Appl. Mater. Interfaces* **2017**, *9* (44), 38242–38254.
- (6) Murray, R. A.; **Escobar, A.**; Bastús, N. G.; Andreozzi, P.; Puentes, V.; Moya, S. E. Fluorescently Labelled Nanomaterials in Nanosafety Research: Practical Advice to Avoid Artefacts and Trace Unbound Dye. *NanoImpact* **2018**, *9*, 102–113.
- (7) Fu, F.; Wang, Q.; Ciganda, R.; Martinez-Villacorta, A. M.; **Escobar, A.**; Moya, S.; Fouquet, E.; Ruiz, J.; Astruc, D. Electron- and Hydride-Reservoir Organometallics as Precursors of Catalytically Efficient Transition Metal Nanoparticles in Water. *Chem. - A Eur. J.* **2018**, *24* (25), 6645–6653.
- (8) Wang, Q.; Fu, F.; **Escobar, A.**; Moya, S.; Ruiz, J.; Astruc, D. “Click” Dendrimer-Stabilized Nanocatalysts for Efficient Hydrogen Release upon Ammonia-Borane Hydrolysis. *ChemCatChem* **2018**, *10* (12), 2673–2680.
- (9) Fu, F.; Wang, C.; Wang, Q.; Martinez-Villacorta, A. M.; **Escobar, A.**; Chong, H.; Wang, X.; Moya, S.; Salmon, L.; Fouquet, E.; et al. Highly Selective and Sharp Volcano-Type Synergistic Ni₂Pt@ZIF-8-Catalyzed Hydrogen Evolution from Ammonia Borane Hydrolysis. *J. Am. Chem. Soc.* **2018**, *140* (31), 10034–10042.
- (10) Fu, F.; Ciganda, R.; Wang, Q.; Tabey, A.; Wang, C.; **Escobar, A.**; Martinez-Villacorta, A. M.; Hernández, R.; Moya, S.; Fouquet, E.; et al. Cobaltocene Reduction of Cu and Ag Salts and Catalytic Behavior of the Nanoparticles Formed. *ACS Catal.* **2018**, *8* (9), 8100–8106.
- (11) **Ane Escobar**, Nicolás Muzzio, Emerson Coy, Hui Liu, Guocheng Wang, Paula

List of Publications

- C. Angelomé, Mihaela Delcea, Marek Grzelczak and Sergio E. Moya. Antibacterial Layer-by-layer Films of poly(acrylic acid)-gentamicin Complexes with a combined burst and sustainable Release of Gentamicin. *Submitted in Advanced Materials Interfaces*
- (12) **Ane Escobar**, Nicolás Muzzio, Omar Azzaroni, Marek Grzelczak, and Sergio E. Moya. Antibacterial Layer-by-layer Films of poly(acrylic acid)-gentamicin Complexes with a combined burst and sustainable Release of Gentamicin. *Submitted in ACS Applied Materials and Interfaces*.
- (13) **A. Escobar**, N. Muzzio, P. C. Angelomé, A. V. Bordoni, A. Martínez, E. Bindini, E. Coy, M. Grzelczak, S. E. Moya. Strontium Titanate (SrTiO₃) mesoporous coatings for enhanced Strontium delivery and osseointegration on bone implants. *In preparation*.
- (14) **A. Escobar**, E. Bindini, N. Muzzio, A. Martinez, M. Grzelczak, S. E. Moya, A. V. Bordoni and P. C. Angelomé. COOH-functionalized mesoporous titania film for complexation and controlled release of bioactive ions. *In preparation*.